In Situ UV-VIS-NIR Absorption Spectroscopy and Catalysis

Authors:

Max Bols[a], Jing Ma[a], Fatima Rammal, Dieter Plessers, Xuejiao Wu, Sara Navarro-Jaén, Alexander J. Heyer, Bert Sels*, Edward Solomon*, Robert Schoonheydt*

Contact corresponding authors at: Bert.sels@kuleuven.be, Edward.solomon@stanford.edu, Robert.schoonheydt@kuleuven.be

[a] These authors contributed equally

Abstract: *This review highlights in situ UV-VIS-NIR range absorption spectroscopy in catalysis. A variety of experimental techniques identifying reaction mechanisms, kinetics, and structural properties is discussed. Stopped flow techniques, use of laser pulses, and use of experimental perturbations are demonstrated for in situ studies of enzymatic, homogeneous, heterogeneous, and photocatalysis. They access different time scales and are applicable to different reaction systems and catalyst types. In photocatalysis, femto- and nanosecond resolved measurements through transient absorption are discussed for tracking excited states. UV-VIS-NIR absorption spectroscopies for structural characterization are demonstrated especially for Cu and Fe exchanged zeolites and metalloenzymes. This requires combining different spectroscopies. Combining magnetic circular dichroism and resonance Raman spectroscopy is especially powerful. A multitude of phenomena can be tracked on transition metal catalysts on various supports, including changes in oxidation state, adsorptions, reactions, support interactions, surface plasmon resonances, and band gaps. Measurements of oxidation states, oxygen vacancies, and band gaps are shown on heterogeneous catalysts, especially for electrocatalysis. UV-VIS-NIR absorption is burdened by broad absorption bands. Advanced analysis techniques enable the tracking of coking reactions on acid zeolites despite convoluted spectra. The value of UV-VIS-NIR absorption spectroscopy to catalyst characterization and mechanistic investigation is clear, but could be expanded.*

Table of contents

1. Introduction 3
2. The role of *in situ* UV-VIS-NIR absorption spectroscopies 4
   2.1 Characteristics of UV-VIS-NIR absorption spectra in catalysis 5
   2.2 Collection and processing of *in situ* absorption spectra 9
      2.2.1 Modes of irradiation and light collection 9
         2.2.1.1 Transmission and diffuse reflectance spectroscopy 10
         2.2.1.2 Fiber optics 11
         2.2.1.3 Improving time and spatial resolution 12
      2.2.2 Conditions- and time-dependent measurements 13
         2.2.2.1 Varying temperature and magnetic field 13
         2.2.2.2 Time dependent measurements 15

2.2.3 Processing of spectroscopic data 18
2.2.3.1 The Lambert-Beer and Kubelka-Munk functions 18
2.2.3.2 Band gap energies 20
2.3 Coupling to complementary techniques 23
3. Research in catalysis with *in situ* UV-VIS-NIR spectroscopy 25
3.1 Heterogeneous thermal catalysis 25
3.1.1 Tracking metal and metal oxide bulk and surface properties 25
3.1.1.1 Supported noble metal nanoparticles 25
3.1.1.2 Transition metal oxide catalysts 31
3.1.2 Identification and tracking of dispersed catalytic molecular clusters 34
3.1.2.1 UV-VIS-NIR fingerprinting on Cu and Fe exchanged zeolites 35
3.1.2.2 Partial oxidation of methane to methanol with Cu-zeolites 37
3.1.2.3 Selective catalytic reduction of NO by NH_3 with Cu zeolites 42
3.1.2.4 Selective catalytic reduction of NO by NH_3 with Fe zeolites 46
3.1.2.5 N_2O decomposition with Fe zeolites 48
3.1.2.6 C-H bond activation with α-O on Fe-zeolites 50
3.1.2.7 Non-zeolitic single atom catalysts 51
3.1.3 Tracking chromophoric products 51
3.1.3.1 zeolite catalyzed methanol to hydrocarbons 51
3.2 Homogeneous thermal catalysis 59
3.2.1 Organometallic catalysts 60
3.2.1.1 Selected applications of stopped flow absorption 60
3.2.1.2 Applications of C-term MCD 62
3.2.1.3 Applications of CD 64
3.2.1.4 Further reactions 65
3.2.2 Non-organometallic transformation 71
3.2.2.1 Imide reduction 71
3.2.2.2 Cycloaddition 72
3.3 Enzymes 73
3.3.1 Kinetics: stopped-flow absorption and rapid freeze quench trapping 74
3.3.2 Resonance Raman profiling of absorption bands 75
3.3.3 The application of magnetic circular dichroism spectroscopy 77
3.3.4 Correlation of enzyme active site intermediates to metallozeolite catalysts 81
3.4 Electrocatalysis 82
3.5 Photocatalysis 86
3.5.1 Transient absorption to monitor ultrafast processes (fs-to-s time scale) 87

3.5.2 Time-course spectra to monitor reaction changes (s-to-day time scale).....91
4. Outlook and Conclusions.....94
5. References 95
6. Acknowledgements 118
7. List of abbreviations 118
8. Biographies.....120
9. Abstract figure 123

1. Introduction

The Ultraviolet-Visible-Near Infrared (UV-VIS-NIR) range of photon energies encompasses wavenumbers between 4 000 - 50 000 cm^{-1}, or wavelengths between 200 – 2 500 nm. It corresponds to the energies of several chemically relevant electronic excitations, but excludes ionizations that require vacuum UV energies or above. The electronic excitations most notably include $n \rightarrow \pi^*$ and $\pi \rightarrow \pi^*$ transitions in organic molecules, the d-d, ligand-to-metal charge transfer (LMCT) and metal-to-ligand charge transfer (MLCT) transitions in transition metal ions (TMI) complexes, various transitions in the electronic shells of rare earth metals, and band gaps of semiconductors. Also structural defects in materials can be effectively probed through their effect on electronic transition energies. In the NIR region overtones and combinations bands of O-H, C-H and N-H vibrations are observed. This plethora of possibilities to study atoms, molecules and solids has moved researchers to use UV-VIS-NIR spectroscopy in the study of catalysts and catalytic reactions, especially those involving 3d TMIs. Their d-d transitions are observed in the VIS-NIR region and their MLCT absorption bands lie mainly in the UV-VIS. For centrosymmetric complexes, d-d transitions are symmetry (Laporte) forbidden, and often they are also spin forbidden. Therefore they are often weak. LMCT and MLCT transitions on the other hand are usually symmetry and spin allowed and therefore intense (e.g. Figure 1). Two standard reference works on ligand field theory are the books by Lever and Solomon covering the fundamentals and interpretation of d-d and charge transfer transitions.[1, 2] Further selection rules can be exploited to derive structural and electronic insight on molecules using circular dichroism (CD) and magnetic circular dichroism (MCD).

Spectroscopic investigation of a catalyst under reaction conditions is called *in situ* spectroscopy. If the reaction products are simultaneously measured - for instance by gas chromatography (GC), liquid chromatography (LC), or mass spectrometry (MS) - at the outlet of the reactor, the term *operando* spectroscopy is used. In this review the umbrella term *in situ* spectroscopy is preferably used whether or not the reaction products are analyzed, unless the measurement of reaction products is of particular relevance. For photon absorption spectroscopy, commonly used measurements are transmission mode, specular reflection, and diffuse reflectance spectroscopy (DRS). *In situ* spectroscopy requires spectroscopic reaction cells. For solid or powdered catalysts fibre optic spectroscopy is used. An overview of such setups is given in Weckhuysen's recent book chapters,[3, 4] and the reaction cells have been discussed by Bravo-Suarez and Srinivasan.[5] Whether these reaction cells deliver relevant kinetic data was discussed by Valecillos et al.[6] Given the ample attention the topic has received in excellent recent reviews, we will not focus on this aspect.

The review starts with some fundamentals of UV-VIS-NIR absorption spectroscopy. The selection rules for the absorption of non-polarized and circularly polarized light are mentioned. Subsequently different techniques and analysis methods to extract valuable information on catalysis are discussed. UV-VIS-NIR absorption spectroscopy has been applied in all areas of catalysis: heterogeneous, homogeneous, enzymatic catalysis, photocatalysis and electrocatalysis, and will be discussed per subfield in separate sections. Techniques and spectroscopies that are specific for one area will be highlighted by state-of-the-art examples in that section. In the area of heterogeneous catalysis zeolites with TMIs are given ample attention. In zeolites TMIs can occupy well-defined crystallographic sites enabling the measurement of site-specific or fingerprint spectra of the active sites. Such spectra, or specific bands in these spectra, can be used for kinetic measurements and they serve as guides to identify these sites in other catalysts. Other types of heterogeneous catalysts, including supported nanoparticles, metal oxide surfaces, and single atom catalysts are then explored. For homogeneous and enzymatic catalysis the focus lies on metal-organic transition metal complexes. The use of various techniques to measure kinetics is highlighted, as well as the use of (magnetic) circular dichroism in the UV-VIS-NIR range. Coupled amperometry and other electrochemical analytics, and UV-VIS-NIR absorption under different applied potentials are central in the examples given in the electrocatalysis section. In the photocatalysis section, attention is given to ultrafast measurements through transient absorption (TA).

The contents of this review provide an integrated update of several related publications, with a widened scope and a deeper focus on experimental methods with recent literature examples. The starting points are the reviews and chapters by Jentoft, Weckhuysen and Schoonheydt.[4, 7, 8] Related topics were also recently reviewed specifically for photocatalysis,[9] and electrocatalysis.[10] Further elements are treated on (magnetic) circular dichroism, modelling of the absorption spectra, and the use of time- and conditions dependent measurements. While theoretical backgrounds are provided in brief, a selection of handbooks is referred to for further reading. At the end critical conclusions and an outlook on the further potential of *in situ* UV-VIS-NIR absorption spectroscopy for catalysis are given.

2. The role of *in situ* UV-VIS-NIR absorption spectroscopies

Spectroscopies in the UV-VIS-NIR range enable access to structural and electronic information for several categories of materials in both gas phase and condensed phase. It can do so using relatively low cost equipment and for a range of physical conditions. Several experimental and data analysis methodologies that include UV-VIS-NIR range spectroscopy can be employed for different purposes.

Table 1 gives an overview of the topics included in this review. The application of *in situ* UV-VIS-NIR spectroscopy in each of these catalysis types will be presented and the findings of the studies will be discussed.

Table 1. Overview of the catalysis studies using *in situ* UV-VIS-NIR spectroscopy discussed in this review.

Catalysis type	Reactions	Coupled spectroscopies [a]

Heterogeneous catalysis	Partial oxidation of methane to methanol with Cu-zeolites	XAS, Mössbauer, rR, Raman, MCD, IR, NMR, EPR
	NH_3-SCR with Cu- and Fe- zeolites	
	N_2O decomposition and C-H activation with Fe-zeolites	
	Methanol to hydrocarbons with zeolite	
	Oxidation reactions (e.g. CO oxidation and water-gas shift reaction) with supported Au catalysts	
	Hydrogenation reactions (e.g. hydrogenation of CO and CO_2 to methanol and reverse water-gas shift reaction) with supported Au catalysts	
	Dehydrogenation of isobutane with supported CrO_x catalysts	
	NH_3-SCR and oxidative dehydrogenation of propane with supported VO_x catalysts	
	Reverse water-gas shift reaction with cubic In_2O_3	
Homogenous catalysis	Metathesis reactions, ligand substitution and catalytic oxidation of H_2O to O_2 with Grubbs catalysts	IR, Raman, NMR, EPR
	Synthesis of organometallic complexes	
	Oxidative addition of organometallic complexes	
	C-C coupling reactions with high-valent Ni complexes catalysts	
	C-C cross-coupling reactions with Fe-SciOPP catalysts	
	Michael addition of malonate to nitrostyrenes with asymmetric copper catalyst	
	Ethylene oligomerization, alcohol oxidation, asymmetric hydrogenation, dehydroperoxidation of cyclohexyl hydroperoxide and formic acid dehydrogenation with organometallic catalysts	
	Non-organometallic transformation (e.g. Imide reduction and cycloaddition)	
Enzymatic catalysis	Methane to methanol with soluble methane monooxygenase	IR, rR, MCD, EPR
	Monooxygenation by the enzyme tyrosinase	
	Selective substrate halogenation by the α-ketoglutarate dependent Fe enzyme SyrB2	
Electrocatalysis	Electrocatalytic hydrogen evolution with Co-based MOF	XPS, IR
	CO_2 reduction in water with Co-based COF	
	Electrocatalytic oxygen evolution with Ir-based and Ni-based catalysts	
Photocatalysis	H_2 generation with CdSe/CdS-Pt and CdS-Pt NRs	IR, NMR, EPR
	CO_2 reduction with Ni^{II} complex, Cu/TiO_2 and Re-COF catayst	
	Lignin conversion with cadmium sulfide quantum dots	
	Degradation of the intelligent ink with TiO_2	

[a] Refers to coupled spectroscopies in the studies discussed in this review, not to the spectroscopies used in the field in general

2.1 Characteristics of UV-VIS-NIR absorption spectra in catalysis

This section briefly runs through a few fundamentals on absorption spectroscopy in the UV-VIS-NIR range. To find a more rigorous and extensive treatment of the topic, the handbook by Lever et al.[1] is advised. It explains the theory behind electronic spectroscopy in general, and also includes chapters on symmetry and group theory. An updated version focusing more on inorganic compounds was published in 2000 by Lever and Solomon.[2] A recent counterpart on organic molecules is more difficult to find. There are the publications on solvatochromisms by P. Suppan and the handbook by Mataga and Kubota, as well as the spectrum database by Hirayama and Kenzo.[11-13] For a fundamental treatment of the physical chemistry the handbook by Atkins and Friedman is advised.[14]

The UV-VIS-NIR absorption spectrum is visualized as photon intensity that remains after irradiation of the sample, plotted against photon energy. Usually this is displayed relative to a reference measurement. The photon energy can be plotted in several units. The use of frequency (commonly as wavenumbers in cm^{-1}) is popular, as well as wave period (commonly as wavelength in nm). The latter is however inversely proportional to energy and therefore not recommended. Another common unit is electronvolts (eV) popular in band gap analysis.

An electronic absorption spectrum of a catalytic system is generally challenging to interpret due to the multitude of possible excitations and their limited spectral resolution under relevant conditions. Each absorption event has its particular excitation energy and intensity. The excitation energy associated with a single electronic excitation event is spread over an energy range mainly through vibronic coupling due to excited state distortion. This results in a Poisson distribution that becomes Gaussian at large distortion. Other contributions to absorption band broadening are temperature dependent doppler broadening (Gaussian profile), and subtle inhomogeneities in the coordination sphere. This broadening leads to overlapping absorption bands that can be difficult to resolve. In solutions, dynamic solvent interactions additionally contribute to broadening. Absorption bands may also become asymmetrical depending on the predominant broadening phenomena. To deconvolute spectra, single absorption bands are most regularly approximated by Gaussian or more general Voight distributions which are then superimposed to approach the experimental spectrum (example in Figure 1).[15, 16] Especially in condensed matter with conjugated systems or in composites, macromolecules, and in solutions, discerning individual bands becomes difficult (e.g. Figures 32-34,44,45,57), but also for nearly single site supported TMI complexes this can be the case (e.g. the low energy d-d bands in Figure 1). Increasing density of energy levels eventually culminates in continuous energy bands, leading to a bandgap spectrum (e.g. Figures 10,11). As a consequence, while electronic absorption energies are highly sensitive to structure, they are difficult to use as unique identifiers absent a good preliminary understanding of the material structure and composition.

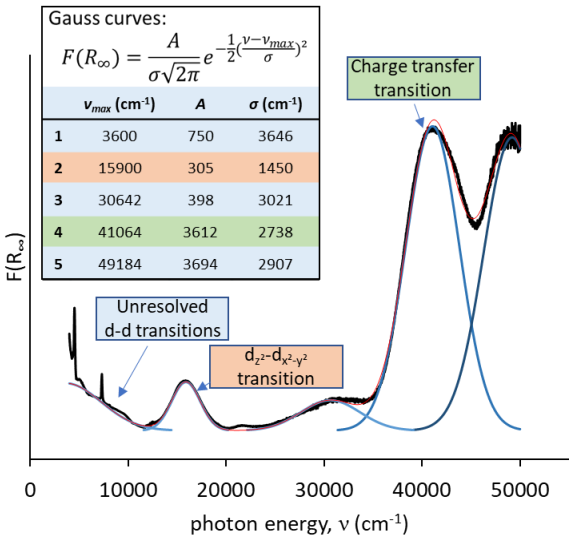


Figure 1. Room temperature diffuse reflectance spectrum of a calcined *BEA zeolite (Si/Al=12.5) loaded with 0.3 wt. % Fe (black curve) to contain nearly single site square planar coordinated Fe^{2+}.[17] The spectrum is deconvoluted with five gaussian band shapes (blue), the sum of the gaussian bands is given by the red curve. The insert gives the parameters of the gaussian bands; obtained from experiment. Copyright 2016 Springer Nature.

Traditionally, the analysis of UV-VIS-NIR absorption spectra has been based on databases of well identified complexes, looking for structural similarities. The book by Lever remains an

important reference work for transition metal complexes, and the collection by Hirayama and Kenzo for organic molecules.[1, 12] Simple spectra can, at least qualitatively, be explained with crystal field theory or ligand field theory. Important parameters are the coordination environment (symmetry and composition) and orbital energies determining band energy and absorption coefficients. Band interpretation is also aided by the band shape, and vibronic structure. Various selection rules arise from theory resulting in widely varying absorption probabilities that dictate the absorption intensity for individual electronic excitations.[1] For the UV-VIS-NIR range of electronic excitations the most important selection rules are eq 1 and eq 2.

$$\text{The spin selection rule: } \Delta S = 0 \tag{1}$$

$$\text{The orbital ('Laporte') selection rule: } \Delta l = +1 \text{ or } -1 \tag{2}$$

Both arise from the predominant excitation mechanism which occurs through the interaction of the photon and electronic transition electric dipole moments, together with the assumption that the spin (θ_s) and orbital (φ) parts of the electronic wavefunctions can be considered independently. Formally, the absorption probability is proportional to the square of the transition moment integral $\bar{P}$ (eq 3).

$$\bar{P} = \langle \varphi_2 | \bar{r} | \varphi_1 \rangle \langle \theta_{1,s} | \theta_{2,s} \rangle \tag{3}$$

Where the ground and excited state wavefunctions are denoted with respective subscripts 1 and 2, and with $\bar{r}$ the electric dipole operator.

The orbital selection rule is dependent on the symmetry of the involved orbitals, but also of the polarization of the incident light. Linear polarization can reveal the transition's electric dipole orientation, but requires an oriented sample and is not useful for the randomly oriented samples (powders, solutions, …) generally encountered in *in situ* spectroscopy for catalysis. Circular polarization is sensitive to enantiomers, but is scarcely applied to the *in situ* study of catalysts. The differential absorption of differently polarized light can be measured, resulting in linear or circular dichroism spectroscopy.. CD intensity is determined by the projection of the electric dipole transition moment into the magnetic dipole moment. Evaluating circular dichroism in a longitudinal magnetic field under varying temperatures and magnetic field strengths results in variable-temperature-variable-field (VTVH) magnetic circular dichroism (MCD), which has been applied to TMI catalysts (*vide infra*). In this case the magnetic field is used to lift the degeneracy of ground and/or excited electronic states, resulting in different transition moments and enabling circular dichroism for non-chiral absorption centra.[18, 19]

For ligand field transitions the selection rules are generally relaxed, and the degree to which they are relaxed determines the absorption probability. Typical ranges for absorption coefficients are given in Table 2. Foremost, the classification of TMI complexes' electronic transitions into d-d and charge transfer (CT) transitions is an approximation. Molecular orbitals of TMI complexes have a mixed metal and ligand character and the electronic transitions have varying degrees of CT and d-d (or f-f) character. Symmetry imposed selection rules are relaxed through non-centrosymmetric distortion of the ligand field and through vibronic coupling to odd parity vibrations. The spin selection rule is relaxed through spin-orbit coupling.[14]

Table 2. Typical ranges for molar absorption coefficients for UV-VIS-NIR electronic transitions depending on the relaxation of the selection rules.[1]

Type of Transition	Molar absorption coefficient range, ε (cm^{-1} M^{-1})

Spin & Laporte forbidden	10^{-3} - 10^{2}
Spin allowed & Laporte forbidden	10^{0} - 10^{4}
Spin & Laporte allowed	10^{2} – 10^{6}

The previous points indicate that the assignment and interpretation of individual absorption bands, let alone of the full spectra, is difficult. Both the excitation energies and the absorption probabilities depend on a large number of factors, and it is generally not feasible to obtain accurate orbital energies and absorption probabilities without computational aids. Several computationally implemented molecular modelling methods to simulate absorption spectra (including CD and MCD) from an optimized geometry are available.[20] The most popular is time-dependent density-functional theory (TD-DFT) which offers an appropriate balance between accuracy and speed to model systems of a size relevant in catalysis research. It is important that the chosen TD-DFT method is benchmarked for the type of system for which the spectrum is simulated, but also that the fundamental shortcomings of the method are carefully considered.[21, 22] More advanced methods (e.g. multireference and coupled cluster) can yield more accurate results, but they are computationally heavy. Therefore their application is limited to small structures, or small parts of larger structures.[20] Also here lies a risk for accuracy as long range charge transfer character may be missed, besides other misspecifications that can be made in setting up the calculation. Also for species in solution further extensions of the models are needed to accurately simulate the spectroscopy, introducing quantum mechanics/molecular mechanics (QM/MM) approaches.[23] In addition, further information on individual absorption bands can be obtained by coupling other analytic techniques, site selective spectroscopies, or exploiting synthesis-spectroscopy relations. In turn these can guide the computational modelling.

Unlike many other characterization techniques, UV-VIS-NIR absorption spectroscopy probes events and characteristics that are directly catalytically relevant. This is true especially for photocatalysis (Figure 2 B), but electronic ground and excited states are generally relevant to catalytic reactions as interpreted through frontier molecular orbitals (FMO) (Figure 2 A). The highest occupied molecular orbitals (HOMO) and lowest unoccupied orbitals (LUMO) play central roles in catalysis and in reactivity in general. The HOMO-LUMO gap often falls in the UV-VIS-NIR range. In many cases the LUMO functions as an electron acceptor in catalytic mechanisms (e.g. Figure 2 A, C). However, depending on the type of catalysis the electronic excitation may be induced via different mechanisms following different selection rules. Especially the possibility to study these electronic states *in situ* enables unique insights into catalysis.

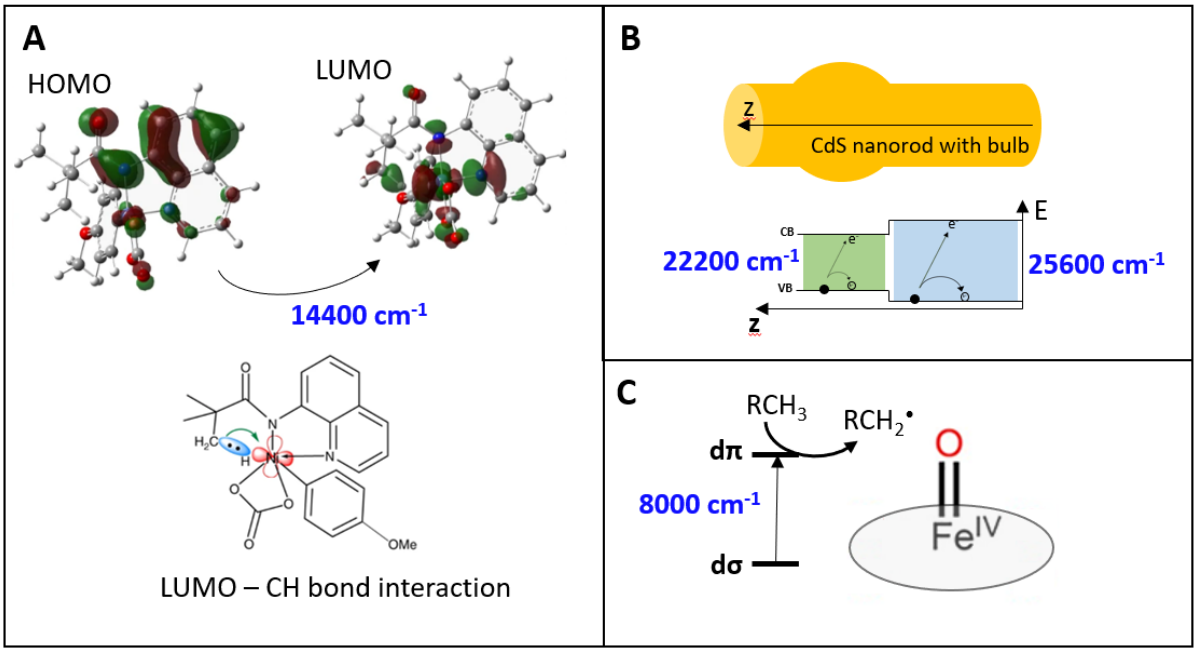


Figure 2. (A) The HOMO and LUMO and HOMO-LUMO gap of a homogeneous aryl-Ni^{IV} complex and the role of its LUMO in C-H bond activation. **(B)** A CdS nanorod photocatalyst with a bulge along its z-axis, with band gaps in the UV-VIS-NIR range. The band gap is affected along the z-axis by the presence of the bulge. **(C)** The SyrB2 non-heme Fe^{IV}-oxo active site, similar to other non-heme Fe^{IV}-oxo sites in homogeneous, enzymatic and heterogeneous catalysis, with its NIR-accessible excited state playing a key role in H atom abstraction. Adapted from refs. [24-26]. Copyrights 2019 Springer nature, 2014 and 2022 American chemical society.

2.2 Collection and processing of *in situ* absorption spectra

Before quantitative analysis is possible, also the irradiance, photon collection, and detection processes must be considered. In the calculation of extinction coefficients it is assumed that all photons get the chance to excite the electron, and that all not-absorbed photons are measured. This is not always the case, and depends on the measurement mode and interfering processes. Therefore processing of raw experimental spectra is required. Moreover, measurement conditions as well as the light absorption itself can significantly influence the state of the absorption centra and thereby influence further absorption. Such phenomena can be exploited to gain insight in specific catalyst properties through data collection and processing techniques.

2.2.1 Modes of irradiation and light collection

Several spectroscopic methodologies have been developed for the UV-VIS-NIR range to study different reaction systems and answer different questions on catalyst structure and catalytic mechanisms. In lab scale heterogeneous catalysis, also including electrocatalysis and some photocatalysis, the catalyst is usually a powdered solid with a high surface area. DRS is then commonly used, in combination with reaction setups that enable the collection of spectra at high temperature, and under a flow of reagent and product molecules. Alternatively mulls can be prepared enabling transmission spectroscopy, but this is less common. UV-VIS-NIR spectra on homogeneous and enzymatic catalysis are typically collected in transmission mode as the reactions generally occur in a translucent solvent. With the addition of inert particles or for suspensions and colloids in general, DRS can also be used (Figure 3 B).[27-30] For both transmission and DR modes cells for *in situ* characterization are technically feasible and commercially available.[4]

2.2.1.1 Transmission and diffuse reflectance spectroscopy

For sufficiently translucent samples, the absorption spectrum can be easily obtained by measuring the portion of light that remains of an incident light beam after passing through the sample, i.e. the transmission. This approach is applicable to translucent liquid solutions and very thin solid wafers, and other translucent samples. For opaque samples other approaches are needed. When samples are opaque due to strong absorption, dilution is an option. When they are opaque due to scattering, diffuse reflectance is used. The latter is relevant for the study of solid phase catalysts, which are mostly studies in powdered form, or as deposits forming a rough surface. This allows a better approximation of the intended use of catalysts in packed beds, fluidised beds or on electrodes, and yields more representative *in situ* measurements.

For powders or rough surfaces with particle sizes of the order of the wavelength the incident light is partially scattered and partially absorbed, as schematically shown in Figure 3 A. The particles in the bed are illuminated from all possible directions by the scattered light. Consequently the scattered light escapes the particle bed in all possible directions. In the ideal case all angles of incidence are equally probable and the same holds for the scattered light leaving the bed of particles. If there is no transmission through the bed of particles (infinitely thick bed) the light is either absorbed or scattered, and the scattered beam escaping from the surface can be detected. This is diffuse reflectance spectroscopy (DRS).

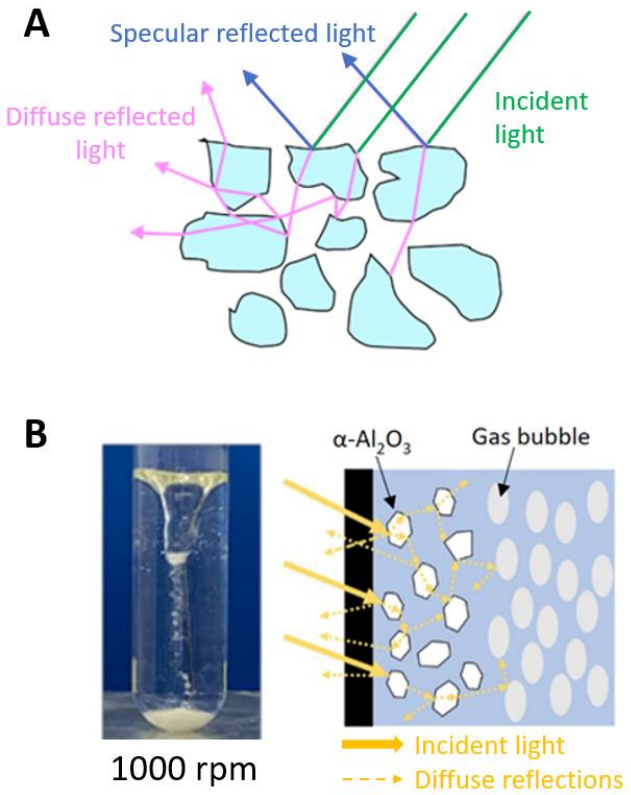


Figure 3. (A) Visualization of the interaction between the incident light and the rough surface. **(B)** The suspension of α-Al_2O_3 in a stirred liquid medium to enable diffuse reflectance mode measurement.[30] Copyright 2022 Royal society of chemistry.

When using DRS quantitatively, a particular challenge is the determination of the pathlength of the light 'through' the sample (Figure 3 A). In DRS, the (average) pathlength is affected by

the scattering events, and by the absorption itself. With more scattering, photons 'bounce around' in the surface layer longer giving a higher probability of absorption. With higher absorption, the observed diffuse reflected photons are more likely to have spent less time in the surface layer, and their average pathlength is decreased. The result is a complex non-linear problem that depends on material properties. The Beer-Lambert law for processing transmission measurements and equations for processing DRS absorption data will be discussed further in section 2.2.3.1.

2.2.1.2 Fiber optics

Spectroscopic investigation of a working catalyst requires a spectroscopic cell that also functions as a reactor, best designed to accurately measure kinetics. The light must be guided to and from the catalyst at high temperatures and pressures. On heterogeneous catalysts this is best achieved using glass fibre optics bundles in heat resistant UV-VIS-NIR probes. These irradiate the sample and collect reflected and scattered light.

For a gas phase reaction, a homogeneous flow of reagent molecules over the catalyst bed is required. For a powdered catalysts, the powder should be loaded as pellets smaller than 10% of the inner diameter of the reactor tube. The dead volume must be kept as small as possible, and the conversion should be small to avoid temperature and pressure gradients.[31-35] Measurements at the top and bottom are not representative of the catalyst bed. Thus, the high temperature probe of the spectrometer is placed outside the reactor against a quartz tube containing the catalyst to probe the middle of the catalyst bed and achieve proper kinetic data. Multiple measurements at different locations on the bed can also provide information on the spatial evolution (e.g. see Figure 34). If the NIR region is probed together with the VIS region the quartz must be high grade quartz with a low amount of OH groups. A schematic representation is shown in Figure 4. More generally, the design of kinetically appropriate spectroscopic cells has been discussed by Meunier.[31]

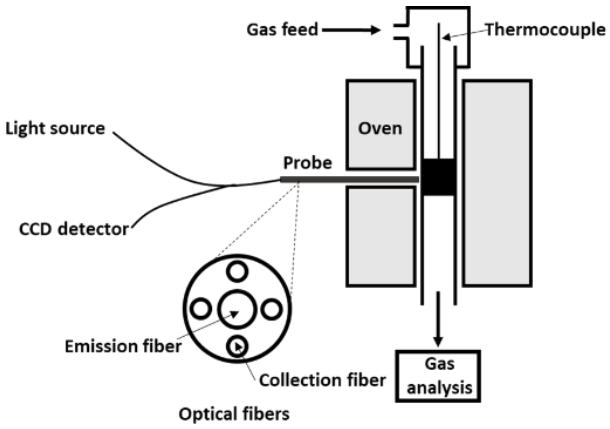


Figure 4. Scheme of an *in situ/operando* spectroscopy set up. Reproduced from ref. [31]. Copyright 2010 Royal Society of Chemistry.

As an illustration (Figure 4), a fiber optic reflection probe could contain five fibers: one central irradiation or emission fiber and four read or collection fibers. Depending on the distance to the sample, such fibers analyze a smaller or larger area of the sample, but usually this is below 1 mm^2. This is an extremely small fraction of the surface of the catalyst bed, and a supplementary reason to repeat the spectroscopic measurements at different heights of the bed. This simultaneously verifies that a uniform distribution of the absorption centers in the catalyst bed is present.

With the optical fiber probe as shown in Figure 4, the catalyst is illuminated perpendicularly to the catalyst bed and the scattered light is collected under the same angle. This means that diffuse reflection and specular reflection are measured together at every wavelength. *In situ/operando* cells that irradiate the sample at 45° and collect the light either at 90° (diffuse reflectance only) or at –45° (specular reflectance only) also exist,[36] but they give other practical difficulties.

2.2.1.3 Improving time and spatial resolution

Time-dependent processes are of interest in catalysis research and high measurement frequencies are needed to resolve them. On stable analytes, high quality UV-VIS-NIR absorption spectra can be obtained using a light source that is passed through a monochromator. Such measurement can take several minutes, too long for many experiments. The required and desired measurement time depend respectively on the system studied and on the phenomenon of interest (Figure 9). The timescale of the UV-VIS-NIR absorption spectroscopy measurement itself lies in the attosecond range (10^{-18} s). A single photon absorption, the transformation to an electronic excited state, and the thermalization of 'hot' electrons all occur on the attosecond (10^{-18} s) scale. Such measurements are of value in characterizing excited states and are relevant for understanding photocatalysis in particular.

In most cases one wants to experimentally track the statistical conversion of many particles through activated processes, adding a probabilistic component (e.g. looking at half lives). This brings the photon absorption and electronic excitation time scale to the femtosecond (10^{-15} s) range. The decay of electronic excited states can occur with half-lives ranging from femtoseconds to hours. Similarly, the time scales of activated chemical reactions can vary strongly. A selection was tabulated in a review by Shi, Lercher and Yu.[14, 37]

With commercially available UV-VIS-NIR spectrophotometers, sufficient signal-to-noise is generally obtained for sub-second resolution, enabling relevant operando UV-VIS-NIR absorption measurements. In this case, the time resolution limit is set by the method of irradiation since, on the collection side, array charge coupled device (CCD) detectors allow collection over the full UV-VIS-NIR range in milliseconds.[38] This is still insufficient to track the short lived excited states exploited in photocatalysis.

Nanosecond and femtosecond range experiments can be achieved using laser pulses and transient absorption spectroscopy (TAS).[39] For easily repeated experiments (e.g. repeated excitation with laser pulses) step-scan measurements can be used. Independent single measurements are aggregated into a time series of spectra with good signal-to-noise.[39] A good overview of irradiation methods and detectors is given in a book chapter by Skoog et al.[40] A diagram of the femtosecond and nanosecond resolution setups and experiments is shown in Figure 9.

Choosing the spatial resolution is a trade-off between analyzing a sufficient catalyst portion to be relevant for the full catalyst bed and capturing the heterogeneities that exist in the bed. The best spatial resolution therefore depends on the research question. Generally high spatial resolution is targeted and the results are then validated for larger areas, or with repeatedly displaced high resolution measurements. A lot of advances have been made in the latest decade using microspectroscopy, achieving resolutions on micrometer scales.[3, 4] UV-VIS-NIR absorption microspectroscopy studies remain so far limited to the study of surface bound aromatics and coke formation involving molecules with high absorption coefficients.[3, 41-43]

2.2.2 Conditions- and time-dependent measurements

In situ spectroscopic setups enable the collection of spectroscopic data at selected conditions. One can choose to simulate the conditions relevant to the intended catalytic process, or to vary conditions for analytical purposes. The former generally implies elevated temperatures and reactant feeding, and is often used in combination with catalytic measurements resulting in *operando* spectroscopy. The latter approach involves the addition of probe molecules or redox conditions, the application of external magnetic fields, temperature conditions, and/or electric potential, the trapping of intermediates, and the monitoring of responses to pulses and step changes in various conditions. Numerous reviews have addressed setups and applications of *in situ/operando* setups.[4, 7, 8, 39] In this section we will give an overview of some experimental spectroscopy techniques to gain further electronic and structural information.

2.2.2.1 Varying temperature and magnetic field

The population of excited states depends on temperature through the Boltzmann distribution, eq 4.

$$\frac{N_{ex}}{N_g} = \frac{g_{ex}}{g_g} e^{-(E_{ex}-E_g)/k_B T} \tag{4}$$

with N_{ex} and N_g the populations in the excited and ground states, g_{ex} and g_g the degeneracies of the excited and ground states, E_{ex} and E_g the energies of the excited and ground states, k_B the Boltzmann constant and T the temperature.

For energy levels separated by photon energies in the UV-VIS-NIR range ($E_{ex} - E_g > 4000$ cm^{-1}), the population of the electronic excited states is very limited (e.g. still < 1% at 1250 K), but for close lying electronic states the relative populations can be drastically adjusted with large changes in the UV-VIS-NIR absorption spectrum. A recent example is the in situ variable-temperature measurement of S=0 to S=2 spin crossover in pseudo-tetrahedral $[BP_3]Fe^{II}$-X complexes from 188 K to 373 K (Figure 5).[44] Additionally, smaller separations are achieved by splitting (near) degenerate electronic states energy levels according to their spin and orbital angular momenta by applying an external magnetic field. The relative population of these levels depends on the strength of the applied field and temperature. Such experiments are called 'variable temperature variable field' (VTVH) spectroscopy, and are applied in various spectroscopies (Electron paramagnetic resonance (EPR), Mössbauer, X-ray absorption spectroscopy (XAS), …). Applying an external magnetic field is particularly interesting in UV-VIS-NIR range circular dichroism measurements, resulting in magnetic circular dichroism (MCD).

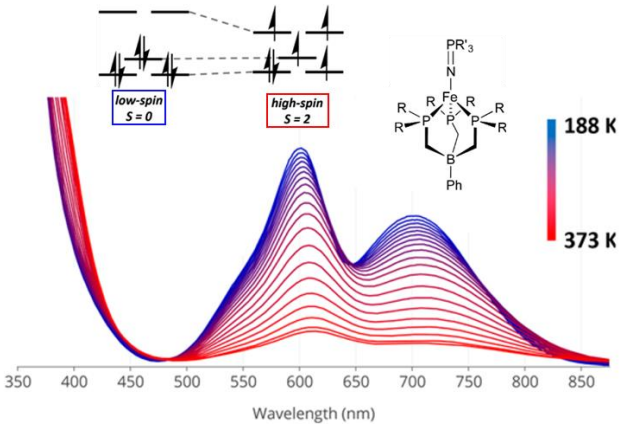


Figure 5. Variable temperature UV-VIS-NIR absorption of [$PhBP^{Ph}_3$]Fe($NPPh_3$) showing its temperature dependent transition from a low spin state to a high spin state. Adapted from ref. [44] Copyright 2016 American chemical society.

MCD observes the differential absorption of left and right circularly polarized light by a sample in a large magnetic field parallel to the propagation direction of the circularly polarized light. There are three different intensity mechanisms (A-term, B-term and C-term), but the richest information is gained from bands with C-term intensity. Its analysis has been particularly useful to probe the coordination geometry of non-heme iron catalysts, and examples of this are found for Fe-zeolites, homogeneous catalysts, and enzymes in sections 3.1.2., 3.2.1.2 and 3.3.3. C-term intensity originates from degenerate ground states that are Zeeman split in a magnetic field. At low temperatures, this splitting results in a different Boltzmann population of the spin sublevels. From the selection rules (LCP: $\Delta L = +1$; RCP: $\Delta L = -1$), different sublevels absorb light selectively depending on the circular polarization. The difference in absorption of left vs right circular polarized light is detected in MCD using modulation methods to enhance signal to noise (Figure 6).[18]

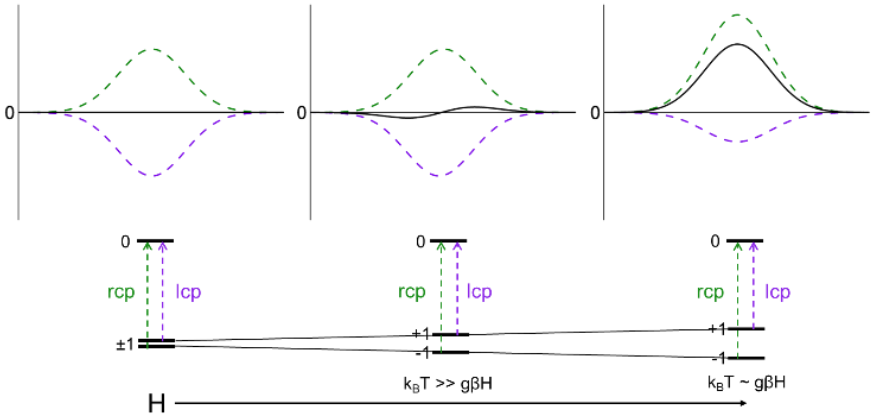


Figure 6. Magnetic circular dichroism C-term intensity with increasing field at low temperature. Absorption of left circularly polarized (lcp) light (green), absorption of right circularly polarized (rcp) light (purple), and the differential absorption (solid black) due to the differences in Boltzmann population of the m = +1 and m = –1 levels as the Zeeman splitting increases towards the right.

The selection rule for C-term intensity requires two perpendicular electric dipole transition moments. Low symmetry metal sites, like those in metalloenzymes, have nondegenerate electronic states, thus electronic transition dipoles to an excited state are in one direction. Thus, to have the two perpendicular transition dipole moments in one transition, there must be spin orbit coupling (SOC) between states. Metal atoms have much larger SOC constants compared to the atoms on the ligands. Thus, the greater the metal character of a transition, the greater the SOC, and the greater the MCD C-term intensity relative to absorption intensity (referred to as a C_0/D_0 ratio, see also Figure 50 for an example). This is important in observing and assigning bands. Ligand field transitions have large C_0/D_0 ratios due to the transitions being largely localized on the metal center. This allows these bands to be observed in MCD at low temperature. LMCT transitions have small C_0/D_0 ratios due to the transition being more centered on ligands, with smaller SOC constants. VTVH-MCD experiments on C-terms are typically conducted over a domain of 0 - 7 T and 2 - 50 K. Saturation magnetization isotherms and isofields are derived for individual absorption bands that give information on the spin state, zero-field splitting, and magnetization of both the ground and excited state (see also Figure 51 for an example). MCD on C-terms is thus always measured at cryogenic temperatures and is

not useful for *operando* spectroscopy in catalysis. A- and B-terms on the other hand are accessible at room temperature, but they lack the rich information content of C-terms.[19, 45]

In conventional UV-VIS-NIR absorption spectroscopy the shifts obtained in practically feasible magnetic fields are small and difficult to resolve, so VTVH perturbations are not used. In situ cells are, however, used to measure spectra in controlled atmospheres and temperatures. The example of spin crossover of Fe complexes was already given.[44] Different roto-vibrational levels are also easily populated at achievable temperatures, vibronic coupling can be resolved at cryogenic measurements, and different coordination numbers, adsorption modes, other equilibrium distributions, and geometric isomers may be obtained depending on the atmosphere composition, pressure, and temperature. Recent examples are the cryogenic observation of vibronic coupling on Ru^{II} complexes of tridentate bisphosphino-oligothiopentene (Figure 7), and cycloreversion of dithienylethene compounds.[44, 46-49] These types of variable-temperature measurements are currently mostly limited to homogeneous complexes and enzymes. Cryogenic measurements in diffuse reflectance mode (*vide infra*) are scarce, but it has been successfully applied to study thermochromism in Salicylideneanilines.[47] In general the application of both VTVH-MCD and VT UV-VIS-NIR absorption spectroscopy to extract information on electronic structure and adsorption behavior remains scarce on heterogeneous catalysts, despite its potential.

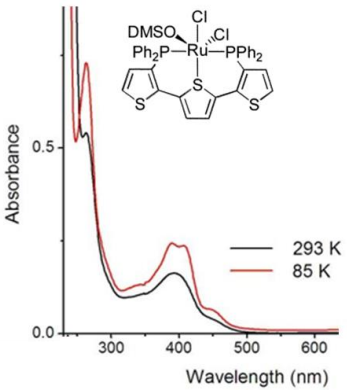


Figure 7. UV-VIS-NIR absorption spectra of the $Ru^{II}(DMSO)_4Cl_2$ complex recorded at 293 K and 85 K. The low temperature spectrum resolves the vibronic coupling in the 390 nm absorption band. Adapted from ref. [48]. Copyright 2011 Royal Society of Chemistry.

2.2.2.2 Time dependent measurements

While the measurement of UV-VIS-NIR absorption spectra on systems in equilibrium or steady state can contain features of reaction intermediates, more mechanistic insight can be derived from time-dependent spectroscopic tracking. Several types of experiments have been developed to enable the tracking of different types of processes with absorption spectroscopy. Both UV-VIS-NIR absorption spectroscopy and circular dichroism are used as the analytical methods, although the former is much more common, especially in catalysis. Some examples of CD used in stopped-flow and ultrafast transient-response experiments exist in literature, and a very limited number of time-resolved MCD spectroscopy can be found, both applied mostly to protein analysis.[50-57]

Depending on the rate of the process under investigation, different methods are employed. To track slow transformations, simple spectroscopic tracking of an ongoing reagent limited reaction is sufficient, e.g. with a setup as shown in Figure 4. From the temperature and concentration or pressure dependence of the transformations kinetic information can be

obtained. Arrhenius plots can be constructed to derive activation energies, Eyring plots for transition state (TS) entropy and enthalpy, and concentration dependence plots for reaction orders. Some examples in section 3 are the tracking of methane oxidation to methanol with Cu-zeolites, N_2O reduction with Fe zeolites, and coking on solid acids.

For reactions in liquid phase with millisecond-range kinetics, and to observe short-lived intermediates, a stopped-flow setup can be used (e.g. Figure 35). This is especially popular in the study of enzymatic catalytic cycles. Often these progress through a series of multiple key intermediates which would not be observed under steady state conditions where only the rate determining step is revealed. Stopped-flow experiments can be designed so that only a single turnover is performed and the formation and decay of intermediates can be observed and measured (example in Figure 8).[58] Separate solutions of catalyst and substrate are rapidly driven into a mixing chamber, and UV-VIS absorption spectra are rapidly collected with an array detector.[59, 60] Measuring the decay of an intermediate at various temperatures allows derivation of an Eyring plot to extract out the enthalpic and entropic contributions to reactivity. Additionally, by isotopically labeling substrates, the appearance of (or lack of) kinetic isotope effects provides insight in the reaction mechanism.

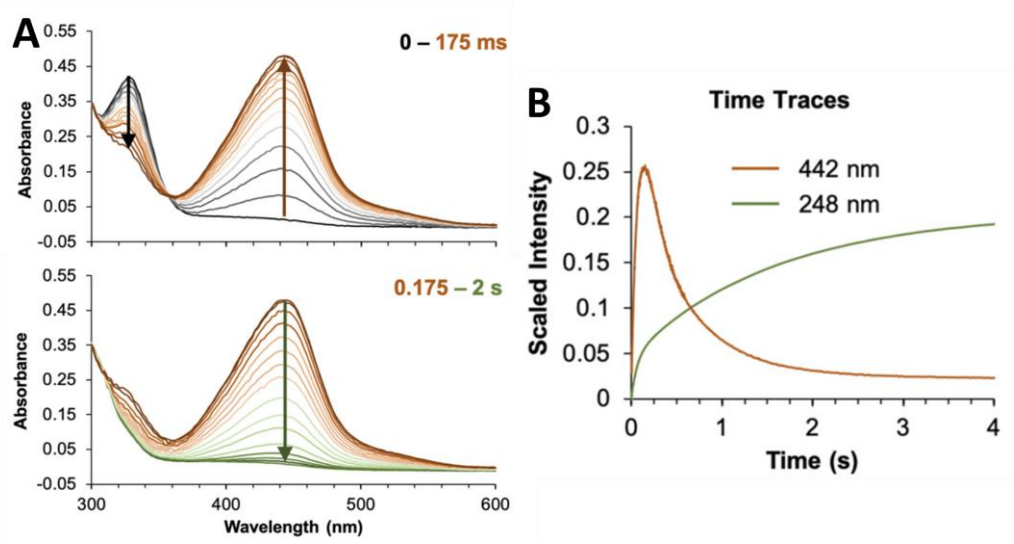


Figure 8. (A) Stopped-flow UV-VIS absorption spectra of Fe^{II}-tryptophan hydroxylase with O_2. From 0 - 175 ms (top) and 0.175 - 2 s (bottom). **(B)** Speciation curve for formation and decay of intermediates. Adapted from ref. [58]. Copyright 2021 National Academy of Sciences.

For still faster reactions, where the system reaches equilibrium too quickly for the measurement of enough absorption spectra, the equilibrium can be disturbed in various ways (Table 3 and Figure 9, bottom) after which the response can be tracked spectroscopically. The fastest response technique, achieving femtosecond resolutions, is transient absorption spectroscopy (TAS) tracking the relaxation of electronic excited states after ultrafast laser pulses for photocatalyst characterization (Figure 9 top and middle).[39, 61, 62] Another class is modulation excitation spectroscopy (MES) producing periodic disturbances that can be of various types, and chemical composition perturbation methods such as transient analysis of products (TAP) and steady state isotope transient kinetic analysis (SSITKA), using for example a setup as show at the bottom of Figure 9.[63-65] These techniques can detect and temporarily concentrate short lived intermediates, map reaction networks, quantify adsorbed species, and access kinetic parameters. While they are combined most commonly with *in situ* infrared (IR), Raman, XAS and X-ray diffraction (XRD) spectroscopies, they can be particularly helpful tools in

understanding complex UV-VIS-NIR absorption spectra as well, especially for heterogeneous catalysts. They were recently reviewed in separate chapters in a book edited by Wachs and Bañares.[66]

Table 3. Overview of techniques that enable tracking the response to equilibrium disturbances

Transient / step response techniques	Methodology
Transient absorption spectroscopy	Pump-probe technique
Modulation Excitation Spectroscopy	Periodic application of stimulus (e.g. reactant concentration, temperature, pH, light flux, and electric field.)
Transient analysis of products	Introduction of short pulse reactant with low concentration
Steady state isotope transient kinetic analysis	An abrupt switch to the corresponding isotopically labelled feed stream with identical flow and pressure under steady state

After re-stabilization, the disturbance can be repeated to collect more data and reduce further the signal-to-noise through step-scan measurements. The time scales depend strongly on the setup and on the system under study. Kinetic models are needed to analyze the transient response in the reaction. The analysis of the absorption spectra time series can be aided by statistical methods including regression models and data reduction tools such as factor analysis, principal components analysis (PCA), non-negative matrix factorization (NNMF) and multivariate curve resolution (MCR).[67]

For further analysis with different ex-situ techniques, or to enable longer measurement times, rapid freeze quenching techniques, or less involved quench procedures depending on the sample stability, can be used to trap intermediate samples from any of the methods described above.[68]

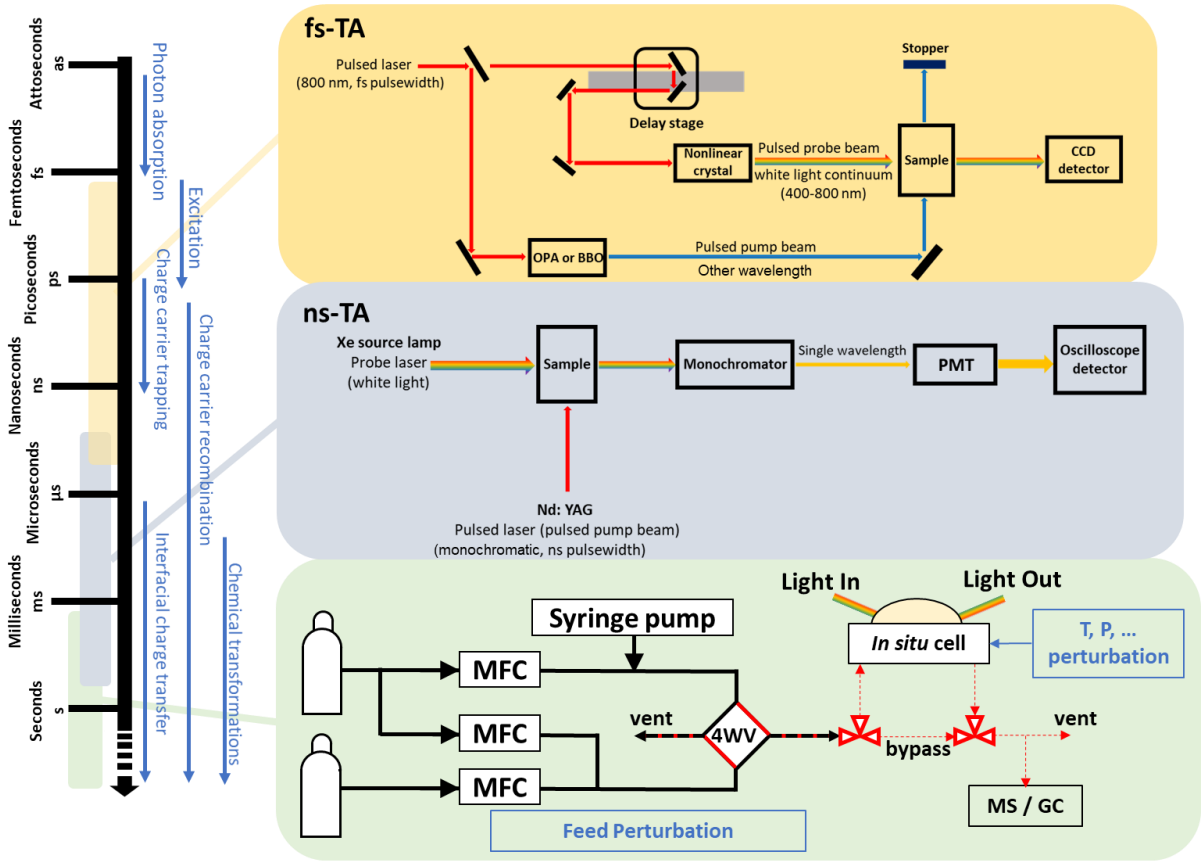


Figure 9. Timescales of some different processes related to in-situ UV-VIS-NIR absorption spectroscopy, and specialized techniques used to access these time scales. Fs-TA = femtosecond transient absorption, OPA = optical parametric amplifier, BBO = beta barium borate, CCD = charge-coupled device, ns-TA = nanosecond transient absorption, YAG = Yttrium Aluminum Garnet, PMT = photomultiplier module, MFC = mass flow controller, 4WV = four-way valve, MS = mass spectrometer, GC = gas chromatographer. Adapter from refs. [61, 63]. Copyrights 2023 and 2019 Royal Society of Chemistry.

2.2.3 Processing of spectroscopic data

The primary data obtained from an absorption experiment gives the ratio of detected light intensity vs incident light intensity versus photon energy, usually relative to a reference. It is commonly preferred to transform the measure of absorption into a form that correlates linearly with the concentration of the analyte. For transmission mode absorption spectroscopy the Beer-Lambert law is used, and the absorption is quantitatively measured by 'absorbance' (*A*). For diffuse reflection mode the Kubelka-Munk (K-M) formula is most popular yielding a quantitative measure in 'Kubelka-Munk units'. Further processing usually involves deconvolution of the individual absorption bands from the spectrum. Popular band shapes were already mentioned in section 2.1. For quantitatively correct deconvolution one should naturally first apply the Beer-Lambert or Kubelka-Munk transformation to the full spectrum and then extract the individual absorption bands. Quantitative tracking through time or with changing conditions then allows to derive information on kinetics and thermodynamics. Arrhenius, Eyring, and isotherm plots are easily derived provided a reliable quantitative deconvolution can be obtained.

Apart from the measurement and tracking of concentrations, other forms of processing can be used to access different properties. Commonly derived from UV-VIS-NIR absorption are band gap energies through Tauc plots, reaction stoichiometries through Job plots, and equilibrium constants and stoichiometries of reversible complexation with the Benesi-Hildebrand method. In this section we further discuss only the two basic processing functions (Beer-Lambert and Kubelka-Munk) to obtain quantitative data in *in situ* spectroscopy, and Tauc/Cody plots for their intrinsic association to UV-VIS absorption spectroscopy.

2.2.3.1 The Lambert-Beer and Kubelka-Munk functions

Several metrics can be used to quantify experimental absorption, absorbance being the most popular. For transmission measurements on a uniform sample, the Beer-Lambert law, eq 5, describes the decay of light intensity (of a particular photon energy) as it passes through an absorbing translucent sample:

$$A = \log\left(\frac{I_0}{I}\right) = \epsilon l c \tag{5}$$

With absorbance *A*, incident light intensity I_0, *I* the remaining intensity at pathlength *l*, *c* the concentration (or volumetric density) of the absorbing species, and ϵ the absorption coefficient at the particular photon energy. Often A_{10} is used as notation instead of A to specify the use of $\log_{10}$. For mixed samples, a weighted sum of absorption coefficients should be used. For non-uniform samples corrections should be used due to the exponential (non-linear) decay of I_0/I in *A*.

With an analogy to transmission in transmission spectroscopy, the diffusively reflected light intensity (the absolute remittance) of an infinitely thick sample R_∞ is defined by eq 6.

$$R_\infty = \frac{J}{I_0} \tag{6}$$

where J is the intensity of the reflected radiation and I_0 is the intensity of the incident beam. Infinite thickness means that none of the impinging light penetrates through to the bottom of the sample and transmits.

In a classical spectrophotometer an integration sphere with a (near) fully reflecting ('white') inner surface in the UV-VIS-NIR region is installed in the sample compartment. Popular materials are Halon polymeric materials, barium sulphate, or potassium bromide. This sphere contains a sample port and a reference port. The reference measurement is usually performed with a fully reflecting standard material at the sample and reference ports. The diffuse reflectance of the sample at the sample port is then measured against the diffuse reflectance of the standard by eq 7.

$$R'_\infty = \frac{R_{sample}}{R_{standard}} \tag{7}$$

Where $R_{standard}$ and R_{sample} are the light intensity diffusively reflected from an ideally white standard and from the sample respectively. Slight differences between R_∞ and R'_∞ occur if $R_{standard}$ is smaller than 1.

In analogy to transmittance and absorbance in transmission spectroscopy, a relation between absorbance and R'_∞ can be defined by eq 8.

$$\begin{aligned} 100 \times R'_\infty &= \%T \\ \log \frac{1}{R'_\infty} &= A \end{aligned} \tag{8}$$

where T is transmittance and A is 'pseudo-absorbance'. Proceeding from here we will make no further distinction between R_∞ and R'_∞.

In transmission mode the pathlength is simply the linear path through the sample followed by the beam and, for uniform samples, the linear Lambert-Beer law can be used. In DRS the pathlength is affected by the scattering events and by the absorbance itself (*vide supra*, Figure 3 A). The scattering probability increases with $1/\lambda^n$, where n is around 1 for particles of the size in the range of the wavelength. In addition, with higher absorbance, the observed diffuse reflected photons are more likely to have spent less time in the surface layer, and the average pathlength is decreased. To obtain specific absorption coefficients, it is required to solve a complex non-linear problem that depends on material properties. Several approaches have been suggested to give an acceptable representation of the phenomenon.[29, 69] These models make assumptions on how the photons scatter and on certain properties of the rough surface, and they enable a mathematical transformation of the diffuse reflectance into a measure that varies linearly with absorbent's concentration (analogues to Lambert-Beer). Different models may be better suited to different types of materials. In heterogeneous catalysis, the Kubelka-Munk formula (eq 9) is most used, based on the assumptions listed in Box 1.

$$\mathrm{F}(R_\infty) = \frac{(1-R_\infty)^2}{2R_\infty} \tag{9}$$

The full derivation of eq 9 can be found in Kortüm's book and in more recent papers.[7, 69-71]

1. Infinite thickness of the sample
2. Infinite extension of the catalyst bed in the x-y directions
3. Diffuse monochromatic incident light
4. Uniform distribution and small concentration of absorption centers
5. Absence of stray light
6. Absence of fluorescence and specular reflection

7. Constant scattering coefficient over the absorption band
8. Isotropic light scattering

Box 1. The assumptions in the Kubelka-Munk derivations. In orange the least acceptable assumptions in *in situ* DRS measurements on catalysis using a state-of-the-art setup.

Note that it will already be difficult to fulfill these assumptions in the sample setup shown in Figure 3 B and a different treatment will be needed. Also for other scenarios, for example measurements on thin absorbing films on coarse reflective surfaces, other methods should be used.[72, 73] For the application of UV-VIS-NIR DRS to heterogeneous catalysis, a few of the assumptions in Box 1 should be given special attention:

At the surface of a powder sample, a small fraction of light is reflected under the same angle as that of the incoming light beam without absorption. This is called specular reflection. In practice, this fraction is often negligibly small and it can also be adjusted for by modifying the spectroscopic setup. Deviations occur for strongly absorbing materials, i.e. large values of the K-M function. In these cases, the amount of diffusively reflected light is low and the specular reflection part is not negligible. Scattering increases with decreasing wavelength and with decreasing particle size of the catalyst. It is almost constant in the NIR and VIS range and increases continuously in the UV. Absorption bands in the UV region are thus superposed on the increasing scattering background. Both the position of the band maximum and the intensity are influenced, making it very difficult to quantify the absorption bands in the UV region accurately. In the NIR and VIS, with almost constant scattering coefficient S, the K-M function can be written as eq 10.

$$\mathrm{F}(R_\infty) = \frac{K}{S} = \frac{\epsilon\, C}{S} \tag{10}$$

with C the concentration of absorbing species, *S* the K-M scattering constant, and *K* the K-M absorption coefficient. The K-M function for powders can then be considered an analogue of the Lambert-Beer law for solutions. Still, it requires a constant scattering coefficient over the width of the absorption band.

The K-M theory has been critically evaluated by multiple authors, and several alternatives or extensions have been proposed.[29, 69] No alternatives have however been developed that are generally superior without significantly sacrificing on simplicity.

2.2.3.2 Band gap energies

The optical band gap energy (E_g) of a semiconductor is the minimum energy required to absorb a photon transferring a valence band (VB) electron to the conduction band (CB). It is an important parameter for photocatalysis, photovoltaics and photodetection, and an often measured property on heterogeneous catalysts holding structural information. A technique for obtaining E_g for an amorphous semiconductor from the absorption spectrum was originally proposed by Tauc and Vancu in 1966.[74] Their technique is now widely used, although not always in a rigorous manner. Here we review the theory and common errors in its usage applied to catalyst characterization.

Tauc *et al.* demonstrated that the energy-dependent absorption coefficient α can be expressed by eq 11.:

$$(\alpha \cdot h\nu)^{1/2} = B\left(h\nu - E_g\right) \tag{11}$$

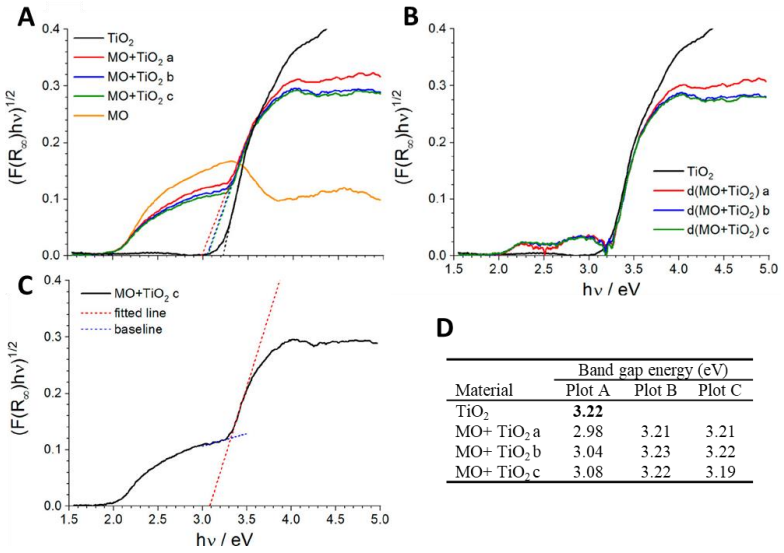
with h Planck's constant, ν photon frequency, and B the band tailing parameter, generally taken to be 1 for amorphous materials. For diffuse reflectance measurements, α can be replaced

by the K-M function (equation 10). For transmission and reflectance (T&R) measurements on thin film semiconductors α is derived using the Beer-Lambert law (equation 5). E_g estimated from (equation 11) is only reliable for sufficient absorption, and could be inaccurate with optically thin films. The multiple-reflection interference model has been proposed as an alternative to determine the absorption coefficient from T&R spectra of thin films.[75, 76]

For crystalline semiconductors the ½ exponent is replaced by γ^{-1}, accounting for the expression for the transition rate depending on the nature of the electronic transition. γ is equal to 1/2, 3/2, 2 or 3 for the direct allowed, direct forbidden, indirect allowed and indirect forbidden transition band gaps respectively. The mathematical derivation of these values can be found in the handbook by M. Cardona and P. Yu, among others.[77] A tangent line in the linear region of a Tauc plot, with $(\alpha \cdot h\nu)^{1/\gamma}$ plotted versus $h\nu$, is extrapolated to the $h\nu$ axis and the zero-intercept gives E_g.

The obtained optical bandgap is, however, very sensitive to the quality and handling of the spectroscopic data, and to the choice of γ. This leads to diverging bandgap values reported in literature for the same materials. Firstly, as the method depends on an extrapolation making use of a wide energy domain of the spectrum, extra care is needed to guard the assumptions behind deriving α, for example using the Beer-Lambert or Kubelka-Munk relations. Photon energy dependent scattering may stand in the way of correct linearization, and absolute deviations from α may affect the slope of the tangent line. Secondly, a proper baseline must be used. In a defect-free crystalline semiconductor the absorption spectrum abruptly terminates at the energy gap, but for defected, doped, bulk or surface modified materials and amorphous semiconductors inter-band gap states give so-called 'Urbach tails' in the absorption spectrum.[78-80] Heterogeneous catalysts typically belong to these last categories.

Depending on the exponential tail region different approaches are appropriate. When unrelated absorption bands are present in the tail region (e.g. interbands, sub-bands, or absorption by intermixed species), extra care should be taken. An example is given by Makula *et al.*[78] Tauc plots of pure TiO_2 are compared to those with methyl orange added (MO + TiO_2) in different amounts (indicated with a, b and c) (Figure 10 A). The changes in the measured E_g are substantial. It is necessary to subtract the contribution of MO from the spectrum (Figure 10 B). Since it can be challenging to deconvolute the K-M spectrum into spectra of individual components, alternatively, a linear fit is applied for the slope below the investigated absorption (baseline fitting) to estimate the E_g (Figure 10 C). Both methods allow decent fitting of the TiO_2 optical bandgap (Figure 10 D).



Material	Band gap energy (eV) Plot A	Plot B	Plot C
TiO_2	**3.22**		
MO+ TiO_2 a	2.98	3.21	3.21
MO+ TiO_2 b	3.04	3.23	3.22
MO+ TiO_2 c	3.08	3.22	3.19

Figure 10. (A) Tauc plots of pure TiO_2, MO and MO + TiO_2 samples with different MO addition (a, b, c), including the Tauc lines. **(B)** Tauc plots after subtraction of the MO contribution from the spectrum. **C)** Tauc plot of MO + TiO_2 with baseline fitting. **(D)** Table with the optical band gaps obtained from the methods in the plots of panels A-C. Adapted from ref. [78] Copyright 2018 American Chemical Society.

With mixed phases, multiple bandgaps of intermixed semiconductor phases may be present. Alternatively a single semiconductor material may boast both an indirect bandgap energy and a direct bandgap energy, and the different values of γ^{-1} should be evaluated. Finally, one should avoid vertically correcting the absorption spectrum based on a false assumption of incomplete light collection.[81]

When this is all done correctly, there can still be a significant method-dependence in drawing the tangent line. An automated approach is therefore advised, for example as developed by Schwarting et al.[82] Note that also when using an algorithmic bandgap derivation, the outcome should be evaluated equally critically.

Alternative methods were proposed to deal with the limitations of Tauc plots. Some are of the same type as the Tauc method, but are based on slightly different assumptions.[83] These include the Cody method (eq 12), which generally yields better linearity and therefore a less ambiguous fit,[84] and the Sokolov or Mott-Davis modifications of the Tauc method.[85]

$$(\alpha/hv)^{1/\gamma} = B\left(hv - E_g\right) \tag{12}$$

In still other methods simply the inflection point is taken as the direct optical band gap, or a certain cut-off value of the absorption coefficient is chosen. Zanetta *et al.* propose the fitting of a sigmoidal curve onto the pure semiconductor edge to derive both the direct and indirect optical bandgaps (Figure 11).[86] One may ask the question what the definition of an optical bandgap should be, and which methods yield the most correct result in agreement with this definition. For now, it is mostly advised to be clear in the methodology of obtaining the reported optical bandgaps.

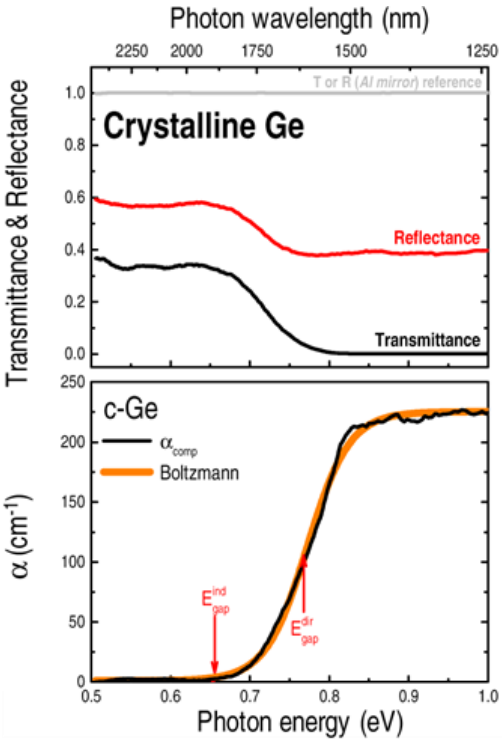


Figure 11. Absorption spectra and Boltzmann sigmoidal curve fitting with indication of the derived direct and indirect optical bandgap energies for crystalline Germanium. Adapted from ref. [86]. Copyright 2019 Springer Nature.

2.3 Coupling to complementary techniques

The measurement of UV-VIS-NIR absorption spectra enables fast, cheap, and non-destructive measurement of experimental parameters related to the electronic structure of the species under investigation, and to kinetic properties. The technique is also flexible in measurement temperature and pressure. However, it is almost never sufficient to derive a full characterization. A few challenges are relevant. The computational simulation of absorption spectra is not very accurate (errors of 2000 cm^{-1} are not uncommon, even with complete active space perturbation theory 2 (CASPT2)).[87, 88] The electronic structure parameters give only indirect information on the geometry, and especially on the elemental composition. In many applications, the absorption spectrum is poorly resolved and is a superposition of several unrelated spectra of coexisting species. Therefore, the link between a model structure and its simulated spectrum on the one hand and the actual structure and its experimental spectrum is ambiguous. Moreover, UV-VIS-NIR range spectroscopies may encounter more difficulties than other spectroscopies in measuring across phases (e.g. through bubbles in electrocatalysis) and on strongly absorbing support materials (e.g. graphene), and it is surface specific. For certain applications, interference by fluorescence and phosphorescence may be an issue. Especially in the UV range, irradiation damage can still occur giving erroneous results, especially for organic materials.

For these reasons UV-VIS-NIR absorption spectroscopy is rarely used as a standalone characterization technique. As will repeatedly be demonstrated in section 3, and summarized in Table 1, multiple spectroscopies and other analytical techniques are usually combined. These can provide complementary information on elemental composition, atomic vibrations, oxidation states, stability, electronic properties, geometry, reactivity and catalysis, … . Some commonly used complementary techniques are listed in Table 4. Some complementary techniques can easily be implemented simultaneously under the same conditions ('*in situ*'). For

some combinations specific cells or setups (e.g. stopped flow) may be required to achieve good *in situ* overlap, for others still sample isolation is needed. For example, through a rapid freeze quench (RFQ) where the reactants are first rapidly mixed and then frozen in a medium (e.g. isopentane) after an optimized mixing time that maximizes the concentration of an intermediate as determined through stopped-flow kinetic measurements.[68] Alternatively, closed sampling systems can be used.

Examples of *in situ* cells include those used for UV-VIS-NIR absorption in combination with Nuclear magnetic resonance (NMR), EPR, various synchrotron measurements, ….[4-6, 39, 89-92] Also in this category are *operando* measurements of catalysis, spectrophotometric titration, temperature programmed desorption, -oxidation and -reduction, and kinetics. Alternatively the complementary measurements can be '*ex situ*', after isolating a sample. Some examples using a quench procedure are found in section 3.3.1. For some analytical techniques popular in catalysis research, UV-VIS-NIR absorption spectroscopy is an excellent partner. Three examples stand out. 1) The '*in situ*' monitoring of radiative damage in X-ray experiments,[93, 94] 2) providing a fast response *operando* spectroscopy dimension to kinetic measurements with online MS or GC analysis (e.g. TAP, SSITKA, step response),[95-98] and 3) selectively probing specific absorption features which we elaborate on further.

Table 4. Characterization techniques used simultaneously with *in situ* UV-VIS-NIR absorption spectroscopy.

Complementary technique	Derived information
DRIFTS	Bond vibration energies, change in dipole moment selective
Raman	Bond vibration energies, change in polarizability selective
NMR	Element specific atomic chemical environment
EPR	Electron spin and its interactions
EXAFS	Element specific, sample averaged local structure
XANES	Element specific, sample averaged oxidation state & coordination
XPS	Electron binding energies
XRD	Crystallographic structure
GC	Product characterisation and quantification
MS	Product characterisation and quantification
Voltammetry	Electrochemical properties

The complementary information derived from the coupled techniques enables site-selective spectroscopy, where the spectroscopic data are unambiguously linked to the same UV-VIS-NIR absorption band. Most notably is the combined use of absorption, MCD and resonance Raman (rR), originally popular in the study of metalloenzymes, but by now also applied to TMI zeolites and other catalysts. The features typically analyzed in Raman are those where the scattered light is redshifted from the incident radiation by the energy of a vibrational mode (referred to as Stokes scattering). The selection rules for Raman are based on the change in the polarizability of the molecule upon distortion in the vibrational mode, providing a method to view vibrations complementary to those observed through infrared spectroscopy.[99] Raman spectroscopy often involves weak transitions that are difficult to observe in dilute mixtures. Resonance Raman spectroscopy solves this issue. Whereas normal Raman scattering involves using a laser at a non-absorbing wavelength, rR specifically tunes a laser into an intense absorption feature, generally a LMCT transition. In the charge transfer (CT) excited state, the molecule distorts along ligand-metal bonds, selectively enhancing the vibrations associated with this excited state distortion. This resonance Raman effect greatly enhances the intensity of these totally symmetric vibrational modes. In the case of metalloenzymes, this allows vibrational modes of an active site buried in a dilute protein to be clearly observed. Additionally, it associates these vibrations with a particular charge transfer band (and its associated intermediate in a mixture) as the intensity is only enhanced when the laser is tuned into the absorption band. Based on the types of vibrations enhanced, this can also provide additional

information on the nature of the charge transfer band as the enhanced vibrations indicate how the molecule is distorted in the excited state.[99] Examples for the identification of catalytic active sites and intermediated are given for Cu and Fe zeolites in section 3.1.2. and for oxy-hemocyanin in section 3.3.2.

3. Research in catalysis with *in situ* UV-VIS-NIR spectroscopy

3.1 Heterogeneous thermal catalysis

In situ UV-VIS-NIR spectroscopy has been applied to metal (oxide) clusters and TMIs dispersed on zeolites, and other high-surface-area metal oxides, which show remarkable catalytic performance in a range of reactions. Studies concerning TMI zeolites are particularly relevant as they can host well defined TMI complexes. Regarding other metal oxides, research has focused on the tracking of surface properties of the catalyst, including oxidation state(s), defects and oxygen vacancies relevant to redox catalytic processes. This section highlights the *in situ* UV-VIS-NIR based research in the field of TMI-based heterogeneous catalysis and further presents the most recent works on supported metal oxide catalysts. Due to their partially filled d-shell and multiple oxidation and spin states, TMIs are relevant to the catalysis of oxidation-reduction reactions.[100-102] Most of these reactions are carried out in the liquid or in the gas phase. In these applications, the use of solid catalysts is beneficial as separation of the catalyst and reaction mixture is facilitated. As such, supported transition metal catalysts show promise as they combine the superior redox capabilities of TMIs with the practical advantages of using a stable, solid support.[100, 103, 104] The section also covers the measurement of chromophoric organic products from zeolite based acid catalysis. Recent research on methanol to hydrocarbons is shown.

3.1.1 Tracking metal and metal oxide bulk and surface properties

Metals and metal oxides supported on non-microporous oxides are widely used commercial catalysts. They are preferred for their easily scaled up synthesis, simple structure, stability, and good thermal and mass transport properties. Their versatile elemental composition provides the freedom to substitute elements (doping) and many oxides exist in amorphous form as well as in different crystal phases with diverging properties.[105, 106] Besides functioning as structural supports, the oxides also influence catalysis through induced electronegativity and polarizability or by offering storage for surface intermediates.[107] In many cases, the oxides play an active role in catalysis through oxygen vacancies, surface functional groups, surface defects or electron-hole pairs, and these can be tracked with UV-VIS-NIR range spectroscopies. The active oxides may in turn be supported on porous materials or on other oxides. They may be the only catalytically active phase or they may be a contributing phase to a bi- or multifunctional catalyst.[108]

3.1.1.1 Supported noble metal nanoparticles

Nanometer scale metal particles (NPs) boast increased surface-to-volume ratio, and electronic and geometric structures that differ from the bulk.[109, 110] This unlocks their remarkable catalytic properties, particularly when dispersed on a support. The support can play a direct role in the catalytic performance or an indirect one. It may influence the size and morphology of the metal NPs, enable charge transfer from or to the metal, provide metal-support interactions, or stabilize the active metal species.[111, 112] The catalytic performance of these materials therefore depends on numerous aspects which can be difficult to unravel and control. Several of these properties have been tracked with UV-VIS-NIR absorption spectroscopy.

Surface plasmon measurements on noble metal nanoparticles

Noble metals exhibit localized surface plasmon resonance (LSPR), a unique optical feature in the UV-VIS-NIR range from the oscillation of electrons in the conduction band of metal NPs with an electromagnetic field.[113] The LSPR spectrum holds information on the size and shape of the metal NPs, as well as on the refractive index (RI) of the surrounding media.[114, 115] These are relevant properties to catalysis, and a handful of articles have tracked LSPR bands in this context, mainly focused on gold-based catalysts.

Au-based catalysts catalyze a variety of oxidation and hydrogenation reactions, such as CO oxidation,[116-118] the water-gas shift (WGS), the reverse water-gas shift (RWGS),[119-121] and the hydrogenation of CO and CO_2 to methanol.[122, 123] Understanding the interaction of Au supported catalysts with O_2 and H_2 is of interest to identify key intermediates and conversions. Srinivasan et al. studied the adsorption of oxygen and hydrogen at 398 K by in situ UV-VIS DRS in a series of Au catalysts supported on SiO_2, Al_2O_3, ZrO_2, ZnO and TiO_2 P-25.[98] The Au plasmon peak position was analyzed as a function of the exposure time for 5 hours. Before exposure to an oxidative or reductive atmosphere, a broad Au plasmon centered at ~570 nm was measured. After exposure to O_2, the peak slightly redshifted in all cases, whereas the subsequent exposure to H_2 caused a blueshift. The blueshift indicates an increase in the conduction band electron density due to charge transfer from H_2 to the Au NPs. Interestingly, the largest Au plasmon energy shifts occurred for catalysts supported on reducible oxides (Au/ZnO ($\Delta\lambda$= 11 nm) and Au/TiO_2 ($\Delta\lambda$= 9 nm)) (Figure 12). Although TiO_2 is more rapidly reduced by H_2 than ZnO, the higher $\Delta\lambda$ on the ZnO-supported catalyst indicates a smaller Au particle size on ZnO than on TiO_2. This demonstrated that the adsorption capacity is a function of both the reducibility of the support and the Au surface sites density.

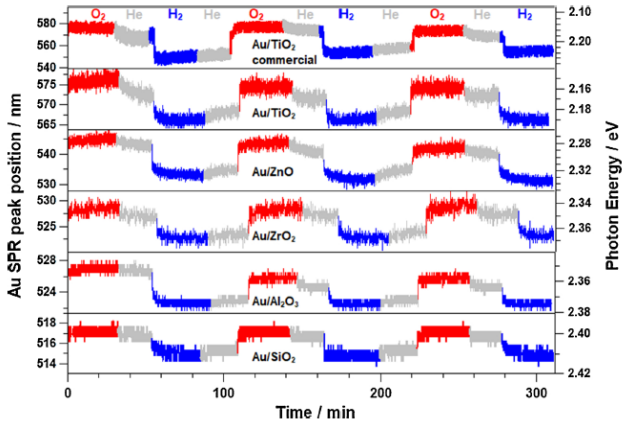


Figure 12. Au plasmon position changes as determined from *in situ* UV-VIS absorption spectroscopy after exposure to alternating H_2 and O_2 flows at 398 K. Reproduced from [98]. Copyright 2021 Elsevier.

In the most accepted hypotheses, adsorption and catalysis occur at the gold-support interface.[124, 125] To evaluate the nature of the active sites in the Au-based catalysts, the authors analyzed the relative change of electron density ($\Delta N/N$) in Au NPs during O_2-H_2 switching with *in situ* UV-VIS-NIR absorption spectroscopy. After flushing with He, O_2 and H_2 were found to adsorb only weakly on undercoordinated (coordination number = 6,7) top sites, indicating that the majority of O_2 or H_2 species should adsorb at the Au-support interface. For further characterization of the adsorbed species, UV-VIS-NIR absorption spectroscopy is less

informative and complementary *in situ* and *operando* IR or Raman spectroscopies are usually used. In this sense, Wang et al. combined transient *in situ* diffuse reflectance infrared fourier transform spectroscopy (DRIFTS) and UV-VIS-NIR reflectance spectroscopy to monitor the changes induced by the CO oxidation reactants (CO and O_2) in the Au NPs structure of an Au/TiO_2 catalyst.[126] FTIR results showed a sudden intensity increase of the CO vibrational band together with an intensity decrease of the CO_2 band and a redshift of the CO band. The increase of the adsorbed CO band was not related to an increase of the CO_2 formation rate, indicating that during this unstable state the O_2 coverage was decreased probably due to structural changes on the Au/TiO_2 surface, which were tracked by *in situ* UV-VIS-NIR reflectance spectroscopy. UV-VIS-NIR absorption analysis of the Au/TiO_2 LSPR at ~600 nm (Figure 13 B) showed that exposure to the CO + O_2 mixture immediately affected the LSPR, pointing at a change in the Au electronic properties.

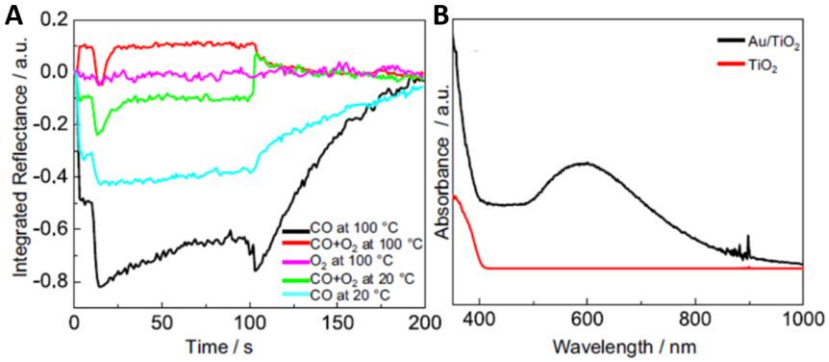


Figure 13. (A) Integrated UV reflectance in the 750-950 nm range as a function of time during CO adsorption, O_2 adsorption and CO oxidation at 20 and 100 °C. **(B)** UV-VIS DRS spectra of TiO_2 and Au/TiO_2. Reproduced from [126]. Copyright 2022 Springer Nature.

The LSPR region was not uniformly affected. The 500-600 nm region changed little while in the 750-950 nm region reflectance increased, indicating that only a subset of the Au NPs was involved (Figure 13 A). In good agreement with the FTIR results, the addition of the CO + O_2 mixture first sharply decreased the 750-950 nm reflection to then grow back. The change in the Au NPs structure that leads to the change in LSPR can therefore be related to the deactivation period. The separate introduction of CO and O_2 demonstrated that the Au structural changes were induced by CO adsorption, but also that in the presence of CO, O_2 was needed for the reconstruction of the Au NPs. It was shown that O_2 adsorption on Au/TiO_2 is hindered, leading to a lower CO oxidation activity before reaching the steady state characterized by an enhanced catalytic performance.

Effect of the catalytic support: transition metal and rare-earth oxides

Transition metal and rare-earth (lanthanide) oxides have some properties that make them interesting support materials for catalysis. TiO_2 and CeO_2 have been highlighted for their inherent redox properties derived from intermixed oxidation states (Ti^{3+}/Ti^{4+} and Ce^{3+}/Ce^{4+} pairs), responsible for the presence of oxygen defects with catalytic relevance. *In situ* UV-VIS-NIR absorption spectroscopy has been a useful tool to study these effects by virtue of its sensitivity to different oxidation states.[8]

The RWGS reaction (eq 13) is commonly catalysed with oxide supported gold catalysts. Two main mechanisms are known: the redox mechanism and the associative mechanism.[127, 128] The

redox mechanism applies to Au nanoparticles supported on reducible supports, where CO_2 reoxidizes the partially reduced support, leading to the formation of CO. In the associative mechanism, CO is formed from the decomposition of formate species derived from the interaction of CO_2 with H_2. Since formate species cannot be decomposed on Au nanoparticles, their evolution during reaction is associated with the support material.

$$CO_2 + H_2 \leftrightarrow CO + H_2O \quad (13)$$

Bobadilla et al. investigated the mechanism of the RWGS with Au/Al_2O_3 and Au/TiO_2 commercial catalysts.[129] The catalytic activity of Au/TiO_2 is superior to that of Au/Al_2O_3, and based on DRIFTS results the associative mechanism was followed with Au/Al_2O_3 catalyst while the redox mechanism was followed with Au/TiO_2. TiO_2 in its reduced form (Ti^{3+}) is known to contain a high concentration of oxygen vacancies, which act as sites for CO_2 activation. The authors studied the importance of the TiO_2 oxygen vacancies through the reduction of Ti^{4+} to Ti^{3+} using *in situ* UV-VIS absorption spectroscopy during activation with H_2 and the subsequent RWGS reaction. At room temperature, the spectra of pristine TiO_2 (Figure 14 A) show the TiO_2 band gap at ~320 nm. H_2 causes the appearance of a broad band in the 400-800 nm range, indicative of the reduction of Ti^{4+} to Ti^{3+}. The wide absorption band arises from a continuum of electronic energy levels derived from oxygen vacancies. After switching to the reaction mixture, the 400-800 nm band decreased in intensity, suggesting the participation of the oxygen vacancies in the reaction mechanism. The plasmon of the Au nanoparticles partially overlaps with the band gap edge of TiO_2 (Figure 14 B), so one should be careful with its influence on the band gap estimate. In the difference spectra (Figure 15) a positive difference band centered at ~350 nm is observed, and attributed to the formation of Ti^{3+} modifying the bandgap absorption band. The positive difference feature at 400-800 nm confirms the involvement of oxygen vacancies.

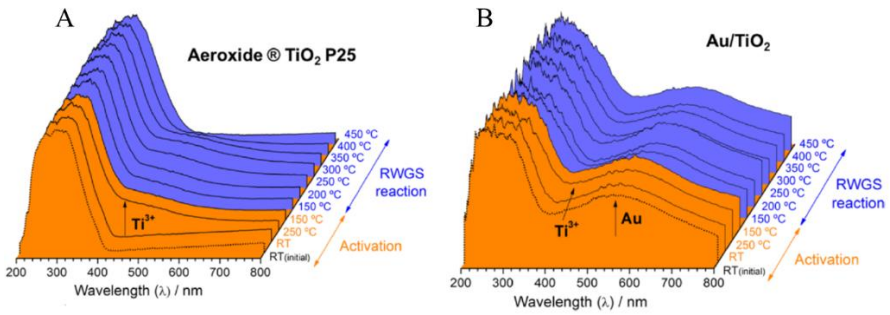


Figure 14. *In situ* UV-VIS absorption spectra as a function of the temperature of **(A)** TiO_2 P25 and **(B)** Au/TiO_2 catalyst during activation under H_2 (orange) and RWGS reaction (blue). Reprinted with permission from [129]. Copyright 2018 American Chemical Society.

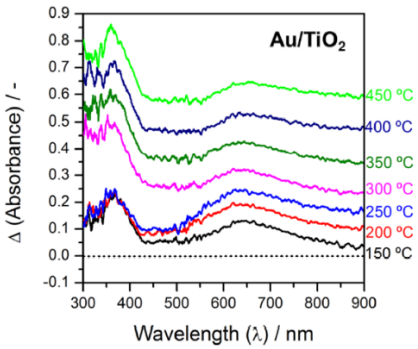


Figure 15. Au/TiO_2 UV-VIS-NIR difference absorption spectra of before and after reaction, for different reaction temperatures. Reprinted with permission from [129]. Copyright 2018 American Chemical Society.

The RWGS catalytic performance on Au/CeO_2 is related to the presence of oxygen vacancies and to the particle shape of the support.[130] Ceria polyhedra (which terminate with the CeO_2 (111) surface) and polycrystalline ceria (which resembles sheets and contains stepped sites) were evaluated as supports by Ziemba et al. using a combination of *in situ* Raman spectroscopy, UV-VIS-NIR absorption spectroscopy, and transient DRIFTS.[131] Changes in the degree of CeO_2 reduction were tracked following the evolution of a VIS absorption band at 550 nm, attributed to a charge transfer from Ce^{3+} to Ce^{4+}.[132] At room temperature, the spectra of Au/CeO_2 catalysts show a ~550 nm absorption band of Au surface plasmons. The CeO_2 polyhedra supported materials give stronger surface plasmon absorption, due to a higher concentration of gold metallic species. When the flow is switched from Ar to H_2/Ar, an increase of the 550 nm absorption is observed for every sample, indicating the reduction of the CeO_2 support. After addition of the reaction mixture (CO_2/H_2/Ar), the absorption intensity decreases due to the re-oxidation of CeO_2. These results evidence changes in the oxygen dynamics as a function of the gas atmosphere.

To gain futher insights, the gold-loaded samples were analyzed by *in situ* UV-VIS-NIR absorption spectroscopy under reductive (H_2/Ar) and oxidative (CO_2/Ar) pretreatments followed by the RWGS reaction (CO_2/H_2/Ar) (Figure 16). Under CO_2 atmosphere, a decrease of the band intensity is observed, especially in the catalyst supported on polycrystalline CeO_2, illustrating that this CeO_2 morphology is more prone to oxidation than the polyhedral counterpart. When the flow is switched to the CO_2 and H_2 mixture, the 550 nm absorption band increases, particularly for the Au/polycrystalline CeO_2 sample. The RWGS reaction after a reductive pretreatment, however, has little effect on the absorption band. Together, the results indicate that the redox mechanism is predominant on bare CeO_2 samples, although the associative mechanism also participates in the CeO_2 polyhedra. The pure redox mechanism in polycrystalline CeO_2 is related to the higher reducibility of the support. The associative mechanism is dominant on Au/CeO_2, although the redox mechanism also takes place.

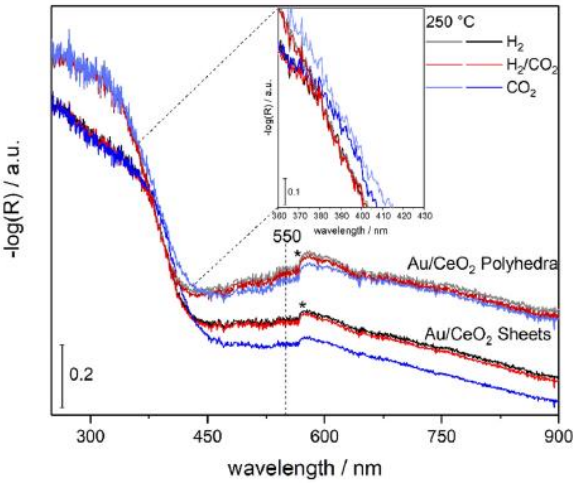


Figure 16. *In situ* UV-VIS-NIR absorption spectra of Au/CeO_2 samples during H_2 pretreatment, CO_2 pretreatment and RWGS reaction. Reproduced from [131]. Copyright 2022 Elsevier.

The same group used time-resolved *in situ* Raman spectroscopy and UV-VIS DRS to study the effect of the pretreatment in the oxygen dynamics of the support in a 0.5 wt.% Au/CeO_2 catalyst and its influence on the room temperature CO oxidation.[133]

The reduction state of the support was elucidated by monitoring of the F_{2g} Raman band and the 570 nm UV-VIS band, as shown in Figure 17. The reducing pretreatment allows a higher degree of CeO_2 reduction than the oxidative one. Under reaction conditions a fast re-oxidation of the CeO_2 surface is detected, but the reducing pretreatment draws out the re-oxidation of the CeO_2 subsurface. These results show a correlation with the catalytic activity, which is higher after the catalyst is subjected to a reducing pretreatment, thus showing a strong influence of the subsurface reduction state in the CO oxidation activity.

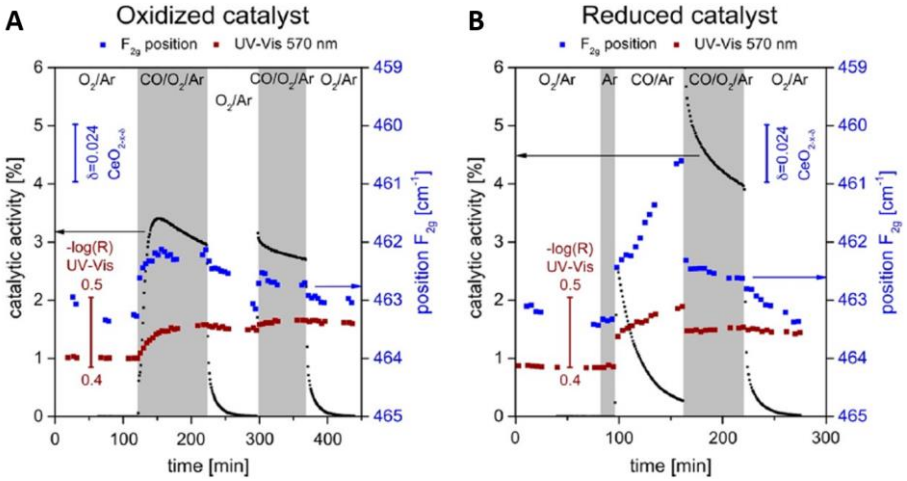


Figure 17. Catalytic activity (black), time-dependent Raman (blue) and UV-Vis bands (brown) evolution for the CeO_2 subsurface reduction state in a 0.5 wt% Au/CeO_2 catalyst, **(A)** after two reaction cycles, **(B)** during CO oxidation after reducing pretreatment. Reproduced from ref. [133].

Spectroscopic results also show that no charge transfer takes place from the support to the Au NPs, contrary to what was previously observed for Au/TiO_2 catalysts. In the Au/CeO_2 catalyst,

the electron is proposed to remain in the support (Ce^{3+}), accelerate oxygen activation and not hamper CO adsorption on the metal particles.

3.1.1.2 Transition metal oxide catalysts

Transition metal oxides (TMO) are catalytically interesting thanks to their partially filled d orbitals, which facilitate electron transfer between reactants and active sites.[134] This feature is complex to investigate due to the multitude of oxidation states and coordination numbers, but is well suited for study with UV-VIS-NIR spectroscopy.[135] Bensalem et al. used *in situ* UV-VIS-NIR DRS to study the reduction kinetics of chromium oxide catalysts supported on Al_2O_3 and SiO_2 in a CO/He mixed atmosphere.[136] By combining *in situ* UV-VIS-NIR DRS, on-line GC analysis and experimental design, Weckhuysen et al. correlated the activity of CrO_x/Al_2O_3 in the dehydrogenation of isobutane with the oxidation state of chromium surface species. The combined amount of surface Cr^{2+} and Cr^{3+} species, tracked by 'pure component' absorption fingerprints constructed by PCA, is a good predictor of dehydrogenation activity.[137]

Supported VO_x catalysts have also been extensively studied due to their promising catalytic behavior in partial oxidation, SCR or oxidative dehydrogenation (ODH) reactions. *In situ* UV-VIS-NIR DRS has provided information about the reduced states of VO_x supported on Al_2O_3, SiO_2, ZrO_2 or TiO_2.[138-140] Among them, TiO_2 was shown to significantly enhance the catalytic properties of VO_x.[141-143] Godiksen et al. studied the V_2O_5/TiO_2 system for its application in the NH_3 assisted SCR, using combined transient UV-VIS-NIR absorption spectroscopy and *in situ* Raman spectroscopy.[144] A 3% V_2O_5/TiO_2 catalyst was first activated at 400 °C under air and then exposed to an SCR gas mixture of 500 ppm NH_3, 500 ppm NO, and increasing O_2 concentrations in He from 0.8 to 10 vol.% O_2.

Raman spectra after activation shows a vanadyl band at ca. 1030 cm^{-1}, ascribed to the terminal V=O bond on anatase. During exposure to NH_3 and NO at 400 °C, the vanadyl band undergoes a redshift and decreases in intensity. This is probably due to the lower absorption coefficient of V^{4+}=O compared to V^{5+}=O, but may also indicate a deeper vanadium reduction to V^{3+}. The addition of O_2 gives rise to V^{4+}=O and V^{5+}=O species, with an increase of V^{5+}=O species with increasing O_2 partial pressure. UV-VIS-NIR absorption spectra were recorded during the flow change from O_2 to the NH_3 and NO mixture. The difference spectra show a decrease of the band at 25 500 cm^{-1}, attributed to CT transitions, as well as the appearance of a band at 15 000 cm^{-1} (Figure 18). The latter is ascribed to d-d transitions of octahedral VO^{2+},[145] thus indicating a reduction of V^{5+} to V^{4+}. The UV-VIS-NIR absorption spectra were compared to those obtained during H_2-TPR. Vanadium undergoes a two-electron reduction under H_2 yielding V^{3+}, whereas under a NH_3 + NO mixture, the reduction is a one-electron process yielding V^{4+}. V^{4+} species were proposed to be part of a $[V^{IV}=O]^{2+}$ unit, detectable in UV-VIS-NIR absorption spectroscopy due to its d^1 electron configuration. Further confirmation of this oxidations state by EPR was not achieved in the study due to paramagnetic interaction at high V loadings.

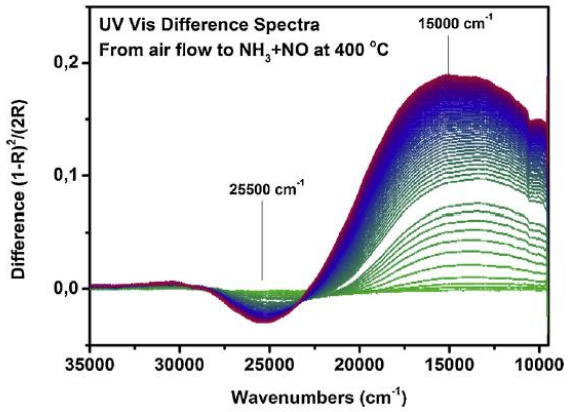


Figure 18. *In situ* UV-VIS-NIR absorption difference spectra of a 3% V_2O_5/TiO_2 catalyst during the gas flow change from O_2 (green) to NO + NH_3 (pink). Reproduced from [144]. Copyright 2019 Elsevier.

Hess and co-workers studied the oxidative dehydrogenation (ODH) of propane over VO_x/TiO_2 (P25) catalysts with different vanadium surface densities (2.5, 1.2, 0.5 and 0.1 V/nm^2).[140] A combination of *operando* UV-Raman, solid state NMR, transient IR and *operando* UV-VIS spectroscopies was used to elucidate the propane ODH reaction mechanism. Bare P25 and vanadia-loaded samples were studied by *operando* UV-VIS spectroscopy under oxidizing and reactive conditions to understand the role of reduced vanadia in the reaction mechanism. When switching from oxidative to reactive conditions, the band gap slightly red-shifts and an absorption band at 520 nm emerges in the UV-VIS spectra of P25 , ascribed to a charge-transfer transition due to reduction of Ti^{4+} to Ti^{3+}, and thus implying the formation of oxygen vacancies. This points to the oxidation of propane by the support lattice oxygen, leading to the formation of oxygen vacancies. UV-VIS spectra of the vanadia-loaded samples do not show a band gap energy shift nor a Ti^{3+} transfer signal, except for the sample containing 0.1 V/nm^2. An intensity increase due to vanadium d-d transitions indicates the reduction of V^{5+} to V^{3+}/V^{4+}.

Yun et al. used *in situ* Raman spectroscopy and UV-VIS-NIR DRS to investigate the electronic changes to VO_x/TiO_2 by nitrogen doping.[146] They then correlated the electronic structure of the vanadium clusters with the activity for selective ethanol to acetaldehyde oxidation. The authors derived the average number of vanadium-oxygen-vanadium covalent bonds (CVB) from the edge energy (E_g) values collected from the UV-VIS-NIR absorption band through the empirically determined eq 14.

$$\text{CVB} = 14.03 - 3.95E_g \text{ (eV)} \quad (14)$$

Changes in the onset energy of the edge (E_g') were used to monitor the formation of reduced vanadium centers during the partial oxidation reaction. The UV-VIS-NIR absorption spectra of the sample supported on pristine TiO_2 (Figure 19 A) are dominated by a broad band in the 1.0-3.5 eV range, ascribed to LMCT transitions of tetrahedral V^{5+} moieties. The broad and weak nature of the absorption in the d-d transition energy range prevents the proper identification of individual V^{4+} components. The redshift of the peak and the appearance of a tail are indicative of the presence of vanadium polymeric species.[139, 147, 148]

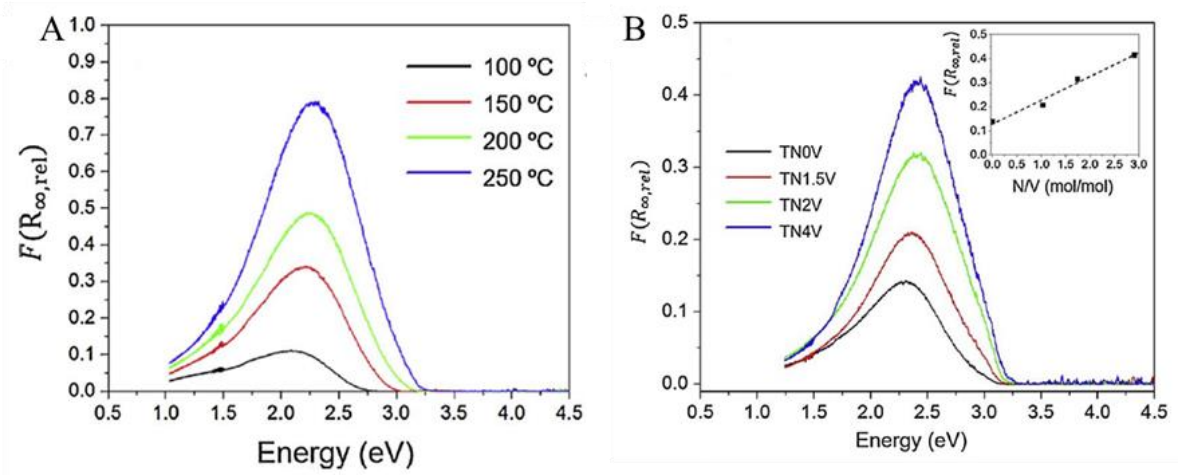


Figure 19. *In situ* UV-VIS-NIR absorption spectra of **(A)** VO_x/TiO_2 after reduction with ethanol at different temperatures for 1 h; **(B)** $VO_x/N\text{-}TiO_2$ catalysts with varying nitrogen content, after reduction with ethanol at 200 °C for 1 h. Inset: UV-VIS-NIR absorption intensity at reduced centers as a function of N/V mol ratio. Adapted from [146]. Copyright 2018 Elsevier.

After reduction with ethanol at temperatures ranging from 100 to 250 °C, E_g' increases with increasing reduction temperature in the N-free samples from 1.5 to 1.8 eV. The values are lower than those previously reported for oxide-supported VO_x reduced species,[138, 149] due to overlap of the V^{4+} and Ti^{3+} signals. The spectrum of the N-free sample after reduction at 200 °C was compared to those obtained for a series of $VO_x/N\text{-}TiO_2$ samples with different nitrogen contents. In the latter, the d-d bands are blue-shifted (Figure 19 B), indicating a larger reduction of vanadia and resulting in an increased number of active sites. Raman spectroscopy reveales minimal geometrical changes of the vanadia moieties, and the exceptional catalytic performance of the N-doped samples was attributed to the enhanced reducibility of VO_x species in the presence of nitrogen.

Recently, cubic In_2O_3 has emerged as efficient catalyst for CO_2 activation.[150, 151] Ziemba et al. used a combination of *in situ* UV-VIS-NIR absorption and impedance spectroscopies to elucidate the CO_2 activation process, the role of oxygen vacancies, and the participation of the adsorbates in the RWGS reaction.[152] The VIS absorption band indicative of oxygen defects at 700 nm was monitored under different gas atmospheres and temperatures, to understand the evolution of the oxygen defects (Figure 20 A). When switching between O_2 and H_2 at 130 °C, the spectrum shows an increase of the absorbance with the simultaneous detection of gas phase H_2O by IR spectroscopy, indicating the reduction of In_2O_3. Under reaction conditions at the same temperature, no CO was detected in the gas phase since CO_2 is not activated at such low temperature. However, the absorbance continues to increase with exposure to H_2 through In_2O_3 reduction. At 160 °C In_2O_3 reduction continues, but still no CO is detected. At 220 °C, the RWGS reaction occurs, giving rise to an absorption increase indicative of catalyst reduction. The absorbance then decreases over the next 30 minutes. The decrease of the absorption is the result of CO_2 conversion, leading to re-oxidation of the surface. The maximum absorption is observed at 190 °C and decreases with temperature, suggesting that catalyst oxidation by CO_2 increases with the temperature, whereas reduction remains constant since the maximum amount of oxygen vacancies was reached. These results suggest CO_2 activation and subsequent CO formation as the rate-limiting step. The above behaviour is confirmed by UV-VIS-NIR absorption experiments at 250 °C, while switching between reactive and reducing conditions

(Figure 20 B). A significant increase of the VIS absorption band at 532 nm can be related to the temperature increase and/or the oxidation. Subsequent H_2 exposure causes an increase of both the absorptions at 532 and 700 nm, together with the detection of H_2O in the gas phase, pointing out the reduction of the (sub)surface and the presence of small metallic indium domains. Under CO_2 atmosphere, a decrease in absorption at 700 nm occurs indicating the reversibility of the reduction process.

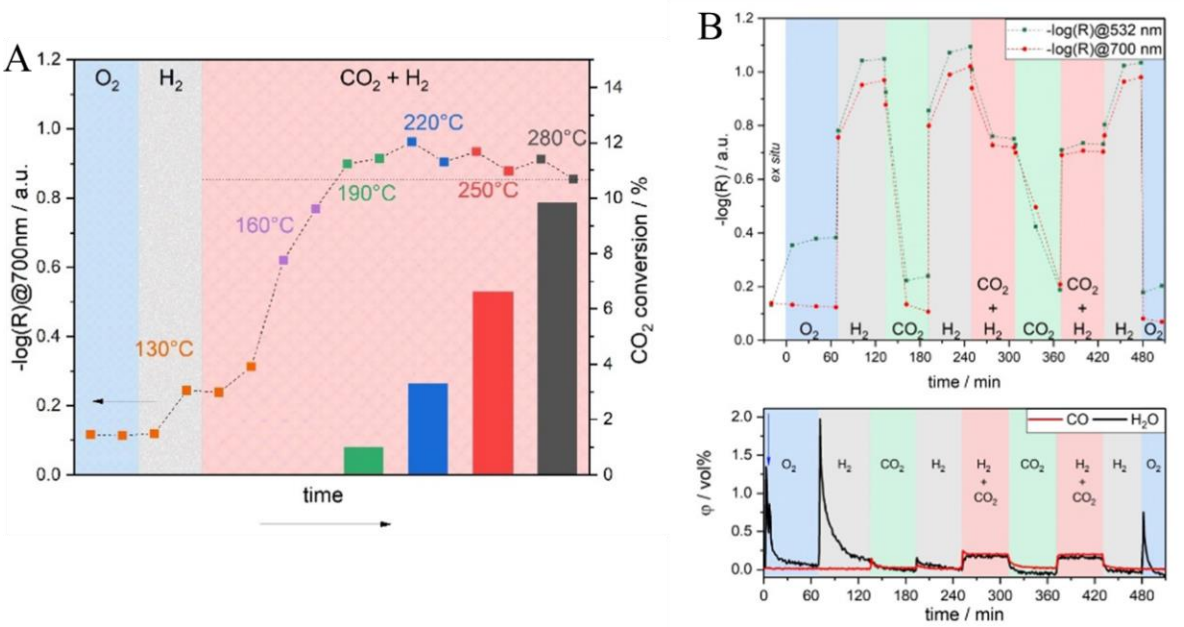


Figure 20. (A) *In situ* and *operando* VIS 700 nm absorption band evolution and CO_2 conversion during O_2 and H_2 exposure at 130 °C followed by RWGS reaction from 130 to 280 °C. **(B)** Top: *In situ* and *operando* UV-VIS-NIR absorption results for In_2O_3 under different gas exposures at 250 °C. Bottom: Gas-phase IR analysis during UV-VIS-NIR absorption measurements. Reproduced from [152]. Copyright 2022 Wiley.

3.1.2 Identification and tracking of dispersed catalytic molecular clusters

In the investigation of transition metal complexes the use of UV-VIS-NIR range spectroscopies has been indispensable. The examples in the later sections on homogeneous and enzymatic catalysis demonstrate their advanced characterization based on absorption, CD and MCD spectroscopies coupled to many more complementary spectroscopies. Their susceptibility to advanced spectroscopic characterization generally enables detailed understanding of the geometry and electronic structure on the molecular level, and consequently of the catalysis. Similar examples exist on heterogeneous catalysts where TMI active sites are successfully dispersed into well-defined molecular clusters. Particularly on TMI exchanged zeolites the advances have been spectacular in the preceding decade.

Zeolites are porous, crystalline aluminosilicates, built from linked $[SiO_4]$ and $[AlO_4]^-$ tetrahedra with every oxygen atom shared between neighboring T-atoms.[32, 33] Different zeolite topologies are distinguished by their crystal structure and pore system. Every $[AlO_4]^-$ leads to the presence of one negative lattice charge which can be charge compensated by exchangeable, extra-framework cations. These can be protons, giving zeolites their well-known acidic properties,[34] or (transition) metal cations. The zeolite matrix thus serves as a support to the acid or metal active sites, usually with a variety of exchange sites offering different coordination geometries and catalytic properties. Relevant zeolite topologies and their exchange sites are

shown in Figure 21. Six or eight membered ring exchange sites will be referred to again in this review and relate to any of the sites in the insert of Figure 21 that have open rings of six or eight tetrahedrons. The crystalline support gives rise to well defined active sites that – to some degree – can be tuned by varying the zeolite topology and the aluminum distribution in the lattice. With these levers, the effect of structural modifications on catalysis can be studied. Additionally, atoms outside the first coordination sphere can contribute to reactivity by guiding the approach of substrate or tuning the TS. These influences are referred to as 'second-sphere effects'.[26, 100, 153] Spectra of TMI-exchanged zeolites tend to be complex superpositions of absorption bands from different TMI species, coordinated in the different exchange sites. Their interpretation is usually complicated, but less so than those of TMI supported on many other materials by virtue of their strong tendency to disperse the supported TMIs. In some cases, the TMI species in the zeolite can be kept down to (quasi) single site, and spectroscopy becomes more evident.

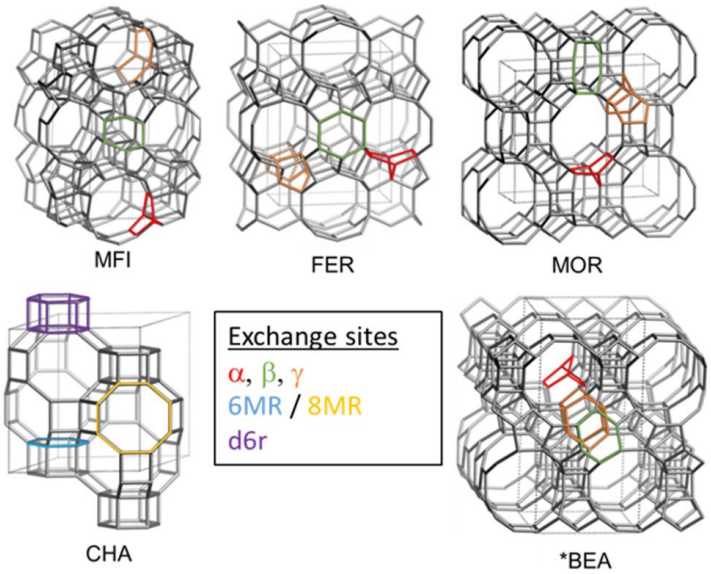


Figure 21. Framework structures and exchange sites of zeolite topologies mentioned in this review. Colors of the exchange sites match their naming in the legend. Adapted from ref. [154]. Copyright 2021 Elsevier.

3.1.2.1 UV-VIS-NIR fingerprinting on Cu and Fe exchanged zeolites

In situ UV-VIS-NIR studies are especially numerous for copper and iron exchanged zeolites with applications in direct oxidation of methane to methanol (MTM),[155, 156] deNO$_x$ catalysis,[157-159] and oxidation of benzene to phenol.[160-162] In these reactions essential steps are the activation of N_2O and O_2 to form reactive surface bound oxygen species that perform challenging selective oxidation reactions. The first is the μ-oxo-dicopper(II) site,[163-167] the second is the α-O site (a mononuclear Fe^{IV}=O).[17, 168-170] The unique spectroscopic handles of μ-oxo-dicopper and α-O in zeolites give the opportunity to study reaction kinetics and mechanisms by following the intensity changes of the relevant bands. Moreover, with good understanding of structure-spectroscopy relations, small structural changes in the species under investigation can be tracked spectroscopically and their impact on the catalytic processes can be studied.[171]

The first step is to determine the structure of the reactive oxygen sites and other intermediates, to unambiguously link the site-specific UV-VIS-NIR absorption handles to the processes of interest. High resolution room temperature UV-VIS-NIR absorption spectra were collected in diffuse reflectance mode using a quartz cell under controlled atmosphere of the materials after exposure and reaction with O_2, nitrogen oxides, CH_4 and benzene.[17, 162, 163, 170] These

measurements are *in situ* in the sense that the sample is reacted and analysed in the same cell preserving the atmosphere. The information from UV-VIS-NIR absorption spectroscopy alone is insufficient to be conclusive on structure and electronic properties. To obtain the required information, the controlled atmosphere UV-VIS-NIR absorption spectroscopy was coupled to *in situ* resonance Raman (rR), Mössbauer, MCD, and X-ray absorption spectroscopy (XAS, including X-ray absorption near edge structure (XANES), extended X-ray absorption fine structure (EXAFS), nuclear resonance vibrational spectroscopy (NRVS)) measurements without disturbing the atmosphere. For the first two, borosilicate transfer tubes were connected to the quartz reactor, for the latter three a sample preserving preparation method in perfluoro-2-methylpentane was used.[17, 163, 169]

The combination of UV-VIS-NIR absorption, resonance Raman, and MCD spectroscopies is particularly powerful. They all use excitations in the UV-VIS-NIR range and the spectroscopic features at the same excitation energies are unambiguously related.[100] The association of Mössbauer, XAS and NRVS spectral features with identical active sites, on the other hand, relies more strongly on statistical correlation of their appearance and on theoretical assumptions (incl. molecular modelling).

Operando UV-VIS-NIR absorption measurements were then used to correlate the structurally assigned spectroscopic handles to reactivity. Finally, time resolved *in situ* UV-VIS-NIR absorption spectroscopy on selected spectroscopic handles provided site-selective kinetic data quantitatively linking reactivity to structure. The *operando* kinetic analysis with *in situ* UV-VIS-NIR absorption spectroscopy is however rarely straightforward. *In situ* spectroscopy provides lower resolution and sensitivity, and usually more targeted synthesis is needed to increase active site loading and purity. This improved synthesis could be guided by the previously acquired structural information (for example see refs. [166, 168, 171, 172]).

If the absorption bands are particularly weak and broad, a careful background correction on the spectral baseline becomes essential and the baseline should be constant during the experiment. The latter condition requires that the reaction is highly selective to avoid contamination of the kinetic measurement from parallel transformations that give overlapping changes in the UV-VIS-NIR absorption spectrum. This has been a particular challenge with Cu zeolites. Multiple $[CuOCu]^{2+}$ species at different locations in the zeolite as well as $[Cu^{II}OH]^{+}$ and spectator species are present in the same material.[166] The spectators do not take part in the reaction, but might have absorption bands that overlap with those of the active site. Likely some published quantitative kinetic data is contaminated by at the time unknown reactive sites that react simultaneously.[164] The amount of spectator Fe species, on the other hand, can easily be limited to < 10% through careful synthesis and low loadings.[172]

Another challenge is the limited area of the catalyst bed that is probed by the optic fiber used in *in situ*/*operando* UV-VIS-NIR spectroscopy. This makes the measurement sensitive to inhomogeneities in the catalyst bed and in the flow, but also to disturbances in the setup. A stable flow and bed temperature must be established before reliable activity data can be collected. For relatively slow reactions the challenge is to keep the system stable over time, and multiple repeated measurements are recommended. Another solution is needed for very fast reactions where a stable flow cannot be achieved in time. The collection of kinetic data on the reaction of the extremely reactive alpha-O site with CH_4 was attempted by cooling down with dry ice and liquid nitrogen, but condensation issues, methane condensation, and diffusion limitations remained problematic and a dedicated cell should be used.[173]

3.1.2.2 Partial oxidation of methane to methanol with Cu-zeolites

The last two decades, both Cu- and Fe-exchanged zeolites have been researched for the selective oxidation of methane to methanol under milder conditions than in syngas routes. These reactions are generally run stoichiometrically because the recovery of the methanol is often achieved through addition of water, deactivating the catalyst. Fe-exchanged zeolites require N_2O as oxidant while Cu exchanged zeolites can be activated with O_2 as well.[100] Recent work also reports the use of H_2O as oxidant using Cu zeolites.[174, 175] One of the challenges in this conversion, especially with N_2O and O_2, is to prevent thermodynamically favored overoxidation.[176] Typically, the MTM process occurs on Cu-zeolites in a stepwise fashion to separate methane from the oxidant and prevent partial oxidation products from overoxidation.[177] First, the Cu-zeolite is activated with O_2 or N_2O to form the active copper-oxygen (Cu/O) species. This step can be split up into an autoreduction step in He at high temperature (~500 °C), and an activation with O_2 or N_2O at lower temperature (~200 °C).[178, 179] In the second step, methane is reacted over the copper zeolite at moderate temperatures, usually between 150 and 200 °C. The methoxy and methanol products are adsorbed onto the zeolite, and need to be extracted with water or steam.[103, 179-182] Many different Cu/O species have been proposed in literature as the active sites for MTM.[177] Mononuclear $[CuOH]^+$ and binuclear $[CuOCu]^{2+}$ species are described most often, based on spectroscopic results and ab initio modelling.[163-165] Their reaction mechanisms are drawn in Figure 22.

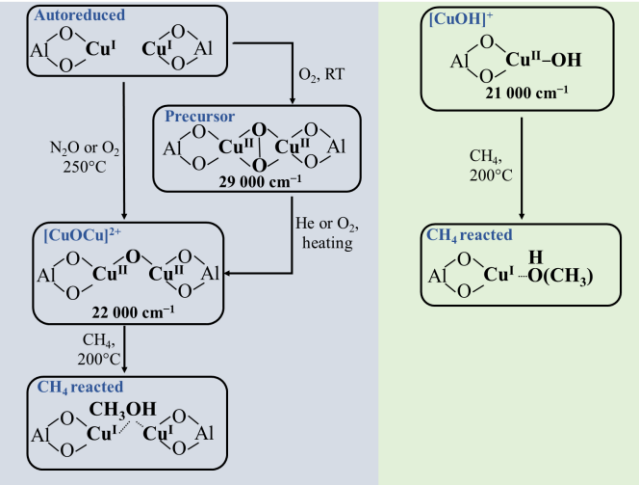


Figure 22. Reaction schemes and intermediates of methane to methanol over Cu-zeolites with (left) $[CuOCu]^{2+}$ and (right) $[Cu^{II}OH]^+$ active sites, including the known UV-VIS-NIR absorption bands.

The most analysed spectroscopic handle connected to MTM with copper zeolites is a ~22 000 cm^{-1} absorption band found in Cu-MFI,[163] Cu-MOR,[153, 164, 167, 183] and Cu-CHA.[165] The ~22 000 cm^{-1} absorption band, through its rR profile, is assigned as a bridging oxo → Cu^{2+} LMCT of an extraframework $[CuOCu]^{2+}$.[164] Recently, also a $[Cu^{II}OH]^+$ in Cu-MOR was found to have an absorption band at 20 700 cm^{-1}, while similar in energy to the 22 000 cm^{-1} band of $[CuOCu]^{2+}$, they are easily distinguished from rR.

which was assigned to an HO^- → Cu^{2+} charge transfer.[166] Given the similar energy of their absorption bands, there is a risk to interpret the results assuming only one of the two sites, and previously published results on site-specific reactivities must be assessed critically. To distinguish the two sites, the UV-VIS-NIR absorption spectroscopy is best coupled with rR and EPR spectroscopy. If accessible, cryogenic UV-VIS-NIR absorption may also be used to resolve the species.

MTM reaction kinetics are useful to disentangle and to compare kinetic parameters of different active sites for MTM versus methanol overoxidation.[184, 185] Experimental kinetic parameters of elementary steps helped identify the electronic structure and crystallographic location.[153, 164, 186] In-silico proposed reaction mechanisms have been verified against the experimental activation barriers,[153, 165] which has helped reveal structure-reactivity relationships.[103, 153, 165] *In situ* UV-VIS-NIR absorption spectroscopy was used to study the mechanism of $[CuOCu]^{2+}$ formation from a binuclear 2 Cu^{+} precursor in Cu-MFI, with O_2 as well as through oxygen atom transfer (OAT) from N_2O.[187] The kinetics of N-O cleavage were evaluated by tracking the growth of the 22 700 cm^{-1} absorption band at different reaction temperatures from 25 to 100 °C. The growth of the absorption band as a function of time was evaluated with a first order rate equation and the obtained rate constant at each particular temperature was used to construct an Arrhenius plot. The resulting Arrhenius plot gave an apparent activation barrier E_a = 2.5 kcal/mol, which is consistent with DFT calculated apparent barriers of pathways with μ-1,1-O and μ-1,3-O,N N_2O-bridged structures as intermediates in the conversion of 2 Cu^{+} to $[CuOCu]^{2+}$ (Figure 23 A).

When the 2 Cu^{+} precursor is contacted with O_2 at room temperature, a 29 000 cm^{-1} absorption band appears (Figure 23 B). This band does not appear with N_2O activation and was related to a μ-η^2:η^2 peroxo-bridged dicopper site $[Cu_2O_2]^{2+}$ based on its characteristic resonance Raman vibrations. The peroxo species is not active in methane oxidation, but it transforms upon heating in inert or O_2 atmosphere into $[CuOCu]^{2+}$ with simultaneous growth of the 22 700 cm^{-1} absorption band and loss of the 29 000 cm^{-1} absorption band. Where the second oxygen of the peroxo bridge ends up has not yet been confirmed.

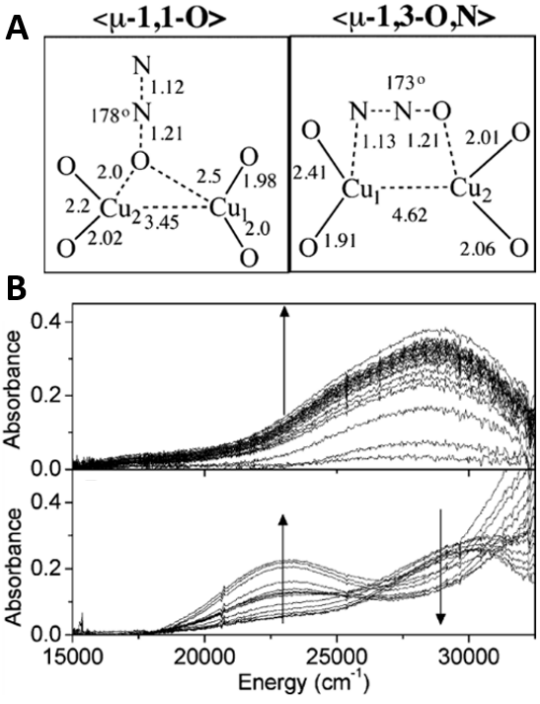


Figure 23. (A) Binding modes of N_2O on the binuclear Cu^{+} center. **(B)** UV-VIS spectra of autoreduced Cu-MFI during O_2 treatment at room temperature (top) and subsequent heating in He atmosphere to form $[CuOCu]^{2+}$ (bottom). Adapted from refs. [187, 188]. Copyright 2014 and 2010 American Chemical Society.

The $[CuOCu]^{2+}$ active sites react with methane with decay of the corresponding 22 700 cm^{-1} absorption band and formation of 2 Cu^{+}. The kinetics of the reaction were evaluated by

monitoring the disappearance of the absorption band at different temperatures on Cu-MFI (Figure 24).[165] From the resulting Eyring plot, thermodynamic parameters of the transition state, including activation enthalpy $\Delta H^{\ddagger}$ and entropy $\Delta S^{\ddagger}$, were obtained (Table 5). Also, a significant KIE was found when reacting with CD_4 instead of CH_4, indicating that C-H bond breaking was involved in the rate limiting step of the CH_4 oxidation.[189] This was further confirmed by NMR product analysis of the reaction with CH_2D_2.

Table 5. Comparison of the TS parameters for the $[CuOCu]^{2+}$ sites in Cu-MFI and Cu-CHA from ref. [165] and for the $[Cu^{II}OH]^{+}$ site in Cu-MOR from ref. [166].

	Site structure	$\Delta H^{\ddagger}$ **(kcal/mol)**	$\Delta S^{\ddagger}$ **(cal/(mol*K))**
Cu-MFI	$[CuOCu]^{2+}$	8.7	-45.5
Cu-CHA	$[CuOCu]^{2+}$	6.2	-51.7
Cu-MOR [a]	$[Cu^{II}OH]^{+}$	15.7	-39.5

[a] Thermodynamic data on $[CuOCu]^{2+}$ in MOR are not included in the comparison. This study,[164] was performed on samples with a mixture of $[CuOCu]^{2+}$, making the deconvolution inaccurate and inferred kinetic parameters unreliable (*vide infra*).

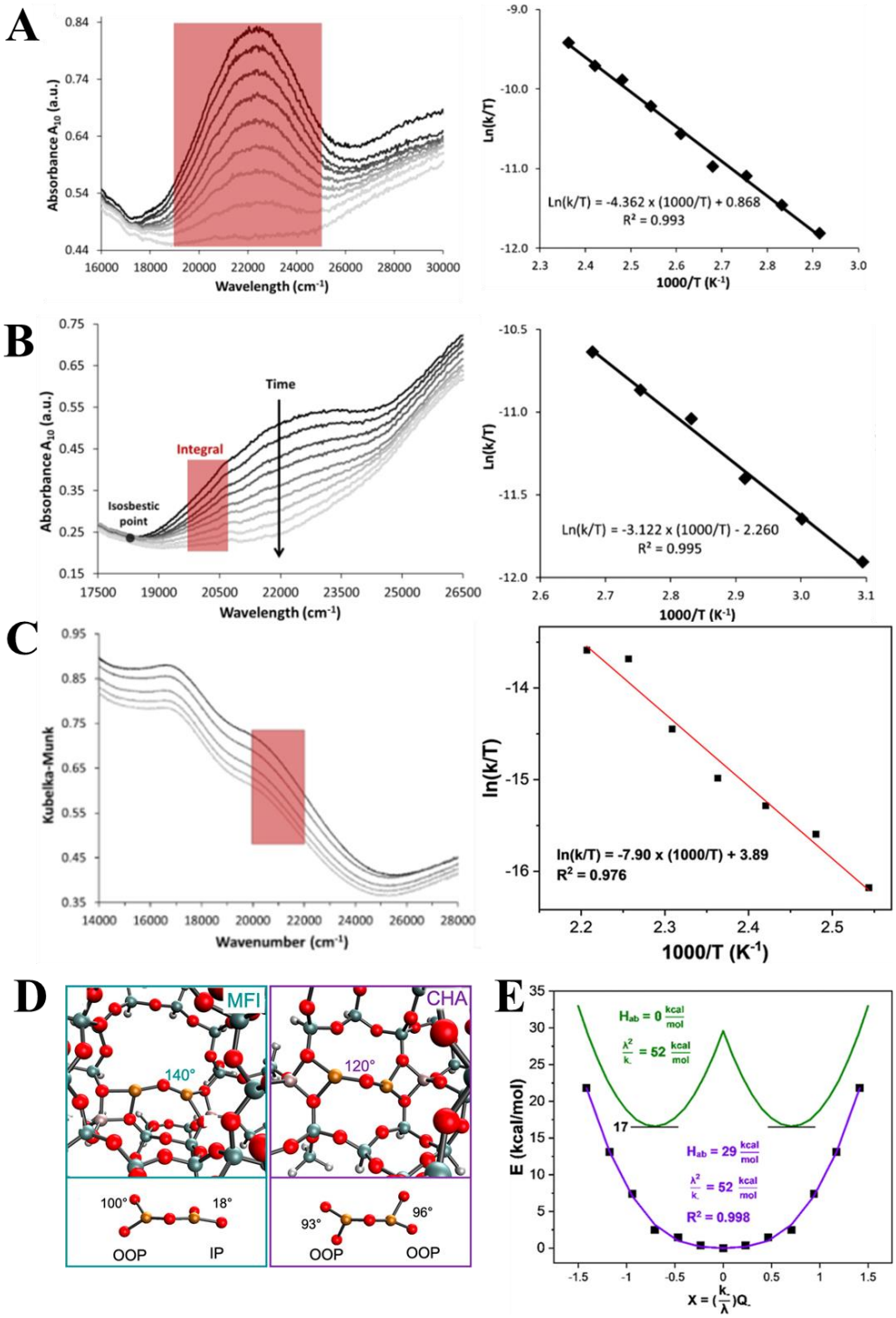


Figure 24. (A) Decay of the 22 700 cm^{-1} absorption band in time during reaction of $[CuOCu]^{2+}$ in Cu-MFI with methane at 90 °C (left) and Eyring plot for the reaction of CH_4 with $[CuOCu]^{2+}$ in Cu-MFI (right). **(B)** Decay of the 22 400 cm^{-1} absorption band in time during reaction of $[CuOCu]^{2+}$ in Cu-CHA with methane at 80 °C (left) and Eyring plot for the reaction of CH_4 with $[CuOCu]^{2+}$ in Cu-CHA (right). **(C)** Decay of the 20 700 cm^{-1} absorption band in time during reaction of $[Cu^{II}OH]^{+}$ in Cu-MOR with methane at 130 °C (left) and Eyring plot for the reaction of CH_4 with $[Cu^{II}OH]^{+}$ in Cu-MOR (right). **(D)** Schematic of bidentate oxygen ligation of $[CuOCu]^{2+}$ cores in Cu-MFI (green box) and Cu-CHA (purple box) assigning out of plane (OOP) and in plane (IP) ligation with respect to the CuOCu plane. **(E)** DFT-calculated potential energy surface of $[CuOCu]^{2+}$ (purple) and of localized structure (green). Adapted from refs. [163, 165, 166]. Copyright 2021 American Chemical Society, 2009 Proceedings of the National Academy of Sciences and 2022 American Chemical Society.

If the absorption band of the species under study overlaps with other absorption bands, one best integrates the absorption band used for kinetic tracking in a range where the influence of the superposing absorption band is limited. This is illustrated for the UV-VIS-NIR tracking of the reaction of $[CuOCu]^{2+}$ with CH_4 in Cu-CHA.[165] The decay of the band during reaction at 80 °C is shown in Figure 24 B. An isosbestic point was observed on the low energy side of the absorption band but not at the high energy side, indicating overlap with another higher energy absorption band connected to a different chemical transformation. Since a reliable deconvolution of the spectrum was unavailable, the integration was limited to the lower energy-range. $[CuOCu]^{2+}$ in Cu-CHA is significantly more reactive than the $[CuOCu]^{2+}$ species in MFI. The high reactivity of Cu-CHA is due to a comparatively low enthalpy barrier $\Delta H^{\ddagger}$ (Table 5). Further DFT calculations show that the relative rotations of the two bidentate oxygen ligands with respect to each other significantly affect the interaction between Cu atoms and the bridging oxo (Figure 24 D). The near 0° relative rotation of ligand sets in Cu-CHA leads to a destabilization of the $[CuOCu]^{2+}$ core and makes it more reactive compared to the structural analogue in MFI, in which the bidentate ligands have a ~90° relative rotation. This shows how the rigid zeolite lattice can enforce an unstable active site geometry, reminiscent of the entatic state effect in metalloprotein chemistry.

The 22 400 cm^{-1} DR UV-VIS absorption band was also observed in O_2 or N_2O activated Cu-MOR, where it was shown to be an unresolved superposition of the absorption bands of three slightly distinct $[CuOCu]^{2+}$ cores designated as MOR1, MOR2 and MOR3.[153, 164, 167] MOR1 is in the eight membered ring side pocket that is exposed to the twelve membered ring channel. MOR2 and MOR3 are on the other side of the eight membered ring side pocket, across the compressed eight membered ring channel (see Figure 21) that runs parallel to the twelve membered ring main channel.[164, 167] However, due to a lack of reliable deconvolution for the 22 000 cm^{-1} absorption band into its three constituents, no accurate kinetics of each $[CuOCu]^{2+}$ active site can be obtained. In ref. [164] the MOR1 and MOR2 CH_4 activation energies were compared, but considering the more recently revealed contributions of also MOR3 and $[Cu^{II}OH]^{+}$ to the absorption in the ~22 000 cm^{-1} region, the $\Delta H^{\ddagger}$ and $\Delta S^{\ddagger}$ values should be re-evaluated. The $[Cu^{II}OH]^{+}$ species in Cu-MOR is already present in the autoreduced material, in absence of the $[CuOCu]^{2+}$ species that require activation with O_2 or N_2O. Without this spectral overlap, its kinetics were obtained by monitoring its 20 700 cm^{-1} charge transfer band with DR UV-VIS-NIR absorption spectroscopy (Figure 24 C). The first order rate constants were extracted and Eyring plots were constructed.[166] $[Cu^{II}OH]^{+}$ has a 9.5 kcal/mol higher enthalpic barrier than $[CuOCu]^{2+}$ in Cu-CHA (Table 5). From experimentally validated DFT models, the electron delocalization via the bridging O over the two Cu atoms in $[CuOCu]^{2+}$ stabilizes the hydrogen atom abstraction (HAA) first product ($[Cu^{I}OHCu^{II}]^{2+}$) by 17 kcal/mol compared to the localized structure (Figure 24 E). Therefore, it is proposed that the higher reactivity of binuclear $[CuOCu]^{2+}$ sites compared to mononuclear $[CuOH]^{+}$ sites is a direct result of stabilization of the $[Cu^{I}OHCu^{II}]^{2+}$ product by electron delocalization over the two Cu cations via the bridging ligand, indicating the importance of copper nuclearity on reactivity.

It should be noted that Cu speciations may be significantly impacted by the activation protocol, and this limits the consensus in the literature. In the above discussion, when the Cu-CHA is first autoreduced in He at high temperature and subsequently activated with O_2 or N_2O at lower temperature, mainly $[CuOCu]^{2+}$ active sites form. As shown in Figure 25, a broad LMCT band between 22 200 and 35 000 cm^{-1} disappears upon exposure of the O_2 or N_2O activated Cu-CHA to methane at 473 K. This suggests that the absorption features of active copper species fall in this range. Based on their characteristic Raman vibrations, Ipek et al. propose that trans-

μ-1,2-peroxo dicopper(II) and $[CuOCu]^{2+}$ form on Cu-CHA following O_2 or He treatment at 723 K, although this assignment has been criticised.[165, 190] O_2 treatment then results in a higher concentration of this species.

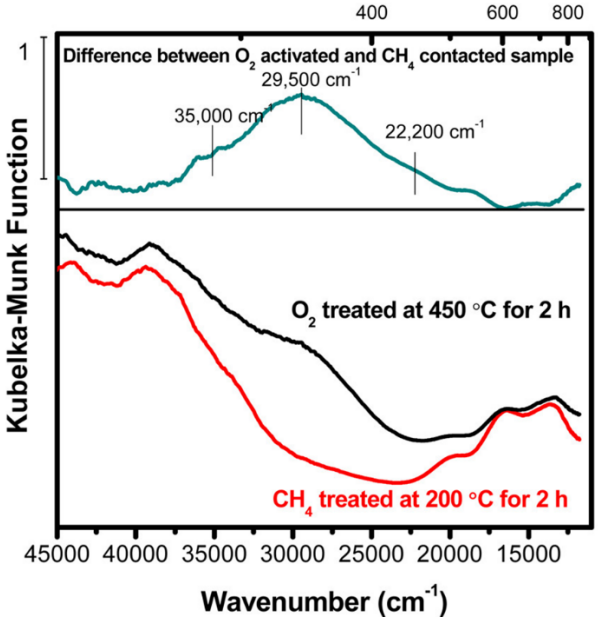


Figure 25. UV-VIS absorption spectra of Cu-CHA after O_2 treatment at 723 K (black) followed by 2 h CH_4 treatment at 473 K (red). The difference spectrum is shown in green. Adapted from ref. [190] Copyright 2017 American Chemical Society.

3.1.2.3 Selective catalytic reduction of NO by NH_3 with Cu zeolites

Selective catalytic reduction (SCR) of NO_X by NH_3 (NH_3–SCR) to N_2 and water is currently the leading deNO_X technology for diesel engine emissions control.[191] eq 15 is a standard low temperature (<250 °C) NH_3-SCR reaction of NO.

$$4NO + 4NH_3 + O_2 \rightarrow 4N_2 + 6H_2O \quad (15)$$

Among various catalysts studied, Cu-CHA has been widely investigated and commercialized owing to its remarkable catalytic reactivity, low selectivity toward undesirable N_2O production, and excellent hydrothermal stability.[157, 158] Great efforts have been devoted to reveal the catalytic chemistry underlying the conspicuous performance of Cu-CHA in standard low temperature NH_3-SCR reaction. *In situ* UV-VIS-NIR studies have contributed greatly to understanding the complex mechanism, particularly in combination with EPR, XAS and DRIFTS.[158, 190, 192-197] Figure 26 illustrates a representative reaction scheme. It has been well established that isolated Cu^{2+} and $[Cu^{II}OH]^+$ species coordinated to the zeolite lattice (Figure 27 B) act as the main active centers in Cu-CHA.[192-194] The Cu^{2+} species are associated with exchange sites with two Al substitutions in the lattice, separated by one or two Si tetrahedral sites in the same six-membered ring, while the $[Cu^{II}OH]^+$ motif is ligated by one Al center and prefers to anchor near 8MR windows.[198, 199] Fundamental SCR mechanistic studies demonstrate that NH_3-SCR over Cu-zeolites proceeds via a redox cycle of Cu^{2+} and Cu^+. NO and NH_3 reduce Cu^{2+} to Cu^+ and O_2 reoxidizes Cu^+ to Cu^{2+}.[200-202] The active Cu^{2+} and $[Cu^{II}OH]^+$ sites exhibit a strong affinity toward NH_3, leading to the generation of $[Cu(OH)(NH_3)_3]^+$ and $[Cu(NH_3)_4]^{2+}$ complexes detached from the zeolite framework.[203] Subsequently, NO interacts with these mobile, NH_3-ligated Cu^{2+} complexes, leading to NO decomposition and the generation of $[Cu(NH_3)_2]^+$ complexes (note the reduction of Cu^{2+} to Cu^+ in this step). The small

size and low, delocalized charge of Cu^+ ammine allow its migration through the zeolite pore structure. Two $[Cu(NH_3)_2]^+$ species combine with dioxygen to form a $[Cu_2O_2(NH_3)_4]^{2+}$ intermediate, which then regenerates two isolated Cu^{2+} species.[192, 204] This mechanism is reminiscent of O_2-assisted oxidation of Cu^+ sites via multinuclear intermediates in bioinorganic chemistry.[205-207]

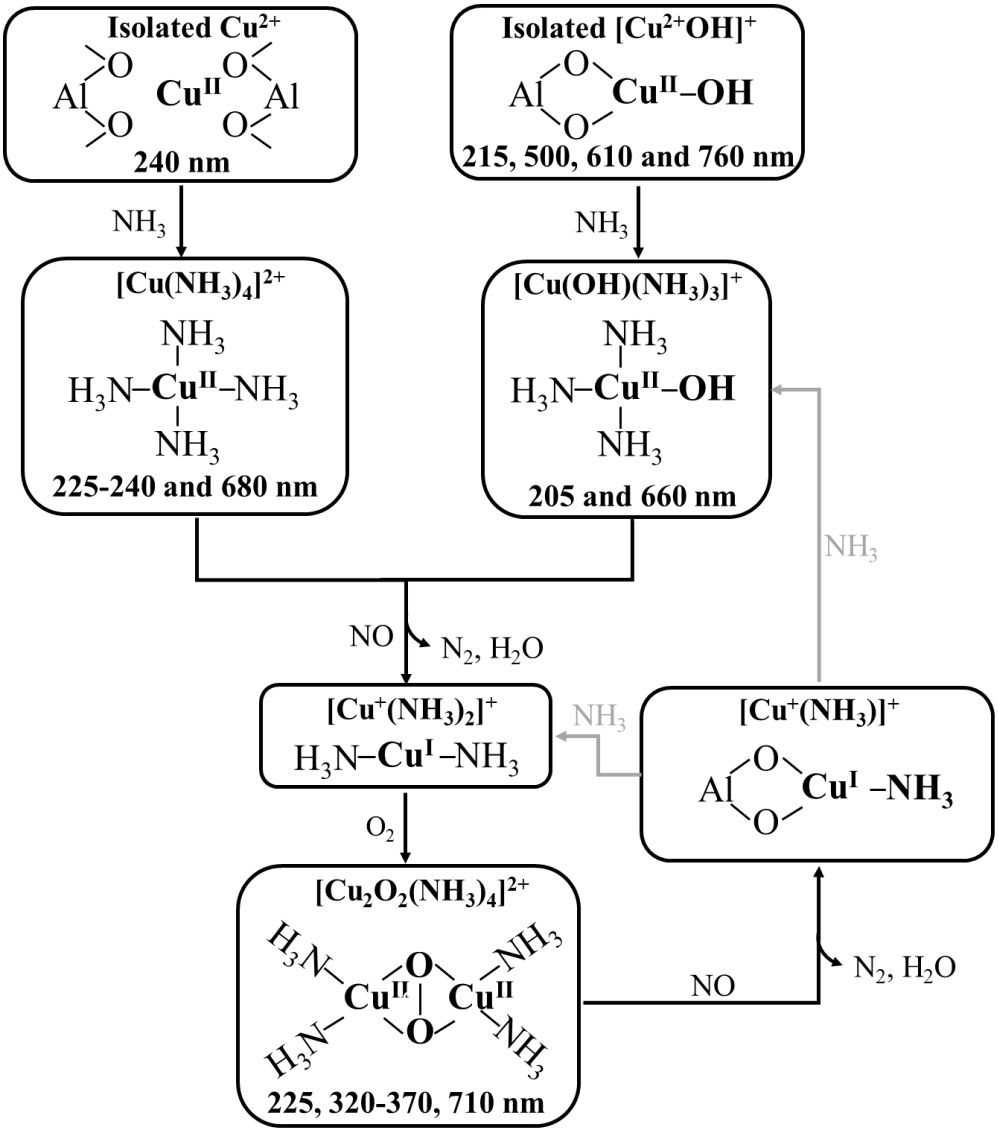


Figure 26. A proposed reaction scheme and intermediates of standard low temperature NH_3-SCR with Cu-zeolites, including suggested UV-VIS-NIR absorption bands, based on the spectroscopic studies in ref. [196].

As Cu^+ has a fully occupied d shell ($3d^{10}$), d-d transitions are only observable for Cu^{2+} ($3d^9$). Therefore, monitoring the d-d transitions during the NH_3-SCR reaction makes it possible to track the consumption and regeneration of Cu^{2+} species. Moreover, the d-d and CT transition energies are highly sensitive to coordination environment and therefore excellent features to probe the copper bound intermediates throughout the reaction scheme. After the high temperature oxidation treatment, the UV-VIS-NIR absorption spectrum of Cu-CHA shows three absorption features at ~500, ~610, and ~760 nm (Figure 27 A), which are attributed to d-d transitions of zeolite-coordinated Cu^{2+} species.[208] Through combined DRIFTS data, it was derived that the dominant Cu^{2+} species in the O_2-activated Cu-CHA sample was the isolated

$[Cu^{II}OH]^+$, and all three bands are generally attributed to $[Cu^{II}OH]$.[198, 209] However, speciation of Cu species in Cu-CHA catalysts is significantly influenced by Si/Al ratio and Cu loading,[210] and the band assignments cannot be generalized to all Cu-CHA samples. The isolated Cu^{2+} and $[Cu^{II}OH]^+$ contents in Cu-CHA can be controlled by adjusting the Si/Al and Cu/Al ratios (Figure 27 B).[193, 198, 199]

Upon exposure to NH_3, a noticeable blueshift of the d-d transition absorption peak to 640 nm is observed, and the d-d features of the $[Cu^{II}OH]^+$ disappear, corresponding to the exchange of O-ligands for N-ligand. Subsequent reaction of the Cu^{2+}-$[NH_3]_x$ complexes with NO decreases the intensity of the 640 nm band, and simultaneous N_2 release is observed.[208] For the investigation of the oxidation half cycle, various oxidizing gas mixtures were fed to Cu-CHA after reduction by NO + NH_3, with simultaneous UV-VIS-NIR absorption measurements. The oxidation treatments increases the intensity of the d-d absorption band, indicating the oxidation of Cu^+ to Cu^{2+}. Interestingly, the intensity of the d-d band is slightly higher under oxidation by NO/O_2 and $NO/NO_2/O_2$ than by O_2, suggesting that O_2 acts as the primary oxidant in the oxidation half cycle, and that the presence of NO_X promotes this step. The right panel of Figure 27 A shows the kinetic curves for N_2 formation and the intensity of the 760 nm band during NH_3-SCR - reduction - NH_3-SCR transient reactions, in which the gas feed was changed from NH_3+NO+O_2 to NH_3+NO, and then reverted to NH_3+NO+O_2.[208]

While the *in situ* UV-VIS-NIR spectra enable the tracking of the copper oxidation state and its dependence on reaction conditions, the assignments of the specific absorption bands to well defined intermediates has been more involved. From EPR, XAS, DRIFTS and DR-UV-VIS-NIR spectroscopies, across different *in situ* studies, the $Cu^{2+} \rightarrow Cu^+$ half cycle with Cu-CHA is generally agreed upon (eq 16).[209-211]

$$[Cu^{II}(OH)(NH_3)_3]^+ + NO \rightarrow [Cu^{I}(NH_3)_2]^+ + N_2 + 2H_2O \quad (16)$$

Of particular importance was the XAS study by Paolucci et al. showing the mobilization of Cu^+ through its solvation by NH_3, allowing it to migrate through the zeolite and cyle between multinuclear and mononuclear intermediates.[192] This mobilization, in combination with dependency on reaction conditions, gives access to multiple options for the rest of the reaction cycle, which is still debated. The DR-UV-VIS-NIR absorption spectra are generally convoluted and not fully understood, but some features, besides the d-d transitions of $[Cu^{II}OH]^+$, have been (tentatively) assigned on Cu-CHA (see also Figure 27).

Based on their behaviour on samples of different Si/Al and Cu/Al, Zhang et al. [209] assigned two LMCT bands at 215 nm and 240 nm respectively to isolated $[Cu^{II}OH]^+$ and Cu^{2+} sites. An additional 355 nm band is also present in their spectra for a Si/Al = 30 Cu-CHA. this is commonly assigned to binuclear Cu-oxo species.[190, 195] With increasing temperature, the intensity of the 215 nm and 355 nm bands in the Si/Al = 30 sample respectively decrease and increase. Therefore, they proposed that upon O_2 activation, two $[Cu^{II}OH]^+$ sites are bridged into a binuclear Cu-oxo intermediate, tentatively described as a $[Cu_2O_2]^{2+}$ site. Upon exposure to NH_3, mobile $[Cu(NH_3)_4]^{2+}$ and $[Cu(OH)(NH_3)_3]^+$ complexes are proposed. UV-VIS-NIR absorption features at ~240 & 680 nm and at 205 & 660 nm are respectively linked to these two complexes.[209] Oda et al. reported a 370 nm absorption band on Cu-AEI zeolite that is only observed under steady-state NH_3-SCR conditions, and therefore related to an unstable intermediate, which they also suggest for Cu-CHA.[212] The O_2 dependence of this band is shown in Figure 27 C, when the O_2 concentration is gradually reduced from 10 to 0%, the intensity of the 370 nm band decreases until it finally disappears. When the O_2 supply is restored the 370 nm band reappears. The intermediate was trapped and isolated by reducing the reaction

temperature. The 370 nm band develops significantly below 473 K and reaches a maximum at 323 K. It was further identified by *in situ* UV-VIS DRS studies coupled with XAS and measurements of reactivity towards NO, NH_3 and a mixture of NO and NH_3 at low reaction temperatures.[196] Through spectroscopic similarity to antiferromagnetically coupled $S = 0$ μ-η^2:η^2 peroxo-bridged dicopper(II) present in Cu proteins and other relevant model complexes,[205, 213, 214] the intermediate species was finally assigned as the μ-η^2:η^2 peroxo-bridged diamino dicopper(II) ($[Cu_2O_2(NH_3)_4]^{2+}$). Additionally, a d-d transition at 14 000 cm^{-1} (~710 nm) and LMCT bands between 27 000 and 31 000 cm^{-1} (320-370 nm) were assigned to this species. Very recently Lei et al.[197] observed a transient absorption band at 225 nm on Cu-CHA in NH_3 + NO atmosphere below 250 °C. Combining DRIFT and TD-DFT, and observing its correlation to an absorption band at 350 nm, they assigned this also to an LMCT of the confined μ-η^2:η^2 peroxo-bridged diamino dicopper(II).

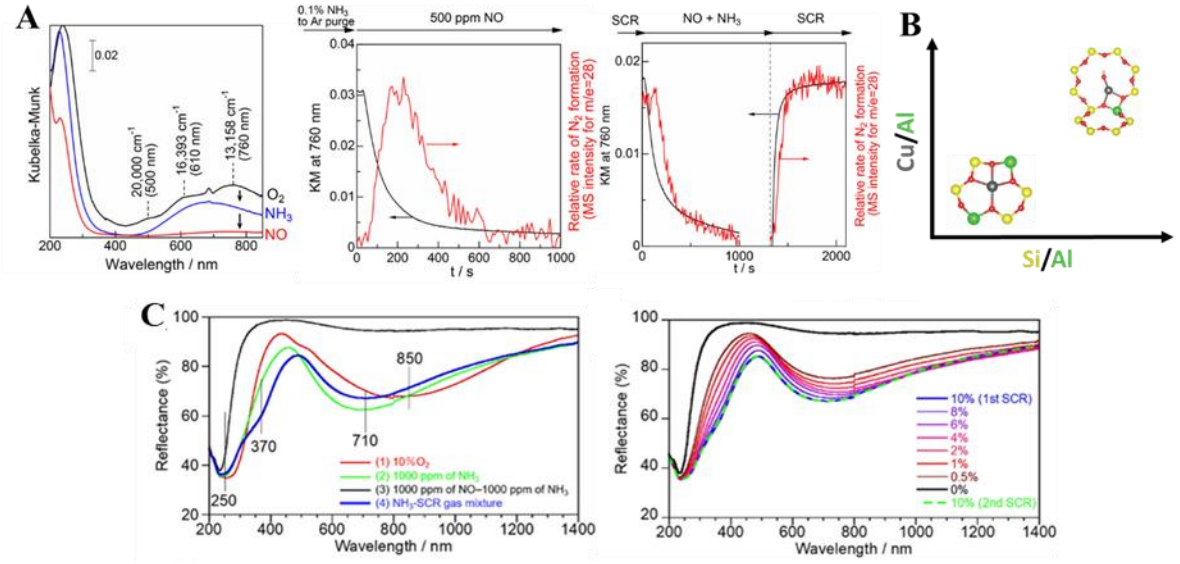


Figure 27. (A) (left) *In situ* UV-VIS absorption spectra of Cu-CHA during reduction half cycle. The catalyst was first oxidized under O_2, followed by exposure to NH_3 and then to NO. Time dependence of d-d transition band intensity of Cu^{2+} species and MS intensity of N_2 during (middle) reduction half cycle and during (right) NH_3-SCR - reduction - NH_3-SCR transient reaction. **(B)** Cu-speciation in the Cu-CHA catalyst as a function of Si/Al and Cu/Al. **(C)** *In situ* UV-VIS-NIR absorption spectra of Cu-AEI under (left) different gas mixtures at 473 K and (right) NH_3-SCR at 473 K with different O_2 concentration. Adapted from refs. [196, 208, 209, 212]. Copyright 2020 Wiley, 2022 American Chemical Society, and 2020 American Chemical Society.

The assignment of UV-VIS-NIR absorption bands to specific complexes on Cu-CHA in NH_3-SCR conditions is severely obstructed by the multitude of intermediates present and the sample dependence of the copper speciation. Nevertheless, the absorption bands mentioned above have been used to derive mechanistic insight and to identify the active sites. Zhang et al.[209] monitored the CT bands of isolated Cu^{2+} and $[Cu^{II}OH]^+$ in the NH_3-SCR reaction over Cu-CHA at different temperatures. While the ~210 nm band of $[Cu^{II}OH]^+$ starts to diminish at low temperature, the 240 nm band of isolated Cu^{2+} decays at higher temperature, indicating $[Cu^{II}OH]^+$ sites are more active. The 355 nm band of binuclear Cu-oxo species is present below ~180 °C for Cu-CHA with Si/Al = 30, and below ~200 °C for Si/Al = 6. It then decreases with temperature, showing the formation of reduced dimers. Negri et al.[196] tracked the 370 nm (27000 cm^{-1}) LMCT band of $[Cu_2O_2(NH_3)_4]^{2+}$ through pretreatment in O_2, subsequent reduction in NH_3+NO, and reoxidation with O_2 at the SCR reaction temperature. Upon exposure to NH_3, the d-d transition and LMCT band intensities decrease, although they do not

disappear completely (Figure 28), indicating NH_3 reacts with $[Cu_2O_2(NH_3)_4]^{2+}$ and reduces a fraction of the Cu^{2+} ions to Cu^+. When $[Cu_2O_2(NH_3)_4]^{2+}$ is exposed to NO, the corresponding absorption bands decrease faster with simultaneous formation of N_2, indicating that $[Cu_2O_2(NH_3)_4]^{2+}$ is more reactive toward NO than NH_3, and low-temperature NH_3-SCR reaction likely involves the reaction of $[Cu_2O_2(NH_3)_4]^{2+}$ with NO. From XANES data, the copper site is proposed to be reduced to a $[Cu^I(NH_3)]^+$ in this step.[196] The role of O_2 in the SCR mechanism, and the mechanism for its activation were further investigated by Lei et al.,[197] using the 225 nm absorption band of the peroxo bridged dicopper species. They observed increased N_2 evolution in the cofeeding of O_2 which they correlated to the intensity of the transient 225 nm feature. They thus propose the $[Cu_2O_2(NH_3)_4]^{2+}$ as a key intermediate in the low temperature NH_3-SCR of NO with Cu-CHA.

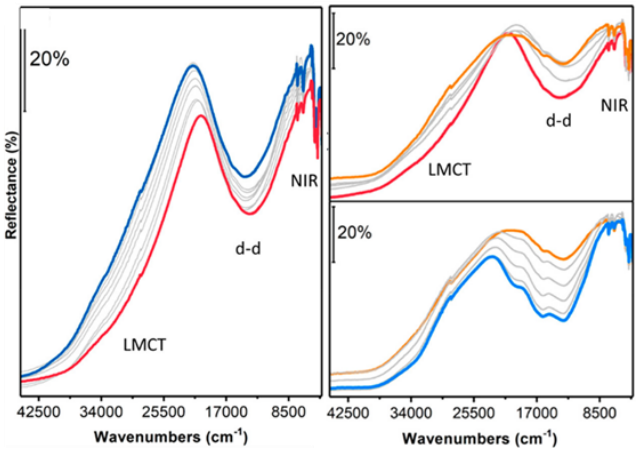


Figure 28. UV-VIS-NIR DR absorption spectra of Cu-CHA exposure to (left) NH_3/He and (right) NO/He at 200 °C after forming the $[Cu_2O_2(NH_3)_4]^{2+}$ complexes. Top and bottom panels on the right are initial and subsequent evolution of DR UV-VIS-NIR absorption spectra respectively. Blue thick line: after NH_3/He exposure, red thick line: spectrum collected after forming the $[Cu_2O_2(NH_3)_4]^{2+}$ complexes, grey thin lines: intermediates, light blue thick line: after NO/He exposure, orange thick line: the final spectrum in the panel. Adapted from ref. [196]. Copyright 2020 American Chemical Society.

3.1.2.4 Selective catalytic reduction of NO by NH_3 with Fe zeolites

Cu-zeolites are effective NH_3-SCR catalysts at low operating temperatures (< 400 °C), but they are less performant at higher temperatures where copper aggregates into inactive clusters, and where N_2O is formed as a by-product. Fe-zeolites on the other hand are better suited for high temperature NH_3-SCR as they demonstrate improved stability and high-temperature SCR selectivity compared to their Cu-exchanged counterparts.[215-220] While in Cu zeolite SCR small pore zeolites like CHA are preferred because they reduce the copper clustering, with Fe zeolite SCR, large pore zeolites (e.g. MOR and *BEA) are preferred. During the NH_3-SCR reaction, the Fe active sites cycle between Fe^{2+} and Fe^{3+},[220, 221] and several active sites have been proposed. These include Fe oxide particles, binuclear Fe^{3+} species and isolated Fe cations.[157, 222, 223] UV-VIS-NIR absorption spectra of Fe-zeolites are generally analyzed in three regions: < 300 nm, 300-400 nm and > 400 nm, which are roughly correlated to isolated Fe^{3+} species, aggregated Fe^{3+} species and Fe_2O_3 nanoparticles respectively.[224, 225] In the case of the isolated Fe^{3+} species, only the CT bands of O ligands to Fe^{3+} are observable in the UV-VIS-NIR spectra since the d-d transitions are symmetry and spin forbidden. Typically two CT bands, which arise from the $t_1 \rightarrow t_2$ and $t_1 \rightarrow e$ transitions, are observed for each Fe^{3+} species and their exact energies depend on the number of ligands.[226] For four-coordinated isolated Fe^{3+} the two absorption bands are both below 250 nm while for octahedrally coordinated Fe^{3+} the two bands

are at 187-234 and 244-305 nm, respectively. With these characteristic handles to follow, *in situ* UV-VIS spectroscopy has been employed to investigate the NH_3-SCR process catalyzed by Fe-zeolites.

Yasumura et al. conducted an *in situ* UV-VIS-NIR absorption study on Fe-MOR to investigate the redox cycle of NH_3-SCR.[227] A charge transfer band centered at 265 nm and a shoulder above 300 nm indicate the presence of octahedrally coordinated Fe^{3+} species and oligomeric Fe^{3+} species as the main Fe species (Figure 29 A).[227, 228] The 265 nm absorption band decreases upon exposure to NO + NH_3 with simultaneous N_2 formation and subsequently recovers in O_2 or NO + O_2 flow, indicating the NH_3-SCR over Fe-MOR proceeds through a redox cycle. In addition, the recovery of the Fe^{3+} species is faster under NO + O_2 flow than under the O_2 flow, suggesting that NO promotes the reoxidation of Fe^{2+}.

Structural changes of Fe species in Fe-*BEA during NH_3-SCR were also probed by *in situ* UV-VIS-NIR spectroscopy.[223] The UV-VIS-NIR spectrum of the untreated Fe-*BEA sample is characterized by two bands at ~220 and 275 nm (Figure 29 B), indicating ion-exchanged Fe species are mainly present as octahedral coordinated Fe^{3+} species. During heating from 423 K to 723 in O_2, absorption increases below 250 nm and between 300-400 nm, indicating the formation of Fe^{3+} species in tetrahedral coordination and Fe-O-Fe species. The transformation of Fe species upon heating in O_2 results from the removal of hydroxyl and water ligands on extra-framework Fe^{3+} cations. Under NH_3-SCR conditions, there is only a small change in the overall intensity of the spectra, indicating these *in situ* formed Fe species during O_2 oxidation are still present under NH_3-SCR conditions. The deconvolution of the UV-VIS-NIR spectra further indicates that part of octahedrally coordinated Fe^{3+} species is restored at the expense of bridging Fe-O-Fe species (320 nm) at 423 K. Heating to 523 K, however, reverses this, as confirmed by *in situ* EXAFS analysis. These results suggest that the octahedral coordinated Fe^{3+} species are key intermediates for the reversible changes of Fe species during the NH_3-SCR reaction. In addition, the low catalytic activity at 423 K is attributed to the significant dissociation of binuclear Fe clusters into isolated octahedral coordinated Fe^{3+} species.

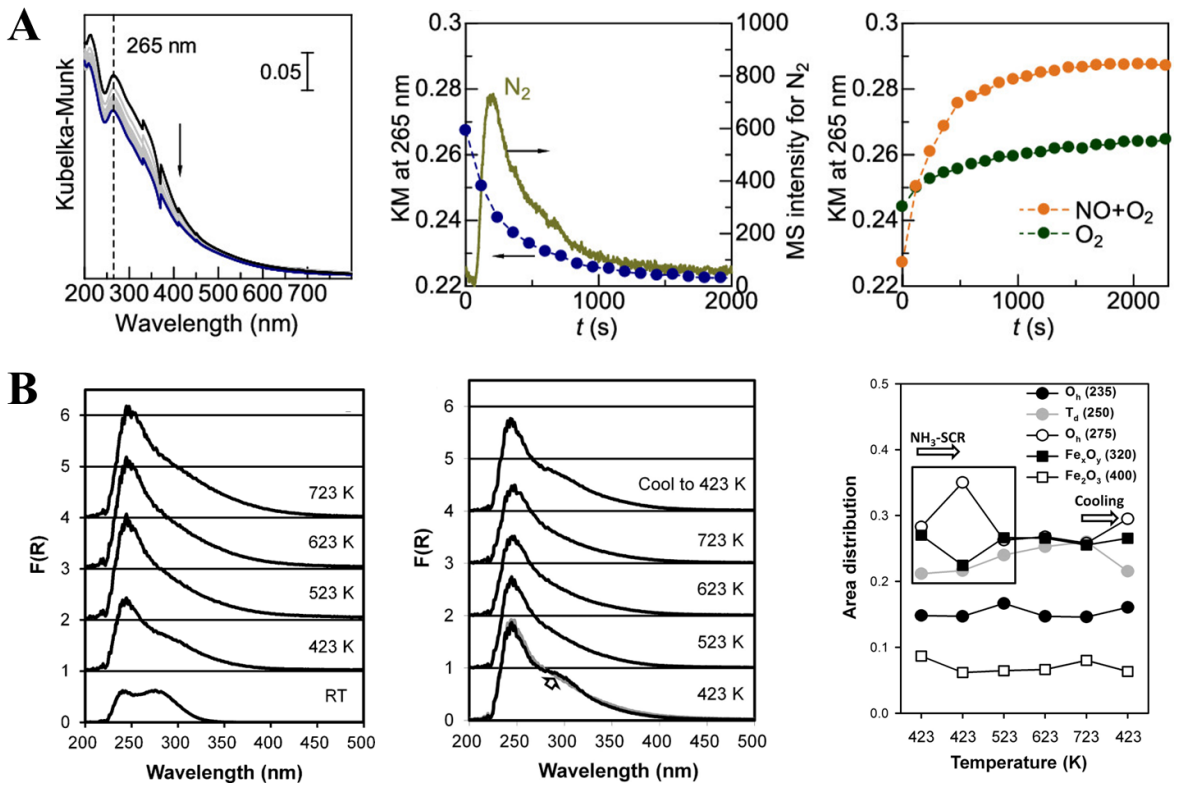


Figure 29. (A) (left) UV-VIS absorption spectra of Fe-MOR during exposure to NO + NH_3 at 300 °C. (middle) Changes in the UV–VIS absorption intensity at 265 nm in NO + NH_3 and the MS signal of N_2. (right) Time course of the UV-VIS absorption intensity at 265 nm under O_2 or NO + O_2. (B) UV-VIS absorption spectra of Fe-*BEA during (left) heating in O_2 and NH_3–SCR reaction at different temperatures. (right) Deconvolution results of UV-VIS spectra of Fe-*BEA during NH_3–SCR reaction at different temperatures. Adapted from refs. [223, 227]. Copyright 2022 and 2013 American Chemical Society.

3.1.2.5 N_2O decomposition with Fe zeolites

Fe-zeolites of several topologies can stabilize a S=2 square planar Fe^{2+} site, commonly named α-Fe^{II}, with an interesting capability to abstract the oxygen atom from N_2O forming a surface oxygen and releasing N_2.[17, 168] At higher temperatures the surface oxygen recombines and is released as O_2 making the N_2O decomposition catalytic. While the site offers a good hypothesis for the lower N_2O release in NH_3-SCR with Fe-zeolites compared to Cu-zeolites, its role in SCR has never been specifically investigated despite the availability of very clear spectroscopic probes.

The α-Fe^{II} site can be prepared in almost pure form enabling full attribution of spectroscopic features. Key absorption band assignments are summarized in Figure 30. The experimental UV-VIS-NIR absorption features of α-Fe^{II} were fully explained with the Fe^{2+} electronic structure by Hallaert et al.[229] α-Fe^{II} in Fe-*BEA exhibits a particularly high energy ligand field band at 15 900 cm^{-1}, distinctive for the square planar ligand field of the high spin Fe^{II}. For α-Fe^{II} this ligand field band is particularly intense (see also Figure 1). Similar, but weaker absorption bands are observed in Fe-ZSM-5, Fe-FER and Fe-CHA. The surface oxygen formed upon oxygen atom abstraction from N_2O remains bound to the α-Fe^{II}, yielding a high spin square pyramidal $[Fe{=}O]^{2+}$, commonly named α-O. Also α-O can be produced in high purity, and there is a clear fingerprint experimental UV-VIS-NIR absorption spectrum. On Fe-*BEA the α-O spectrum includes an intense 16 900 cm^{-1} CT absorption band with a high energy

shoulder (also CT) at ~20 000 cm^{-1} and broad absorption at ~6000 cm^{-1} from a d-d transition with vibronic coupling. Contrary to α-Fe^{II} the exact matching of electronic excitations to their corresponding experimental absorption bands in inconclusive for α-O.[230] However, the lower energy d-d transition band shows vibronic coupling when observed in MCD, with a frequency of ~1000 cm^{-1}.[17] It can thus tentatively be linked to the $d\pi$-d_{z^2} ligand field transition. The Fe=O stretch can also be observed with NRVS for α-O on Fe-*BEA at 885 cm^{-1}.[169]

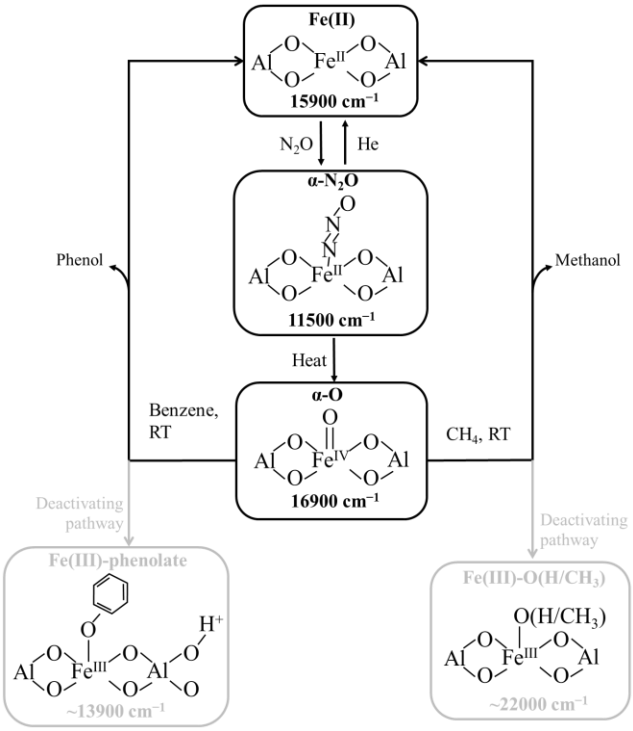


Figure 30. Reaction schemes and intermediates of N_2O decomposition and C-H activation with Fe zeolites, including the known UV-VIS-NIR absorption bands.

In situ UV-VIS-NIR absorption spectroscopy coupled to Mössbauer and Fourier-transform infrared spectroscopy (FTIR) spectroscopy were used to identify the N_2O ligation onto α-Fe^{II} that precedes oxygen atom abstraction.[170] Around room temperature, N_2O binds reversibly to the α-Fe^{II} end-on via the N atom to form a square pyramidal complex (α-N_2O) with ligand field absorption bands at 5 000 and 11 500 cm^{-1}. At low temperatures, a second N_2O binds at the same side of the Fe^{II} site, as observed in low temperature Mössbauer and FTIR. When heated, the oxygen atom is abstracted to form α-O and N_2. The thermodynamics of N_2O adsorption were measured by tracking the 11 500 cm^{-1}/15 900 cm^{-1} equilibrium on Fe-*BEA in different partial pressure of N_2O at various temperatures (Figure 31 A). The different conditions shifted the equilibrium between both ligand field bands with a clear isosbestic point at 13 500 cm^{-1} indicating a single reversible transformation. The adsorption was evaluated using a Langmuir adsorption model and the equilibrium constants were determined for the different temperatures (Figure 31 C). With the Van 't Hoff equation the enthalpy of adsorption of $\Delta H^o = -4.8 \pm 0.1$ kcal/mol and an entropy of adsorption of $\Delta S^o = -7.1 \pm 0.4$ cal/mol·K were derived.

The oxygen atom abstraction was tracked by the decay of the 11 500 cm^{-1} absorption band of α-N_2O and the simultaneous growth of the 16 900 cm^{-1} and 28 000 cm^{-1} bands of α-O (Figure 31 B). An isosbestic point was observed at 14 000 cm^{-1} indicating a single transformation, selectively converting the adsorbed N_2O into α-O. From a first order reaction model and an

Eyring plot (Figure 31 D), the enthalpy and entropy of the TS were determined to be $\Delta H^{\ddagger}$ = 17.7 ± 1.4 kcal/mol and $\Delta S^{\ddagger}$= −22.4 ± 3.8 cal/mol·K.

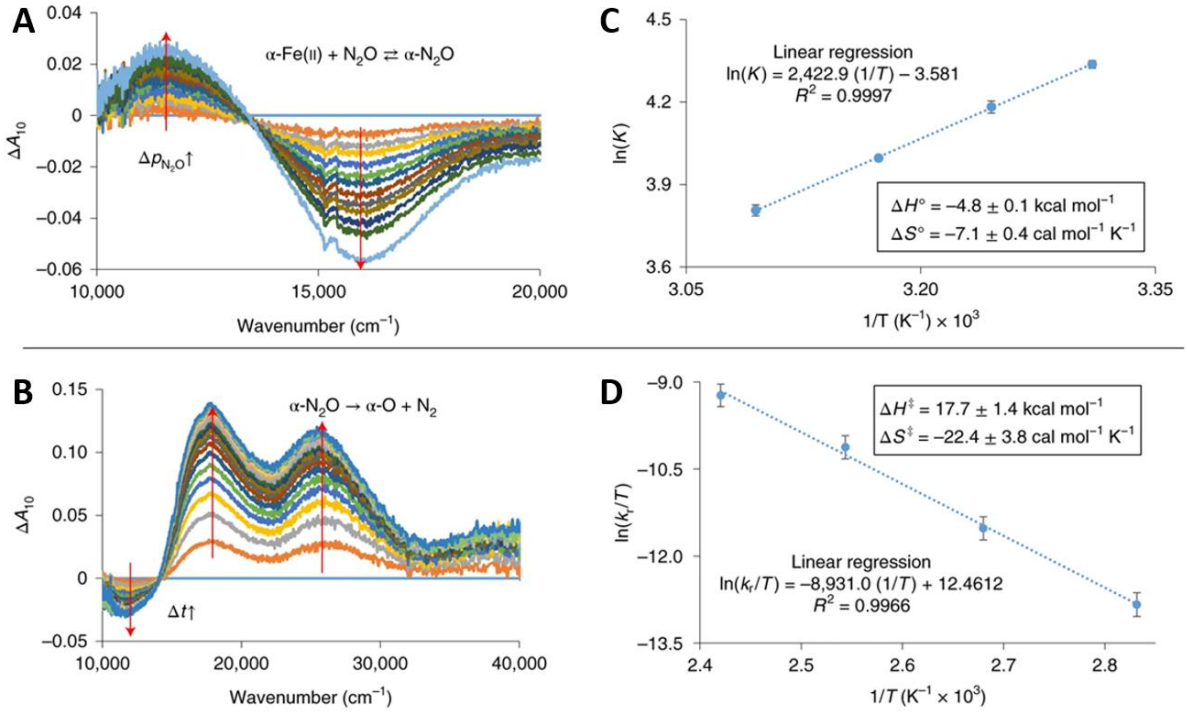


Figure 31. UV-VIS-NIR absorption spectroscopy of α-N_2O and its thermodynamics. **(A)** (left) *In situ* UV-VIS-NIR absorption difference spectra of Fe-*BEA at 308 K after high temperature He treatment with $p_{(N_2O)}$ ranging from 0 to 0.05 atmosphere. **(C)** Van 't Hoff plot of data derived from the adsorption data from *in situ* UV-VIS-NIR absorption spectra analogous to those shown in the left. **(B)** (left) *In situ* UV-VIS-NIR absorption difference spectra of Fe-*BEA at 373 K following the transformation of α-N_2O to α-O over a time interval of 15 minutes in an atmosphere of 35 vol.% N_2O in He. **(D)** Eyring plot of data derived from *in situ* UV-VIS-NIR absorption spectra analogous to those shown in the left. Adapted from ref. [170]. Copyright 2021 Springer Nature.

The spectroscopic and thermodynamic data were used to build an experimentally validated reaction mechanism that was evaluated with molecular modelling. This revealed the role of the coordination geometry of α-Fe^{II}. A distortion of the square planar geometry where the Fe atom is pulled out of the plane of oxygen atoms strengthens the η^1-O binding of N_2O and lowers the apparent activation barrier for oxygen atom abstraction. Interestingly, this structural difference exists between the α-Fe^{II} sites in Fe-*BEA and Fe-CHA. The comparison of their N_2O binding and activation thermodynamics has, however, not yet been made. Note that the two α-Fe^{II} sites also differ in other aspects (second coordination sphere, pore system, ligand field strength) so that the comparison would still not be a perfect experimental representation of the molecular modelling findings.

3.1.2.6 C-H bond activation with α-O on Fe-zeolites

The α-O site is highly reactive for partial oxidations of methane, other alkanes and benzene. The products of these reactions have been investigated with coupled *in situ* spectroscopies including UV-VIS-NIR absorption, rR, MCD, EPR, NRVS and XAS.[162, 231] From the benzene reaction on Fe-ZSM-5, a deactivating Fe^{III}-phenolate was identified with a spectroscopic handle at 13 900 cm^{-1}, which is composed of two overlapping bands at 11 600 and 13 300 cm^{-1}. The pathway to the Fe^{III} phenolate competes with the catalytic pathway to phenol that leads to the regeneration of the α-Fe^{II} precursor to α-O. On Fe-*BEA the analogous absorption feature

lies at 15 200 cm^{-1}. A 10 500 cm^{-1} band was identified as the adsorption complex of benzene on α-Fe^{II}. Similarly, in the reaction of α-O with methane, a deactivating pathway to Fe^{III}-OH and Fe^{III}-OCH_3 was identified through their UV-VIS-NIR absorption handles around 22 000 cm^{-1}. Here the pathway competes with the catalytic route to methanol and α-FeII. For both reactions, the spectroscopic handles are known, the intermediates are identified, and interesting conclusions for better catalyst design have been derived, but *in situ* UV-VIS-NIR tracking of the kinetics and thermodynamics remains to be achieved.

3.1.2.7 Non-zeolitic single atom catalysts

Zeolite supported TMI catalysts are especially interesting to study with UV-VIS-NIR absorption because well-defined TMI sites alleviate the disadvantageous low spectral resolution of the technique. Increasingly, other methods to prepare uniformly dispersed TMI species are developed. Notably 'single atom catalysts' (SAC) have emerged as a hot topic in catalysis in recent years, referring to heterogeneous catalysis with single isolated atoms decorated on a support. These materials are used for thermal heterogeneous catalysis as well as electro- and photocatalysis.[232-234] While UV-VIS-NIR absorption spectroscopy would clearly be a powerful tool in their *in situ* study, there are only few examples to be found in literature so far and the technique is not commonly listed as an important characterization technique.[233] A common limitation is the strong absorption of the support material hampering the detection of weaker TMI single atom absorption bands. The scarce examples that can be found often involve band gap energies measured using the Tauc plot method, but rarely involve the identification of ligand field environment and electronic structure as with zeolites.[235, 236] An exception is the detection of a unique redshift of the cinnamyl alcohol π-π* absorption band upon contact with atomically dispersed Pd on Al_2O_3.[237] Other examples are the appearance of a clearly resolved charge transfer band of atomically dispersed Ru on defective TiO_2 nanosheets,[236] and the description of a copper species on amorphous silica with an absorption band at 22700 cm^{-1} active in methane oxidation.[238]

3.1.3 Tracking chromophoric products

Besides the absorption of the catalyst itself, also chromophoric reagents and products may be tracked spectroscopically. In general these enable simple and cheap analytical methods to track reaction mechanisms and kinetics, and they are explained in standard analytical chemistry textbooks.[40]

3.1.3.1 zeolite catalyzed methanol to hydrocarbons

Industrial methanol conversions to hydrocarbons (MTH) are typically catalysed by acid zeolites (HZSM-5, HSSZ-13) or zeotype catalysts (HSAPO-34). The selectivity toward different hydrocarbons is directed by choosing the suitable catalyst and appropriate reaction conditions.[239] The resulting products are either rich in gasoline, olefins, or aromatics, and the corresponding processes are then referred to as methanol-to-gasoline (MTG), methanol-to-olefins (MTO), or methanol-to-aromatics (MTA). Since the MTH process was discovered and patented by the Mobil Research Laboratory in the late 1970s,[240, 241] mechanistic understanding of MTH has steadily grown,[242-245] which facilitates better catalyst design and preparation,[246, 247] as well as process development.[248-250]

Although the formation mechanism of the first C-C bond remains under debate,[251-254] the steady state formation of hydrocarbons is believed to proceed indirectly through a hydrocarbon pool (HCP), in which the active species include polyalkylated aromatics, carbocations and olefins.[255] The HCP is then methylated by methanol and dealkylated to yield the desired olefins. However, the exact nature of the HCP and detailed reaction mechanism are still the subject of

debate.[239, 256, 257] In addition, the HCP can further develop into species that are inactive for MTH, such as heavy aromatic coke, that ultimately lead to catalyst deactivation. Inside the zeolite, the size of hydrocarbon species is constrained by the nanospace defined by the zeolite framework giving rise to the 'shape selectivity' of zeolites. However, the hydrocarbon species can grow into bulky polyaromatic molecules on the outer surface of the catalyst particles, which tend to block the pores of the catalyst.

In situ and *operando* UV-VIS-NIR absorption spectroscopy is a vital tool to follow the formation of the HCP species inside zeolite catalysts during methanol conversion. The technique can differentiate between carbocationic HCP species and their neutral counterparts, which have distinct bands in a UV-VIS-NIR absorption spectrum resulting from the shifted π-π* and n- π* relative energies.[258] In addition, UV-VIS-NIR DRS can help track the accumulation of deactivation species (cokes) in and on the zeolite crystals.[259] Coking generally involves a complex mixture of organic molecules, mainly polyaromatic molecules and cations with absorption bands in the UV-VIS range. As coke builds up in the catalyst particles, the catalyst darkens in color corresponding to an increase of broad unresolved ranges in the absorption spectrum. Through deconvolution the absorption spectra into Gaussian bands, meaningful information on cokes composition can be extracted.[259] Assignments of UV-VIS DR adsorption bands of hydrocarbon species formed in the zeolite catalyzed MTH reaction are summarized in Table 6. However, the observed absorption bands are usually weak and broad, and UV-VIS-NIR absorption spectroscopy alone is not always sufficiently sensitive to understand the chemical composition of the cokes. This is exemplified by hexamethylbenzenium (HMB^+) and methylnaphthyl cation, which are both potential intermediates in the MTH process and exhibit a similar absorption band ~390 nm.[260] The HMB^+ serves as an active HCP species, whereas methylnaphthyl cations are deactivation coke. To achieve a more accurate interpretation of UV-VIS-NIR absorption spectra, solid-state NMR and FTIR are generally used to supplement the analysis.[258]

Table 6. Characteristic UV-VIS-NIR absorption bands in zeolite catalyzed methanol conversion reactions.

Species	Wavelength (nm)	References
Neutral (methylated) benzenes / cyclopentadienyl species	≤295	255, 261, 262
Monoenylic/dienylic carbocations	300-330	263
Less methylated benzene carbocations (up to three methyl groups)	340-360	262, 264
Highly methylated benzene carbocations (4-6 methyl groups)	385-410	259, 260
Methylated naphthalene carbocations	400-435	265, 266
Neutral/charged polyaromatics (coke)	≥600	259, 260

UV-VIS spectroscopy has been extensively applied to investigate the impacts of zeolite topology, acidity, and reaction conditions on the formation of hydrocarbon species, which closely correlate to the reaction and deactivation routes in the MTH process. The nature of hydrocarbon species during the MTH process over the CHA zeolites (HSSZ-13 and HSAPO-34) was investigated at different temperatures by *in situ* UV-VIS-NIR DRS with the aid of NNMF analysis.[259, 263, 267, 268] The NNMF analysis allows for the division of the time-resolved

UV-VIS-NIR spectra into two groups of spectra with different kinetic behaviours, which separates the manifold of formed hydrocarbon species into two main groups. The first group of species increased with the conversion, peaked at full conversion, and subsequently declined with time on stream. Therefore, these species are strongly associated with catalyst activity. The formation of the second group commenced at the maximum formation of the first group of hydrocarbon species and continued to increase until the catalyst completely deactivated. Thus, these species are related to catalyst deactivation. The nature of the species appears to be similar for HSSZ-13 and HSAPO-34 (Figure 32 A-D). At low temperature (573 K), the first group of species of both zeolites contain absorption bands at 33 650 cm^{-1} (300 nm) and 26 000 cm^{-1} (385 nm), which can be attributed to monoenylic and highly methylated benzene carbocations, respectively. The second group of species on CHA zeolites are characterized by absorption bands at 30 000 cm^{-1} (330 nm) and 24 000 cm^{-1} (415 nm), corresponding respectively to low methylated benzene and methylated naphthalene carbocations. Interestingly, the reaction temperature significantly influences the chemistry of the hydrocarbon species. At higher reaction temperatures (> 673 K), low methylated benzene carbocations (31 000 cm^{-1}, 320 nm) and methylated naphthalene carbocations (24 000 cm^{-1}, 415 nm), identified as the deactivation species during low temperature MTH process, become the predominant HCP active species, while the formation of highly conjugated neutral polyaromatics deposited on the external surface of the catalysts leads to a featureless spectrum of the second group. It was proposed that at low reaction temperature deactivation occurs because of pore filling with methylated naphthalene carbocations while at higher reaction temperature highly conjugated polyaromatics on the external surface block the pores. Besides, it was noted that the active hydrocarbon species in HSAPO-34 were more stable than in HSSZ-13. This is likely due to the stronger acidity of HSSZ-13, which promotes the formation of more conjugated and bulky hydrocarbon species.[259]

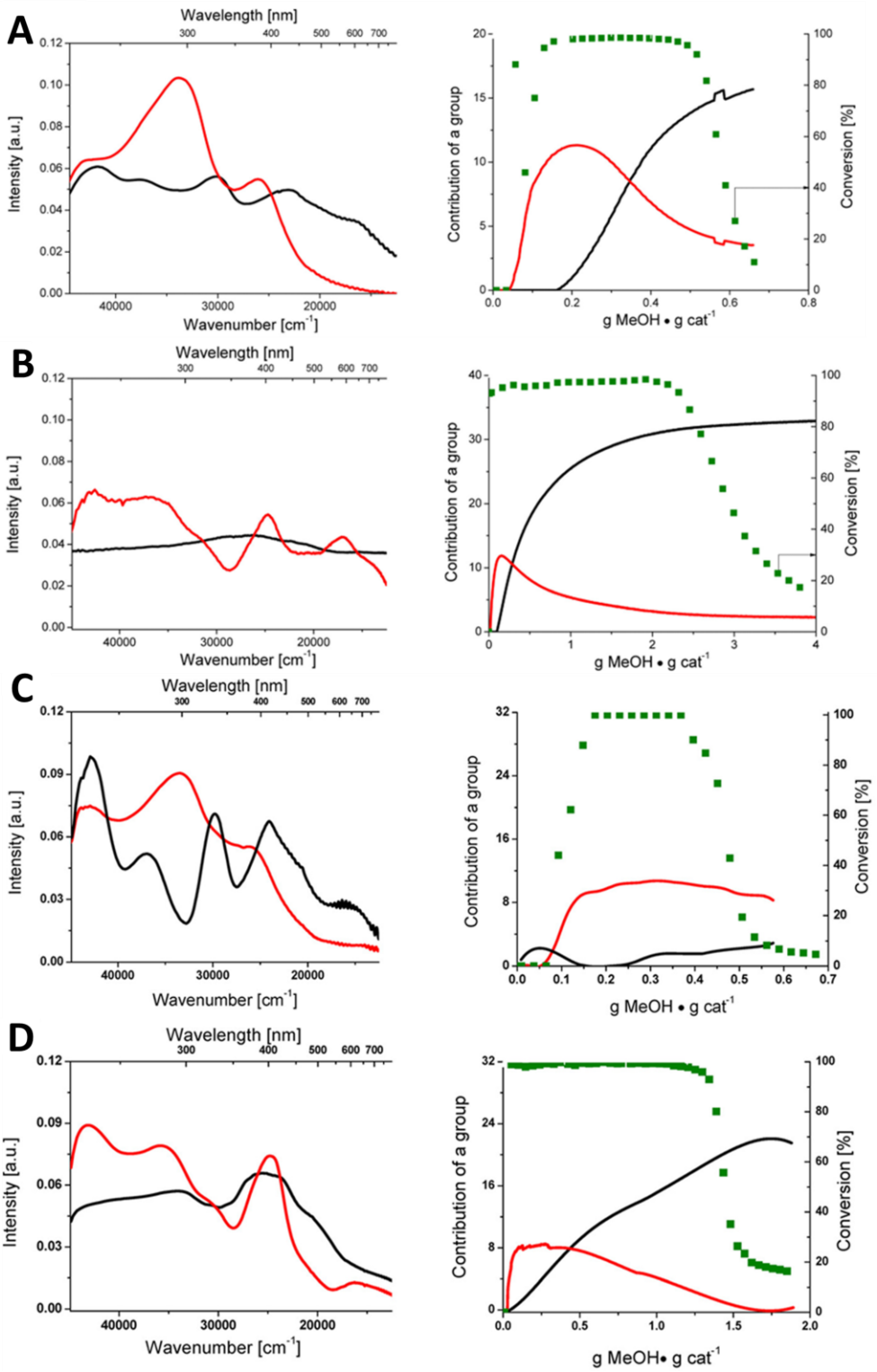


Figure 32. (left in each panel) Deconvolution of the UV–VIS-NIR absorption spectra into two groups of bands by NNMF analysis. (right in each panel) The evolution of each group as a function of methanol loading on the catalyst material of HSSZ-13 catalyzed methanol conversion at **(A)** 573 K and **(B)** 723 K and HSAPO-34 catalyzed methanol conversion at **(C)** 573 K and **(D)** 673 K. (red: active hydrocarbon species, black: deactivating hydrocarbon species). Reproduced from refs. [259, 267]. Copyright 2014 Wiley and copyright 2015 American Chemical Society.

In situ UV-VIS-NIR spectroscopy was applied to investigate how different small pore zeolites catalyse the MTO process. [263, 268] Figure 33 shows the formation and evolution of retained hydrocarbon species in small pore zeolites CHA, DDR, and LEV topologies tracked by *in situ* UV-VIS spectroscopy during MTO. Concurrently, *in situ* X-ray diffraction was used to track the zeolite lattice expansion. Although the pore structures of the three zeolite material are similar, as they consist of large zeolite cages interconnected by eight-membered-ring windows, it was demonstrated that small differences in size and shape of the cages have a substantial impact on retained hydrocarbon species that lead to the lattice expansion. The interaction between the retained hydrocarbon species and the structures of the zeolite framework results in distinct degrees and orientations of lattice expansion for each zeolite frameworks. In CHA zeolite, where the largest expansion was observed, methylated naphthalene and pyrene are the predominant species. For DDR zeolite, 1-methylnaphthalene and phenalene are the primary species formed. In LEV zeolite, methylated benzene and naphthalene are the main observed species. To study the kinetics of the involved hydrocarbon species during MTO process, the time evolution of the *in situ* UV-VIS spectra during the conversion of methanol over CHA, DDR, and LEV zeolites were analyzed using Multivariate Curve Resolution-Alternating Least Squares (MCR-ALS). With MCR-ALS the series of UV-VIS spectra could be deconvoluted into components with similar kinetic behaviours. For DDR, three components were extracted (Figure 33 B), corresponding to the dominant species during the three stages of MTO process: the induction period, the active period, and the deactivation period. These allow tracking of the hydrocarbon species. At a lower reaction temperature (623 K), a distinct feature around 25 000 cm^{-1} (400 nm) attributed to 1-methylnaphthalene is observed during the deactivation period. However, at a higher reaction temperature (723 K), this feature appears during the active period. These findings again indicate a temperature-dependent change in the role of the hydrocarbon species, thereby influencing the reaction and deactivation mechanism.

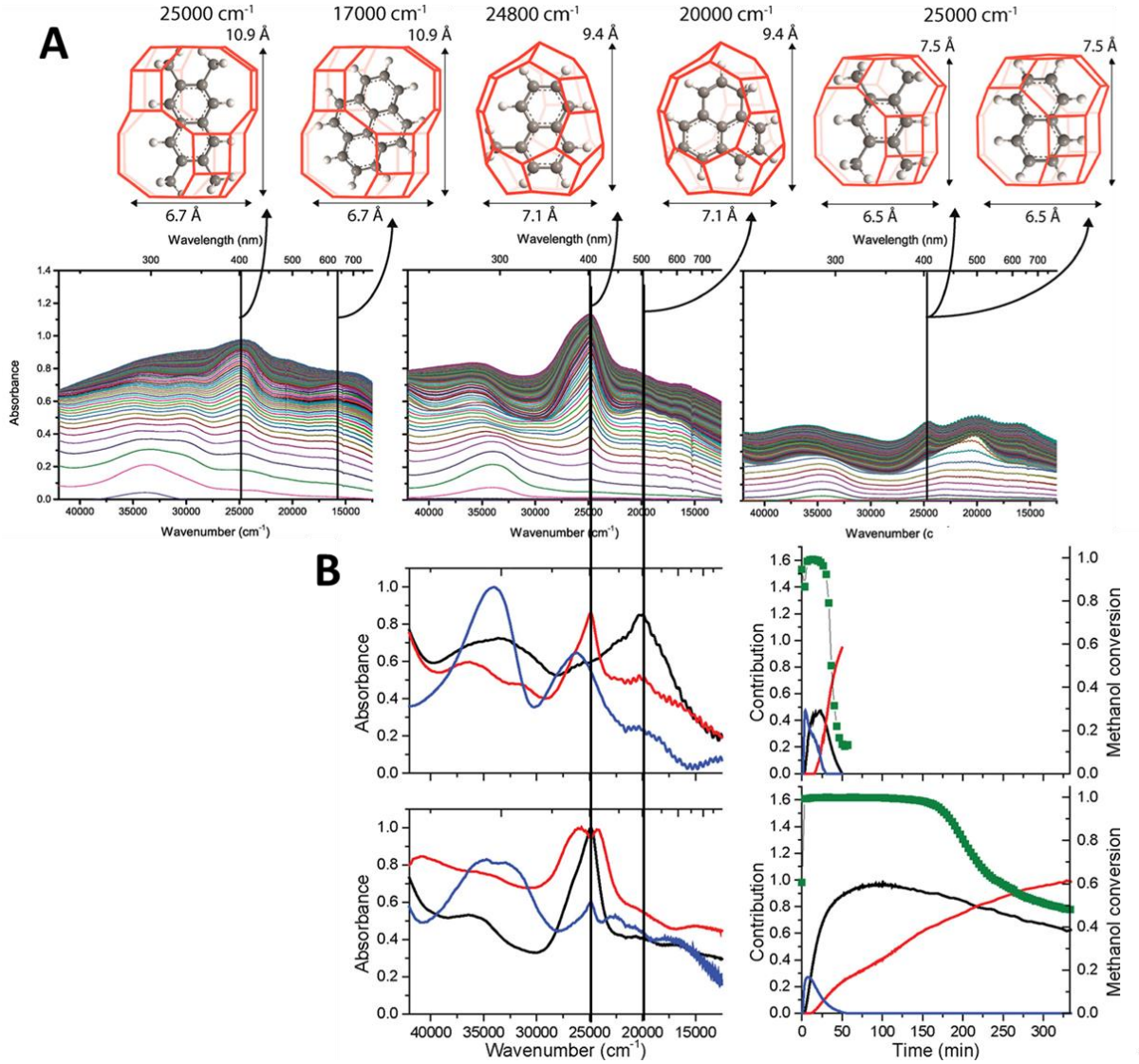


Figure 33. (A) *In situ* UV-VIS spectra during methanol conversion at 673 K and hydrocarbon species corresponding to the UV-VIS absorbance bands over the (left)CHA, (middle) DDR and (right) LEV catalysts. **(B)** (left) MCR-ALS components and (right) their respective contributions to the overall *in situ* UV-VIS spectra versus time for the conversion of methanol over DDR zeolite at a reaction temperature of (top) 623 K and (bottom) 723 K. The colors of the contribution plots correspond to the colors of the components. Reproduced from refs. [263, 269]. Copyright 2017 and 2018 American Chemical Society.

As cokes accumulate in the zeolites, the intensity of the characteristic absorption by polyaromatics above 600 nm gradually increases, making UV-VIS DRS a useful tool to investigate the coke evolution during MTH process. By placing UV-VIS-NIR absorption probes at different positions along the reactor bed, the evolution of active species and coke in the MTO reaction along the catalyst bed can be monitored. Such spatiotemporal approach can track the coke front as it progresses towards the reactor end. Photos of the catalyst bed and the corresponding *in situ* UV-VIS spectra for the first 2 h of MTO reaction over HZSM-5 and MgZSM-5 are shown in Figure 34 A.[268] In the case of MTO process over HZSM-5, coke formed rapidly over the entire catalyst bed at the beginning of the reaction and a broad absorption band below 25 000 cm^{-1} (400 nm) appeared. With reaction time, it shifted to lower wavenumbers. The spectral region below 25 000 cm^{-1} is generally dominated by neutral and charged aromatic species. The redshift corresponds to the growth of larger aromatic

molecules.[260, 270] In contrast, MgZSM-5 exhibited a much lighter color and weaker intensity of absorption bands below 25 000 cm^{-1} compared to HZSM-5, indicating much less formation of coke species. The UV-VIS-NIR absorption spectra of HZSM-5 after feeding a mixture of ethylene and propylene showed band positions and intensities that were very similar to the UV-VIS-NIR absorption spectra during MTO reaction, while adsorption below 25 000 cm^{-1} was not observed during light olefins conversion over MgZSM-5. Coke formation from olefins aromatization, the so-called secondary coke formation, was therefore slower over MgZSM-5. Magnesium in the zeolite leads to a reduction of the strong Brønsted acid sites (BAS) and therefore prevents the formation of secondary coke. The less pronounced olefin aromatization on MgZSM-5 explains its higher selectivity toward light olefins and longer lifetime than H-ZSM-5. The prevention of secondary reactions by incorporating alkaline-earth metals in the zeolite was also reported by Yarulina et al.[271] Figure 34 B shows the *in situ* UV-VIS DR absorption spectra collected during methanol conversion over two HZSM-5 zeolites with different Si/Al ratios, and a Ca-modified ZSM-5 at 773 K. Aromatic species did not accumulate in Ca-modified ZSM-5 as evidenced by the absence of absorption below 25 000 cm^{-1}. For the HZSM-5 zeolites, formation of polyaromatic species (naphthalene and homologues) was observed during the first seconds of MTO. As evidenced by 1 H-1 H double-quantum (DQ) and 1 H-1 H radio frequency driven recoupling (RFDR) magic angle spinning (MAS) NMR, alkaline-earth metals tend to deprotonate BAS, thus neutralizing inherent zeolite acidity and forming Lewis acid sites (LAS) and isolated BAS. UV-VIS DRS revealed that the presence of LAS in Ca-modified ZSM-5 prevented the formation of polyaromatic species during MTO process, thereby extending the lifetime of the catalyst.

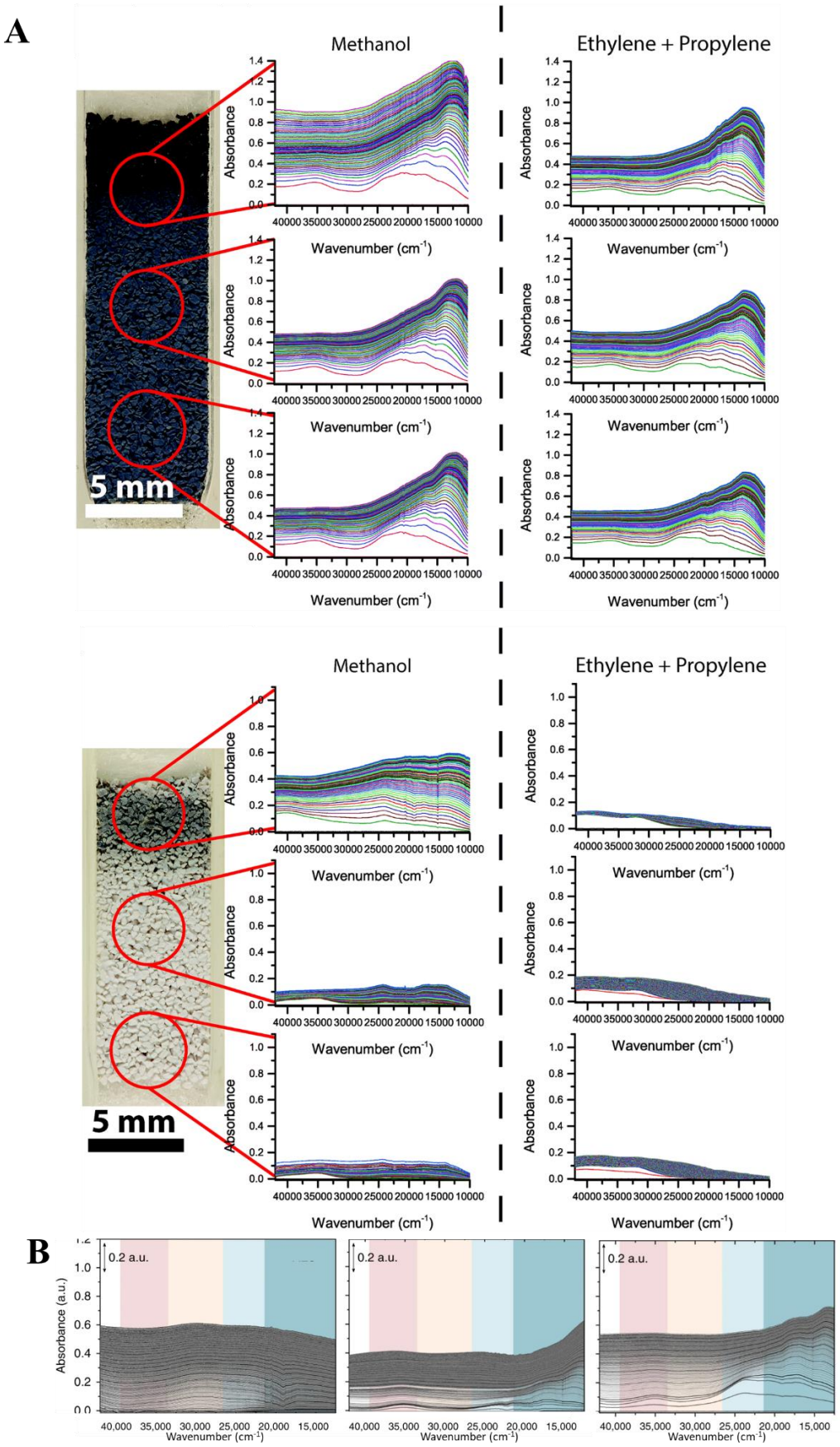

A
Methanol
Ethylene + Propylene
Absorbance
Wavenumber (cm-1)
5 mm
B
0.2 a.u.
Absorbance (a.u.)
Wavenumber (cm-1)

Figure 34. (A) Photo of the reactor bed after 2h MTO reaction and *in situ* UV-VIS absorption spectra of conversion of methanol or a mixture of propylene and ethylene at three positions along the reactor bed over (top) HZSM-5 and (bottom) MgZSM-5. **(B)** *in situ* UV-VIS absorption spectra collected during methanol conversion over (left) AE3, (middle) Z2 and (right) Z1 at 773 K. Reproduced from refs. [268, 271]. Copyright 2018 Royal Society of Chemistry and copyright 2018 Springer Nature.

Thuy et al. reported that coating ZSM-5 with a catalytically inactive siliceous exterior rim dramatically improves diffusion and reduces the accumulation of coke on external surfaces.[272] The Si-zoned ZSM-5 demonstrates an enhanced catalyst lifetime for the MTH process and diffusion properties that resemble particles with a much smaller size. Comparison of the UV-VIS DR spectra for representative homogeneous and Si-zoned samples reveals a notable reduction in both internal and external coke relative to HCP species for the Si-zoned catalyst, suggesting the presence of a siliceous exterior suppresses the formation of cokes. As evidenced by computational simulation, both internal diffusion and surface permeation are enhanced in Si-rich regions of Si-zoned ZSM-5, thereby improving the diffusion properties of nanoporous catalysts.

3.2 Homogeneous thermal catalysis

In homogeneous catalysis, better resolved UV-VIS-NIR absorption spectra are often obtained compared to heterogeneous catalysts. The intermediates are structurally more uniform and the systems are translucent, so that transmission mode measurements with better signal-to-noise can be used. *Operando* and *in situ* spectroscopy are commonly used in homogeneous catalysis to study the reaction mechanism and to understand the catalytic cycle at the molecular level.[273] Often the tracking of these transformations yields spectral evolutions with clear isosbestic points. Through the detection, identification and quantification of reaction intermediates and organic compounds, kinetic models are proposed, and the structure-performance relationships of the homogeneous catalyst are understood. Thus, the gained insights are valuable for a rational optimization of the system and for the design of novel catalysts.

From a technical point of view, the *operando* and *in situ* spectroscopy reactor must meet the requirements of a homogeneous reaction, such as stirring, thermostable conditions, and controlled atmosphere. Therefore, different configurations can be used, such as reactors with submersible optometers, a fiber optic spectrometer in a special Schlenk vessel, or a stopped flow combined with a diode array to monitor reactions at small time intervals (see reference [274] for technical details and [275] for analytical insights).

Within the field of homogeneous catalysis, *in situ* UV-VIS-NIR absorption spectroscopy is mainly applied to the study of organometallic catalysis, as it allows the detection of metal associated electronic transitions, in addition to the formation of organic molecules. [276, 277] Notably, the UV-VIS-NIR absorption spectrum of transition metal complexes involves two types of transitions; d-d transitions at lower energy levels and with lower absorption coefficients, and CT transitions at higher energies and with higher absorption coefficients (see also section 2.1). The UV-VIS-NIR absorption pattern of organometallics is dependent on the metal center, the ligands, and the solvent. The number of combinations that can be made is therefore very large and the attribution of absorption bands to specific transitions is usually derived from literature databases and pure component spectra ('fingerprint spectra').[275] For instance, the π-π* transition of a Schiff base Ni complex is observed between 339-350 nm, whereas for the Au complex, the transition is found in the range of 291-331 nm.[278, 279] On the other hand, for a Ru Schiff base complex, the π-π* transition lies at 203-223 nm, and the n-π* and d-d transitions lie in the 355-406 nm and 616-630 nm range, respectively. Replacing the

ligand by tridentate pyridinediimine (pydim), shifts the transition bands to 278-318 nm, 425-449 nm, and 536-566 nm.[280]

Due to their sensitivity to UV-VIS-NIR range spectroscopies, most of this section will handle organometallic complex catalysts, including examples of stopped flow absorption, C-term MCD and CD. Also examples on various types of reactions are given. The section ends with catalysis without organometallic complexes.

3.2.1 Organometallic catalysts

3.2.1.1 Selected applications of stopped flow absorption

Stopped flow is used in homogeneous catalysis to observe short-lived intermediates and study fast reaction events that occur within milliseconds (see also section 2.2.2.2). It uses specifically timed rapid mixing of reagents and halting of the reaction. Through the monitoring of time-dependent changes in spectroscopy and reactant concentrations, reaction rates and intermediates are determined.

Grubbs Catalysts

Grubbs catalysts are ruthenium-based complexes used in metathesis reactions. The reaction mechanism involves an initiation step followed by conversion and decomposition. During the initiation step, a by-product in the form of a styrene derivative is typically generated. This by-product can undergo competitive metathetic reincorporation at the ruthenium center, leading to catalyst regeneration. Notably, third-generation Grubbs catalysts (G-III-X) (where X = H, Cl, Br) exhibit an exceptionally fast initiation step. The lower-limit of the dissociative initiation rate constant (k_1) of G-III-Br has been estimated to be > 4 s^{-1}. Through the use of a stopped-flow system, the reaction between G-III-Br and ethyl vinyl ether (EVE) was successfully monitored and the initiation step was studied (Figure 35). G-III-Br undergoes aerobic oxidation in toluene and exposure to air could intermittently increase the first-order quenching rate of the 348 nm feature during successive runs. Refinements were made to the stopped-flow system to ensure anaerobic conditions (Figure 35 A). The kinetics could thus be confidently attributed to metathesis initiation. A 354 nm centered absorption band, believed to originate from a metal to benzylidene-π^* MLCT was tracked.[281]

The band appears approximately 8 milliseconds after mixing a solution of G-III-Br + 3-Br-pyridine (L) with solutions of ethyl vinyl ether in toluene at 5 °C (Figure 35 B). To determine the empirical first-order rate constants of the reaction, a non-linear regression analysis was applied to the exponential decay in absorbance. Subsequently, the empirical rate constants ($k_{obs.}$) were calculated by averaging data from a minimum of 10 experiments for each concentration variation. The kinetics derived from these experiments support a mechanism wherein the dissociative and associative pathways converge at the pyridyl-free complex (alkene coordination complex), preparing the alkene to undergo metathesis with the benzylidene. The authors propose that both the associative and dissociative pathways play significant roles in the initiation process.

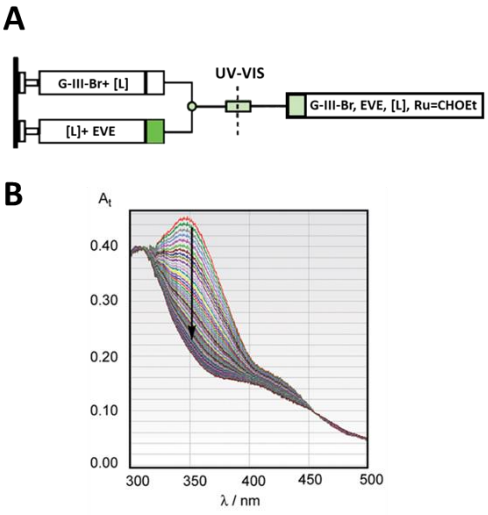


Figure 35. (A) Schematic of reactants mixing *via* stopped-flow (UV-VIS), G-III-Br: third-generation Grubbs catalyst, [L]: exogenous ligand such as 3-Br-pyridine, EVE: ethyl vinyl ether, Ru=CHOEt: initiation product; **(B)** UV-VIS spectra of the reaction of G-III-Br+[L] with EVE. Adapted from ref. [281]. Copyright 2019 Royal Society of Chemistry.

Stopped flow experiments also enable in-depth kinetic investigation of ligand substitution and catalytic oxidation of H_2O to O_2 on ruthenium complexes bearing the pentapyridyl ligand (6,6''-(methoxy(pyridin-2-yl)methylene)di-2,2'-bipyridine: L-OMe).[282] The complex trans-$[Ru^{II}(Cl)(L\text{-}OMe\text{-}\kappa\text{-}N^5)]^{1+}$, referred to as trans-1^+, undergoes a substitution of the sixth coordination ligand in an aqueous solution containing trifluoromethanesulfonic acid/trifluoroethanol (used to enhance solubility), leading to the formation of the Ru aquo complex trans-2^{2+}. This substitution process is relatively slow, with a pseudo-first-order rate constant of k_1=3.3*10^{-4} s^{-1} and a half-time of $t_{1/2}$=35 minutes. In contrast, the analogous complex with the L-Me ligand shows faster reactivity under the same conditions, with a rate constant of k_1'=1.5*10^{-3} s^{-1} and half time of $t_{1/2}$=8 min.

The authors then investigated the substitution reaction of trans-1^+ upon one-electron oxidation in presence of cerium^{IV} ammonium nitrate, towards a trans-$[Ru^{III}(Cl)(L\text{-}OMe\text{-}\kappa\text{-}N^5)]^{2+}$ complex denoted (trans-1^{2+}). This rapid outer-sphere oxidation reaction was monitored using stopped-flow UV-VIS spectroscopy and fitted to a second-order kinetic profile, with a rate constant of k_2=8.0*10^4 M^{-1} s^{-1}. Interestingly, the obtained spectra reveal a second, slower process occurring simultaneously with the formation of the oxidized complex (trans-1^{2+}), corresponding to the isomerization of (trans-1^{2+}) to (cis-1^{2+}), which remains in equilibrium.

Tracking complex formation

The synthesis of organometallic complexes is commonly studied using *in situ* UV-VIS absorption spectroscopy. An example is the formation of μ-chloro binuclear diphosphine (PP) rhodium complexes $[Rh(PP)(\mu\text{-}Cl)]_2$, with the ligands BINAP, SegPhos, DM-SegPhos, and DiFluorPhos, through two consecutive steps starting from the precursor $[(Rh(COD)(\mu\text{-}Cl))_2]$ (COD = cyclooctadiene).[283] UV-VIS absorption spectra were used to study the kinetics of diolefin exchange with chelating diphosphine in the rhodium coordination sphere. For the BINAP exchange, an isosbestic point was observed at 338.5 nm, indicating a single transformation. The second order rate constants for each step were derived from stopped flow experiments with a diode array spectrophotometer. However, the kinetic studies were hindered by an equilibrium between the starting and target complex on one side, and the intermediate on the other. Therefore, the competitive reaction steps were separated and then successfully

quantified using UV-VIS spectroscopy. It was found that the *in situ* formation of these catalyst precursors requires a longer time than typically expected, and that the second step is rate-determining.

In further studies the formation of an unexpected monomeric pentacoordinated neutral complex of the type [RhCl(PP)(diolefin)] was reported in equilibrium with the dimeric target compound $[Rh(PP)(\mu\text{-}Cl)]_2$.[284] The *in situ* UV-VIS absorption spectroscopy showed that this pentacoordinated complex is an intermediate of the reaction that may arise from the generated target complex $[Rh(PP)(\mu\text{-}Cl)]_2$ through reaction with the free diolefin, or even directly from $[Rh(diolefin)(\mu\text{-}Cl)]_2$ and the diphosphine. Thus, the quantitative formation of this pentacoordinate mononuclear complex can be avoided with a proper choice of the rhodium source and the ligands, and by controlling the reaction conditions such as the solvent and the temperature. To conclude this work, further detailed mechanistic investigations using *in situ* UV-VIS absorption monitoring of the $[Rh(diphosphine)(\mu\text{-}X)]_2$ preparation were performed.[285] The reaction spectra revealed different reactivity and intermediates formation depending on the precursor complex, the type of ligand, and the reaction conditions, especially the reaction temperature and the used solvent.

Catalytic cycles

The oxidative addition of organometallic complexes is often the rate-determining step in a catalytic cycle and therefore a relevant subject for *operando* and *in situ* UV-VIS absorption studies.[286] In this context, Guilera *et al.* monitored the addition of iodobenzene to $[(PPh_3)_2Pd(dba)]$ by means of *in situ* stopped flow UV-VIS absorption spectroscopy. The disappearance of the absorption bands of $[(PPh_3)_2Pd(dba)]$ (at 491 and 432 nm), was monitored and synchronized on the millisecond scale with dispersive EXAFS.[287] The study allowed the determination of the order and rate constant of this step, and revealed that the concerted oxidative addition takes place in a cis configuration, followed by a *cis-trans* isomerization.

3.2.1.2 Applications of C-term MCD

Magnetic circular dichroism spectroscopy is useful to investigate the electronic structure and bonding of homogeneous catalysts, especially of paramagnetic metal and f-element complexes. It offers insights in the interactions between ligands and the metal center.[288, 289] As with metalloenzymes, C-term MCD intensity is most frequently analyzed due to its ability to provide highly informative bands. Still, its application to non-enzymatic organometallic reactions has so far been limited. Herein, we present lead examples that highlight the importance of C-term MCD in understanding reaction mechanisms, and in determining reactive species of various transition metal catalysts used in C-C cross-coupling reactions.[290]

C-term MCD spectroscopy was used to determine the structures and coordination number of high-valent Ni complexes catalyzing C-C coupling.[291] This catalyst shows interesting variations in the rate of reductive elimination, contingent upon both the oxidation state of the transition metal center and the characteristics of the coordinated ligands. MCD allowed the determination of the C-to-Ni charge transfer energies, revealing that the C-C bond formation during reductive elimination and the charge transfer transitions involve the same frontier molecular orbitals, allowing its usage for kinetic tracking.

Iron-bisphosphine complexes represent another class of catalysts used in C-C cross-coupling reactions. The nature of the *in situ* formed iron species, the active form of the catalyst, and the catalytic mechanisms remain uncertain.[292] Neidig *et al.* conducted a study on the Fe-SciOPP-catalyzed Kumada cross-coupling of MesMgBr and primary alkyl halides, using C-term MCD spectroscopy to identify the reactive iron species.[293] Upon adding one equivalent of MesMgBr

to $FeCl_2$(SciOPP), the NIR MCD spectrum displays two transitions, indicating the formation of a tetrahedral high-spin Fe^{II} complex, FeBrMes(SciOPP) (Figure 36 A). With the addition of a second equivalent of MesMgBr, three new transitions emerge in the NIR MCD spectrum, indicating the formation of a square planar Fe^{II} complex, $FeMes_2$(SciOPP) (Figure 36 B). When an excess of the Grignard reagent is introduced, the MCD spectrum reveals the formation of the $FeMes_3^-$ complex (Figure 36 C, D). Based on these observations, it was suggested that the $FeMes_2$(SciOPP) complex serves as the active species in this reaction. It first reacts with the primary alkyl halide to generate the C-C product and the mono-mesitylated species. Then, the mono-mesitylated species reacts with another equivalent of MesMgBr, leading to the regeneration of the active bis-mesitylated species, completing the catalytic cycle.

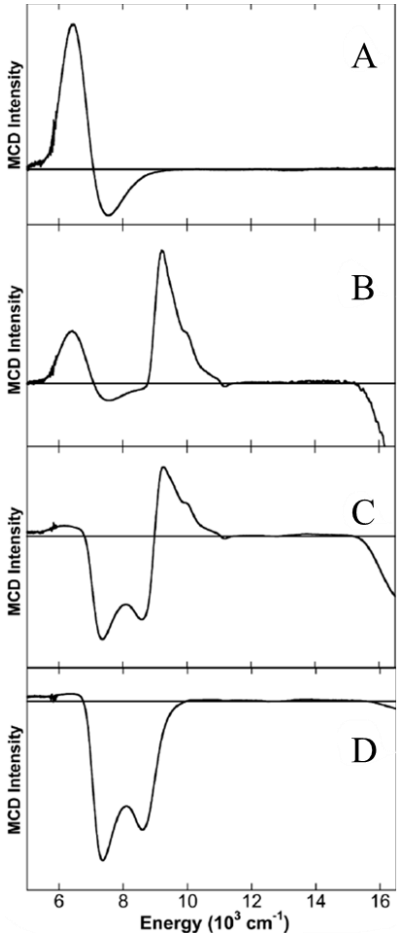


Figure 36. 5 K, NIR MCD spectra for the reaction of $FeCl_2$(SciOPP) with one equiv. **(A)**, two equiv. **(B)**, 20 equiv. **(C)**, and 100 equiv of MesMgBr (D). Adapted with permission from ref. [293]. Copyright 2014 American Chemical Society.

In a subsequent investigation, C-term MCD spectroscopy was used to study the Fe-SciOPP catalyst in the cross-coupling reaction involving phenyl nucleophiles and secondary alkyl halides.[294] VTVH MCD analysis enabled the determination of crucial parameters such as the coordination number, oxidation state, and spin state of paramagnetic organometallic species generated *in situ*. VTVH MCD reveals that when two equivalents of PhMgBr are added to $FeCl_2$(SciOPP), a four-coordinate $FePh_2$(SciOPP) species is formed. It was further determined that this species adopts a high-spin distorted square pyramidal geometry. These findings indicate that unlike the coupling of MesMgBr and primary alkyl halides, the reactive species in these reactions is the mono-phenylated iron complex.

3.2.1.3 Applications of CD

Circular dichroism (CD) spectroscopy is an optical technique highly sensitive to chirality, making it a valuable tool for analyzing and distinguishing analytes within a chiral host-guest system. It finds practical application in high-throughput screening (HTS) processes. In the realm of enantioselective organometallic transformations, CD spectroscopy has been employed to determine the enantiomeric excess (*ee*) for chiral catalysts.

For metal complexes exhibiting CD-active MLCT bands, the addition of a chiral guest allows modulation of the MLCT bands, facilitating the differentiation of enantiomers, and thus the calculation of *ee*.

On the other hand, Exciton-Coupled Circular Dichroism (ECCD) is used when dealing with compounds that contain two or more chromophores arranged in a helical manner. To establish the absolute configuration of the analyte the Cotton effect is analyzed. This method is particularly useful for resolving the handedness or stereochemistry of complex chiral molecules. However, the enantiomeric excess values determined from CD have relatively high absolute errors compared to chiral high performance liquid chromatography (HPLC) analysis, and therefore additional optimization should be implemented to enhance the accuracy and reliability of this technique.[295]

ECCD was employed as an optical readout for the asymmetric copper catalyst used in the Michael addition of malonate to nitrostyrenes. This catalyst includes a helically chiral ligand, and the absolute configuration of the ligand is reversed depending on the oxidation state of the copper center, which in turn controls the stereoselectivity of the reaction.[296] ECCD spectroscopy proved instrumental in differentiating between the two possible pseudo-enantiomeric states of the catalyst that arise after reduction or oxidation. The CD spectra obtained for the Cu^{II} and Cu^{I} complexes displayed mirror images, consistent with the inversion of the asymmetric orientation of the chromophores upon change in oxidation state (Figure 37). These findings strongly suggest that ligand reorganization occurs alongside the inversion of helicity, as anticipated.

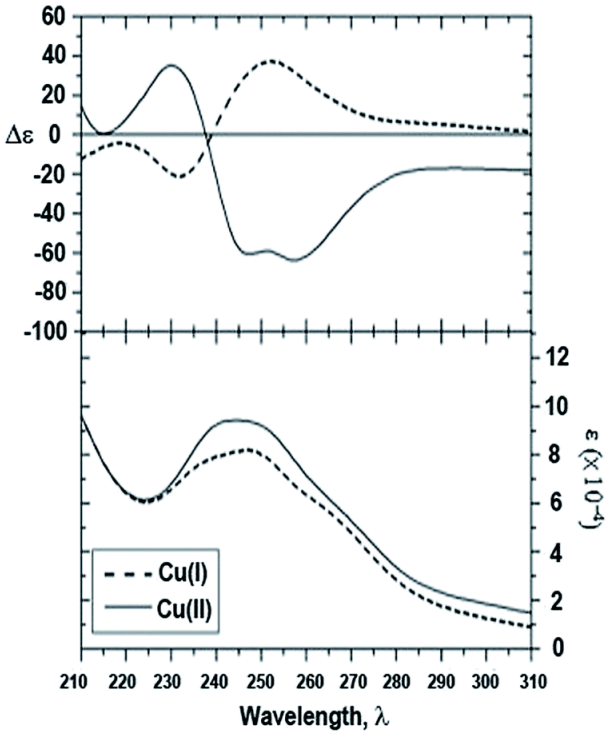


Figure 37. CD (L.mol^{-1}.cm^{-1}) and UV (L.mol^{-1}.cm^{-1}) spectra of the reduction/oxidation induced switching between Cu^{II} and Cu^{I}. Adapted from ref. [296] with permission from the Royal Society of Chemistry.

3.2.1.4 Further reactions

A large variety of chemical transformations is catalyzed using soluble organometallics. Examples of their *in situ* tracking of UV-VIS-NIR absorption are given in this section to emphasize the wide application. In our selection, we cover ethylene oligomerization, alcohol oxidation, asymmetric hydrogenation, dehydroperoxidation, and the dehydrogenation of formic acid.

Ethylene oligomerization

In situ UV-VIS was used to study the oligomerization of ethylene into metallacyclopentanes using for instance the rac-(ebthi)M(η^2 -Me_3SiC_2- $SiMe_3$) complex (with ebthi = 1,2-ethylene-1,1'-bis(η^5 -tetrahydroindenyl)) as a catalyst.[297, 298] Two different organometallics with M= Zr (Figure 38 A) and M= Hf (Figure 38 B) were tested. The obtained reaction spectra of the Zr based complex with ethylene (Figure 38 C) have an isosbestic point at 436 nm indicating a pseudo first-order reaction with the pseudo-rate constants $k' = k$.[ethylene] = 0.0365 s^{-1} determined by a non-linear curve fit. Plotting k' as a function of the ethylene concentration allows deriving the rate constant, here 0.35 L*mol^{-1}*s^{-1}.

With the analogous Hf complex (Figure 38 B), the UV-VIS-NIR absorption spectra during reaction do not exhibit isosbestic points (Figure 38 D), and the corresponding extinction diagrams show two distinct straight lines indicating a consecutive reaction, wherein the first reaction is fast and the second is considerably slower. This allows a separate treatment of the two steps. However, the reaction of **1-Hf** with ethylene is reversible towards **2-Hf** at room temperature, whereas the consecutive reaction yielding **3-Hf** requires 100 °C (Figure 38 B). Hence, an intermediate **B** was suggested, whose formation can occur from the reverse reaction of **2-Hf** in presence of ethylene through an S_N2 mechanism (Figure 38 B). This reveals an influence of ethylene on the observed overall rate formation of **2**.[298, 299] Plotting the observed rate constants $k'_{obs.1}$= 78.6 s^{-1} and $k'_{obs.2}$= 2.4 s^{-1}, obtained from the reaction UV-Vis spectra

vs. the ethylene concentration results in the rate constants $k_{obs.1}$= 929 L*mol^{-1}*s^{-1} and $k_{obs.2}$= 32 L*mol^{-1}*s^{-1} for both reactions.

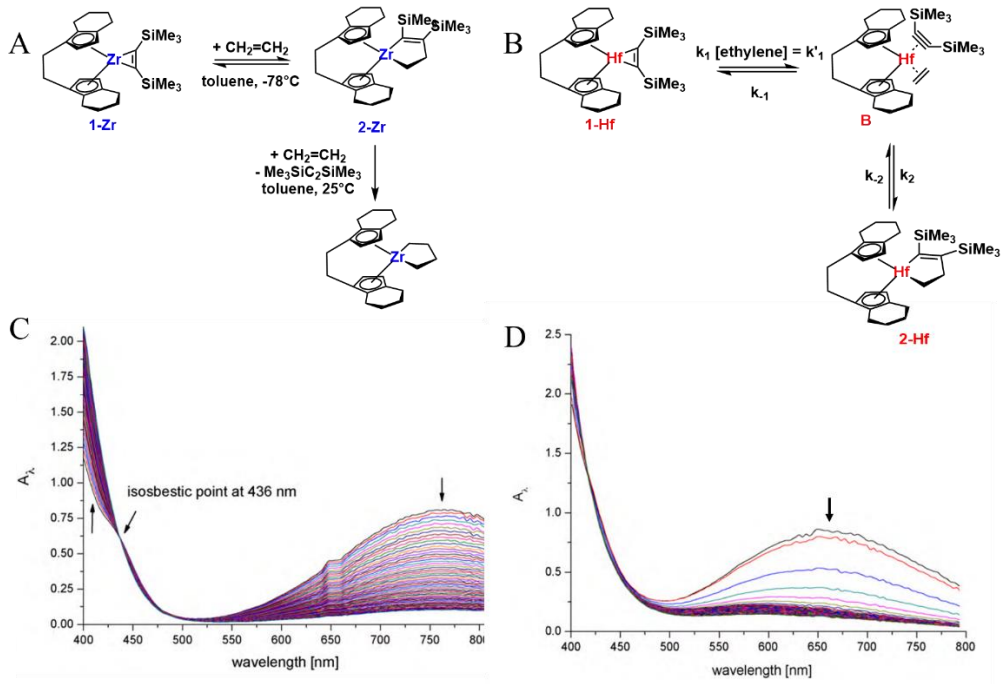


Figure 38. (A) Reaction of rac-(ebthi)Zr(η^2 -Me_3SiC_2- $SiMe_3$) with ethylene; **(B)** Reaction of rac-(ebthi)Hf(η^2 -Me_3SiC_2- $SiMe_3$) with ethylene via intermediate **B**; **(C)** UV-VIS absorption spectra for the reaction of rac-(ebthi)Zr(η^2 -Me_3SiC_2- $SiMe_3$) with ethylene in toluene at r.t., k' = 0.0365 s^{-1} (the pseudo-rate constants k' for the formation of **3-Zr** as a function of ethylene concentration, rate constant k was determined from the slope of the linear regression); **(D)** UV-Vis spectra for the reaction of rac-(ebthi)Hf(η^2 -Me_3SiC_2- $SiMe_3$) with ethylene in toluene, at room temperzture, $k'_{obs.1}$ = 78.6 s^{-1}, $k'_{obs.2}$ = 2.4 s^{-1}). Adapted from ref. [297]. Copyright 2010 Elsevier.

Chromium-based organometallics complexes were also used for ethylene oligomerization.[300] These catalysts promote the production of hexene or octene from ethylene, and are commonly employed in the reaction as precatalysts, that require an activator. In this process, methylaluminoxane or alkylaluminum reagents are typically employed as activators, playing a crucial role in reducing the Cr complex to generate the active intermediate. UV-VIS absorption spectroscopy was used by the group of Sydora and Blakemore to understand the activation processes, as well as the redox chemistry of these chromium-based precatalysts, prior to olefin oligomerization. Therefore, a family of Cr(P,N)Cl_3(THF) complexes (where (P,N) represents a bidentate phosphorus- and nitrogen-containing ligand) were studied, and the UV-VIS spectra show two d-d absorption bands at 450 and 650 nm prior to the activation. The addition of decamethylcobaltocene Cp^*_2Co as a reducing agent, results in a decrease in absorbance at λ = 247 and 350 nm, and a significant increase in absorbance at λ = 298 nm. Two isosbestic points at 237 and 276 nm are observed, indicating the reduction of the Cr^{III} complex to Cr^{II}. On the other hand, the reactivity of the Cr^{III} complex was probed with the $AlEt_3$ activator. The UV-VIS spectra show an increase in absorbance at λ = 227 and 342 nm, a decrease in absorbance at λ = 297 nm, as well as two isosbestic points at 244 and 310 nm, demonstrating the conversion of the Cr^{III} complex to a new reduced Al-bound Cr species. This was then titrated with Cp^*_2Co, resulting in a decrease of bands at λ = 221 and 358 nm, an increase at λ = 290 nm, with two isosbestic points at 254 and

323 nm, indicating the formation of a two-electron-reduced species. Based on these findings, the authors proposed that the Lewis acidity and the reductive activity of alkylaluminum reagents enables the multi-electron reduction of Cr^{III}, permitting its backbonding with coordinated ethylene ligands, thus promoting the oligomerization reaction.

Furthermore, the effect of different AlR_3 activators on the performance of the Cr complex in the oligomerization of ethylene was investigated by Grauke *et al*.[301] The authors used UV-VIS absorption spectroscopy to monitor the Cr complex formation upon mixing the $Cr(acac)_3$ precursor, the (PNP) ligand ($Ph_2PN(^iPr)PPh_2$), and the activator. An intra-ligand transition band at 260 nm and a LMCT complex transition band at 337 nm were identified for $Cr(acac)_3$ in cyclohexane, which remain unchanged after the addition of PNP, indicating no coordination to the metal center (Figure 39 A). However, upon addition of modified methylaluminoxane (MMAO) (used as a reference), the formation of $(PNP)Cr^{II}(CH_3)_2$ is detected by the appearance of a 325 nm absorption band. A higher band intensity is observed in the case of $AlMe_3$, indicating an effective methylation of the Cr center. With Al^tBu, on the other hand, the alkylation is less efficient (Figure 39 B). Complementary *in situ* EPR, ATR-IR, and XANES/EXAFS studies were then conducted to better understand the valence state of Cr, and its coordination environment. The results show that one-electron reduction is possible in presence of all Al activators, whereas deep reduction to Cr^I requires bulky activators such as $AlOct_3$.

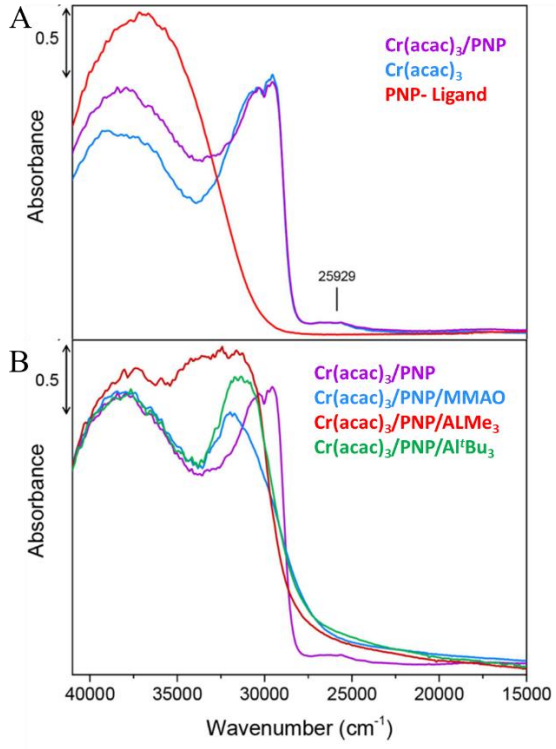


Figure 39. (A) *In situ* UV-VIS absorption spectra of $Cr(acac)_3$ before and after adding PNP ligand; **(B)** Spectra of $Cr(acac)_3$/PNP in presence of different activators. Adapted from ref. [301]. Copyright 2019 Wiley.

Alcohol oxidation

The aerobic oxidation of benzylic and aliphatic alcohols using Cu/TEMPO (TEMPO = (2,2,6,6-tetramethylpiperidin-1-yl)oxyl) is an important reaction for the synthesis of fine chemicals.[302, 303] *In situ* UV-VIS-NIR absorption spectroscopy coupled with EPR and

attenuated total reflection (ATR)-IR, and later extended to simultaneous *operando* EPR/XANES/EXAFS/UV-VIS-NIR/ATR-IR, enabled a better understanding of the mechanism.[283, 304] Prior to the reaction, a MLCT band at 310 nm is observed when adding the catalyst precursor $Cu^{I}OTf$ in MeCN. This band is shifted to a higher wavelength (348 nm), and a new MLCT band appears at 450 nm when bpy (2,2'-bipyridine) is added, indicating the replacement of the coordinated solvent by the ligand (Figure 40). The band shift revealed the dipolar interaction of the $(bpy)Cu^{I}$ complex with O_2, indicating a stabilization of the Cu^{I} species against oxidation as the band at ~660 nm, corresponding to Cu^{II} d-d transitions, remains negligible (Figure 40). However, coordination of NMI (*N*-methylimidazole) to the $(bpy)Cu^{I}$ complex reduces the Cu^{II}/Cu^{I} reduction potential and raises its ability to reduce O_2 towards $(bpy)(NMI)(CH_3CN)Cu^{II}$-OOH and $(bpy)(NMI)Cu^{II}(\mu\text{-}OH)_2Cu^{II}(bpy)(NMI)(CH_3CN)$.[305] This binuclear species is cleaved during reaction with TEMPO to form $(bpy)(NMI)(OOH)Cu^{II}$-TEMPO and $(bpy)(NMI)(CH_3CN)Cu^{II}$OOH-TEMPO, which are considered to be the active species in the alcohol oxidation.

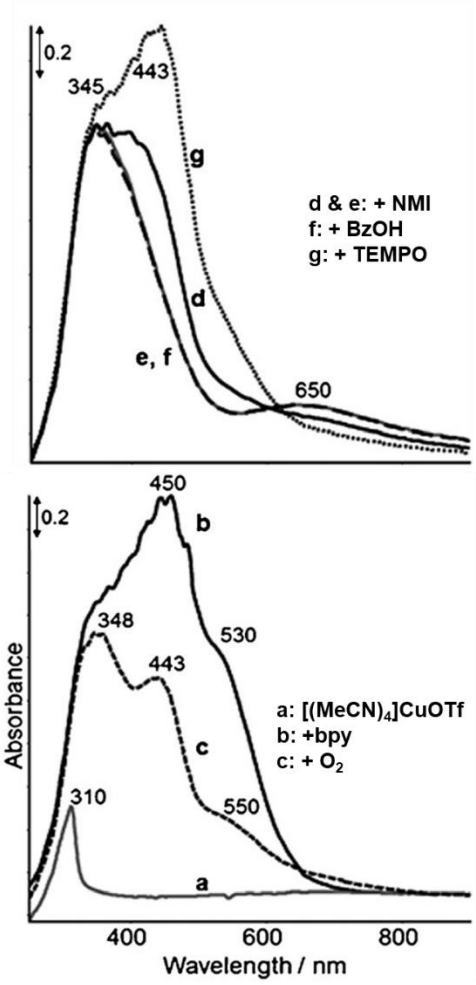


Figure 40. (a) UV-VIS spectra of $[(MeCN)_4]CuOTf$ complex in MeCN (b)+bpy (c) after 20 min bubbling O_2 at 20 °C (d) +NMI (e) +NMI after 15 min (f) +BzOH (g) +TEMPO. Adapted from ref. [304]. Copyright 2015 Wiley.

Asymmetric hydrogenation

The rhodium diphosphine complex $[Rh(Me\text{-}Duphos)(cod)]BF_4$ (structure 4, Figure 41 A) was reported as a catalyst for the *in situ* hydrogenation of the cylooctadiene group (cod) in MeOH. This catalyst generates the corresponding solvated complex, which is the active catalytic

species in the reaction (Figure 41 A).[297] Due to low amount of the cod hydrogenation intermediate (cyclooctene complex (coe)),[306] the consecutive reaction can be regarded as a pseudo-first-order reaction with a pseudo-rate constants k'_{2cod}. The recorded UV-VIS absorption spectra during the reaction showed four isosbestic points indicating a kinetically uniform reaction (Figure 41 B). From nonlinear curve fitting of the decay, and fitting the evolution to a pseudo-first order kinetic equation, the pseudo rate constant k'_{2cod} was calculated to be 0.119 min^{-1}.

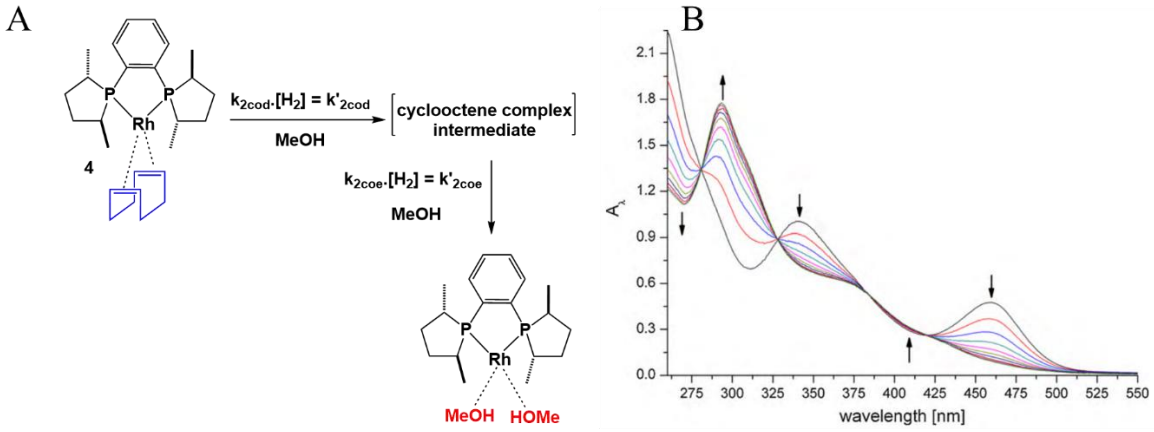


Figure 41. (A) The formation of the solvate complex [Rh(Me-DuPHOS)$(MeOH)_2$]BF_4 via coe intermediate; **(B)** Reaction spectra for the hydrogenation of [Rh(Me-Du-PHOS)(cod)]BF_4 in MeOH at r.t. Adapted from ref. [297]. Copyright 2010 Elsevier.

Similarly, the authors investigated the deactivation mechanism of the rhodium diphosphine complexes in asymmetric hydrogenation. The presence of aromatic solvents in the reaction such as benzene and toluene have the potential to inhibit these reactions. Hence, the stability constants of the rhodium diphosphine complexes were obtained via UV-VIS absorption monitoring of the benzene titration of [Rh(DPPE)$(MeOH)_2$]BF_4 to derive the desired stability constant of 18 l/mol after linearization using the Benesi-Hildebrand equation.[307]

An enantioselective version of this reaction was explored using the chiral [Rh(dipamp)][BF_4] complex as a catalyst for the selective hydrogenation of ethyl-(*Z*)-α-acetamidocinnamate (mac) to *N*-acetyl-(R)-phenylalanine.[308] The reaction intermediate [Rh(dipamp)(mac)]$^+$, generated upon coordination of mac to the rhodium center via the C=C and the oxygen atom of the amide group, normally leads to the formation of the S conformer. Thus, to understand this unique stereoselectivity, *in situ* UV-VIS absorption spectroscopy was used for thorough kinetic studies. The results revealed that the reactivity of the intermediate diastereoisomers towards hydrogen is at the origin of the observed enantioselectivity.

In another study, [309] the transfer hydrogenation of acetophenone using the Ikariya–Noyori complex [(mesitylene)RuCl(*R*,*R*)-(TsDPEN)] in presence of formic acid/triethylamine mixtures was studied using *operando* UV-VIS-NIR absorption and NMR spectroscopy to monitor the reaction intermediates. The generated formate complex was detected by NMR, while the UV-VIS-NIR absorption spectroscopy allowed tracking the unsaturated reaction intermediate during the reaction based on its characteristic absorbance at 565 nm. The UV-VIS absorption data imply an almost quantitative transformation of the unsaturated intermediate during the reaction towards the formate complex in presence of formic acid, but a less favorable decarboxylation of the latter towards the Ru-hydride complex. These findings suggest that three reactions can compete with the hydride complex formation, (1) a re-insertion of CO_2 forming

the formate complex, (2) hydrogen transfer to form the desired product and (3) protonation by the excess of formic acid, which causes its consumption and a decrease in the reaction performance.

Dehydroperoxidation

In 2018, Schaub and coworkers investigated the chromium catalyzed dehydroperoxidation of cyclohexyl hydroperoxide (CHHP) to cyclohexanone.[276] With *in situ* UV-VIS-NIR absorption spectroscopy, the metal complex species were detected, a reaction mechanism was proposed, and the reaction conditions were optimized. The absence of strong absorption bands between 300-1000 nm in the pure catalyst spectra indicates the +6 oxidation state (Ar electron configuration) of the Cr center. Further addition of CHHP leads to a decrease of the absorption band at 450 nm linked to the coordination of the substrate to the Cr^{VI}. Since no new bands are observed around 600 nm, the oxidations state is considered unchanged. Interestingly, a new absorption band at 480 nm, assigned to a peroxy to Cr^{VI} CT, appears, indicating the formation of the cyclohexylperoxychromium(VI)complex (Figure 42). A blueshift of the absorbance to 420 nm occurs with the decomposition of this complex into $CrO_2(OH)_2$. The authors propose that the decomposition of cyclohexyl hydroperoxide proceeds via a non-radical, non-redox mechanism, through formation of the cyclohexylperoxy chromium complex as the reactive intermediate. This was confirmed by further NMR and DFT studies.

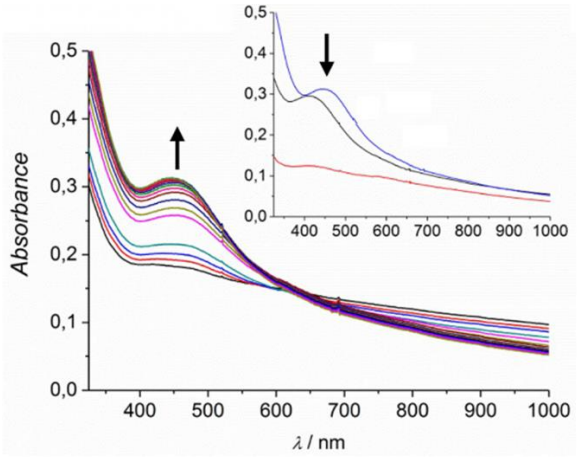


Figure 42. UV-VIS-NIR absorption spectra of the reaction of CrO_3*py in presence of CHHP in α,α,α-trifluorotoluene at 5 °C. Insert: (blue line) Spectrum of the formed cyclohexylperoxychromium(VI) complex after 2 min; (shifted black line) decomposition after 10 min and (red line) full decomposition after 48 h. Adapted from ref. [276]. Copyright 2018 Wiley.

Formic acid dehydrogenation

Formic acid decomposes into CO_2 and H_2 and is therefore a liquid carrier for these gases under acidic conditions and at ambient temperature. The Fe/PP_3 iron catalyst system, formed *in situ* from $Fe(BF_4)_2$-$6H_2O$ and the tetradentate ligand tris[(2-diphenylphosphino)-ethyl]phosphine ($P(CH_2CH_2PPh_2)_3$, PP_3), is an effective catalyst for this reaction.[310, 311] *In situ* Raman, ATR-IR, and UV-VIS absorption spectroscopies were used to identify the intermediate complexes.[312] The UV-VIS absorption spectrum of the Fe/PP_3 system in THF shows the $\pi \rightarrow \pi^*$ and MLCT transitions of the formed complex (bands at 277 and 508 nm, respectively), as well as the interaction between the Fe/PP_3 complex and the additional THF ligand (318 nm absorption band) (Figure 43). Upon addition of formic acid, the band at 318 immediately disappears, and the MLCT band loses intensity and shifts to 499 nm. The formic acid coordinates onto the Fe/PP_3 catalytic system by displacing the previously coordinated THF to form the Fe-PP_3-bidentate formate complex, which is considered the catalytically active complex for the release

of CO_2 and H_2. The addition of NaCl led to the formation of a deactivated $[FeCl(PP_3)]BF_4$ complex in THF, as chlorine is preferentially coordinated over formic acid. This appears in the UV-VIS absorption spectrum through absorption bands at 327 and 380 nm, and a redshift of the 499 nm absorption band (Figure 43).

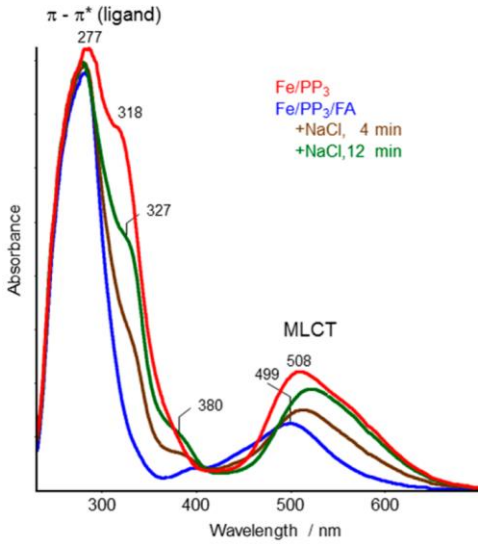


Figure 43. *In situ* UV-VIS absorption spectra obtained from Fe/PP_3 in THF, after addition of formic acid and further addition of NaCl. Adapted from ref. [313]. Copyright 2014 American Chemical Society.

A recently introduced setup to study homogeneous catalysts with *in situ* DRS uses a suspension of α-Al_2O_3 to diffusively reflect the incident light (Figure 3 B). The signal is processed using the K-M formula, with *K*/*S* assumed directly proportional to the concentration of measured species in the solution. The scattering coefficient was calculated as the reciprocal average distance between the α-Al_2O_3 particles.[30] This system was used to study the catalytic dehydrogenation of formic acid to H_2 and CO_2 catalyzed by the iridium complex $[Cp^*Ir(4DHBP)(OH_2)]SO_4$ at 80 °C. The turnover frequency (TOF) and turnover number (TON) of the reaction were determined at 5467 h^{-1} and 15094, respectively, in agreement with previous studies. Advantages of the approach are a high signal-to-noise ratio and the reliable collection of spectra without mechanical errors from gas meters. However, the impact of the escaping light should be critically evaluated, as the K-M assumption of infinite sample thickness (see section 2.1.1) is clearly not fulfilled.

3.2.2 Non-organometallic transformation

3.2.2.1 Imide reduction

The reduction of imides and amides in the presence of phenylsilanes as hydrogenating agent, is a good example of homogeneously catalyzed non-organometallic reactions. They are commonly studied by *in situ* UV-VIS-NIR absorption, ATR-IR, and Raman spectroscopy. Using boronic acid,[314] or fluoride catalysts,[315] two scenarios are proposed. The catalyst can either activate the target reagents or the hydrogenating agent.[313] For the tetra-*n*-butylammonium fluoride (TBAF)-catalyzed reaction, the *in situ* UV-VIS absorption spectra show no interaction between the imide (*N*-methylphthalimide) and TBAF, as the imide bands at 265, 302, and 324 nm remain unchanged over time in the presence of the catalyst (Figure 44 A). However, upon the addition of Ph_2SiH_2, the 324 nm absorption starts fading indicating the

onset of the carbonyl group reduction. A new absorption band at 370 nm appears from the desired product (*N*-methylisoindolinone). An additional band at 536 nm indicates the formation of small amounts of chromophores as side products. It was derived that in the first stage of the reaction, TBAF is coordinated to the silicon atom of Ph_2SiH_2 forming a reactive penta-coordinated silicon species. This readily attacks the carbonyl group of the imide yielding a hexacoordinated silicon species where the hydride transfer can take place.

In the boronic acid-catalyzed reduction of *N*,*N*-dimethylbenzamide to *N*,*N*-dimethylbenzamine, interaction of boronic acid with the amide via hydrogen bonding is observed by *in situ* UV-VIS absorption spectroscopy (Figure 44 B). The addition of $PhSiH_3$ to the boronic acid reveals no change in the spectra whereas the further addition of the amide causes a significant blueshift indicating the interaction (Figure 44 B, C). The mechanism is proposed to be initiated by the activation of the carbonyl group of the amide by the boronic acid, enabling attack of the silane towards the formation of the corresponding siloxane and the desired amine. Thus, in both reactions with boronic acid or fluoride, the formation of phenylsiloxanes is believed to be the driving force.

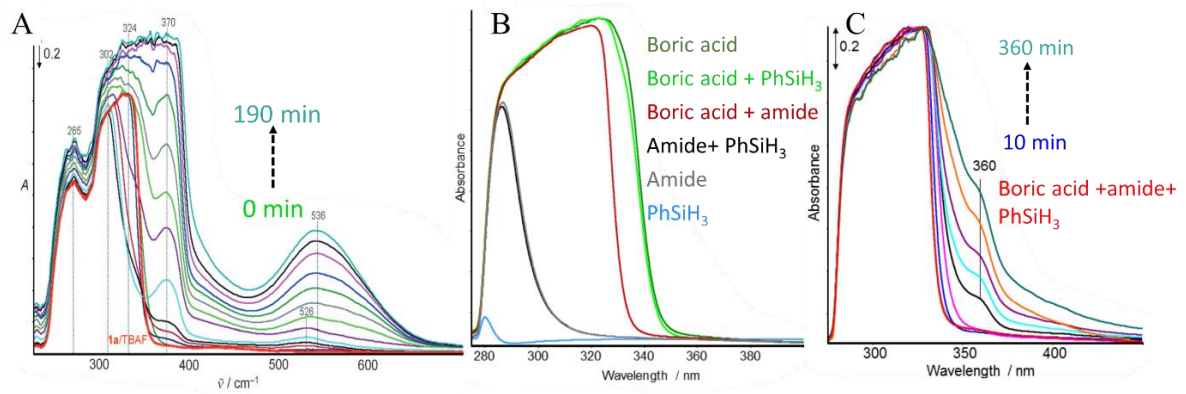


Figure 44. (A) *In situ* UV-VIS absorption spectra for the reaction of *N*-methylphthalimide and Ph_2SiH_2 using TBAF as catalyst; **(B)** UV-VIS absorption spectra of *N*,*N*-dimethylbenzamide, $PhSiH_3$, and the boric acid and their mixtures in toluene; **(C)** *in situ* UV-VIS absorption spectra for the reaction of N,N-dimethylbenzamide and $PhSiH_3$ with the boric acid in toluene. Adapted from refs. [314, 315]. Copyright 2011 Wiley and 2013 Wiley.

3.2.2.2 Cycloaddition

Another example of non-organometallic transformations studied by *in situ* UV-VIS is the [3 + 3] cyclocondensation reaction of ketene acetals with a diene. Depending on the nature of the Lewis acid and its interaction with the ketene acetal, different products can be obtained. The use of both $AlCl_3$ and $TiCl_4$ leads to the generation of salicylate,[316] but via a different mechanism.[317] A strong redshift of the absorption edge is observed in the case of $TiCl_4$, indicating an increase in electron density of the C-O bond of the ketene-acetal by electron delocalization (Figure 45). This is due to the $TiCl_4$ attack, transforming the group into a chlorine-containing titanium bis-chelate complex, active in the UV-VIS region. For $AlCl_3$ the absence of dπ electrons prevents the formation of metal-donor resonance structures, and the absorption edge in the UV-VIS absorption spectrum is accordingly slightly blue-shifted. An aluminum tris-chelate complex without chlorinated ligands is formed instead.

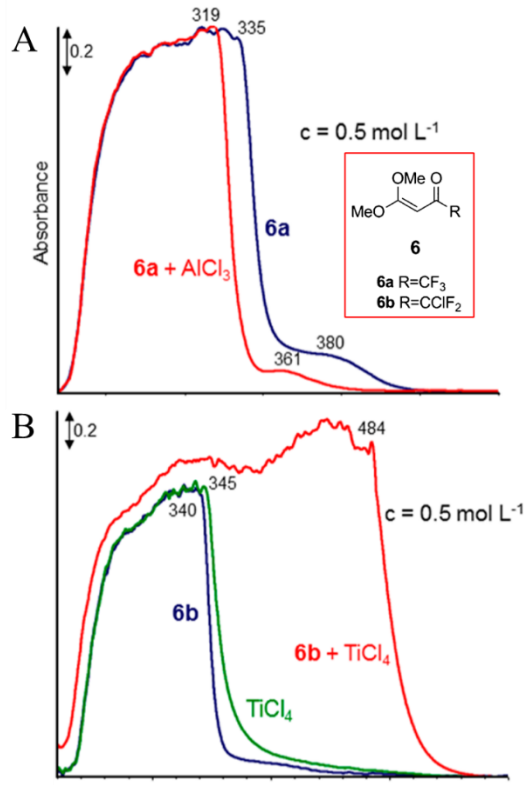


Figure 45. *In situ* UV-Vis absorption spectra recorded during the **(A)** $AlCl_3$- and **(B)** $TiCl_4$-mediated reaction using ketenacetale (6a & 6b) in CH_2Cl_2. Adapted from ref. [313], using data with permission from refs. [316, 317]. Copyrights 2013 American Chemical Society, 2011 Wiley and 2013 Elsevier.

As illustrated above, *in situ* UV-VIS spectroscopy has proven its relevance for monitoring homogeneous transformations, especially when organometallic complexes are involved. Nevertheless, IR and NMR spectroscopies are preferably used in this field, as shorter wavelengths (higher energy radiation) often promote side reactions.[318] As also shown in this section, detailed analysis and interpretation of UV-VIS-NIR absorption bands is rather rare in homogeneous catalysis studies. Instead, single transformations with clear isosbestic points in the absorption spectrum are commonly performed, and any dynamics in the region of the absorption spectrum can be used for kinetic measurements. As with heterogeneous catalysis, no single spectroscopy can provide full understanding of the relevant properties, and the coupling of different spectroscopies is common.[319] This applies for instance to organometallic reactions, where UV-VIS-NIR absorption spectroscopy is often combined with attenuated total reflection (ATR)-IR and Raman spectroscopy to identify the metal complexes as well as the intermediate species.[320]

3.3 Enzymes

Using complex metal-containing active sites, metalloenzymes perform some of the most difficult and selective catalytic reactions. Metalloenzyme catalysis involves active sites that combine properties of heterogeneous and homogeneous catalysis. They involve a large variety of ligated complexes that influence UV-VIS-NIR sensitive properties, derived from electronic transitions both on the metals and on the ligands, as observed for homogeneous TMI complexes. Besides this, they also are influenced by their mantle, similarly to the support effects in heterogeneous catalysis, but supplemented with properties unique to the extended protein ligand. This section shows examples of typical methods used in the kinetic and mechanistic

study of metalloenzyme catalysis with *in situ* UV-VIS-NIR spectroscopy. Then the power of combined absorption, rR, and MCD spectroscopy, originating from the field of metalloenzymes, is demonstrated. We summarize two recent applications of stopped-flow absorption combined with a higher resolution spectroscopic method on metalloenzyme intermediates. Spectroscopic definition of these intermediates and stopped-flow derived isotope sensitivity of kinetics (kinetic isotope effects) allowed determination of key reaction mechanisms. These intermediates also parallel relevant intermediates defined in heterogeneous metallozeolite catalysts from site selective spectroscopic studies.

A challenge common to all characterisation of enzymes remains the measurement of *in vivo* properties in the setups used for *in situ* characterisation.[321, 322] In heterogeneous catalysis one often refers to the 'pressure gap' to indicate the discrepancies between the productive conditions and the conditions under which spectroscopic measurement is possible. For enzymes the gap is of another nature. In vivo conditions often imply low enzyme concentrations and specific environments (e.g. cofactors, ionic strength, pH, temperature, embedding in cellular membranes, …). Deviations from these conditions can induce non-negligible changes to enzyme structure and reactivity. Naturally, one may just as well be more interested in enzyme characterization in reactor conditions for industrial purposes. Both types of settings can bedifficult to correspond with *in situ* measurements, commonly on isolated, up-concentrated enzymes at low temperatures. The fragility and redox sensitivity of enzymes, as well as their strong diversity can present additional challenges to sample preparation and to scholarly consensus. An well-known example is the discussion on the structure of the active site in particulate monooxygenase.[323] Moreover radiative damage makes measurements with high energy radiation problematic.

A more UV-VIS-NIR range specific challenge for the spectroscopic investigation of enzyme catalysis is the interfering absorption by the surrounding mantle. Aromatic amino acids absorb strongly in the UV and this can make certain active site signals difficult to discern. An option is to measure instead on smallermodel complexes, but then any relevant effect of the greater protein structure is no longer considered.

3.3.1 Kinetics: stopped-flow absorption and rapid freeze quench trapping

In their catalytic cycles, metalloenzymes progress through a series of key intermediates; understanding these individual steps is necessary to unlock deep insight into enzyme function. Stopped-flow UV-VIS absorption spectroscopy is used to investigate them. This technique is particularly useful for metalloenzymes since the open shell metal centers within the active site have clear absorption features that can be tracked. A great example is the measurement of a critical intermediate and its reactivity in the catalysis of soluble methane monooxygenase (sMMO). sMMO is a binuclear non-heme iron enzyme capable of oxidizing methane to methanol at ambient conditions, a difficult feat given the strong C-H bond of methane.[324] Stopped-flow UV-VIS absorption was essential in observing the CH_4 reactive intermediate Q of sMMO through appearance of its distinct 430 nm absorbance feature.[325] This feature provided a handle for tracking the kinetics of the reaction of intermediate Q with CH_4. The rate of decay of the 430 nm feature with CH_4 allows extraction of Q's very low CH_4 reaction barrier ($\Delta G^{\ddagger}$ = 10.3 kcal/mol).[326] Substituting CH_4 for CD_4 allows determination of an H/D kinetic isotope effect of 50 via the change in rate of decay of the 430 nm feature (Figure 46).[327] This large KIE indicates Q reacts with CH_4 via hydrogen atom abstraction (HAA) in a tunneling mechanism. These and other data have been used recently to rationalize the low barrier of HAA from CH_4 by using the front oxo of the two oxo bridges of the diferryl active site to overlap

with the H-C bonding orbital of CH_4 and using the oxo bridge at the rear to stabilize the electron gained from the HAA (Figure 47).[328]

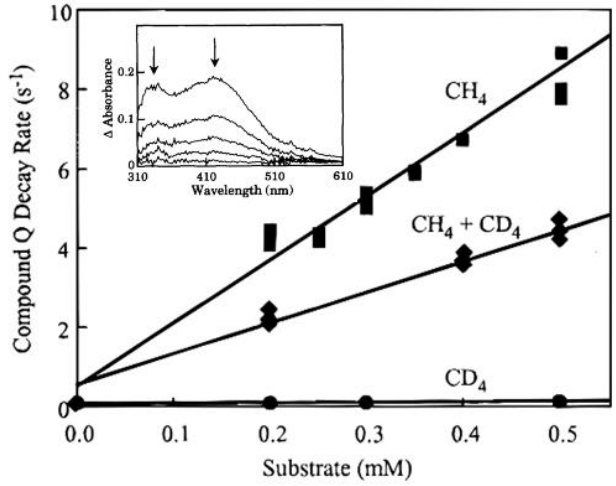


Figure 46. Change in the rate of decay of intermediate Q with varying CH_4 and CD_4 concentrations. (Inset) Stopped-flow UV-VIS absorption spectra of decay of intermediate Q from 4 to 30 s. Adapted from refs. [325, 327]. Copyright 1993 The American Society for Biochemistry and Molecular Biology and copyright 1996 American Chemical Society.

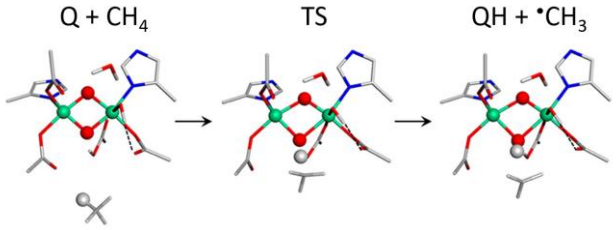


Figure 47. Density functional theory model of sMMO's intermediate Q performing H-atom abstraction on CH_4. (Color scheme: red = O, green = Fe, grey = C, blue = N, and white = H). Adapted from ref. [328]. Copyright 2021 American Chemical Society.

The absorption features still lack the capacity to probe the chemical structure of intermediates, necessitating the use of methods that can be coupled to the absorption band for higher resolution analysis. This requires trapping of the intermediates through RFQ. Other key spectroscopies, also using UV-VIS-NIR range light, can be subsequently used to gain information from the absorption features of the intermediate in the frozen mixture. For charge transfer bands that have high absorption intensity, rR spectroscopy can be used to gain vibrational information on the active site of the intermediate. For ligand field bands, which are often too weak to observe in stopped-flow UV-VIS absorption, MCD at low temperature can allow visualization of these bands. Additionally, magnetic information on the ground state of the intermediate's active site can be obtained through VTVH MCD of the excited state intensity. Background on these techniques and metalloenzyme applications paralleling studies on metallozeolites are explored below, but for a more in-depth background we point readers to our previous review.[100]

3.3.2 Resonance Raman profiling of absorption bands

In the case of the protein oxy-hemocyanin, the vibrations of a small four atom core in a 73 kDA protein that has a ~3 mM concentration can be observed in rR and used to assign the the vibrations and electronic structure of its μ-η^2:η^2-peroxide dicopper(II) core (Figure 48 A, B).[205,

[329] Isotope perturbation (or lack of perturbation) was extremely helpful in vibrational assignments of $^{18}O_2$ oxy-hemocyanin, assigning both the O-O stretch at 744 cm^{-1} from the significant redshift upon ^{18}O labeling and the Cu-Cu stretch at 286 cm^{-1} from the lack of isotope perturbation.[329] Additionally, non-totally symmetric vibrations are not resonance Raman allowed, resulting in weak intensity like the 543 cm^{-1} Cu-O (B_{3u}) mode in oxy-hemocyanin; however, the first overtone at 2x the energy of the fundamental is symmetric and resonance Raman allowed, giving the intensity seen in the 1087 cm^{-1} vibration (Figure 48 B). Finally, the intensity of all these vibrations is measured at different laser excitation wavelengths to generate a resonance Raman excitation profile, helping assign the two LMCT bands of hemocyanin as the peroxide σ and peroxide π CT bands at higher and lower energy respectively (Figure 48 C).[205]

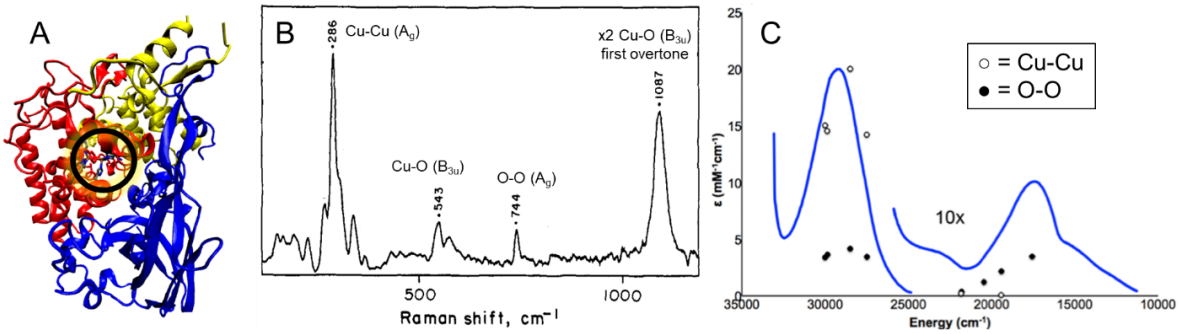


Figure 48. (A) Arthropod hemocyanin with active site highlighted. (B) Resonance Raman spectrum of oxy-hemocyanin. (C) Resonance Raman excitation profile of the 286 cm^{-1} (Cu-Cu) and 744 cm^{-1} (O-O) vibrations of hemocyanin. Adapted with permission from refs. [205, 329]. Copyright 1994 and 2014 American Chemical Society.

Stopped-flow UV-VIS absorption spectroscopy coupled to rR spectroscopy was critical in solving a major outstanding issue in bioinorganic chemistry, the mechanism of monooxygenation by the enzyme tyrosinase. Tyrosinase (Ty) is a coupled binuclear Cu enzyme that binds O_2 to catalyze the rate-limiting step in melanin biosynthesis. Oxy-Ty uses a μ-η^2:η^2-peroxide dicopper(II) core to monooxygenate L-tyrosine to L-DOPA (Figure 49 A); this core can then oxidize catechols to ortho-quinones that couple to form melanins. This core has two clear peroxide to Cu^{II} charge transfer transitions at 345 and 650 nm. The same transitions are observed in oxy-hemocyanin. Lasers can be tuned into these CT bands to reveal the same set of rR features as in oxy-Hemocyanin: the Cu-Cu stretch at 280 cm^{-1}, the O-O stretch at 739 cm^{-1}, and the rR allowed first overtone of the forbidden B_{3u} Cu-O stretch at 1078 cm^{-1} (Figure 49 B).[205] These CT bands also provided a handle to gain kinetic information on active site reactivity via stopped-flow UV-VIS absorption spectroscopy.

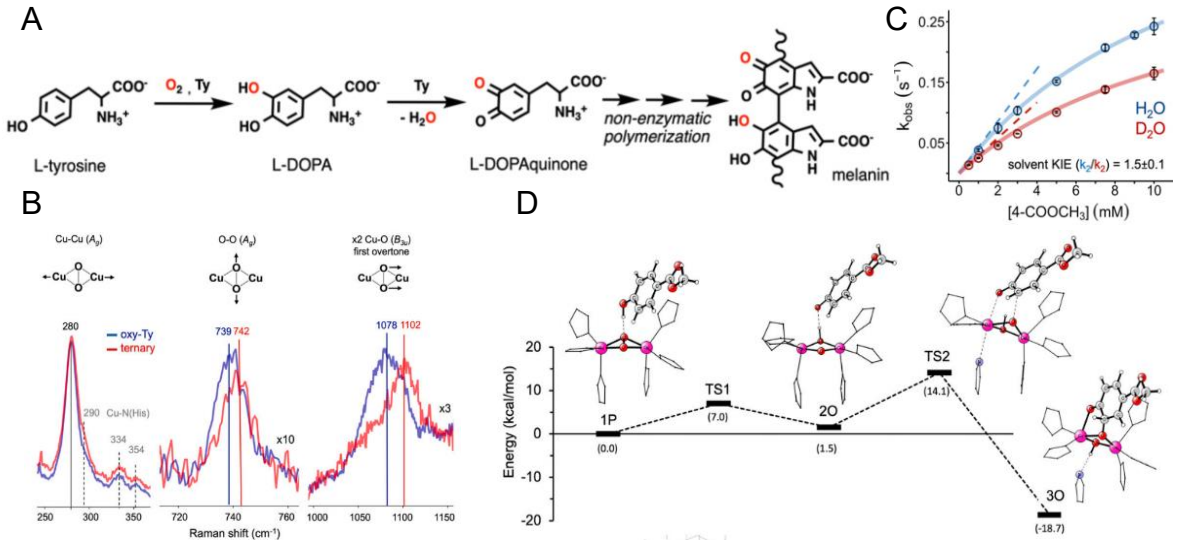


Figure 49. (A) Conversion of L-tyrosine to L-DOPAquinone by the enzyme tyrosinase in melanin biosynthesis. **(B)** The main vibrational modes of the Cu_2O_2 core in tyrosinase. Resonance Raman spectra of oxy-Ty (blue) and the ternary intermediate of tyrosinase (red). **(C)** Dependence of k_{obs} on substrate concentration in H_2O (solid blue) and D_2O (solid red) with a linear fit of the low substrate regime (dashed). **(D)** QM/MM reaction coordinate for the monooxygenation of phenol by tyrosinase. Adapted from ref. [330]. Copyright 2022 National Academy of Sciences.

Under single turnover conditions where oxy-Ty solely monooxygenates the phenolic substrate, the rate of decay of the oxy-Ty intermediate's 345 nm feature has linear dependence at low substrate concentrations, but deviates from linearity at higher substrate concentrations (Figure 49 C). This nonlinear dependence indicates the rapid formation of a ternary intermediate upon binding of substrate.[330] RFQ of deoxy-Ty mixed with an O_2 saturated buffered solution containing substrate allows trapping of this ternary intermediate. Tuning a laser into the 345 nm feature of this intermediate for rR spectroscopy reveals the same three features as in Oxy-Ty, but with the O-O stretch and the B_{3u} overtone shifted by +3 cm^{-1} and +24 cm^{-1}, respectively. This indicates the preservation of the μ-η^2:η^2-peroxide dicopper(II) core but with an active site perturbation from binding of substrate. This spectroscopic perturbation combined with a solvent secondary kinetic isotope effect (Figure 49 C) was a significant revelation as it ruled out past models for the ternary complex in tyrosinase including direct bonding of a deprotonated phenol to one of the copper atoms or oxidation of the Cu^{II} to Cu^{III}. Multiple QM/MM models were evaluated for possible substrate binding to the active site with one model reasonably matching the spectroscopic observations. This model has the phenolic substrate bound protonated above the μ-η^2:η^2-peroxide dicopper(II) core and hydrogen bonding to one of the oxygen atoms of the peroxide (Figure 49 D left). Understanding this key intermediate allowed derivation of the reaction mechanism for monooxygenation. The docking of the protonated substrate at the core with the hydrogen bond to the peroxide allows proton transfer to the active site upon breaking the O-O bond. The subsequent non-protonated bridging oxo is then able to attack the ortho carbon of the aromatic core of the substrate to form the C-O bond.[330]

3.3.3 The application of magnetic circular dichroism spectroscopy

MCD spectroscopy was a particularly helpful characterization tool for the blue copper site in the intensely blue colored protein plastocyanin where the CT bands at higher energy (Figure 50 bands 1-4) have smaller C_0/D_0 ratios whereas the low energy ligand field transitions (Figure

50 bands 5-8) have larger C_0/D_0 ratios. The low energy of the ligand field transitions coupled to ligand field theory first showed that the blue copper site has a distorted tetrahedral structure.[331]

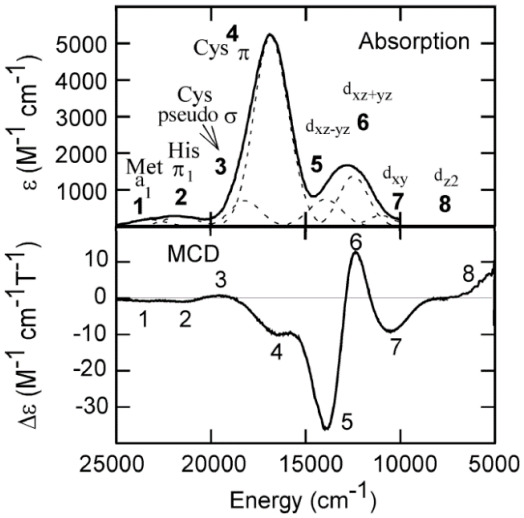


Figure 50. (Top) low-temperature absorption and (bottom) low-temperature MCD of plastocyanin. Adapted with permission from ref. [331]. Copyright 2004 American Chemical Society.

Additionally, as indicated by the scheme in Figure 6, changes in MCD intensity with variation in the temperature and applied field of the sample also reflect the magnetic properties of the ground state. VTVH MCD can be plotted (Figure 51) and fit to extract spin Hamiltonian parameters of the ground states of key intermediates. This has been extremely useful in the case of non-Kramers systems (i.e. integer spin) like high spin Fe^{II} and Fe^{IV} (S = 2) systems that are generally not detectable by EPR spectroscopy.[332] These spin Hamiltonian parameters provide complimentary insight into geometric and electronic structure. These changes in intensity with temperature and field are also dependent on the polarization of the electronic transition, providing information that is valuable for band assignment.[18, 333]

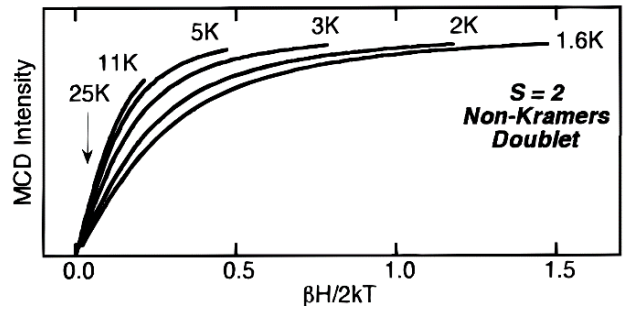


Figure 51. (Top) Saturation magnetization VTVH MCD for an S = 2 system. Adapted with permission from ref. [332]. Copyright 2013 American Chemical Society.

UV-VIS absorption spectroscopy of a key intermediate was critical in understanding the mechanism of selective substrate halogenation by the α-ketoglutarate dependent Fe enzyme SyrB2, although here through coupling to variable-temperature (VT) MCD. SyrB2 is a mononuclear non-heme enzyme involved in the synthesis of the phytotoxin syringomycin E.[334] This enzyme reacts with O_2 to form a high-spin Fe^{IV}=O intermediate that performs H-atom abstraction to selectively halogenate specific C-H bonds.[335] This key Fe^{IV}=O intermediate can be clearly observed through stopped-flow UV-VIS absorption spectroscopy through

appearance and decay of a distinct 318 nm absorbance feature with additional lower energy weaker bands. These absorption features are broad and overlap, giving minimal information (Figure 52 top). However, MCD of the trapped intermediate at low temperature reveals detailed insight into these electronic transitions with three clear bands observed at low energy (Figure 52 bottom, bands I-III). VT MCD of these bands at a strong magnetic field (7 T) was correlated to the zero field splitting of the ground state of the intermediate (D = +7 cm^{-1} and E/D = 0.02).[336]

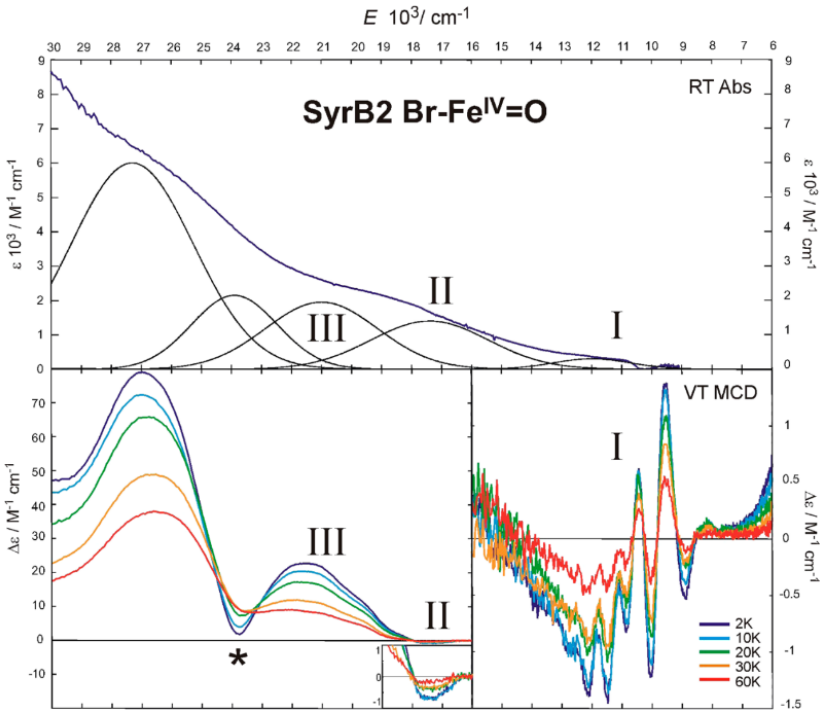


Figure 52. Absorption (top) and 7 T VT MCD (bottom) of the Br-Fe^{IV}=O intermediate in SyrB2. The lowest energy bands are labeled with roman numerals. *Minor heme contaminant. Adapted from ref. [336]. Copyright 2016 American Chemical Society.

The derivative shape of band I between 8 000 and 14 000 cm^{-1} combined with its C_0/D_0 ratio and temperature dependence allowed its assignment as the ligand field $d_{xz/yz}\pi^* \rightarrow d_{z^2}\sigma^*$ transition. The higher resolution of the low temperature MCD spectrum reveals the vibronic coupling of the Fe-O stretch in this electronic transition. Two sets of vibronic progressions are necessary to fit Band I, indicating a split in the energy of the degenerate $d_{xz/yz}\pi^*$ set to two transitions at ~9 500 cm^{-1} and 10 200 cm^{-1} (Figure 53 A). This is due to the halide binding to the Fe^{IV} along the y-axis in the equatorial plane of the halogenase active site that π-donates and raises the energy of the d_{yz} orbital compared to the d_{xz} orbital; the d_{xz} orbital has a stronger interaction with the oxo p π orbital due to lack of competition with the halide ligand. Parameters extracted from the vibronic progressions allowed mapping of the excited state potential energy surfaces (Figure 53 B). The Fe-O bond elongates as this enzyme approaches the transition state. This elongation has a more dramatic effect on the d_{xz} orbital compared to the d_{yz} orbital due to its greater interaction with the oxo p π orbital. Thus, at the transition state, the $d_{xz} \rightarrow d_{z^2}$ transition is lower in energy and more polarized towards an Fe^{III} oxyl in the xz plane for H-atom abstraction (Figure 53 C).[336]

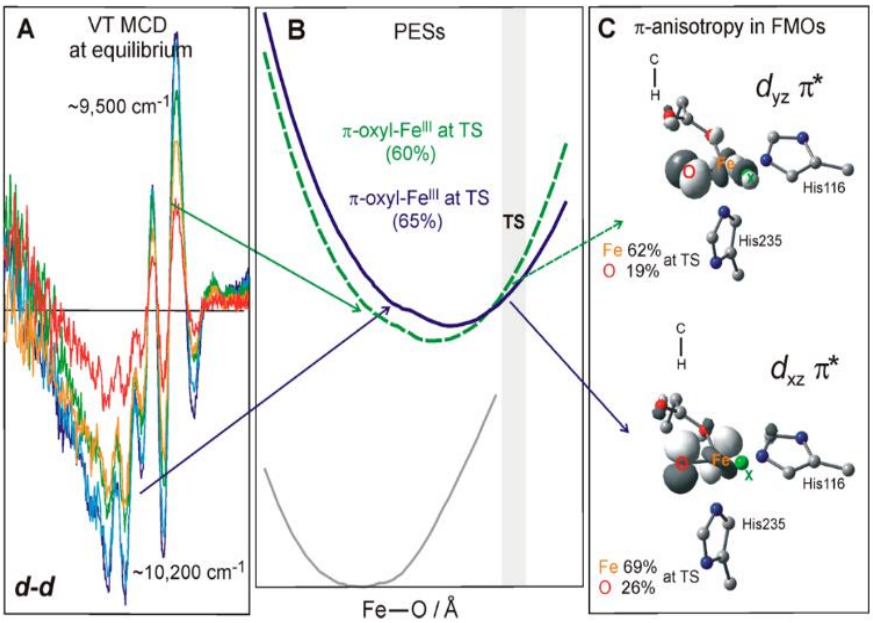


Figure 53. (A) VT MCD spectrum of band I, the $d_{xz/yz}\pi^* \rightarrow d_{z^2}\sigma^*$ transitions in the Fe^{IV}=O intermediate in SyrB2. **(B)** Potential energy surfaces of the ground state and two lowest energy excited states. **(C)** FMO contours of the Fe^{IV}=O intermediate at the transition state with potential approach of the C-H bond in the yz plane (top) and xz plane (bottom). X refers to the halide. Adapted from ref. [336]. Copyright 2016 American Chemical Society.

Thus, there are two potential routes for approach of the reactant's C-H bond for HAA: parallel to the Fe-O bond through the d_{z^2} orbital with oxo p_σ character, the σ pathway, or perpendicular to the Fe-O bond through the d_{xz} orbital with oxo p_π character, the π pathway. The π pathway requires promotion of an electron from the d_{xz} to d_{z^2}, which is high in energy (~32 kcal/mol) at the ground state geometry (Fe-O = 1.64 Å). However, as the Fe-O bond elongates to reach the TS at a bond length of 1.82 Å, this promotion energy lowers to ~7 kcal/mol (Figure 54).[337] This decreased promotion energy combined with the greater oxyl character of the LUMO in the excited state results in roughly equal barriers for HAA through either the σ or π channel, parallel or perpendicular to the Fe-O bond respectively.

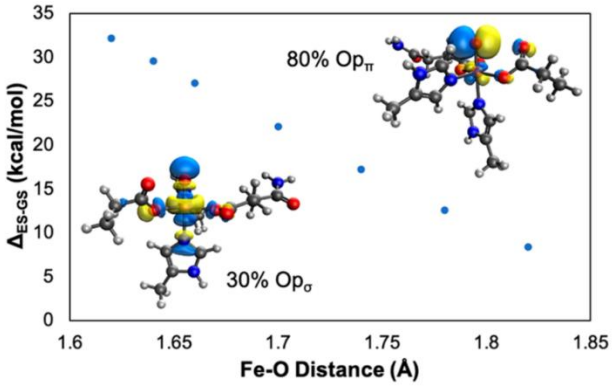


Figure 54. Change in the promotion energy from the dπ* to dσ* orbital with elongation of the Fe^{IV}=O bond. Ground state dσ* LUMO with O character (bottom left) and excited state dπ* LUMO with O character (top right). Adapted from ref. [337]. Copyright 2020 American Chemical Society.

HAA through the σ channel can only allow rebound hydroxylation due to the orientation of the resulting radical along the resulting Fe^{III}-OH bond. However, HAA through the π channel orients the radical above the Fe(OH)Cl plane (Figure 55 left), allowing kinetic feasibility for

either rebound hydroxylation or halogenation. Although hydroxylation is thermodynamically favored, the lower driving force of halogenation is compensated by the lower intrinsic barrier for halogenation rebound making it the favorable reaction pathway for the native substrate (Figure 55).[338] This requires the second-sphere of the protein to play a large role in promoting halogenation. It orients the C-H bond to approach through the π channel to prevent the hydroxylation that would occur through the σ channel. It also positions the substrate radical for good overlap with the halide dπ orbital to promote halogenation. Stopped-flow absorption spectroscopy identified the key Fe^{IV}=O intermediate and RFQ coupled to low temperature MCD (and nuclear resonance vibrational spectroscopy)[339] allowed elucidation of its geometric and electronic structure that determine its reactivity.

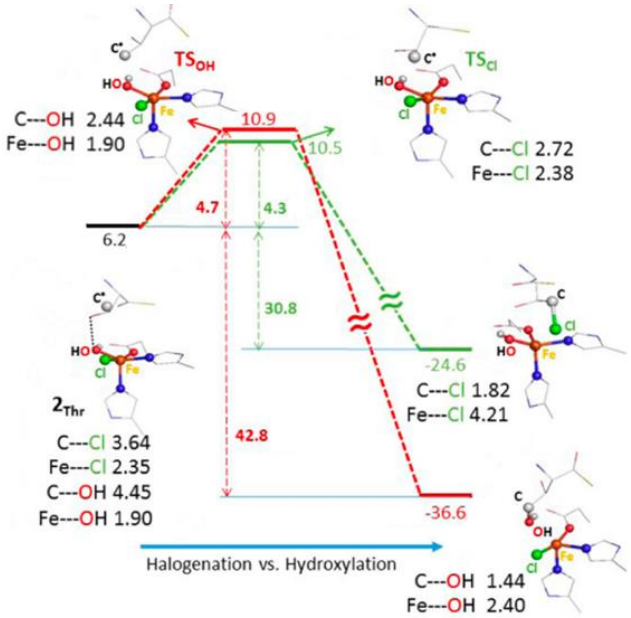


Figure 55. DFT model of the Cl-Fe^{III}-OH SyrB2 intermediate chlorination (green) vs hydroxylation (red) after HAA reaction coordinate through the π channel. Adapted from ref. [338]. Copyright 2017 American Chemical Society.

3.3.4 Correlation of enzyme active site intermediates to metallozeolite catalysts

The constraints of the protein on the first coordination sphere of the metal cofactor and the complex second-sphere interactions of their active site pockets with the substrate bring about their highly selective and difficult chemistry. These have some parallels in heterogeneous catalysts. Specifically, metallozeolites are known to both bind metals with a rigid first coordination sphere and have complex second-sphere interactions with substrates that dictate reactivity.[26, 100, 177] Thus, understanding of key intermediates in metalloenzymes gained from a combination of stopped-flow absorption spectroscopy, RFQ, rR, and MCD can provide insight into metallozeolite intermediates. This is enhanced by the site-selectivity of rR and VT MCD in probing an active site in a mixture.

In particular, the μ-η^2:η^2-peroxide dicopper(II) core seen in the coupled binuclear copper enzyme family is also observed in copper containing zeolites. In copper zeolite O_2 chemistry, this μ-η^2:η^2-peroxide dicopper(II) intermediate is a precursor that upon heating converts to the methane reactive mono-μ-oxo dicopper(II) active site (section 3.1.2.2).[188] Understanding this active site in biology can provide insight into how the μ-η^2:η^2-peroxide dicopper(II) converts to the mono-μ-oxo dicopper(II) core in zeolites, a phenomenon that is not well understood. It also indicates the potential reactivity of this μ-η^2:η^2-peroxide dicopper(II) precursor site in

zeolites. Monooxygenation of benzene at low temperature has been observed in Fe zeolites[162] but is a relatively uncultivated field in copper zeolites. The presence of a core that is known to monooxygenate phenol in copper biology could provide insight into whether copper zeolites can perform similar low temperature monooxygenation chemistry.

Additionally, the Fe^{IV}=O core seen in a variety of iron containing enzymes also plays an important role in zeolite catalysis. The α-O Fe^{IV}=O intermediate in iron zeolites is able to oxidize methane to methanol at room temperature (section 3.1.2.5).[17] The knowledge gained from understanding Fe^{IV}=O FMOs in these biological systems provides insight into the mechanism of HAA in α-O. Specifically, the lowest energy MCD band observed in α-O appears to have vibronic structure very similar to the lowest energy band in the Fe^{IV}=O intermediate of SyrB2. Just as analysis of this key ligand-field band in SyrB2 unlocked understanding of the HAA and rebound mechanisms occurring through specific d-orbital FMOs, similar insight in α-O could provide deeper insight into its mechanism of HAA and rebound that relates to differences in zeolite topology.

3.4 Electrocatalysis

In electrocatalysis, an external electric potential is used as the driving force, pushing reactions by shifting thermodynamic equilibria, and enabling thermally inaccessible reaction pathways and chemical intermediates.[10] Electron transfer and changes in oxidation state are central to this type of catalysts, which are consequently mostly based on transition metals. The systems make use of solid state electrodes of conducting material and a catalyst that is either in solution or supported on the electrodes.[340] UV-VIS-NIR excitations probe properties that are directly relevant to electrocatalysis, and it is therefore a very popular technique in their study. The measurement of high quality spectra can, however, be challenged by the multiphase nature of the systems and by the need for diffuse reflectance mode measurements. Moreover, while in thermal heterogeneous catalysis the surface is often most relevant and representative for the studied catalysis, in electrocatalysis electron exchange further below the surface may be relevant.[341] This is less accessible for UV-VIS-NIR radiation. The occurrence of preferential conduction paths may lead to non-uniformities and non-representative measurements.[342, 343] Also research into electrochemical batteries and sensors, both driven by similar processes as electrocatalysis, is well supported by UV-VIS-NIR absorption spectroscopy. The use of *operando* UV-VIS spectroscopy for (photo)electocatalysis was very recently reviewed by Mesa et al.[10] In this section we will therefore limit ourselves to some recent examples.

Despite decades of extensive research, the efficiency and stability of electrocatalytic processes still remain low.[344] Of particular interest is the identification of bottlenecks and contributions to overpotentials, the elucidation of the preferential redox couples, and the investigation of their reversibility. Ott et al. used *in situ* UV-VIS-NIR absorption spectroscopy to monitor the reversible redox behavior of cobalt species in metal-organic framework (MOF) UU-100(Co).[345] Under an applied potential of -1.50 V in DMF, freshly prepared UU-100(Co)(Co^{III}) undergoes reduction and new absorption bands at ~520 and 670 nm linked to Co^{I} appear (Figure 56 A). Reoxidation of the catalyst by stepping the potential back to -0.05 V results in a 670 nm bleach band and a slight redshift (~1-2 nm) of the 520 nm peak, which indicates the formation of Co^{II}. With repetitive electrochromic switching experiments and monitoring the absorbance changes at 520 and 670 nm, the reversibility of the Co^{I}/Co^{II} switching was shown. The switch between Co^{I} and Co^{III}, on the other hand, was found to be prohibited (Figure 56 B). A similar $Co^{I} \leftrightarrow Co^{II}$ system was investigated with *in situ* UV-VIS absorption spectroscopy by Song et al., who observed the same absorption bands (Figure 56 C).[346]

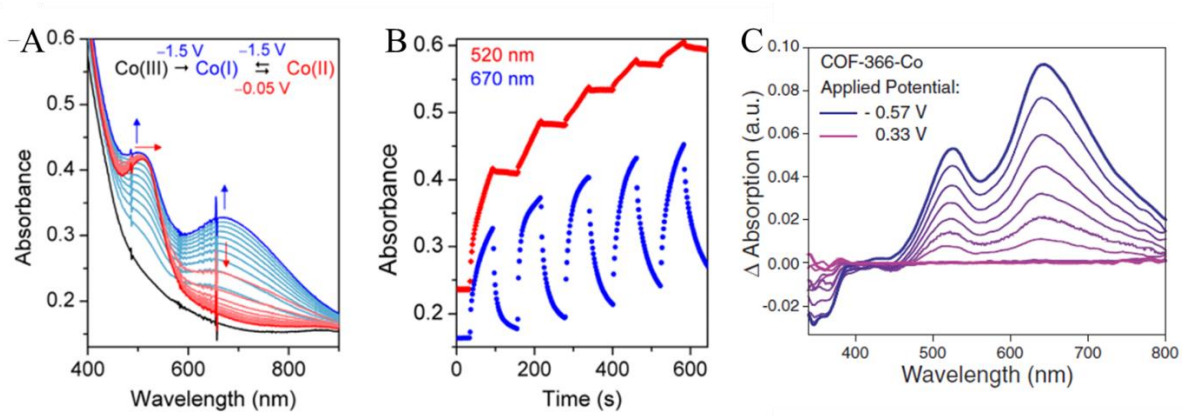


Figure 56. UV-VIS-NIR absorption data on **(A)** UU-100(Co) thin film switching between -1.5 and -0.05 V, and **(C)** COF-366-Co at steady-state at different applied potentials. **(B)** Optical Absorbance kinetics curve of the UU-100(Co) thin films measured at 520 and 670 nm by switching the potential from -0.05 to -1.5 V. Adapted from ref. [345, 346]. Copyrights 2019 American Chemical Society and 2015 American Association for the Advancement of Science.

The evolution of the UV-VIS-NIR absorption was followed in electrocatalytic water oxidation over an Ir-based catalyst.[347, 348] From the UV-VIS-NIR absorption spectra of IrO_x under applied potentials (Figure 57 A, left) and cyclic voltammetry (CV) of the IrO_x films, Carlota and coworkers identified three redox transitions and three redox states beyond the starting redox state as well as their characteristic absorption bands above the open-circuit potential (OCP).[347] By taking the spectroscopic handles identified by comparison to the absorption spectra of Ir mono-μ-oxo dimers containing Ir^{III}-Ir^{III}, Ir^{IV}- Ir^{IV}, Ir^{IV}- Ir^{V} and Ir^{V}- Ir^{V} moieties as a reference, the three redox transitions, at 600, 800 and 460 nm, are assigned to the sequential oxidation of Ir^{III}-Ir^{III} to Ir^{III}-Ir^{IV}, Ir^{IV}-Ir^{IV}, and Ir^{IV}-Ir^{V}, respectively.[349] With a model using the Lambert-Beer law and Gaussian distributions of concentration over potential, the absorption spectra were deconvoluted and concentrations of each redox state at different potentials were derived (Figure 57 B). Analysis of the bias-dependent optical signals reveals the change of these redox species with increasing applied potential from an OER pre-catalytic Ir^{III} state to an OER active Ir^{IV}-containing state. The kinetics of the redox states in IrO_x were further analyzed through the decay of the absorption bands centered at 600, 800 and 460 nm, respectively. To access the OER reaction kinetics of the active redox state as a function of its concentration, the decay was measured after turning off the applied potential. The decay is attributed to the depletion of Ir^{IV}. Its faster decay after turning off at more positive applied potentials implies a greater reactivity of this state at increasing potentials (Figure 57 C). Such spectral evolution is also observed in the case of an Ir dimeric molecular ($Ir_{molecular}$) catalyst (Figure 57 A, right).[348] The optical signals related to the three redox transitions in IrO_x and $Ir_{molecular}$ have broadly similar features. The concentration distributions in $Ir_{molecular}$ shift anodically by ~100 mV with respect to IrO_x for all the three redox transitions. However, in contrast with IrO_x, $Ir_{molecular}$ exhibits potential independent OER reaction kinetics (Figure 57 C). The difference between the molecular catalyst and the heterogeneous oxide film in terms of OER kinetics is attributed to the lack of co-operative effects in the $Ir_{molecular}$ system with isolated Ir centers.

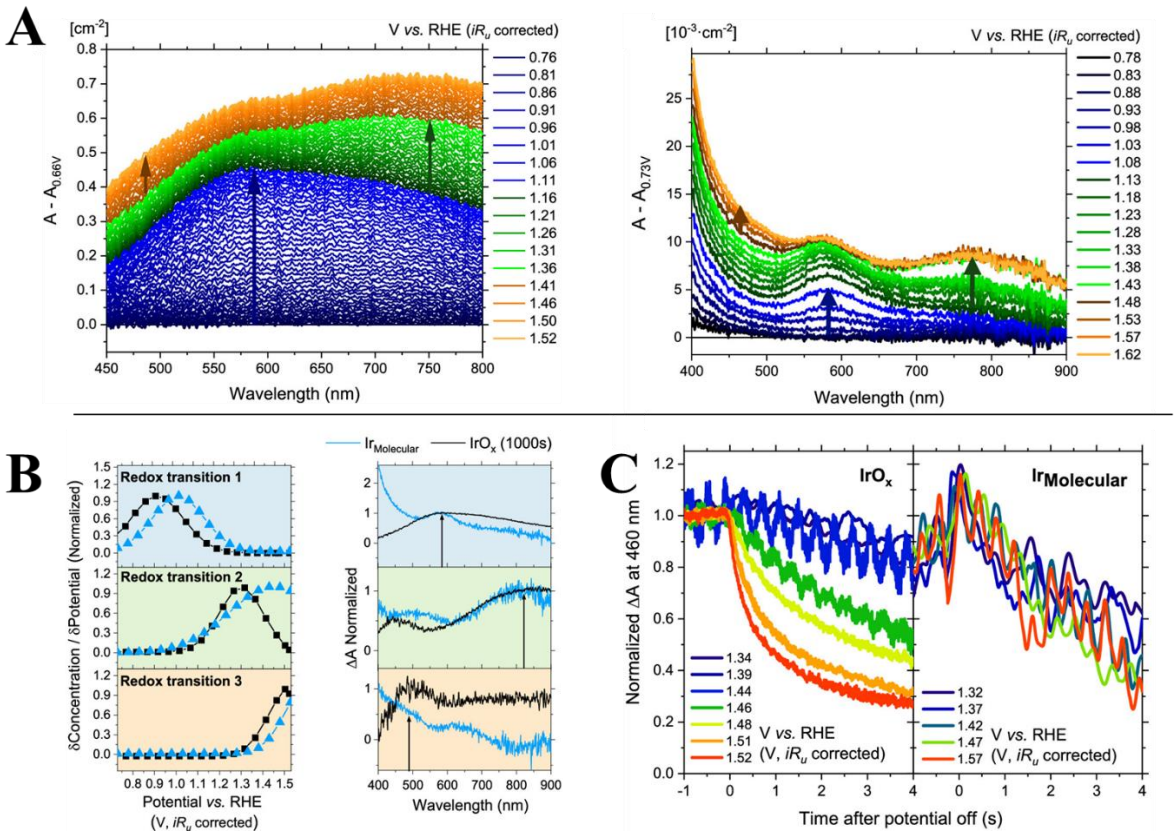


Figure 57. (A) Absorption changes of (right) IrO_x and (left) $Ir_{molecular}$ on mesoporous indium tin oxide upon applying an oxidative potential in 0.1 M $HClO_4$ aqueous solution at pH 1.2. **(B)** Normalized deconvolution of the spectroelectrochemical data of $Ir_{molecular}$ and IrO_x. **(C)** Absorption decay after turning the potential off. Adapted from refs. [347-349]. Copyrights 2021 and 2022 American Chemical Society.

Zachary et al. used *operando* UV-VIS-NIR absorption spectroscopy to elucidate redox behavior of pure Ni and Fe-doped NiFe catalysts for OER.[350] When the applied potential increases, both Ni and NiFe catalysts develop a spectroscopic feature that corresponds to the band-edge absorption due to the decrease of band gaps of both the Ni and NiFe catalysts upon proton-coupled oxidation (Figure 58 B, D). The similar absorption onsets of Ni and NiFe systems (~1.5 eV) are consistent with the calculated band gaps. Figure 58 A, C illustrates the absorption at 2.5 eV as a function of applied potential, which demonstrates a direct correlation between the optical and redox changes in the catalyst. In the pure Ni catalyst system, the UV-VIS-NIR absorbance depends on the applied potential before the onset of oxygen evolution reaction (OER) activity. According to first-principles calculations, the Ni is oxidized from Ni^{2+} to Ni^{3+} followed by further oxidation to a mixed $Ni^{3+/4+}$ state at a potential that coincidences with the onset of OER activity and both $Ni^{3+}$and Ni^{4+}contribute to the conduction band minimum (CBM) in the Ni catalyst. In contrast, absorbance changes are negligible in a NiFe catalyst before the onset of OER activity due to the formation of significant amount of Fe^{4+}, which is revealed as the dominant species for CBM in a NiFe catalyst. Within the catalytic wave, absorbance of both Ni and NiFe catalysts are independent of the applied potential because rapid water oxidation impedes the formation of species with higher oxidation states given these species have neither significant population nor lifetime.

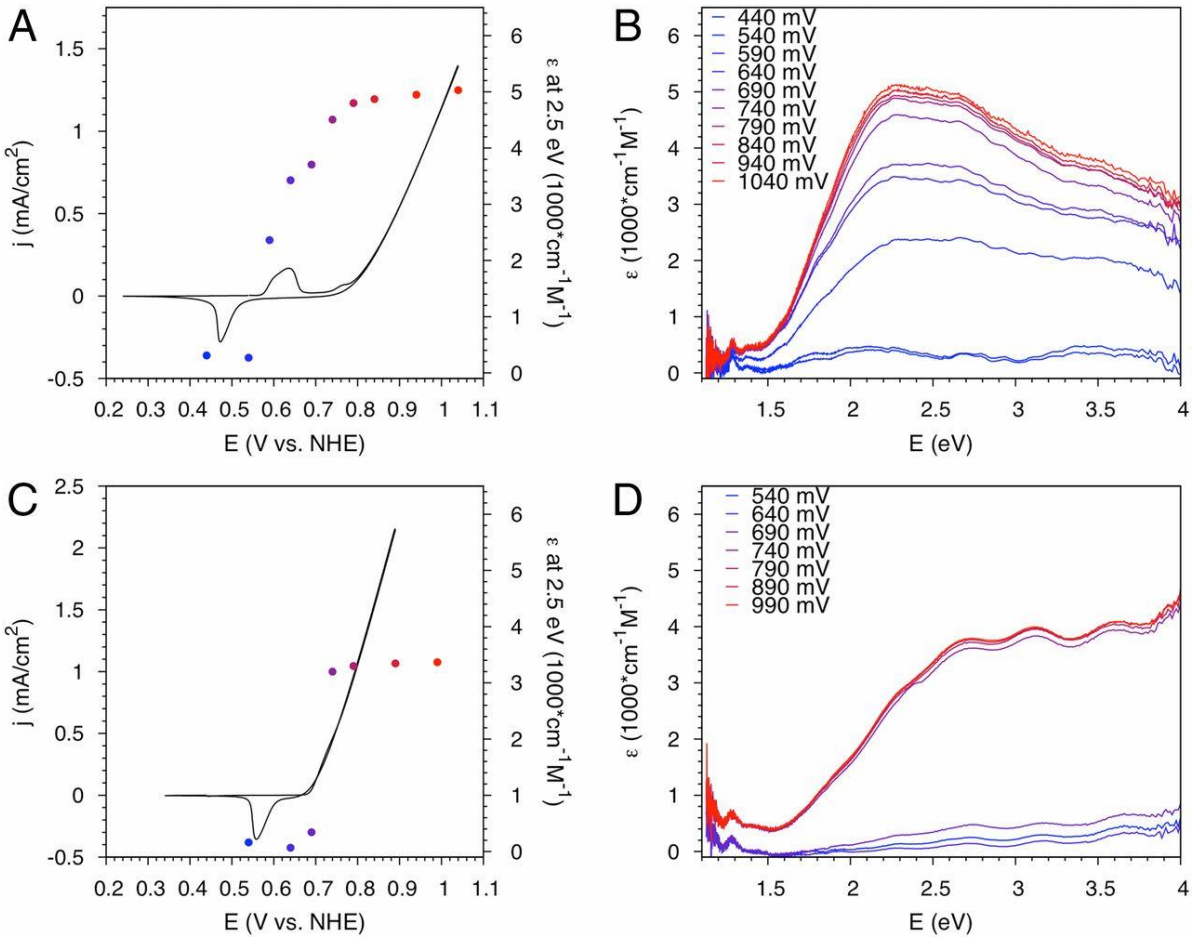


Figure 58. Cyclic voltammograms (CVs) (Left) and UV-VIS-NIR absorption spectra (Right) of the **(A) & (B)** pure Ni and **(C) & (D)** 25% Fe films. Data points in the CVs correspond to the absorbance at 2.5 eV with the same color coding as in the spectra. Adapted from ref. [341]. Copyright 2017 National Academy of Sciences.

By performing *in situ* UV-VIS-NIR absorption spectroscopy with varying sample thickness, one can differentiate between the surface and bulk reaction process occurring over a catalyst. This is exemplified by Sacha et al. in the case of NiO_x catalyst in water oxidation. Relationships between film thickness and UV-VIS-NIR absorbance were obtained in pre-catalytic and catalytic conditions.[341] Increasing film thickness results in greater absorption at potentials prior to the onset of the OER, indicating that pre-catalytic oxidation of NiO_x to NiOOH in alkaline electrolyte is a bulk oxidation process (Figure 59 A). In contrast, absorption on the electrode during the catalytic process is unaffected by the film thickness, suggesting that the intermediate species that formed during water oxidation catalysis are limited to the near surface of the catalyst (Figure 59 B).

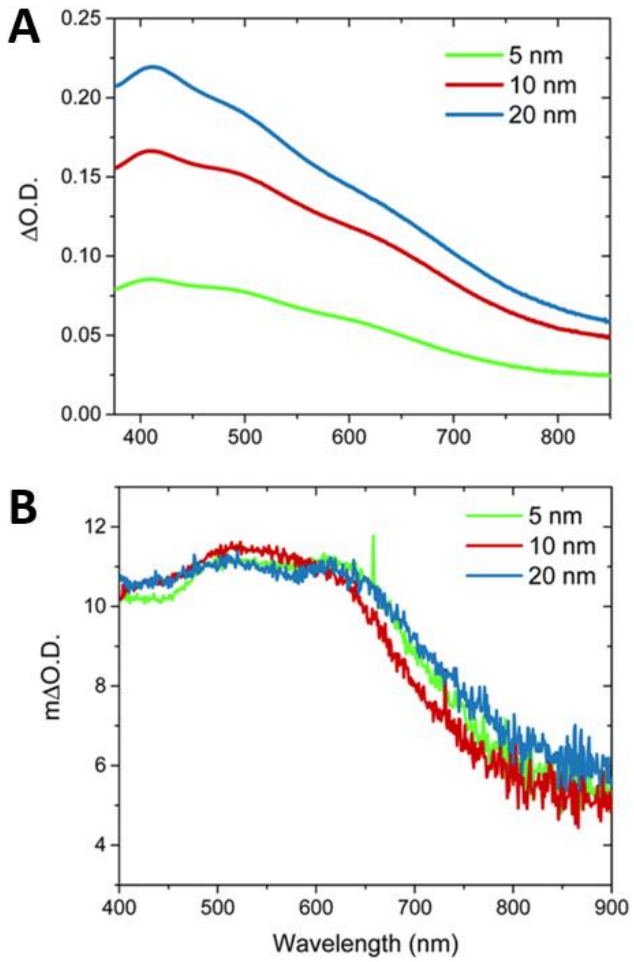


Figure 59. Change in UV-VIS-NIR absorption spectra of each sample; **(A)** after activation with respect to the absorbance before activation, and **(B)** after catalysis onset with respect to the absorbance before catalytic process. Adapted from ref. [341]. Copyright 2020 Royal Society of Chemistry.

3.5 Photocatalysis

Photocatalysis harvests photon energy for chemical transformations. It has been widely investigated for applications including hydrogen evolution, pollutant degradation, organic synthesis, and biomass valorization, and is found in enzymatic catalysis.[351-355] In general, photocatalysis begins with light absorption, which transforms the photocatalyst to an excited state. Most commonly electronic excitations are leveraged using abundantly available solar UV-VIS-NIR range radiation, with the catalytic valorisation of NIR range excitations being more cumbersome.[356] The excited photocatalyst then activates the reactant directly or catalyzes the generation of active species for indirect reactant conversion.[354] The catalyst may be heterogeneous, homogeneous or enzymatic, preferably in a form that maximizes the potential for light harvesting. Currently, the efficiencies of most photocatalytic systems are too low for industrial application, and further material development backed by deeper fundamental understanding is needed.

UV-VIS-NIR range spectroscopies are highly relevant characterization tools in photocatalysis, given the intrinsic similarity between the spectroscopically probed electronic transitions and the catalytically relevant excitation. Moreover the technique is easily matched with *in situ* and *operando* conditions.[10] *In situ* and *operando* spectroscopies in general for photocatalysis were

very recently reviewed by Hamoud et al.[39] Here we limit the section to representative demonstrations of UV-VIS-NIR absorption measurements for *in situ* photocatalysis studies, covering the broad timescales that are relevant.

Light absorption, charge separation, and transfer of charges to the reaction centers are elementary steps in photocatalysis that mainly take place in fs-s time scales. Commonly, but not exclusively, semiconductor materials are used where an electron from the valence band (VB) is excited into the conduction band (CB) leaving an electron hole in the VB. Alternatively molecular reactive electronic excited states may be generated. Active species generated in these ultrafast processes, including electron-hole pairs and photo-excited chemicals – mainly radical intermediates – are typefied by their highly reactive features and short lifetimes. These photo-induced short-lived excited states can cause characteristic optical absorption features in the UV-VIS-NIR spectral range. With the help of pump lasers, UV-VIS-NIR absorption spectroscopy is used to study photo-induced processes *in situ* down to the femtosecond regime (see also technical details in section 2.2.1.3 and Figure 9),[62] in a technique known as ultrafast UV-VIS-NIR absorption spectroscopy or transient absorption (TA) spectroscopy. In addition to the ultrafast monitoring of the dynamics of excited species, electronic and structural changes at the catalyst surface can be monitored in combination with reaction progress over hours or days under different conditions providing mechanistic insight.[357-359]

3.5.1 Transient absorption to monitor ultrafast processes (fs-to-s time scale)

The TA spectroscopy measurement is accomplished by the pump-probe technique, wherein a fraction of the molecules are first promoted to an electronically excited state using a pump pulse. A probe pulse is then sent through the sample with a time delay (τ) relative to the pump pulse. The resulting TA signals are typically presented as the difference between the absorbance of the excited and ground state samples as expressed by eq 17.

$$\Delta A(\lambda, \tau) = A(\lambda, \tau) - A(\lambda)_{ground\ state} \quad (17)$$

where $A(\lambda, \tau)$ and $A(\lambda)_{ground\ state}$ are respectively the absorbance of the excited state at delay τ and of the ground state. In general, a TA spectrum contains contributions from ground state bleach (GSB, negative), excited state absorption (ESA, positive) and stimulated emission (SE, negative) (Figure 60). All these contributions can be tracked for catalytic insight,[360] although mostly the SE and bleach bands are used in the UV-VIS-NIR range. ESA bands can be difficult to resolve, and may hinder the tracking of the SE and bleach bands.[361] ESA bands can also be tracked by their vibrational excitations in the IR.[362, 363]

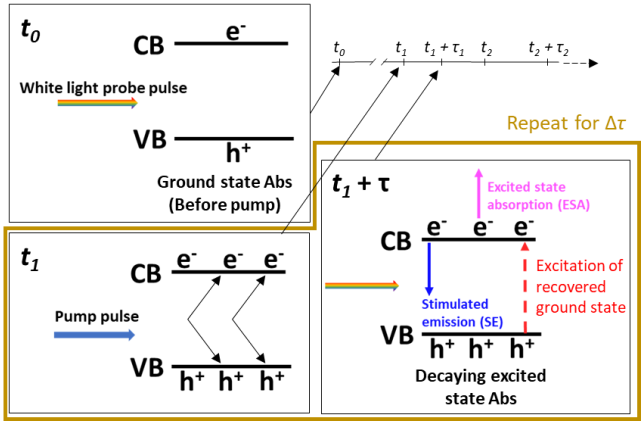


Figure 60. Schematic of a pump-probe transient absorption experiment. At t_0 the ground state absorption spectrum is measured, before applying a pump pulse. This is used as the reference spectrum $A(\lambda)_{ground\ state}$ in eq 17. At a later

time t_1, the probe pulse is applied selectively exciting electrons from the ground state to an excited state (in this case from VB to CB). Then with delay τ, the absorption spectrum is measured again to get $A(\lambda,\tau)$ of eq 17. These pump-probe sequences are repeated for different τ to produce a time series of TA spectra.

TA spectroscopy was performed to reveal the mechanism of ligand-controlled performance of cadmium sulfide (CdS) quantum dots (QDs) for the conversion of lignin.[364] Electron decay processes of CdS QDs with different ligands were observed after applying laser pulses of 400 nm. The ligands CdS-C3, CdS-C6, and CdS-C9 are schematically illustrated in Figure 61 A. They were monitored over ~2.4 ns after excitation. The decay of photogenerated electrons was tracked based on the ~460 nm bleaching band, which corresponds to the excitation of CdS QDs from the ground to the first excited state (Figure 61 B). Figure 61 C shows CdS-Cx QDs decay almost independently of ligand length, indicating that intrinsic decay is largely responsible for the recovery of QDs. However, recovery kinetics depend strongly on ligand length in the presence of a lignin model compound, 2-phenoxy-1-phenylethanol (PPol) (Figure 61 D). Increasing electron decay rates are observed with decreasing ligand lengths, which corresponds to the catalytic efficiency of CdS QDs for lignin conversion, i.e., CdS-C3 > CdS-C6 > CdS-C9. The electron decay kinetic curves were fitted into a multiexponential equation, which indicates three electron decay processes, a fast process (<50 ps), a slow process (~100 ps), and a nanosecond range process (2 - 5 ns). The slow and nanosecond processes were assigned to the intrinsic decay of CdS QDs while the fast process was attributed to the electron transfer from the QDs to PPol.[364] The weighted contribution of the corresponding decay process indicates that the electron transfer from QDs to PPol dominates the decay kinetics for CdS-C3 and CdS-C6 QDs in the presence of PPol. The TA spectroscopy not only illustrates the electron decay pathways in CdS-QDs with different ligands but also demonstrates that surface ligands control the electron transfer process.

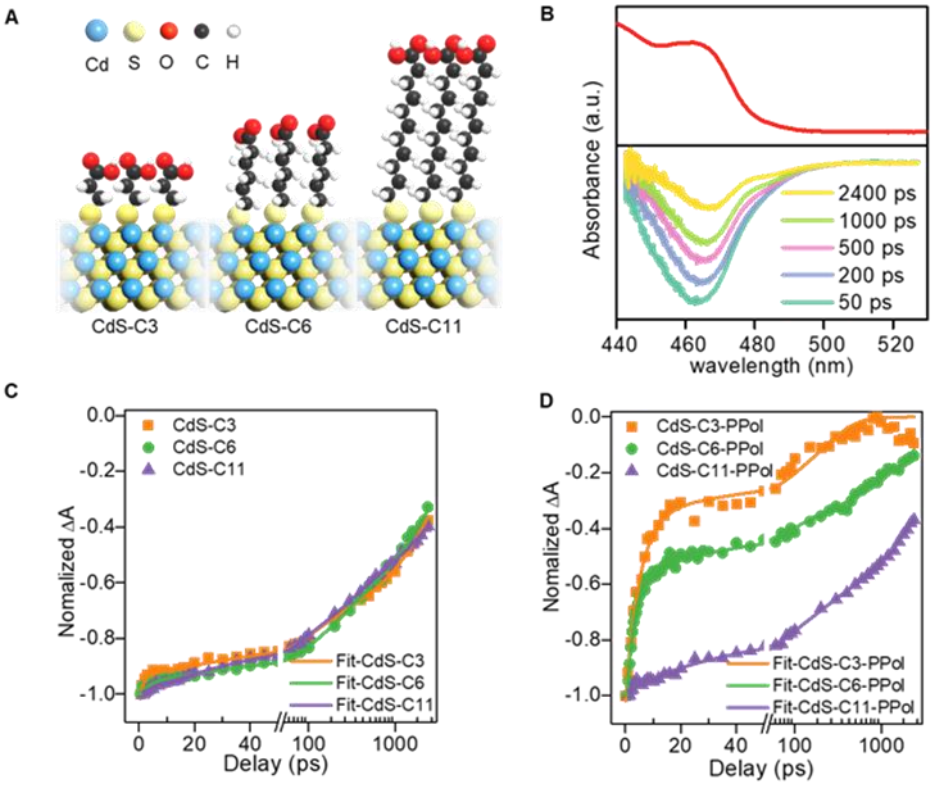


Figure 61. (A) Schematic illustration of CdS-C3, CdS-C6, and CdS-C9. **(B)** The steady-state absorption spectrum of CdS-C6 (red line, upper) and transient absorption spectra of CdS-C6 after 400 nm excitation (bottom). TA

dynamics probed at 460 nm of CdS-Cx QDs in the **(C)** absence and **(D)** presence of lignin model compound PPol. Reproduced from ref. [364]. Copyright 2019 American Chemical Society.

Charge dynamics resolved by TA have tracked the mechanism of photocatalytic CO_2 reduction using a Ni^{II} complex as catalyst, a Ru^{II} complex as photosensitizer, and 1,3-dimethyl-2-phenyl-2,3-dihydro-1Hbenzo[d]imidazole (BIH) as the electron donor.[365, 366] Upon laser excitation at 440 nm, the bleaching signal of the ground-state Ru^{II} appears at 446 nm and the absorption attenuation signal of the excited-state $*Ru^{II}$ at 365 nm. The addition of BIH gives a new band (510 nm) indicating the formation of Ru^{I} through the quenching of the excited $*Ru^{II}$ state with BIH. Upon further addition of Ni^{II}, the decay of the Ru^{I} signal is accelerated. The following reaction pathway was derived: Ru^{II} is excited into $*Ru^{II}$ upon irradiation, BIH quenches $*Ru^{II}$ to form Ru^{I}, and then Ru^{I} turns back into Ru^{II} by donating an electron to Ni^{II}, converting it into Ni^{I}. Other *in situ* spectroscopic techniques, including time-resolved XAS, DRIFTS, and *operando* surface-enhanced Raman spectroscopy as well as theoretical modelling demonstrated that the reduced Ni^{I} is the catalytically active species for CO_2 reduction.[365, 366]

The lifetime of photogenerated charge carriers can be monitored by TA to evaluate the electron transfer rate of different processes.[367, 368] An informative example is the photocatalytic degradation of intelligent ink, with glycerol and resazurin as major components. TiO_2 in the anatase phase is a ~30 times more efficient catalyst than the rutile phase for this degradation. The phase-dependent lifetimes of electrons and holes in these systems were investigated using TA,[368] using absorption peaks at 900 nm (photogenerated electrons) and 550 nm (photogenerated holes) to track the decay kinetics. TA spectra in presence of glycerol, resazurin dye, and intelligent ink, were recorded separately (Figure 62 A, B). Fitting of the electron decay indicates the addition of glycerol for anatase results in long-lived excited electrons with a lifetime in the second range. For rutile, on the other hand, the excited electron was short-lived with a lifetime in the millisecond range (Figure 62 C, D). Comparing the phase-dependent lifetimes of electrons in the presence of different reactants, the authors proposed that the lower activity of rutile is due to the deficiency of its photogenerated holes to efficiently drive glycerol oxidation.[368]

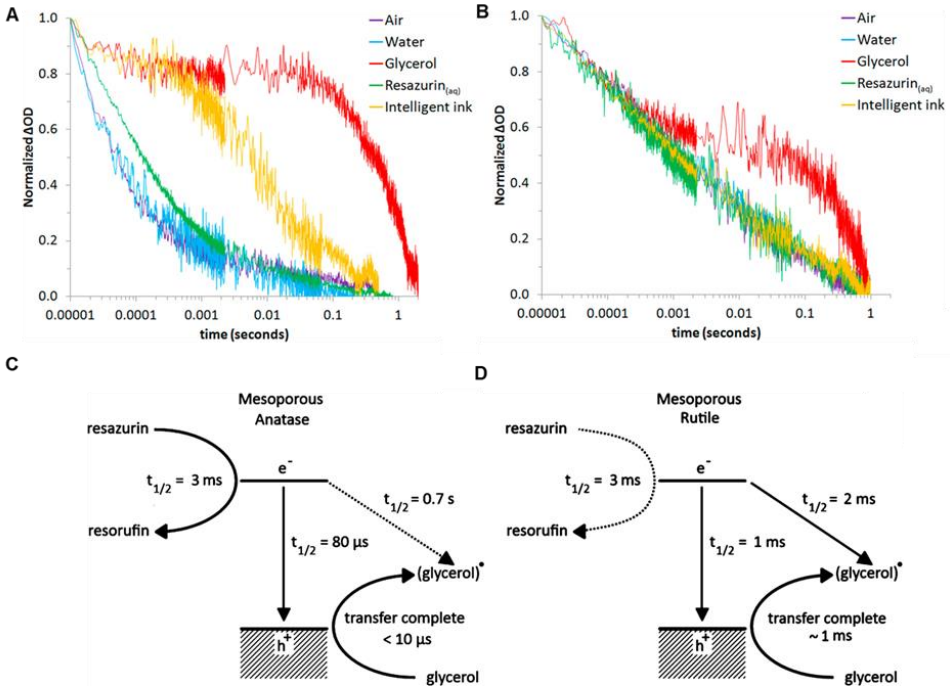


Figure 62. The normalized transient decays from TA for **(A)** anatase and **(B)** rutile probed at 900 nm. Summary of different time scales from TA dynamics of the photocatalytic processes with **(C)** anatase and **(D)** rutile. Reproduced from ref. [368]. Copyright 2015 American Chemical Society.

Another example is the derivation of the Z-scheme structure of black/red phosphorus (BP/RP) hetero-phase junction photocatalysts.[369, 370] Excitation of BP/RP induces a broad absorption band centered at 550 nm linked to surface-trapped electrons. Its decay time profile was fitted by a function with two exponentials indicating the lifetime of electrons trapped at shallow (τ_1) and deep sites (τ_2). The decay lifetimes decreased from pure RP (τ_1: 15.9 ps; τ_2: 315.2 ps) to BP/RP (τ_1: 6.5 ps; τ_1: 166.2 ps) indicating interfacial electron transfer. With a similar methodology, the Z-scheme structure for TiO_2/Ce_2S_3 was clarified using the decay of a 645 nm absorption band.[369]

The wavelength of TA curves can provide information regarding the evolution/decay of various intermediate species involved in chemical reactions.[371-373] Using the TA spectra, the dynamics of three distinct types of excitons of CdSe/CdS-Pt, 1D CdS nanorods (NRs) with a CdSe "seed" inside and a Pt "dot" at one end, were examined. These excitons are classified by their localized area, which can be differentiated by their absorption peak wavelengths. More specifically, the peak at ~540 nm is attributed to excitons localized in the CdSe seed (X3), the profound peak at ~ 450 nm is attributed to excitons localized in the CdS rod (X1), while the small shoulder at 470 nm is attributed to both excitons localized in the CdS bulb region surrounding the CdSe seed (X2) and in the CdSe seed (X3) (Figure 63).[371, 372] Fitting these TA spectra to multiexponential functions reveals the formation probabilities and half-lives of different excitons, i.e., ~46%, 22.5 ns for excitons localized in the CdS rod (X1), 7%, 32.1 ns for excitons localized in CdS bulb region surrounding the CdSe seed (X2), and 47%, 8.3 ns for excitons localized in the CdSe seed (X3).[372] These distinct features were used to study the photocatalytic H_2 generation over CdSe/CdS-Pt and CdS-Pt NRs and the electron-donor dependence of these catalysts.[371] When weakly reductive MeOH is used as electron donor, the trapped-hole transfer rate in CdS NRs is slower than that of the CdSe core. On the other hand, sulfite as electron donor can provide enough driving force for trapped holes in CdS NRs to transfer. Hole transfer from the CdSe core is more difficult since core-confined holes are harder to access by the electron donor.[371] These trapped holes in distinct spatial locations, which were characterized and monitored by TA spectra, result in different activity depending on the electron acceptors.

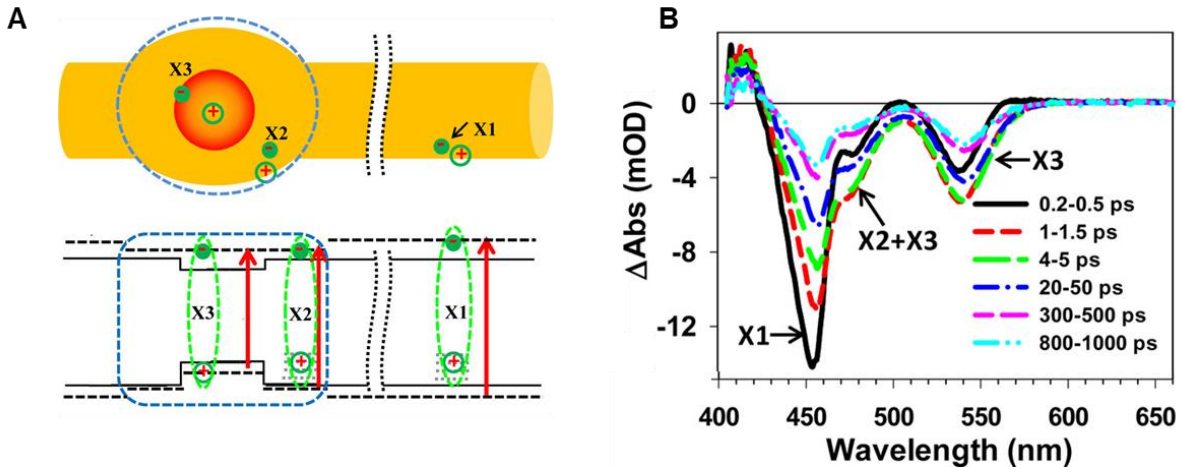


Figure 63. (A) Schematic illustration of three distinct exciton states (X1, X2, and X3) in CdSe/CdS-Pt nanocrystals (upper panel) and their corresponding energy level diagram (lower panel). X1, X2, and X3 refer to excitons localized in the CdS rod, the CdS bulb region surrounding the CdSe seed, and the CdSe seed, respectively. Excitation energy decreases in the order X1 > X2 >X3. **(B)** TA spectra after 400 nm excitation for 0.2 to 1 000 ps. Reproduced from refs. [371, 372]. Copyright 2013 American Chemical Society.

TA can also be used to track chemical reactions that take place at ultra-fast speeds. Phenothiazine (PTZ) can be used as a hole acceptor to facilitate H_2 generation from water splitting through the efficient extraction of photo-generated holes.[374] The monitoring of PTZ oxidation is possible with the well-separated characteristic absorptions of PTZ^+ (~520 nm) and the bleaching band of CdS NRs (~450 nm). TA in the 500-600 nm spectral range, which includes the signal of the trapped hole, decays with a time constant of ~3.6 ns. This feature is accompanied by the appearance of the PTZ^+ absorption band at ~520 nm. These spectral features are direct evidence of the trapped hole transfer from CdS NRs to PTZ molecules. Fitting TA kinetics with multiexponential curves shows the trapped holes are extracted by PTZ (half-life = 3.8 ± 1.7 ns), leading to the formation of long-lived charge-separated states (CdS^- PTZ^+, half-life = 310 ± 50 ns). A high extraction efficiency of 94.7 ± 9.0% was achieved, contributing to the much faster hole transfer rates to PTZ than the slow conduction band electron–trapped hole recombination (half lifetime of 67 ± 1 ns). These TA results illustrate that the key to efficient photocatalytic H_2 evolution over CdS nanocrystals is the efficient extraction of trapped holes to prevent electron-hole recombination.

3.5.2 Time-course spectra to monitor reaction changes (s-to-day time scale)

In addition to monitoring the dynamics of excited species in an ultrafast way, *in situ*/*operando* UV-VIS-NIR absorption spectroscopy can also be employed to track the change of reaction systems parallel to the whole reaction course over hours or days under different conditions. Copper on porous titanium dioxide aerogel (Cu/TiO_2) exhibit high efficiency in photocatalytic CO_2 reduction to CO in an aqueous solution. Interestingly, the CO_2 reduction rate improves in the presence of O_2. As the O_2 content increases, CO production reaches a maximum at 0.5 vol%, while the competing H_2 evolution is limited.[357] *In situ* UV-VIS absorption spectroscopy was applied to monitor changes in Cu/TiO_2 after different irradiation times in the presence and the absence of O_2. Before irradiation, Cu/TiO_2 is characterized by the band gap of TiO_2 at 350 nm and several less defined broad bands between 400 and 900 nm, which are ascribed to charge transfer transitions in TiO_2 and CuO (below 450 nm) and d-d transitions of Cu^{II} (600-900 nm). This indicates that Cu^{II} is the main species in fresh Cu/TiO_2. The *in situ* UV-VIS absorption spectra were expressed relative to fresh Cu/TiO_2. A band with a maximum of 380 nm, assigned to Cu^I, is observed when the catalyst is exposed to 100% CO_2 after 1 min irradiation (Figure 64 A). Its intensity increases within the first 2 min of irradiation, and then disappears. After exposure to light for 10 min, a sharp minimum at ~580 nm caused by the formation of metallic Cu is observed. Cu^0 and Cu^I species are also formed in presence of O_2 with concentrations of 0.1 and 0.5 vol % (Figure 64 B, C).[357] The kinetics of Cu^{II} reduction and accordingly the fraction of different Cu species are affected by O_2. Temporal changes in the UV-VIS absorption spectra suggested O_2 leads to slower Cu^{II} reduction to Cu^I and Cu^0 as well as a lower Cu^0 fraction. The highest rate of CO formation is achieved at the beginning of the photocatalytic process, *i.e.*, within the first 30 min regardless of the O_2 content. UV-VIS absorption spectra indicate Cu^I is present at this time and is therefore responsible for CO_2 photoreduction. On the other hand, Cu^0 is the main species after 30 min, the amount of CO formed between 30 min and 20 h is lower than that formed between 0 and 30 min, indicating a low intrinsic activity of Cu^0. At O_2 concentrations higher than 0.5 vol%, Cu^{II} cannot be reduced to Cu^I, thus resulting

in lower activity. Therefore, Cu^{I} was proposed to be the active species of Cu/TiO_2 for CO_2 photoreduction to CO (Figure 64 D).

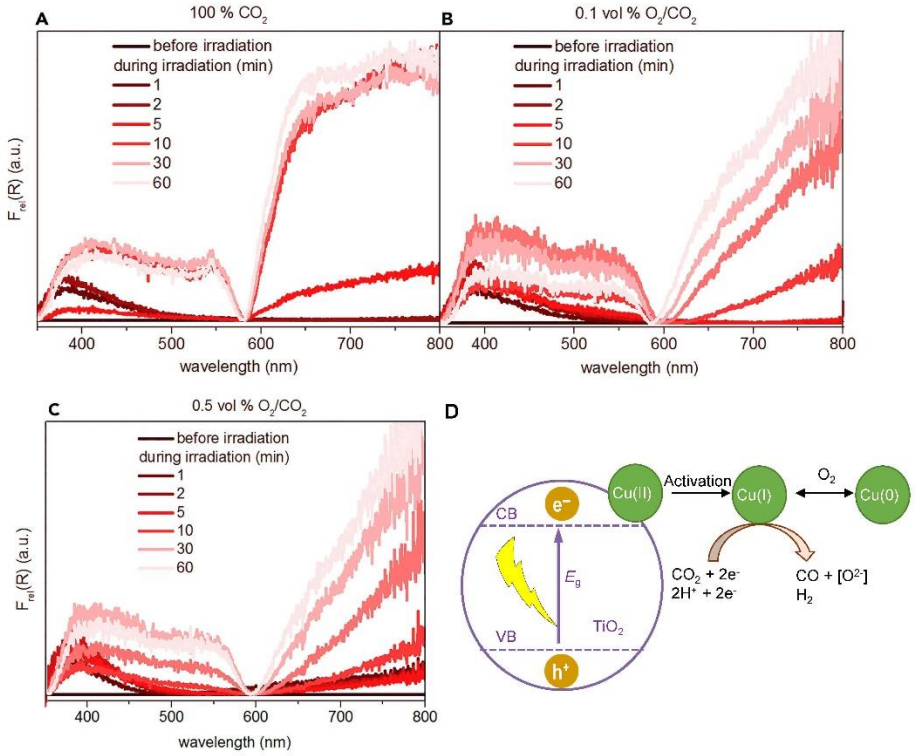


Figure 64. UV-VIS absorption spectra (Kubelka-Munk) of Cu/TiO_2 after different irradiation times in **(A)** 100% CO_2, **(B)** 0.1 vol % O_2/CO_2, and **(C)** 0.5 vol % O_2/CO_2. **(D)** Proposed mechanism for photocatalytic conversion of CO_2 over Cu/TiO_2 and the nature of active copper species. Reproduced from ref. [357]. Copyright 2019 Cell Press.

In situ UV-VIS DRS was conducted to gain mechanistic insight into photocatalytic CO_2 reduction on a covalent organic framework (COF) photocatalyst, consisting of a photoactive two-dimensional triazine COF and a Re-based molecular catalyst (Re-COF) (Figure 65 A).[358] An induction period of about 15 min is observed over the Re-COF (Figure 65 B). As shown in Figure 65 C, in the initial 15 min (denoted Step I), prominent absorption in the 550 - 800 nm region that resembles the broad absorption of the intramolecular charge transfer (ICT) band of triazine increases, accompanied by decreasing absorption at 400 - 500 nm with an isosbestic point at 539 nm. This indicates the formation of the excited ICT state. Similar spectra are observed in the absence of CO_2. The spectral evolution during the first 15 min can thus be attributed to the accumulation of charge separation (CS) state, before catalysis initiates (Step I, Figure 65 A). Following Step I, the absorption at 550 - 800 nm decreases significantly (Figure 65 C, denoted Step II), while the absorption at <430 nm grows with a new isosbestic point at 430 nm. The distinct features of Step I and Step II suggest the formation of different intermediate species. Indeed, step II evolution is negligible in the system without CO_2 or when Re-COF is replaced by COF, indicating that the newly formed intermediate species is associated with CO_2 and Re molecules. The spectra remain almost constant in Step III, suggesting that the system reaches equilibrium after Step II, and this is consistent with the time window for steady generation of CO (Figure 65 B).[358]

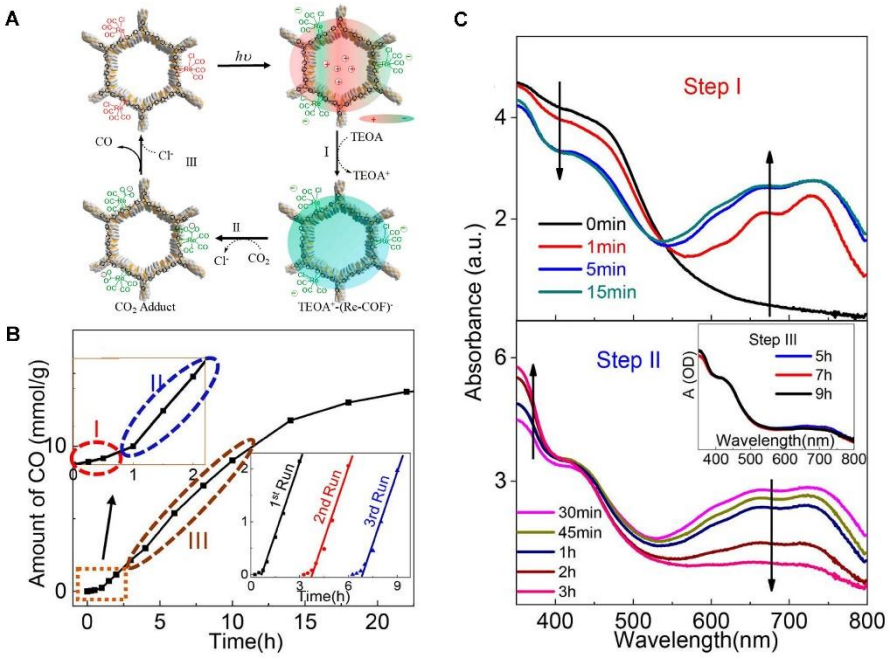


Figure 65. (A) Schematic illustration of Re-COF structure and the proposed catalytic mechanism for CO_2 reduction over Re-COF. **(B)** Production of CO as a function of time from the photocatalytic conversion of CO_2 over Re-COF. **(C)** The *in situ* DRS UV–VIS absorption spectra of Re-COF under photocatalytic conditions within 15 min (upper panel) and 3 h (lower panel). The inset in lower panel shows the *in situ* spectra collected from 5 to 9 h. Reproduced from ref. [358]. Copyright 2018 American Chemical Society.

A fully automated triple combination of *in situ* illumination, UV-VIS-NIR absorption spectroscopy, and NMR spectroscopy enabled the simultaneous and time-resolved detection of paramagnetic and diamagnetic species to study the photoreduction of aryl halides to aryls with *N*,*N*-bis(2,6-diisopropylphenyl)-perylene-3,4,9,10-bisdicarboximide (PDI) as photocatalyst.[277] UV-VIS-NIR absorption spectroscopy is a powerful tool for the detection of stable radicals, which are often not accessible by NMR spectroscopy. After a few minutes of illumination, the absorption bands of $PDI^{\bullet-}$ at 698 and 794 nm grow in while the absorbance bands of PDI at 455 and 482 nm steadily decrease, enabling a semiquantitative reaction profile for the evolution of $PDI^{\bullet-}$. Complementary to the UV-VIS absorption spectra, NMR spectra give full quantitative information about diamagnetic reactants and products in the reaction.

The coupled UV-VIS absorption, EPR, and IR spectroscopies were employed for mechanistic studies of a copper-iron system for photocatalytic H_2 generation from water.[359] The copper-iron system contains a heteroleptic copper photosensitizer $[Cu(P\wedge P)(N\wedge N)]^+$, which includes bidentate P∧P (Xantphos) and N∧N (2,9-dimethyl-4,7-diphenyl-1,10-phenanthroline) chelate ligands, and an iron-based water reduction catalyst. The role of the copper photosensitizer $[Cu(P\wedge P)(N\wedge N)]^+$, which can be oxidized or reduced after photoexcitation, in the copper-iron system was investigated. $[Cu(P\wedge P)(N\wedge N)]^+$ exhibits a UV-VIS adsorption feature at 390 nm, which decreases after several redox cycles, while a new band at 475 nm assigned to $[Cu(N\wedge N)_2]^+$ arises. UV-VIS absorption spectroscopy reveals the *in situ* change of the original heteroleptic photosensitizer toward a $[Cu(N\wedge N)_2]^+$ species during catalysis, proving the presence of the oxidative cycle. EPR spectroscopy shows the presence of the reductive cycle, and *in situ* FTIR spectroscopy provided evidence for the formation of a catalytic diiron intermediate.

4. Outlook and Conclusions

In situ UV-VIS-NIR absorption spectroscopy is a simple and cheap technique to study catalysts and catalytic reactions. It is in most cases non-destructive and non-intrusive (with exceptions in homogeneous and photocatalysis). The spectra can give information on individual transition metal ions, on nanoparticles of TMI oxides and metals, and on organic molecules, radicals and ions. It is well suited for *in situ* and *operando* measurements in combination with specialized cells, making use of fiber optics, diffuse reflectance spectroscopy, ultrafast laser pulses, and microscopy. This enables its measurement in various methodologies including stopped flow experiments, transient response and step response experiments, transient absorption experiments, electrochemical conditions, and at variable temperatures and magnetic fields. These methodologies give access to a variety of catalytically relevant data including electronic structure and reaction kinetics. Data processing of the absorption spectra is necessary to extract band gap energies and to quantitatively measure concentrations and conversions, and is widely adopted. It is however important to keep track of the sensitivities and assumptions of these methods, particularly for Tauc/Cody plots and the processing of diffuse reflectance data with the Kubelka-Munk formula.

The UV-VIS-NIR range has both its limitations and advantages for *in situ* use. Heterogeneous catalysis is usually carried out well above room temperature. The absorption bands are sensitive to elevated temperatures with absorption bands broadening and shifting through vibronic coupling. If the bands are weak, they may almost completely disappear in the background at high temperature. Such bands are of no use in e.g. kinetic or structural analysis. Low temperatures are a challenge too due to icing and physical obstructions such as bubbling and separation of phases in liquid environment. In homogeneous catalysis solvents should also not have absorption bands in the UV-VIS-NIR range. In heterogeneous catalysis black supports such as graphene and carbon black prevent UV-VIS-NIR absorption measurements. Finally, the UV-VIS-NIR induced transitions are assumed not to be destructive for the catalyst nor interfering with the processes under study. This is not always the case, most evidently for photocatalysis, but also for homogeneous catalysis in general. We see that in theory the potential of UV-VIS-NIR absorption spectroscopy at varied conditions offers great opportunities in better understanding catalysts' structures and electronic properties with relatively cheap and accessible setups, and that such measurements could alleviate the main drawback of poor spectral resolution. However such measurements remain scarce probably due to practical obstacles and challenges in data analysis.

UV-VIS-NIR absorption offers a window into electronic structure with direct relevance to reactivity and catalysis. Nevertheless this potential remains underused in catalysis research, especially on complex heterogeneous catalysts and on homogeneous catalysts, despite the popular measurement of UV-VIS-NIR absorption spectra on these systems. Exceptions are the examples given on copper and iron exchanged zeolites. The assignment of spectroscopic bands to their electronic transitions is often omitted, using the absorption band merely for fingerprinting and/or kinetic tracking. One of the reasons is again the poor spectral resolution leading to difficult deconvolution, although often better resolutions could be obtained with state-of-the-art spectrophotometers and setups. Another reason is the difficulty in interpretation. The automated use of databases on absorption spectra could help here to benefit from the numerous existing measurements in literature, as well as advanced statistical analysis of time series data on absorption data from transient/step response experiments. Extension of the studies on copper and iron zeolites to other transition metals could provide useful reference data for other more complex catalyst. Moreover, knowledge transfer across the disciplines such

as links of identified species in enzymatic work to heterogeneous metal complexes can be instrumental and should be stimulated. Further advances in the simulation of absorption spectra can also be expected, with better infrastructure and algorithms giving better access to higher level, more accurate methods (e.g. from TD-DFT to coupled cluster and multireference methods). On that note an up-to-date review work on the computational simulation of electronic absorption spectra with guidelines and insights from benchmarking would be a welcome addition to the literature.

There is no doubt that multi-spectroscopic approaches will remain the key to in-depth understanding in catalysis. The electronic information of UV-VIS-NIR absorption spectra is (for example) combined with (1) vibrational information from FTIR and/or rR; (2) with structural information from XANES, EXAFS ….; (3) magnetic information from EPR and/or MCD. Applying these techniques at reaction conditions remains a challenge, as not all spectroscopies are sufficiently sensitive. The technological hurdles to do so have, however progressed strongly.[4] This review has highlighted the compatibility of UV-VIS-NIR spectroscopies with some catalytic systems and measurement techniques. The UV-VIS-NIR range uniquely allows the application of three techniques (absorption, rR and MCD) that give complementary information site-selectively by probing the same excitation events. The direct relation between the spectroscopic data can therefore be established with more confidence than for other spectroscopy combinations. Examples of *in situ* UV-VIS-NIR absorption spectroscopy combined with rR and MCD have been given for copper and iron zeolites and for metalloenzymes. This could be extended beyond these applications.

Numerous advances can be expected for *in situ* UV-VIS-NIR absorption spectroscopy. Developments continue in optical equipment for transient absorption to further expand its range into the attoseconds. Improved cells enable the combined measurement of more spectroscopies. Improved light collection and sample irradiation, and the more widespread use of statistical analysis and the availability of databases may alleviate the limits on spectral resolution. These developments will be important beyond the field of catalysis. With the exponential development of sensors and electrochemical batteries, UV-VIS-NIR spectroscopies have also entered the broader material science field. In the case of battery research S-based batteries are very well suited for UV-VIS-NIR range spectroscopy as each polysulfide has an absorption band in the UV-VIS range.[372, 375, 376] Sensors are often semiconductors with a band gap or nanotarticles with surface plasmon resonance in the UV-VIS-NIR range.[377, 378] An example is the NIR surface plasmon resonance of starch capped CuS quantum dots, sensitive to uptake of environmentally relevant divalent heavy metals.[379] Hopefully the more widespread use will spur developments in spectroscopy, to the benefit of better understanding advanced materials in general.

5. References

(1) Lever, A. B. P. *Inorganic electronic spectroscopy*; 1984.
(2) Solomon, E. I.; Lever, A. B. P. *Inorganic electronic structure and spectroscopy. Volume 1: Methodology*; 2000.
(3) van Vreeswijk, S. H.; Weckhuysen, B. M. Emerging analytical methods to characterize zeolite-based materials. *Natl Sci Rev* **2022**, *9*,
(4) Vogt, C.; Wondergem, C. S.; Weckhuysen, B. M. Ultraviolet-visible (uv-vis) spectroscopy. In *Springer handbook of advanced catalyst characterization*, Wachs, I. E., Bañares, M. A. Eds.; Springer International Publishing, 2023; pp 237-264.

(5) Bravo-Suárez, J. J.; Srinivasan, P. D. Design characteristics of in situ and operando ultraviolet-visible and vibrational spectroscopic reaction cells for heterogeneous catalysis. *Cat Rev - Sci Eng* **2017**, *59*, 295-445.
(6) Valecillos, J.; Elordi, G.; Cui, M.; Aguayo, A. T.; Castaño, P. Evaluating catalytic (gas–solid) spectroscopic cells as intrinsic kinetic reactors: Methanol-to-hydrocarbon reaction as a case study. *Chem Eng J* **2022**, *450*,
(7) Jentoft, F. C. Chapter 3 ultraviolet–visible–near infrared spectroscopy in catalysis. Advances in catalysis, 2009; pp 129-211.
(8) Schoonheydt, R. A. Uv-vis-nir spectroscopy and microscopy of heterogeneous catalysts. *Chem Soc Rev* **2010**, *39*, 5051-5066.
(9) Mu, C.; Lv, C.; Meng, X.; Sun, J.; Tong, Z.; Huang, K. In situ characterization techniques applied in photocatalysis: A review. *Adv Mater Interfaces* **2023**, *10*, 2201842.
(10) Mesa, C. A.; Pastor, E.; Francàs, L. Uv–vis operando spectroelectrochemistry for (photo)electrocatalysis: Principles and guidelines. *Curr Opin Electrochem* **2022**, *35*,
(11) Suppan, P.; Ghoneim, N. *Solvatochromism*; Royal Society of Chemistry, 1997.
(12) Hirayama, K. *Handbook of ultraviolet and visible absorption spectra of organic compounds*; Springer US, 1967.
(13) Mataga, N.; Kubota, T. *Molecular interactions and electronic spectra*; Marcel Dekker Incorporated, 1970.
(14) Atkins, P. W.; Friedman, R. S. *Molecular quantum mechanics*; OUP Oxford, 2011.
(15) Electronic absorption spectroscopy-vibronic coupling and band shape analysis. *Comments Inorg Chem* **2007**, *3*, 300-318.
(16) Al-Jalali, M. A.; Aljghami, I. F.; Mahzia, Y. M. Voigt deconvolution method and its applications to pure oxygen absorption spectrum at 1270nm band. *Spectrochim Acta A Mol Biomol Spectrosc* **2016**, *157*, 34-40.
(17) Snyder, B. E.; Vanelderen, P.; Bols, M. L.; Hallaert, S. D.; Bottger, L. H.; Ungur, L.; Pierloot, K.; Schoonheydt, R. A.; Sels, B. F.; Solomon, E. I. The active site of low-temperature methane hydroxylation in iron-containing zeolites. *Nature* **2016**, *536*, 317-321.
(18) Mason, W. R. *A practical guide to magnetic circular dichroism spectroscopy*; John Wiley & Sons, 2007.
(19) Kobayashi, N.; Muranaka, A.; Mack, J. *Circular dichroism and magnetic circular dichroism spectroscopy for organic chemists*; The Royal Society of Chemistry, 2011. DOI: 10.1039/9781849732932.
(20) Jensen, F. *Introduction to computational chemistry*; Wiley, 2017.
(21) Fehér, P. P.; Madarász, Á.; Stirling, A. A practice-oriented benchmark strategy to predict the uv-vis spectra of organic photocatalysts**. *Chemistry–Methods* **2023**, *3*, e202200069.
(22) Latouche, C.; Skouteris, D.; Palazzetti, F.; Barone, V. Td-dft benchmark on inorganic pt(ii) and ir(iii) complexes. *J Chem Theory Comput* **2015**, *11*, 3281-3289.
(23) Gómez, S.; Giovannini, T.; Cappelli, C. Multiple facets of modeling electronic absorption spectra of systems in solution. *ACS Phys Chem Au* **2023**, *3*, 1-16.
(24) Zhang, T.; Liu, S.; Zhu, L.; Liu, F.; Zhong, K.; Zhang, Y.; Bai, R.; Lan, Y. Theoretical study of fmo adjusted c-h cleavage and oxidative addition in nickel catalysed c-h arylation. *Commun Chem* **2019**, *2*, 31.
(25) Wu, K.; Rodríguez-Córdoba, W.; Lian, T. Exciton localization and dissociation dynamics in cds and cds–pt quantum confined nanorods: Effect of nonuniform rod diameters. *J Phys Chem B* **2014**, *118*, 14062-14069.
(26) Rhoda, H. M.; Heyer, A. J.; Snyder, B. E. R.; Plessers, D.; Bols, M. L.; Schoonheydt, R. A.; Sels, B. F.; Solomon, E. I. Second-sphere lattice effects in copper and iron zeolite catalysis. *Chem Rev* **2022**, *122*, 12207-12243.

(27) Chen, Y.-C.; Foo, D.; Dehanov, N.; Thennadil, S. N. Spatially and angularly resolved spectroscopy for in-situ estimation of concentration and particle size in colloidal suspensions. *Anal Bioanal Chem* **2017**, *409*, 6975-6988.
(28) Ohtani, B.; Bowman, R. M.; Colombo Jr, D. P.; Kominami, H.; Noguchi, H.; Uosaki, K. Femtosecond diffuse reflectance spectroscopy of aqueous titanium(iv) oxide suspension: Correlation of electron-hole recombination kinetics with photocatalytic activity. *Chem Lett* **1998**, *27*, 579-580.
(29) Hecht, H. G. The interpretation of diffuse reflectance spectra. *J Res Natl Bur Stand A Phys Chem* **1976**, *80A*, 567-583.
(30) Li, R.; Kodaira, T.; Kawanami, H. In situ formic acid dehydrogenation observation using a uv-vis-diffuse-reflectance spectroscopy system. *Chem Commun (Camb)* **2022**, *58*, 11079-11082.
(31) Meunier, F. C. The design and testing of kinetically-appropriate operando spectroscopic cells for investigating heterogeneous catalytic reactions. *Chem Soc Rev* **2010**, *39*, 4602-4614.
(32) Flanigen, E. M. Chapter 2 zeolites and molecular sieves an historical perspective. In *Introduction to zeolite science and practice*, Studies in surface science and catalysis, 1991; pp 13-34.
(33) Davis, M. E. Zeolites and molecular sieves: Not just ordinary catalysts. *Ind Eng Chem Res* **2002**, *30*, 1675-1683.
(34) Derouane, E. G.; Védrine, J. C.; Pinto, R. R.; Borges, P. M.; Costa, L.; Lemos, M. A. N. D. A.; Lemos, F.; Ribeiro, F. R. The acidity of zeolites: Concepts, measurements and relation to catalysis: A review on experimental and theoretical methods for the study of zeolite acidity. *Cat Rev - Sci Eng* **2013**, *55*, 454-515.
(35) Srinivasan, P. D.; Nitz, S. R.; Stephens, K. J.; Atchison, E.; Bravo-Suarez, J. J. Modified harrick reaction cell for in situ/operando fiber optics diffuse reflectance uv–visible spectroscopic characterization of catalysts. *Appl Catal A Gen* **2018**, *561*, 7-18.
(36) Bernad, B.; Ferrero, A.; Strothkämper, C.; Campos, J.; Pons, A.; Quast, T.; Hauer, K. O.; Schirmacher, A. Deviation of white diffuse reflectance standards from perfect reflecting diffuser at visible and near-infrared spectral ranges. *Metrologia* **2019**, *56*, 055005.
(37) Shi, H.; Lercher, J. A.; Yu, X.-Y. Sailing into uncharted waters: Recent advances in the in situ monitoring of catalytic processes in aqueous environments. *Catal Sci Technol* **2015**, *5*, 3035-3060.
(38) Meirer, F.; Weckhuysen, B. M. Spatial and temporal exploration of heterogeneous catalysts with synchrotron radiation. *Nat Rev Mater* **2018**, *3*, 324-340.
(39) Issa Hamoud, H.; Wolski, L.; Pankin, I.; Bañares, M. A.; Daturi, M.; El-Roz, M. In situ and operando spectroscopies in photocatalysis: Powerful techniques for a better understanding of the performance and the reaction mechanism. *Top Curr Chem* **2022**, *380*, 37.
(40) Skoog, D. A.; West, D. M.; Holler, F. J.; Crouch, S. R. *Fundamentals of analytical chemistry / douglas a. Skoog, donald m. West, f. James holler, stanley r. Crouch*; Brooks/Cole, Cengage Learning, 2014.
(41) Mores, D.; Stavitski, E.; Kox, M. H. F.; Kornatowski, J.; Olsbye, U.; Weckhuysen, B. M. Space- and time-resolved in-situ spectroscopy on the coke formation in molecular sieves: Methanol-to-olefin conversion over h-zsm-5 and h-sapo-34. *Chem - Eur J* **2008**, *14*, 11320-11327.
(42) van Vreeswijk, S. H.; Monai, M.; Oord, R.; Schmidt, J. E.; Vogt, E. T. C.; Poplawsky, J. D.; Weckhuysen, B. M. Nano-scale insights regarding coke formation in zeolite ssz-13 subject to the methanol-to-hydrocarbons reaction. *Catal Sci Technol* **2022**, *12*, 1220-1228.
(43) Verkleij, S. P.; Whiting, G. T.; Parres Esclapez, S.; Li, S.; Mertens, M. M.; Janssen, M.; Bons, A.-J.; Burgers, M.; Weckhuysen, B. M. High-pressure operando uv-vis micro-

spectroscopy of coke formation in zeolite-based catalyst extrudates during the transalkylation of aromatics. *ChemCatChem* **2020**, *12*, 5465-5475.
(44) Creutz, S. E.; Peters, J. C. Spin-state tuning at pseudo-tetrahedral d6 ions: Spin crossover in [bp3]feii–x complexes. *Inorg Chem* **2016**, *55*, 3894-3906.
(45) Safin, F.; Maslov, V.; Gromova, Y.; Korsakov, I.; Kolesova, E.; Dubavik, A.; Cherevkov, S.; Gun'ko, Y. K. Investigation of magnetic circular dichroism spectra of semiconductor quantum rods and quantum dot-in-rods. In *Nanomaterials*, 2020; Vol. 10.
(46) Lee, S.; You, Y.; Ohkubo, K.; Fukuzumi, S.; Nam, W. Highly efficient cycloreversion of photochromic dithienylethene compounds using visible light-driven photoredox catalysis. *Chem Sci* **2014**, *5*, 1463-1474.
(47) Fujiwara, T.; Harada, J.; Ogawa, K. Solid-state thermochromism studied by variable-temperature diffuse reflectance spectroscopy. A new perspective on the chromism of salicylideneanilines. *J Phys Chem B* **2004**, *108*, 4035-4038.
(48) Kuchison, A. M.; Wolf, M. O.; Patrick, B. O. Photophysical and electrochemical properties of ru(ii) complexes containing tridentate bisphosphino-oligothiophene ligands. *Dalton Trans* **2011**, *40*, 6912-6921.
(49) Ekanayake, D. M.; Pham, D.; Probst, A. L.; Miller, J. R.; Popescu, C. V.; Fiedler, A. T. Electronic structures and spectroscopic signatures of diiron intermediates generated by o2 activation of nonheme iron(ii)–thiolate complexes. *Dalton Trans* **2021**, *50*, 14432-14443.
(50) O'Connor, D. B.; Goldbeck, R. A.; Hazzard, J. H.; Kliger, D. S.; Cusanovich, M. A. Time-resolved absorption and magnetic circular dichroism spectroscopy of cytochrome c3 from desulfovibrio. *Biophys J* **1993**, *65*, 1718-1726.
(51) Robert, A. G.; David, S. K. Monitoring protein dynamics with time-resolved cd and mcd spectroscopy. In *Proc.SPIE*, 1993; Vol. 1890, pp 32-39. DOI: 10.1117/12.145257.
(52) Cao, J.; Ye, L.; He, D.; Zheng, X.; Mukamel, S. Magnet-free time-resolved magnetic circular dichroism with pulsed vector beams. *J Phys Chem Lett* **2022**, *13*, 11300-11306.
(53) Rodger, A.; Carey, M. J. Stopped-flow circular dichroism. In *Spectrophotometry and Spectrofluorimetry: A Practical Approach*; Gore, M., Ed.; Oxford University Press, 2000; p 0. DOI: 10.1093/oso/9780199638130.003.0014.
(54) Morgenroth, M.; Scholz, M.; Lenzer, T.; Oum, K. Ultrafast uv–vis transient absorption and circular dichroism spectroscopy of a polyfluorene copolymer showing large chiral induction. *J Phys Chem C* **2020**, *124*, 10192-10200.
(55) Oppermann, M.; Bauer, B.; Rossi, T.; Zinna, F.; Helbing, J.; Lacour, J.; Chergui, M. Ultrafast broadband circular dichroism in the deep ultraviolet. *Optica* **2019**, *6*, 56-60.
(56) Oppermann, M.; Spekowius, J.; Bauer, B.; Pfister, R.; Chergui, M.; Helbing, J. Broad-band ultraviolet cd spectroscopy of ultrafast peptide backbone conformational dynamics. *J Phys Chem Lett* **2019**, *10*, 2700-2705.
(57) Scholz, M.; Morgenroth, M.; Cho, M. J.; Choi, D. H.; Oum, K.; Lenzer, T. Ultrafast broadband transient absorption and circular dichroism reveal relaxation of a chiral copolymer. *J Phys Chem Lett* **2019**, *10*, 5160-5166.
(58) Iyer, S. R.; Tidemand, K. D.; Babicz, J. T., Jr.; Jacobs, A. B.; Gee, L. B.; Haahr, L. T.; Yoda, Y.; Kurokuzu, M.; Kitao, S.; Saito, M.; et al. Direct coordination of pterin to fe(ii) enables neurotransmitter biosynthesis in the pterin-dependent hydroxylases. *Proc Natl Acad Sci U S A* **2021**, *118*,
(59) Gibson, Q. H. [6] rapid mixing: Stopped flow. In *Methods enzymol*, Kustin, K. Ed.; Vol. 16; Academic Press, 1969; pp 187-228.
(60) Gomez-Hens, A.; Perez-Bendito, D. The stopped-flow technique in analytical chemistry. *Anal Chim Acta* **1991**, *242*, 147-177.

(61) Zhang, J.; Zhu, B.; Zhang, L.; Yu, J. Femtosecond transient absorption spectroscopy investigation into the electron transfer mechanism in photocatalysis. *Chem Commun* **2023**, *59*, 688-699.
(62) Maiuri, M.; Garavelli, M.; Cerullo, G. Ultrafast spectroscopy: State of the art and open challenges. *J Am Chem Soc* **2020**, *142*, 3-15.
(63) Srinivasan, P. D.; Patil, B. S.; Zhu, H.; Bravo-Suárez, J. J. Application of modulation excitation-phase sensitive detection-drifts for in situ/operando characterization of heterogeneous catalysts. *React Chem Eng* **2019**, *4*, 862-883.
(64) Urakawa, A.; Bürgi, T.; Baiker, A. Sensitivity enhancement and dynamic behavior analysis by modulation excitation spectroscopy: Principle and application in heterogeneous catalysis. *Chem Eng Sci* **2008**, *63*, 4902-4909.
(65) Müller, P.; Hermans, I. Applications of modulation excitation spectroscopy in heterogeneous catalysis. *Ind Eng Chem Res* **2017**, *56*, 1123-1136.
(66) *Springer handbook of advanced catalyst characterization*; Springen Cham, 2023. DOI: https://doi.org/10.1007/978-3-031-07125-6.
(67) Liu, P.; Zhou, X.; Li, Y.; Li, M.; Yu, D.; Liu, J. The application of principal component analysis and non-negative matrix factorization to analyze time-resolved optical waveguide absorption spectroscopy data. *Anal Methods* **2013**, *5*, 4454-4459.
(68) Bray, R. C. Sudden freezing as a technique for the study of rapid reactions. *Biochem J* **1961**, *81*, 189-193.
(69) Myrick, M. L.; Simcock, M. N.; Baranowski, M.; Brooke, H.; Morgan, S. L.; McCutcheon, J. N. The kubelka-munk diffuse reflectance formula revisited. *Appl Spectrosc Rev* **2011**, *46*, 140-165.
(70) Kortüm, G. *Reflectance spectroscopy*; 1969. DOI: 10.1007/978-3-642-88071-1.
(71) Landi, S.; Segundo, I. R.; Freitas, E.; Vasilevskiy, M.; Carneiro, J.; Tavares, C. J. Use and misuse of the kubelka-munk function to obtain the band gap energy from diffuse reflectance measurements. *Solid State Commun* **2022**, *341*,
(72) William, E. V. Inversion methods from kubelka–munk analysis. *J Opt A - Pure Appl Opt* **2002**, *4*, 452.
(73) Murphy, A. B. Optical properties of an optically rough coating from inversion of diffuse reflectance measurements. *Appl Opt* **2007**, *46*, 3133-3143.
(74) Tauc, J.; Grigorovici, R.; Vancu, A. Optical properties and electronic structure of amorphous germanium. *Phys Status Solidi B* **1966**, *15*, 627-637.
(75) Raciti, R.; Bahariqushchi, R.; Summonte, C.; Aydinli, A.; Terrasi, A.; Mirabella, S. Optical bandgap of semiconductor nanostructures: Methods for experimental data analysis. *J Appl Phys* **2017**, *121*, 234304.
(76) Liu, P.; Longo, P.; Zaslavsky, A.; Pacifici, D. Optical bandgap of single- and multi-layered amorphous germanium ultra-thin films. *J Appl Phys* **2016**, *119*, 014304.
(77) Yu, P.; Cardona, M. *Fundamentals of semiconductors: Physics and materials properties*; Springer Berlin Heidelberg, 2010.
(78) Makuła, P.; Pacia, M.; Macyk, W. How to correctly determine the band gap energy of modified semiconductor photocatalysts based on uv–vis spectra. *J Phys Chem Lett* **2018**, *9*, 6814-6817.
(79) Brik, M. G.; Srivastava, A. M.; Popov, A. I. A few common misconceptions in the interpretation of experimental spectroscopic data. *Opt Mater* **2022**, *127*, 112276.
(80) O'Leary, S. K.; Lim, P. K. On determining the optical gap associated with an amorphous semiconductor: A generalization of the tauc model. *Solid State Commun* **1997**, *104*, 17-21.

(81) Jubu, P. R.; Obaseki, O. S.; Yam, F. K.; Stephen, S. M.; Avaa, A. A.; McAsule, A. A.; Yusof, Y.; Otor, D. A. Influence of the secondary absorption and the vertical axis scale of the tauc's plot on optical bandgap energy. *J Opt* **2022**,
(82) Schwarting, M.; Siol, S.; Talley, K.; Zakutayev, A.; Phillips, C. Automated algorithms for band gap analysis from optical absorption spectra. *Mater Discov* **2017**, *10*, 43-52.
(83) Mullerova, J.; Sutta, P. On some ambiguities of the absorption edge and optical band gaps of amorphous and polycrystalline semiconductors. *Commun - Sci Lett Univ Zilina* **2017**, *19*, 9-15.
(84) Cody, G. D.; Brooks, B. G.; Abeles, B. Optical absorption above the optical gap of amorphous silicon hydride. *Sol Energy Mater* **1982**, *8*, 231-240.
(85) Davis, E. A.; Mott, N. F. Conduction in non-crystalline systems v. Conductivity, optical absorption and photoconductivity in amorphous semiconductors. *Philos Mag* **1970**, *22*, 0903-0922.
(86) Zanatta, A. R. Revisiting the optical bandgap of semiconductors and the proposal of a unified methodology to its determination. *Sci Rep* **2019**, *9*, 11225.
(87) Chibotaru, L. F.; Hendrickx, M. F. A.; Clima, S.; Larionova, J.; Ceulemans, A. Magnetic anisotropy of [mo(cn)7]4- anions and fragments of cyano-bridged magnetic networks. *J Phys Chem A* **2005**, *109*, 7251-7257.
(88) Hendrickx, M. F. A.; Mironov, V. S.; Chibotaru, L. F.; Ceulemans, A. Assignment of the electronic spectra of [mo(cn)8]4- and [w(cn)8]4- by ab initio calculations. *Inorg Chem* **2004**, *43*, 3142-3150.
(89) Beale, A. M.; van der Eerden, A. M. J.; Kervinen, K.; Newton, M. A.; Weckhuysen, B. M. Adding a third dimension to operando spectroscopy: A combined uv-vis, raman and xafs setup to study heterogeneous catalysts under working conditions. *Chem Commun* **2005**, 3015-3017.
(90) O'Brien, M. G.; Beale, A. M.; Jacques, S. D. M.; Di Michiel, M.; Weckhuysen, B. M. Spatiotemporal multitechnique imaging of a catalytic solid in action: Phase variation and volatilization during molybdenum oxide reduction. *ChemCatChem* **2009**, *1*, 99-102.
(91) Capocasa, G.; Sessa, F.; Tavani, F.; Monte, M.; Olivo, G.; Pascarelli, S.; Lanzalunga, O.; Di Stefano, S.; D'Angelo, P. Coupled x-ray absorption/uv–vis monitoring of fast oxidation reactions involving a nonheme iron–oxo complex. *J Am Chem Soc* **2019**, *141*, 2299-2304.
(92) Sakaguchi, M.; Kimura, T.; Nishida, T.; Tosha, T.; Sugimoto, H.; Yamaguchi, Y.; Yanagisawa, S.; Ueno, G.; Murakami, H.; Ago, H.; et al. A nearly on-axis spectroscopic system for simultaneously measuring uv-visible absorption and x-ray diffraction in the spring-8 structural genomics beamline. *J Synchrotron Rad* **2016**, *23*, 334-338.
(93) Makita, H.; Simon, P. S.; Kern, J.; Yano, J.; Yachandra, V. K. Combining on-line spectroscopy with synchrotron and x-ray free electron laser crystallography. *Curr Opin Struct Biol* **2023**, *80*, 102604.
(94) Pfanzagl, V.; Beale, J. H.; Michlits, H.; Schmidt, D.; Gabler, T.; Obinger, C.; Djinović-Carugo, K.; Hofbauer, S. X-ray–induced photoreduction of heme metal centers rapidly induces active-site perturbations in a protein-independent manner. *J Biol Chem* **2020**, *295*, 13488-13501.
(95) Fushimi, R.; Gleaves, J. Recent advances in dynamic chemical characterization using temporal analysis of products. *Curr Opin Chem Eng* **2018**, *21*, 10-21.
(96) Abdel-Mageed, A. M.; Chen, S.; Fauth, C.; Häring, T.; Bansmann, J. Fundamental aspects of ceria supported au catalysts probed by in situ/operando spectroscopy and tap reactor studies. *ChemPhysChem* **2021**, *22*, 1302-1315.
(97) Ovsitser, O.; Cherian, M.; Kondratenko, E. V. In-situ uv/vis and transient isotopic analysis of the role of oxidizing agent in the oxidative dehydrogenation of propane over silica-supported vanadia catalysts. *J Phys Chem C* **2007**, *111*, 8594-8602.

(98) Srinivasan, P. D.; Zhu, H.; Bravo-Suárez, J. J. In situ uv–vis plasmon resonance spectroscopic assessment of oxygen and hydrogen adsorption location on supported gold catalysts. *Molecular Catalysis* **2021**, *507*,
(99) Tang, J.; Albrecht, A. C. *Raman spectroscopy vol. 2*; Plenum, 1970.
(100) Snyder, B. E. R.; Bols, M. L.; Schoonheydt, R. A.; Sels, B. F.; Solomon, E. I. Iron and copper active sites in zeolites and their correlation to metalloenzymes. *Chem Rev* **2018**, *118*, 2718-2768.
(101) Vogiatzis, K. D.; Polynski, M. V.; Kirkland, J. K.; Townsend, J.; Hashemi, A.; Liu, C.; Pidko, E. A. Computational approach to molecular catalysis by 3d transition metals: Challenges and opportunities. *Chem Rev* **2019**, *119*, 2453-2523.
(102) Nakamura, I.; Yamamoto, Y. Transition-metal-catalyzed reactions in heterocyclic synthesis. *Chem Rev* **2004**, *104*, 2127-2198.
(103) Mahyuddin, M. H.; Staykov, A.; Shiota, Y.; Miyanishi, M.; Yoshizawa, K. Roles of zeolite confinement and cu–o–cu angle on the direct conversion of methane to methanol by [cu2(μ-o)]2+-exchanged aei, cha, afx, and mfi zeolites. *ACS Catal* **2017**, *7*, 3741-3751.
(104) Farrusseng, D.; Tuel, A. Perspectives on zeolite-encapsulated metal nanoparticles and their applications in catalysis. *New J Chem* **2016**, *40*, 3933-3949.
(105) Védrine, J. C.; Fechete, I. Heterogeneous partial oxidation catalysis on metal oxides. *Comptes Rendus Chimie* **2016**, *19*, 1203-1225.
(106) Kung, H. H.; Ko, E. I. Preparation of oxide catalysts and catalyst supports — a review of recent advances. *Chem Eng J Biochem Eng J* **1996**, *64*, 203-214.
(107) Li, Y.; Zhang, Y.; Qian, K.; Huang, W. Metal–support interactions in metal/oxide catalysts and oxide–metal interactions in oxide/metal inverse catalysts. *ACS Catal* **2022**, *12*, 1268-1287.
(108) Védrine, J. C. Importance, features and uses of metal oxide catalysts in heterogeneous catalysis. *Chinese J Cat* **2019**, *40*, 1627-1636.
(109) Linic, S.; Christopher, P.; Xin, H.; Marimuthu, A. Catalytic and photocatalytic transformations on metal nanoparticles with targeted geometric and plasmonic properties. *Acc Chem Res* **2013**, *46*, 1890-1899.
(110) Sápi, A.; Rajkumar, T.; Kiss, J.; Kukovecz, Á.; Kónya, Z.; Somorjai, G. A. Metallic nanoparticles in heterogeneous catalysis. *Catal Lett* **2021**, *151*, 2153-2175.
(111) Shekhar, M.; Wang, J.; Lee, W. S.; Williams, W. D.; Kim, S. M.; Stach, E. A.; Miller, J. T.; Delgass, W. N.; Ribeiro, F. H. Size and support effects for the water-gas shift catalysis over gold nanoparticles supported on model al2o3 and tio2. *J Am Chem Soc* **2012**, *134*, 4700-4708.
(112) Jha, A.; Lee, Y.-L.; Jang, W.-J.; Shim, J.-O.; Jeon, K.-W.; Na, H.-S.; Kim, H.-M.; Roh, H.-S.; Jeong, D.-W.; Jeon, S. G.; et al. Effect of the redox properties of support oxide over cobalt-based catalysts in high temperature water-gas shift reaction. *Molecular Catalysis* **2017**, *433*, 145-152.
(113) de Melo, C.; Jullien, M.; Battie, Y.; En Naciri, A.; Ghanbaja, J.; Montaigne, F.; Pierson, J. F.; Rigoni, F.; Almqvist, N.; Vomiero, A.; et al. Tunable localized surface plasmon resonance and broadband visible photoresponse of cu nanoparticles/zno surfaces. *ACS Appl Mater Interfaces* **2018**, *10*, 40958-40965.
(114) Chaiseeda, K.; Nishimura, S.; Ebitani, K. Gold nanoparticles supported on alumina as a catalyst for surface plasmon-enhanced selective reductions of nitrobenzene. *ACS Omega* **2017**, *2*, 7066-7070.
(115) Jeon, H. B.; Tsalu, P. V.; Ha, J. W. Shape effect on the refractive index sensitivity at localized surface plasmon resonance inflection points of single gold nanocubes with vertices. *Sci Rep* **2019**, *9*, 13635.

(116) Liu, J. X.; Filot, I. A. W.; Su, Y.; Zijlstra, B.; Hensen, E. J. M. Optimum particle size for gold-catalyzed co oxidation. *J Phys Chem C Nanomater Interfaces* **2018**, *122*, 8327-8340.
(117) Ha, H.; Yoon, S.; An, K.; Kim, H. Y. Catalytic co oxidation over au nanoparticles supported on ceo2 nanocrystals: Effect of the au–ceo2 interface. *ACS Catal* **2018**, *8*, 11491-11501.
(118) Saavedra, J.; Pursell, C. J.; Chandler, B. D. Co oxidation kinetics over au/tio(2) and au/al(2)o(3) catalysts: Evidence for a common water-assisted mechanism. *J Am Chem Soc* **2018**, *140*, 3712-3723.
(119) González-Castaño, M.; R. Reina, T.; Ivanova, S.; Martínez Tejada, L. M.; Centeno, M. A.; Odriozola, J. A. O2-assisted water gas shift reaction over structured au and pt catalysts. *Appl Catal B Env* **2016**, *185*, 337-343.
(120) Plata, J. J.; Romero-Sarria, F.; Amaya Suarez, J.; Marquez, A. M.; Laguna, O. H.; Odriozola, J. A.; Fdez Sanz, J. Improving the activity of gold nanoparticles for the water-gas shift reaction using tio(2)-y(2)o(3): An example of catalyst design. *Phys Chem Chem Phys* **2018**, *20*, 22076-22083.
(121) Rodriguez, J. A.; Senanayake, S. D.; Stacchiola, D.; Liu, P.; Hrbek, J. The activation of gold and the water-gas shift reaction: Insights from studies with model catalysts. *Acc Chem Res* **2014**, *47*, 773-782.
(122) Strunk, J.; Kähler, K.; Xia, X.; Comotti, M.; Schüth, F.; Reinecke, T.; Muhler, M. Au/zno as catalyst for methanol synthesis: The role of oxygen vacancies. *Appl Catal A Gen* **2009**, *359*, 121-128.
(123) Hartadi, Y.; Widmann, D.; Behm, R. J. Co2 hydrogenation to methanol on supported au catalysts under moderate reaction conditions: Support and particle size effects. *ChemSusChem* **2015**, *8*, 456-465.
(124) Wu, Y. Y.; Mashayekhi, N. A.; Kung, H. H. Au–metal oxide support interface as catalytic active sites. *Catal Sci Technol* **2013**, *3*, 2881-2891.
(125) Vilhelmsen, L. B.; Hammer, B. Identification of the catalytic site at the interface perimeter of au clusters on rutile tio2(110). *ACS Catal* **2014**, *4*, 1626-1631.
(126) Wang, X.; Rosspeintner, A.; Ziarati, A.; Zhao, J.; Burgi, T. Insight into the transient inactivation effect on au/tio(2) catalyst by in-situ drift and uv-vis spectroscopy. *Nat Commun* **2022**, *13*, 5458.
(127) Navarro-Jaén, S.; Bobadilla, L. F.; Romero-Sarria, F.; Laguna, O. H.; Bion, N.; Odriozola, J. A. Evaluation of the oxygen mobility in cepo4-supported catalysts: Mechanistic implications on the water–gas shift reaction. *J Phys Chem C* **2020**, *124*, 16391-16401.
(128) Wang, W.; Wang, S.; Ma, X.; Gong, J. Recent advances in catalytic hydrogenation of carbon dioxide. *Chem Soc Rev* **2011**, *40*, 3703-3727.
(129) Bobadilla, L. F.; Santos, J. L.; Ivanova, S.; Odriozola, J. A.; Urakawa, A. Unravelling the role of oxygen vacancies in the mechanism of the reverse water–gas shift reaction by operando drifts and ultraviolet–visible spectroscopy. *ACS Catal* **2018**, *8*, 7455-7467.
(130) Kim, H. Y.; Henkelman, G. Co oxidation at the interface of au nanoclusters and the stepped-ceo2(111) surface by the mars-van krevelen mechanism. *J Phys Chem Lett* **2013**, *4*, 216-221.
(131) Ziemba, M.; Weyel, J.; Hess, C. Elucidating the mechanism of the reverse water–gas shift reaction over au/ceo2 catalysts using operando and transient spectroscopies. *Appl Catal B Env* **2022**, *301*,
(132) Castleton, C. W.; Kullgren, J.; Hermansson, K. Tuning lda+u for electron localization and structure at oxygen vacancies in ceria. *J Chem Phys* **2007**, *127*, 244704.

(133) Schilling, C.; Hess, C. Real-time observation of the defect dynamics in working au/ceo2 catalysts by combined operando raman/uv–vis spectroscopy. *J Phys Chem C* **2018**, *122*, 2909-2917.
(134) Rao, Y.; Antonelli, D. M. Mesoporous transition metal oxides: Characterization and applications in heterogeneous catalysis. *J Mater Chem* **2009**, *19*,
(135) Tian, Z.-R.; Tong, W.; Wang, J.-Y.; Duan, N.-G.; Krishnan, V. V.; Suib, S. L. Manganese oxide mesoporous structures: Mixed-valent semiconducting catalysts. *Science* **1997**, *276*, 926-930.
(136) Bensalem, A.; Weckhuysen, B. M.; Schoonheydt, R. A. In situ diffuse reflectance spectroscopy of supported chromium oxide catalysts: Kinetics of the reduction process with carbon monoxide. *J Phys Chem B* **1997**, *101*, 2824-2829.
(137) Weckhuysen, B. M.; Verberckmoes, A. A.; Debaere, J.; Ooms, K.; Langhans, I.; Schoonheydt, R. A. In situ uv–vis diffuse reflectance spectroscopy — on line activity measurements of supported chromium oxide catalysts: Relating isobutane dehydrogenation activity with cr-speciation via experimental design. *J Mol Catal A: Chem* **2000**, *151*, 115-131.
(138) Argyle, M. D.; Chen, K.; Resini, C.; Krebs, C.; Bell, A. T.; Iglesia, E. In situ uv-visible assessment of extent of reduction during oxidation reactions on oxide catalysts. *Chem Commun (Camb)* **2003**, 2082-2083.
(139) Burcham, L. J.; Deo, G.; Gao, X.; Wachs, I. E. In situ ir, raman, and uv-vis drs spectroscopy of supported vanadium oxide catalysts during methanol oxidation. *Top Catal* **2000**, *11*, 85-100.
(140) Schumacher, L.; Pfeiffer, J.; Shen, J.; Gutmann, T.; Breitzke, H.; Buntkowsky, G.; Hofmann, K.; Hess, C. Collaborative mechanistic effects between vanadia and titania during the oxidative dehydrogenation of propane investigated by operando and transient spectroscopies. *ACS Catal* **2023**, *13*, 8139-8160.
(141) Yun, D.; Zhao, Y.; Abdullahi, I.; Herrera, J. E. The effect of interstitial nitrogen in the activity of the vox/n-tio2 catalytic system for ethanol partial oxidation. *J Mol Catal A: Chem* **2014**, *390*, 169-177.
(142) Wachs, I. E.; Weckhuysen, B. M. Structure and reactivity of surface vanadium oxide species on oxide supports. *Appl Catal A Gen* **1997**, *157*, 67-90.
(143) He, Y.; Rui, Z.; Ji, H. In situ drifts study on the catalytic oxidation of toluene over v2o5/tio2 under mild conditions. *Catal Commun* **2011**, *14*, 77-81.
(144) Godiksen, A. L.; Rasmussen, S. B. Identifying the presence of [v=o]2+ during scr using in-situ raman and uv vis spectroscopy. *Catal Today* **2019**, *336*, 45-49.
(145) Busca, G.; Centi, G.; Marchetti, L.; Trifiro, F. Chemical and spectroscopic study of the nature of a vanadium oxide monolayer supported on a high-surface-area tio2 anatase. *Langmuir* **2002**, *2*, 568-577.
(146) Yun, D.; Song, Y.; Herrera, J. E. Electronic structure changes introduced by nitrogen on the n-doped vox/tio2 system: Consequences on partial oxidation catalysis. *Molecular Catalysis* **2018**, *448*, 122-134.
(147) Gao, X.; Bare, S. R.; Weckhuysen, B. M.; Wachs, I. E. In situ spectroscopic investigation of molecular structures of highly dispersed vanadium oxide on silica under various conditions. *J Phys Chem B* **1998**, *102*, 10842-10852.
(148) Weckhuysen, B. M.; Keller, D. E. Chemistry, spectroscopy and the role of supported vanadium oxides in heterogeneous catalysis. *Catal Today* **2003**, *78*, 25-46.
(149) Argyle, M. D.; Chen, K.; Resini, C.; Krebs, C.; Bell, A. T.; Iglesia, E. Extent of reduction of vanadium oxides during catalytic oxidation of alkanes measured by in-situ uv−visible spectroscopy. *J Phys Chem B* **2004**, *108*, 2345-2353.

(150) Mhamane, N. B.; Chetry, S.; Ranjan, R.; Raja, T.; Gopinath, C. S. Sustainable co2 reduction on in2o3 with exclusive co selectivity: Catalysis and in situ valence band photoelectron spectral investigations. *ACS Sustain Chem Eng* **2022**, *10*, 3521-3531.
(151) Dang, S.; Qin, B.; Yang, Y.; Wang, H.; Cai, J.; Han, Y.; Li, S.; Gao, P.; Sun, Y. Rationally designed indium oxide catalysts for co2 hydrogenation to methanol with high activity and selectivity. *Sci Adv* **2020**, *6*, eaaz2060.
(152) Ziemba, M.; Radtke, M.; Schumacher, L.; Hess, C. Elucidating co(2) hydrogenation over in(2) o(3) nanoparticles using operando uv/vis and impedance spectroscopies. *Angew Chem Int Ed Engl* **2022**, *61*, e202209388.
(153) Snyder, B. E. R.; Vanelderen, P.; Schoonheydt, R. A.; Sels, B. F.; Solomon, E. I. Second-sphere effects on methane hydroxylation in cu-zeolites. *J Am Chem Soc* **2018**, *140*, 9236-9243.
(154) Plessers, D.; Bols, M. L.; Rhoda, H. M.; Heyer, A. J.; Solomon, E. I.; Sels, B. F.; Schoonheydt, R. A. Single site spectroscopy of transition metal ions and reactive oxygen complexes in zeolites. In *Comprehensive inorganic chemistry iii*, 2023; pp 148-164.
(155) Dinh, K. T.; Sullivan, M. M.; Serna, P.; Meyer, R. J.; Dincă, M.; Román-Leshkov, Y. Viewpoint on the partial oxidation of methane to methanol using cu- and fe-exchanged zeolites. *ACS Catal* **2018**, *8*, 8306-8313.
(156) Ravi, M.; Ranocchiari, M.; van Bokhoven, J. A. The direct catalytic oxidation of methane to methanol-a critical assessment. *Angew Chem Int Ed Engl* **2017**, *56*, 16464-16483.
(157) Beale, A. M.; Gao, F.; Lezcano-Gonzalez, I.; Peden, C. H.; Szanyi, J. Recent advances in automotive catalysis for nox emission control by small-pore microporous materials. *Chem Soc Rev* **2015**, *44*, 7371-7405.
(158) Zhang, R.; Liu, N.; Lei, Z.; Chen, B. Selective transformation of various nitrogen-containing exhaust gases toward n2 over zeolite catalysts. *Chem Rev* **2016**, *116*, 3658-3721.
(159) Xin, Y.; Li, Q.; Zhang, Z. Zeolitic materials for denox selective catalytic reduction. *ChemCatChem* **2018**, *10*, 29-41.
(160) Notté, P. P. The alphoxtm process or the one-step hydroxylation of benzene into phenol by nitrous oxide. Understanding and tuning the zsm-5 catalyst activities. *Top Catal* **2000**, *13*, 387-394.
(161) Panov, G. I.; Sheveleva, G. A.; Kharitonov, A. S.; Romannikov, V. N.; Vostrikova, L. A. Oxidation of benzene to phenol by nitrous oxide over fe-zsm-5 zeolites. *Appl Catal A Gen* **1992**, *82*, 31-36.
(162) Snyder, B. E. R.; Bols, M. L.; Rhoda, H. M.; Vanelderen, P.; Bottger, L. H.; Braun, A.; Yan, J. J.; Hadt, R. G.; Babicz, J. T., Jr.; Hu, M. Y.; et al. Mechanism of selective benzene hydroxylation catalyzed by iron-containing zeolites. *Proc Natl Acad Sci U S A* **2018**, *115*, 12124-12129.
(163) Woertink, J. S.; Smeets, P. J.; Groothaert, M. H.; Vance, M. A.; Sels, B. F.; Schoonheydt, R. A.; Solomon, E. I. A [cu2o]2+ core in cu-zsm-5, the active site in the oxidation of methane to methanol. *Proc Natl Acad Sci U S A* **2009**, *106*, 18908-18913.
(164) Vanelderen, P.; Snyder, B. E.; Tsai, M. L.; Hadt, R. G.; Vancauwenbergh, J.; Coussens, O.; Schoonheydt, R. A.; Sels, B. F.; Solomon, E. I. Spectroscopic definition of the copper active sites in mordenite: Selective methane oxidation. *J Am Chem Soc* **2015**, *137*, 6383-6392.
(165) Rhoda, H. M.; Plessers, D.; Heyer, A. J.; Bols, M. L.; Schoonheydt, R. A.; Sels, B. F.; Solomon, E. I. Spectroscopic definition of a highly reactive site in cu-cha for selective methane oxidation: Tuning a mono-mu-oxo dicopper(ii) active site for reactivity. *J Am Chem Soc* **2021**, *143*, 7531-7540.
(166) Heyer, A. J.; Plessers, D.; Braun, A.; Rhoda, H. M.; Bols, M. L.; Hedman, B.; Hodgson, K. O.; Schoonheydt, R. A.; Sels, B. F.; Solomon, E. I. Methane activation by a mononuclear

copper active site in the zeolite mordenite: Effect of metal nuclearity on reactivity. *J Am Chem Soc* **2022**, *144*, 19305-19316.
(167) Plessers, D.; Heyer, A. J.; Rhoda, H. M.; Bols, M. L.; Solomon, E. I.; Schoonheydt, R. A.; Sels, B. F. Tuning copper active site composition in cu-mor through co-cation modification for methane activation. *ACS Catal* **2023**, *13*, 1906-1915.
(168) Bols, M. L.; Hallaert, S. D.; Snyder, B. E. R.; Devos, J.; Plessers, D.; Rhoda, H. M.; Dusselier, M.; Schoonheydt, R. A.; Pierloot, K.; Solomon, E. I.; Sels, B. F. Spectroscopic identification of the alpha-fe/alpha-o active site in fe-cha zeolite for the low-temperature activation of the methane c-h bond. *J Am Chem Soc* **2018**, *140*, 12021-12032.
(169) Snyder, B. E. R.; Bottger, L. H.; Bols, M. L.; Yan, J. J.; Rhoda, H. M.; Jacobs, A. B.; Hu, M. Y.; Zhao, J.; Alp, E. E.; Hedman, B.; et al. Structural characterization of a non-heme iron active site in zeolites that hydroxylates methane. *Proc Natl Acad Sci U S A* **2018**, *115*, 4565-4570.
(170) Bols, M. L.; Snyder, B. E. R.; Rhoda, H. M.; Cnudde, P.; Fayad, G.; Schoonheydt, R. A.; Van Speybroeck, V.; Solomon, E. I.; Sels, B. F. Coordination and activation of nitrous oxide by iron zeolites. *Nat Catal* **2021**, *4*, 332-340.
(171) Bols, M. L.; Rhoda, H. M.; Snyder, B. E. R.; Solomon, E. I.; Pierloot, K.; Schoonheydt, R. A.; Sels, B. F. Advances in the synthesis, characterisation, and mechanistic understanding of active sites in fe-zeolites for redox catalysts. *Dalton Trans* **2020**, *49*, 14749-14757.
(172) Bols, M. L.; Devos, J.; Rhoda, H. M.; Plessers, D.; Solomon, E. I.; Schoonheydt, R. A.; Sels, B. F.; Dusselier, M. Selective formation of alpha-fe(ii) sites on fe-zeolites through one-pot synthesis. *J Am Chem Soc* **2021**, *143*, 16243-16255.
(173) Bols, M. L. The alpha-fe and alpha-o sites in fe zeolites. KU Leuven, Leuven, 2019.
(174) Sushkevich, V. L.; Palagin, D.; Ranocchiari, M.; van Bokhoven, J. A. Selective anaerobic oxidation of methane enables direct synthesis of methanol. *Science* **2017**, *356*, 523-527.
(175) Koishybay, A.; Shantz, D. F. Water is the oxygen source for methanol produced in partial oxidation of methane in a flow reactor over cu-ssz-13. *J Am Chem Soc* **2020**, *142*, 11962-11966.
(176) Dummer, N. F.; Willock, D. J.; He, Q.; Howard, M. J.; Lewis, R. J.; Qi, G.; Taylor, S. H.; Xu, J.; Bethell, D.; Kiely, C. J.; Hutchings, G. J. Methane oxidation to methanol. *Chem Rev* **2023**, *123*, 6359-6411.
(177) Newton, M. A.; Knorpp, A. J.; Sushkevich, V. L.; Palagin, D.; van Bokhoven, J. A. Active sites and mechanisms in the direct conversion of methane to methanol using cu in zeolitic hosts: A critical examination. *Chem Soc Rev* **2020**, *49*, 1449-1486.
(178) Ikuno, T.; Grundner, S.; Jentys, A.; Li, G.; Pidko, E.; Fulton, J.; Sanchez-Sanchez, M.; Lercher, J. A. Formation of active cu-oxo clusters for methane oxidation in cu-exchanged mordenite. *J Phys Chem C* **2019**, *123*, 8759-8769.
(179) Kulkarni, A. R.; Zhao, Z.-J.; Siahrostami, S.; Nørskov, J. K.; Studt, F. Cation-exchanged zeolites for the selective oxidation of methane to methanol. *Catal Sci Technol* **2018**, *8*, 114-123.
(180) Zhao, Z.-J.; Kulkarni, A.; Vilella, L.; Nørskov, J. K.; Studt, F. Theoretical insights into the selective oxidation of methane to methanol in copper-exchanged mordenite. *ACS Catal* **2016**, *6*, 3760-3766.
(181) Wang, G.; Huang, L.; Chen, W.; Zhou, J.; Zheng, A. Rationally designing mixed cu-(mu-o)-m (m = cu, ag, zn, au) centers over zeolite materials with high catalytic activity towards methane activation. *Phys Chem Chem Phys* **2018**, *20*, 26522-26531.
(182) Mahyuddin, M. H.; Tanaka, T.; Shiota, Y.; Staykov, A.; Yoshizawa, K. Methane partial oxidation over [cu2(μ-o)]2+ and [cu3(μ-o)3]2+ active species in large-pore zeolites. *ACS Catal* **2018**, *8*, 1500-1509.

(183) Vanelderen, P.; Vancauwenbergh, J.; Tsai, M. L.; Hadt, R. G.; Solomon, E. I.; Schoonheydt, R. A.; Sels, B. F. Spectroscopy and redox chemistry of copper in mordenite. *Chemphyschem* **2014**, *15*, 91-99.
(184) Ravi, M.; Sushkevich, V. L.; Knorpp, A. J.; Newton, M. A.; Palagin, D.; Pinar, A. B.; Ranocchiari, M.; van Bokhoven, J. A. Misconceptions and challenges in methane-to-methanol over transition-metal-exchanged zeolites. *Nat Catal* **2019**, *2*, 485-494.
(185) Latimer, A. A.; Kakekhani, A.; Kulkarni, A. R.; Nørskov, J. K. Direct methane to methanol: The selectivity–conversion limit and design strategies. *ACS Catal* **2018**, *8*, 6894-6907.
(186) Bond, G. C. The use of kinetics in evaluating mechanisms in heterogeneous catalysis. *Cat Rev - Sci Eng* **2008**, *50*, 532-567.
(187) Tsai, M. L.; Hadt, R. G.; Vanelderen, P.; Sels, B. F.; Schoonheydt, R. A.; Solomon, E. I. [cu2o]2+ active site formation in cu-zsm-5: Geometric and electronic structure requirements for n2o activation. *J Am Chem Soc* **2014**, *136*, 3522-3529.
(188) Smeets, P. J.; Hadt, R. G.; Woertink, J. S.; Vanelderen, P.; Schoonheydt, R. A.; Sels, B. F.; Solomon, E. I. Oxygen precursor to the reactive intermediate in methanol synthesis by cu-zsm-5. *J Am Chem Soc* **2010**, *132*, 14736-14738.
(189) Wiberg, K. B. The deuterium isotope effect. *Chem Rev* **2002**, *55*, 713-743.
(190) Ipek, B.; Wulfers, M. J.; Kim, H.; Göltl, F.; Hermans, I.; Smith, J. P.; Booksh, K. S.; Brown, C. M.; Lobo, R. F. Formation of [cu2o2]2+ and [cu2o]2+ toward c–h bond activation in cu-ssz-13 and cu-ssz-39. *ACS Catal* **2017**, *7*, 4291-4303.
(191) Han, L.; Cai, S.; Gao, M.; Hasegawa, J. Y.; Wang, P.; Zhang, J.; Shi, L.; Zhang, D. Selective catalytic reduction of no(x) with nh(3) by using novel catalysts: State of the art and future prospects. *Chem Rev* **2019**, *119*, 10916-10976.
(192) Paolucci, C.; Khurana, I.; Parekh, A. A.; Li, S.; Shih, A. J.; Li, H.; Di Iorio, J. R.; Albarracin-Caballero, J. D.; Yezerets, A.; Miller, J. T.; et al. Dynamic multinuclear sites formed by mobilized copper ions in no (x) selective catalytic reduction. *Science* **2017**, *357*, 898-903.
(193) Villamaina, R.; Liu, S.; Nova, I.; Tronconi, E.; Ruggeri, M. P.; Collier, J.; York, A.; Thompsett, D. Speciation of cu cations in cu-cha catalysts for nh3-scr: Effects of sio2/alo3 ratio and cu-loading investigated by transient response methods. *ACS Catal* **2019**, *9*, 8916-8927.
(194) Hun Kwak, J.; Zhu, H.; Lee, J. H.; Peden, C. H.; Szanyi, J. Two different cationic positions in cu-ssz-13? *Chem Commun (Camb)* **2012**, *48*, 4758-4760.
(195) Negri, C.; Signorile, M.; Porcaro, N. G.; Borfecchia, E.; Berlier, G.; Janssens, T. V. W.; Bordiga, S. Dynamic cuii/cui speciation in cu-cha catalysts by in situ diffuse reflectance uv–vis-nir spectroscopy. *Appl Catal A Gen* **2019**, *578*, 1-9.
(196) Negri, C.; Selleri, T.; Borfecchia, E.; Martini, A.; Lomachenko, K. A.; Janssens, T. V. W.; Cutini, M.; Bordiga, S.; Berlier, G. Structure and reactivity of oxygen-bridged diamino dicopper(ii) complexes in cu-ion-exchanged chabazite catalyst for nh(3)-mediated selective catalytic reduction. *J Am Chem Soc* **2020**, *142*, 15884-15896.
(197) Lei, H.; Chen, D.; Yang, J.-y.; Khetan, A.; Jiang, J.; Peng, B.; Simon, U.; Ye, D.; Chen, P. Revealing the formation and reactivity of cage-confined cu pairs in catalytic nox reduction over cu-ssz-13 zeolites by in situ uv–vis spectroscopy and time-dependent dft calculation. *Env Sci Technol* **2023**,
(198) Li, H.; Paolucci, C.; Khurana, I.; Wilcox, L. N.; Goltl, F.; Albarracin-Caballero, J. D.; Shih, A. J.; Ribeiro, F. H.; Gounder, R.; Schneider, W. F. Consequences of exchange-site heterogeneity and dynamics on the uv-visible spectrum of cu-exchanged ssz-13. *Chem Sci* **2019**, *10*, 2373-2384.

(199) Borfecchia, E.; Lomachenko, K. A.; Giordanino, F.; Falsig, H.; Beato, P.; Soldatov, A. V.; Bordiga, S.; Lamberti, C. Revisiting the nature of cu sites in the activated cu-ssz-13 catalyst for scr reaction. *Chem Sci* **2015**, *6*, 548-563.
(200) Paolucci, C.; Verma, A. A.; Bates, S. A.; Kispersky, V. F.; Miller, J. T.; Gounder, R.; Delgass, W. N.; Ribeiro, F. H.; Schneider, W. F. Isolation of the copper redox steps in the standard selective catalytic reduction on cu-ssz-13. *Angew Chem Int Ed Engl* **2014**, *53*, 11828-11833.
(201) Gao, F.; Mei, D.; Wang, Y.; Szanyi, J.; Peden, C. H. Selective catalytic reduction over cu/ssz-13: Linking homo- and heterogeneous catalysis. *J Am Chem Soc* **2017**, *139*, 4935-4942.
(202) Greenaway, A. G.; Marberger, A.; Thetford, A.; Lezcano-Gonzalez, I.; Agote-Aran, M.; Nachtegaal, M.; Ferri, D.; Krocher, O.; Catlow, C. R. A.; Beale, A. M. Detection of key transient cu intermediates in ssz-13 during nh(3)-scr deno (x) by modulation excitation ir spectroscopy. *Chem Sci* **2020**, *11*, 447-455.
(203) Giordanino, F.; Borfecchia, E.; Lomachenko, K. A.; Lazzarini, A.; Agostini, G.; Gallo, E.; Soldatov, A. V.; Beato, P.; Bordiga, S.; Lamberti, C. Interaction of nh3 with cu-ssz-13 catalyst: A complementary ftir, xanes, and xes study. *J Phys Chem Lett* **2014**, *5*, 1552-1559.
(204) Liu, C.; Kubota, H.; Amada, T.; Toyao, T.; Maeno, Z.; Ogura, M.; Nakazawa, N.; Inagaki, S.; Kubota, Y.; Shimizu, K.-i. Selective catalytic reduction of no over cu-afx zeolites: Mechanistic insights from in situ/operando spectroscopic and dft studies. *Catal Sci Technol* **2021**, *11*, 4459-4470.
(205) Solomon, E. I.; Heppner, D. E.; Johnston, E. M.; Ginsbach, J. W.; Cirera, J.; Qayyum, M.; Kieber-Emmons, M. T.; Kjaergaard, C. H.; Hadt, R. G.; Tian, L. Copper active sites in biology. *Chem Rev* **2014**, *114*, 3659-3853.
(206) Solomon, E. I.; Ginsbach, J. W.; Heppner, D. E.; Kieber-Emmons, M. T.; Kjaergaard, C. H.; Smeets, P. J.; Tian, L.; Woertink, J. S. Copper dioxygen (bio)inorganic chemistry. *Faraday Discuss* **2011**, *148*, 11-39.
(207) Solomon, E. I.; Chen, P.; Metz, M.; Lee, S.-K.; Palmer, A. E. Oxygen binding, activation, and reduction to water by copper proteins. *Angew Chem Int Ed* **2001**, *40*, 4570-4590.
(208) Liu, C.; Kubota, H.; Amada, T.; Kon, K.; Toyao, T.; Maeno, Z.; Ueda, K.; Ohyama, J.; Satsuma, A.; Tanigawa, T.; et al. In situ spectroscopic studies on the redox cycle of nh3−scr over cu−cha zeolites. *ChemCatChem* **2020**, *12*, 3050-3059.
(209) Zhang, Y.; Zhang, J.; Wang, H.; Yang, W.; Wang, C.; Peng, Y.; Chen, J.; Li, J.; Gao, F. Selective catalytic reduction of nox with nh3 over cu/ssz-13: Elucidating dynamics of cu active sites with in situ uv–vis spectroscopy and dft calculations. *J Phys Chem C* **2022**, *126*, 8720-8733.
(210) Paolucci, C.; Parekh, A. A.; Khurana, I.; Di Iorio, J. R.; Li, H.; Albarracin Caballero, J. D.; Shih, A. J.; Anggara, T.; Delgass, W. N.; Miller, J. T.; et al. Catalysis in a cage: Condition-dependent speciation and dynamics of exchanged cu cations in ssz-13 zeolites. *J Am Chem Soc* **2016**, *138*, 6028-6048.
(211) Godiksen, A.; Isaksen, O. L.; Rasmussen, S. B.; Vennestrøm, P. N. R.; Mossin, S. Site-specific reactivity of copper chabazite zeolites with nitric oxide, ammonia, and oxygen. *ChemCatChem* **2018**, *10*, 366-370.
(212) Oda, A.; Shionoya, H.; Hotta, Y.; Takewaki, T.; Sawabe, K.; Satsuma, A. Spectroscopic evidence of efficient generation of dicopper intermediate in selective catalytic reduction of no over cu-ion-exchanged zeolites. *ACS Catal* **2020**, *10*, 12333-12339.
(213) Elwell, C. E.; Gagnon, N. L.; Neisen, B. D.; Dhar, D.; Spaeth, A. D.; Yee, G. M.; Tolman, W. B. Copper-oxygen complexes revisited: Structures, spectroscopy, and reactivity. *Chem Rev* **2017**, *117*, 2059-2107.

(214) Halfen, J. A.; Mahapatra, S.; Wilkinson, E. C.; Kaderli, S.; Young, V. G., Jr.; Que, L., Jr.; Zuberbuhler, A. D.; Tolman, W. B. Reversible cleavage and formation of the dioxygen o-o bond within a dicopper complex. *Science* **1996**, *271*, 1397-1400.
(215) Chen, J.; Huang, W.; Bao, S.; Zhang, W.; Liang, T.; Zheng, S.; Yi, L.; Guo, L.; Wu, X. A review on the characterization of metal active sites over cu-based and fe-based zeolites for nh(3)-scr. *RSC Adv* **2022**, *12*, 27746-27765.
(216) Colombo, M.; Nova, I.; Tronconi, E. A comparative study of the nh3-scr reactions over a cu-zeolite and a fe-zeolite catalyst. *Catal Today* **2010**, *151*, 223-230.
(217) Grossale, A.; Nova, I.; Tronconi, E. Study of a fe–zeolite-based system as nh3-scr catalyst for diesel exhaust aftertreatment. *Catal Today* **2008**, *136*, 18-27.
(218) Liu, Q.; Bian, C.; Ming, S.; Guo, L.; Zhang, S.; Pang, L.; Liu, P.; Chen, Z.; Li, T. The opportunities and challenges of iron-zeolite as nh3-scr catalyst in purification of vehicle exhaust. *Appl Catal A Gen* **2020**, *607*,
(219) Li, J.; Chang, H.; Ma, L.; Hao, J.; Yang, R. T. Low-temperature selective catalytic reduction of nox with nh3 over metal oxide and zeolite catalysts—a review. *Catal Today* **2011**, *175*, 147-156.
(220) Pérez Vélez, R.; Ellmers, I.; Huang, H.; Bentrup, U.; Schünemann, V.; Grünert, W.; Brückner, A. Identifying active sites for fast nh3-scr of no/no2 mixtures over fe-zsm-5 by operando epr and uv–vis spectroscopy. *J Catal* **2014**, *316*, 103-111.
(221) Martin, N.; Vennestrom, P. N. R.; Thogersen, J. R.; Moliner, M.; Corma, A. Fe-containing zeolites for nh(3) -scr of no(x) : Effect of structure, synthesis procedure, and chemical composition on catalytic performance and stability. *Chemistry* **2017**, *23*, 13404-13414.
(222) Brandenberger, S.; Kröcher, O.; Tissler, A.; Althoff, R. The state of the art in selective catalytic reduction of noxby ammonia using metal-exchanged zeolite catalysts. *Cat Rev - Sci Eng* **2008**, *50*, 492-531.
(223) Kim, J.; Jentys, A.; Maier, S. M.; Lercher, J. A. Characterization of fe-exchanged bea zeolite under nh3 selective catalytic reduction conditions. *J Phys Chem C* **2013**, *117*, 986-993.
(224) Yu, T.; Li, Z.; Jones, W.; Liu, Y.; He, Q.; Song, W.; Du, P.; Yang, B.; An, H.; Farmer, D. M.; et al. Identifying key mononuclear fe species for low-temperature methane oxidation. *Chem Sci* **2021**, *12*, 3152-3160.
(225) Chen, J.; Peng, G.; Zheng, W.; Zhang, W.; Guo, L.; Wu, X. Excellent performance of one-pot synthesized fe-containing mcm-22 zeolites for the selective catalytic reduction of nox with nh3. *Catal Sci Technol* **2020**, *10*, 6583-6598.
(226) Pérez-Ramírez, J.; Groen, J. C.; Brückner, A.; Kumar, M. S.; Bentrup, U.; Debbagh, M. N.; Villaescusa, L. A. Evolution of isomorphously substituted iron zeolites during activation: Comparison of fe-beta and fe-zsm-5. *J Catal* **2005**, *232*, 318-334.
(227) Yasumura, S.; Qian, Y.; Kato, T.; Mine, S.; Toyao, T.; Maeno, Z.; Shimizu, K.-i. In situ/operando spectroscopic studies on the nh3–scr mechanism over fe–zeolites. *ACS Catal* **2022**, *12*, 9983-9993.
(228) Kovarik, L.; Washton, N. M.; Kukkadapu, R.; Devaraj, A.; Wang, A.; Wang, Y.; Szanyi, J.; Peden, C. H. F.; Gao, F. Transformation of active sites in fe/ssz-13 scr catalysts during hydrothermal aging: A spectroscopic, microscopic, and kinetics study. *ACS Catal* **2017**, *7*, 2458-2470.
(229) Hallaert, S. D.; Bols, M. L.; Vanelderen, P.; Schoonheydt, R. A.; Sels, B. F.; Pierloot, K. Identification of alpha-fe in high-silica zeolites on the basis of ab initio electronic structure calculations. *Inorg Chem* **2017**, *56*, 10681-10690.
(230) Hallaert, S. D. The reactive α-fe and α-o sites in fe-containing zeolites as a biomimetic catalyst for methane hydroxylation: A theoretical insight. KU Leuven, Leuven, 2019.

(231) Snyder, B. E. R.; Bols, M. L.; Rhoda, H. M.; Plessers, D.; Schoonheydt, R. A.; Sels, B. F.; Solomon, E. I. Cage effects control the mechanism of methane hydroxylation in zeolites. *Science* **2021**, *373*, 327-331.
(232) Li, W.; Guo, Z.; Yang, J.; Li, Y.; Sun, X.; He, H.; Li, S.; Zhang, J. Advanced strategies for stabilizing single-atom catalysts for energy storage and conversion. *Electrochemical Energy Reviews* **2022**, *5*, 9.
(233) Kaiser, S. K.; Chen, Z.; Faust Akl, D.; Mitchell, S.; Pérez-Ramírez, J. Single-atom catalysts across the periodic table. *Chem Rev* **2020**, *120*, 11703-11809.
(234) Mitchell, S.; Pérez-Ramírez, J. Single atom catalysis: A decade of stunning progress and the promise for a bright future. *Nat Commun* **2020**, *11*, 4302.
(235) Sui, J.; Liu, H.; Hu, S.; Sun, K.; Wan, G.; Zhou, H.; Zheng, X.; Jiang, H.-L. A general strategy to immobilize single-atom catalysts in metal–organic frameworks for enhanced photocatalysis. *Adv Mater* **2022**, *34*, 2109203.
(236) Kerketta, U.; Tesler, A. B.; Schmuki, P. Single-atom co-catalysts employed in titanium dioxide photocatalysis. In *Catalysts*, 2022; Vol. 12.
(237) Shang, Q.; Tang, N.; Qi, H.; Chen, S.; Xu, G.; Wu, C.; Pan, X.; Wang, X.; Cong, Y. A palladium single-atom catalyst toward efficient activation of molecular oxygen for cinnamyl alcohol oxidation. *Chinese J Cat* **2020**, *41*, 1812-1817.
(238) Bozbag, S. E.; Sot, P.; Nachtegaal, M.; Ranocchiari, M.; van Bokhoven, J. A.; Mesters, C. Direct stepwise oxidation of methane to methanol over cu–sio2. *ACS Catal* **2018**, *8*, 5721-5731.
(239) Wang, C.; Xu, J.; Deng, F. Mechanism of methanol-to-hydrocarbon reaction over zeolites: A solid-state nmr perspective. *ChemCatChem* **2020**, *12*, 965-980.
(240) Chang, C. The conversion of methanol and other o-compounds to hydrocarbons over zeolite catalysts. *J Catal* **1977**, *47*, 249-259.
(241) Chang, C.; Lang, W. H. Process for manufacturing olefins. Unisted States 1976.
(242) Wang, S.; Qin, Z.; Dong, M.; Wang, J.; Fan, W. Recent progress on mto reaction mechanisms and regulation of acid site distribution in the zeolite framework. *Chem Catalysis* **2022**, *2*, 1657-1685.
(243) Plessow, P. N.; Smith, A.; Tischer, S.; Studt, F. Identification of the reaction sequence of the mto initiation mechanism using ab initio-based kinetics. *J Am Chem Soc* **2019**, *141*, 5908-5915.
(244) Ilias, S.; Bhan, A. Mechanism of the catalytic conversion of methanol to hydrocarbons. *ACS Catal* **2012**, *3*, 18-31.
(245) Wang, C.-M.; Wang, Y.-D.; Xie, Z.-K. Insights into the reaction mechanism of methanol-to-olefins conversion in hsapo-34 from first principles: Are olefins themselves the dominating hydrocarbon pool species? *J Catal* **2013**, *301*, 8-19.
(246) Sun, Q.; Xie, Z.; Yu, J. The state-of-the-art synthetic strategies for sapo-34 zeolite catalysts in methanol-to-olefin conversion. *Natl Sci Rev* **2018**, *5*, 542-558.
(247) Yang, M.; Fan, D.; Wei, Y.; Tian, P.; Liu, Z. Recent progress in methanol-to-olefins (mto) catalysts. *Adv Mater* **2019**, *31*, e1902181.
(248) Vora, B. V.; Marker, T. L.; Barger, P. T.; Nilsen, H. R.; Kvisle, S.; Fuglerud, T. Economic route for natural gas conversion to ethylene and propylene. In *Natural gas conversion iv*, Studies in surface science and catalysis, 1997; pp 87-98.
(249) Liang, J.; Li, H.; Zhao, S.; Guo, W.; Wang, R.; Ying, M. Characteristics and performance of sapo-34 catalyst for methanol-to-olefin conversion. *Appl Catal* **1990**, *64*, 31-40.
(250) Koempel, H.; Liebner, W. Lurgi's methanol to propylene (mtp®) report on a successful commercialisation. In *Natural gas conversion viii, proceedings of the 8th natural gas conversion symposium*, Studies in surface science and catalysis, 2007; pp 261-267.

(251) Liu, Y.; Muller, S.; Berger, D.; Jelic, J.; Reuter, K.; Tonigold, M.; Sanchez-Sanchez, M.; Lercher, J. A. Corrigendum: Formation mechanism of the first carbon-carbon bond and the first olefin in the methanol conversion into hydrocarbons. *Angew Chem Int Ed Engl* **2017**, *56*, 7342.
(252) Li, J.; Wei, Z.; Chen, Y.; Jing, B.; He, Y.; Dong, M.; Jiao, H.; Li, X.; Qin, Z.; Wang, J.; Fan, W. A route to form initial hydrocarbon pool species in methanol conversion to olefins over zeolites. *J Catal* **2014**, *317*, 277-283.
(253) Tajima, N.; Tsuneda, T.; Toyama, F.; Hirao, K. A new mechanism for the first carbon−carbon bond formation in the mtg process: A theoretical study. *J Am Chem Soc* **1998**, *120*, 8222-8229.
(254) Chowdhury, A. D.; Houben, K.; Whiting, G. T.; Mokhtar, M.; Asiri, A. M.; Al-Thabaiti, S. A.; Basahel, S. N.; Baldus, M.; Weckhuysen, B. M. Initial carbon-carbon bond formation during the early stages of the methanol-to-olefin process proven by zeolite-trapped acetate and methyl acetate. *Angew Chem Int Ed Engl* **2016**, *55*, 15840-15845.
(255) Wulfers, M. J.; Jentoft, F. C. The role of cyclopentadienium ions in methanol-to-hydrocarbons chemistry. *ACS Catal* **2014**, *4*, 3521-3532.
(256) Dai, W.; Wang, C.; Dyballa, M.; Wu, G.; Guan, N.; Li, L.; Xie, Z.; Hunger, M. Understanding the early stages of the methanol-to-olefin conversion on h-sapo-34. *ACS Catal* **2014**, *5*, 317-326.
(257) Olsbye, U.; Svelle, S.; Lillerud, K. P.; Wei, Z. H.; Chen, Y. Y.; Li, J. F.; Wang, J. G.; Fan, W. B. The formation and degradation of active species during methanol conversion over protonated zeotype catalysts. *Chem Soc Rev* **2015**, *44*, 7155-7176.
(258) Yarulina, I.; Chowdhury, A. D.; Meirer, F.; Weckhuysen, B. M.; Gascon, J. Recent trends and fundamental insights in the methanol-to-hydrocarbons process. *Nat Catal* **2018**, *1*, 398-411.
(259) Borodina, E.; Sharbini Harun Kamaluddin, H.; Meirer, F.; Mokhtar, M.; Asiri, A. M.; Al-Thabaiti, S. A.; Basahel, S. N.; Ruiz-Martinez, J.; Weckhuysen, B. M. Influence of the reaction temperature on the nature of the active and deactivating species during methanol-to-olefins conversion over h-sapo-34. *ACS Catal* **2017**, *7*, 5268-5281.
(260) Van Speybroeck, V.; Hemelsoet, K.; De Wispelaere, K.; Qian, Q.; Van der Mynsbrugge, J.; De Sterck, B.; Weckhuysen, B. M.; Waroquier, M. Mechanistic studies on chabazite-type methanol-to-olefin catalysts: Insights from time-resolved uv/vis microspectroscopy combined with theoretical simulations. *ChemCatChem* **2013**, *5*, 173-184.
(261) Bjorgen, M.; Bonino, F.; Kolboe, S.; Lillerud, K. P.; Zecchina, A.; Bordiga, S. Spectroscopic evidence for a persistent benzenium cation in zeolite h-beta. *J Am Chem Soc* **2003**, *125*, 15863-15868.
(262) Dai, W.; Wu, G.; Li, L.; Guan, N.; Hunger, M. Mechanisms of the deactivation of sapo-34 materials with different crystal sizes applied as mto catalysts. *ACS Catal* **2013**, *3*, 588-596.
(263) Goetze, J.; Meirer, F.; Yarulina, I.; Gascon, J.; Kapteijn, F.; Ruiz-Martinez, J.; Weckhuysen, B. M. Insights into the activity and deactivation of the methanol-to-olefins process over different small-pore zeolites as studied with operando uv-vis spectroscopy. *ACS Catal* **2017**, *7*, 4033-4046.
(264) Kiricsi, I.; Forster, H.; Tasi, G.; Nagy, J. B. Generation, characterization, and transformations of unsaturated carbenium ions in zeolites. *Chem Rev* **1999**, *99*, 2085-2114.
(265) Park, J. W.; Lee, J. Y.; Kim, K. S.; Hong, S. B.; Seo, G. Effects of cage shape and size of 8-membered ring molecular sieves on their deactivation in methanol-to-olefin (mto) reactions. *Appl Catal A Gen* **2008**, *339*, 36-44.

(266) Dai, W.; Scheibe, M.; Guan, N.; Li, L.; Hunger, M. Fate of brønsted acid sites and benzene-based carbenium ions during methanol-to-olefin conversion on sapo-34. *ChemCatChem* **2011**, *3*, 1130-1133.
(267) Qian, Q.; Vogt, C.; Mokhtar, M.; Asiri, A. M.; Al-Thabaiti, S. A.; Basahel, S. N.; Ruiz-Martínez, J.; Weckhuysen, B. M. Combined operando uv/vis/ir spectroscopy reveals the role of methoxy and aromatic species during the methanol-to-olefins reaction over h-sapo-34. *ChemCatChem* **2014**, *6*, 3396-3408.
(268) Goetze, J.; Weckhuysen, B. M. Spatiotemporal coke formation over zeolite zsm-5 during the methanol-to-olefins process as studied with operando uv-vis spectroscopy: A comparison between h-zsm-5 and mg-zsm-5. *Catal Sci Technol* **2018**, *8*, 1632-1644.
(269) Goetze, J.; Yarulina, I.; Gascon, J.; Kapteijn, F.; Weckhuysen, B. M. Revealing lattice expansion of small-pore zeolite catalysts during the methanol-to-olefins process using combined operando x-ray diffraction and uv–vis spectroscopy. *ACS Catal* **2018**, *8*, 2060-2070.
(270) Watson, M. D.; Fechtenkotter, A.; Mullen, K. Big is beautiful--"aromaticity" revisited from the viewpoint of macromolecular and supramolecular benzene chemistry. *Chem Rev* **2001**, *101*, 1267-1300.
(271) Yarulina, I.; De Wispelaere, K.; Bailleul, S.; Goetze, J.; Radersma, M.; Abou-Hamad, E.; Vollmer, I.; Goesten, M.; Mezari, B.; Hensen, E. J. M.; et al. Structure-performance descriptors and the role of lewis acidity in the methanol-to-propylene process. *Nat Chem* **2018**, *10*, 804-812.
(272) Le, T. T.; Qin, W.; Agarwal, A.; Nikolopoulos, N.; Fu, D.; Patton, M. D.; Weiland, C.; Bare, S. R.; Palmer, J. C.; Weckhuysen, B. M.; Rimer, J. D. Elemental zoning enhances mass transport in zeolite catalysts for methanol to hydrocarbons. *Nat Catal* **2023**, *6*, 254-265.
(273) Köhnke, K.; Wessel, N.; Esteban, J.; Jin, J.; Vorholt, A. J.; Leitner, W. Operandomonitoring of mechanisms and deactivation of molecular catalysts. *Green Chemistry* **2022**, *24*, 1951-1972.
(274) Bauer, M.; Heusel, G.; Mangold, S.; Bertagnolli, H. Spectroscopic set-up for simultaneous uv-vis/(q)exafs in situ and in operando studies of homogeneous reactions under laboratory conditions. *J Synchrotron Radiat* **2010**, *17*, 273-279.
(275) Garland, M.; Li, C.; Guo, L. Four criteria for evaluating pure component spectral estimates and the subsequent identification of intermediates in homogeneous catalysis. *ACS Catal* **2012**, *2*, 2327-2334.
(276) Hamann, J. N.; Hermsen, M.; Schmidt, A.-C.; Krieg, S.; Schießl, J.; Riedel, D.; Teles, J. H.; Schäfer, A.; Comba, P.; Hashmi, A. S. K.; Schaub, T. Selective decomposition of cyclohexyl hydroperoxide using homogeneous and heterogeneous crvi catalysts: Optimizing the reaction by evaluating the reaction mechanism. *ChemCatChem* **2018**, *10*, 2755-2767.
(277) Seegerer, A.; Nitschke, P.; Gschwind, R. M. Combined in situ illumination-nmr-uv/vis spectroscopy: A new mechanistic tool in photochemistry. *Angew Chem Int Ed Engl* **2018**, *57*, 7493-7497.
(278) Puthilibai, G.; Vasudhevan, S.; Kutti Rani, S.; Rajagopal, G. Synthesis, spectroscopic characterization, electrochemical behaviour and antibacterial activity of ru(iii) complexes of 2-[(4-n,n'-dimethylaminophenylimino)-methyl]-4-halophenol. *Spectrochim Acta A Mol Biomol Spectrosc* **2009**, *72*, 796-800.
(279) Hussain, I.; Ullah, A.; Khan, A. U.; Khan, W. U.; Ullah, R.; Almoqbil A. Naser, A. A. S.; Mahmood, H. M. Synthesis, characterization and biological activities of hydrazone schiff base and its novel metals complexes. *Sains Malaysiana* **2019**, *48*, 1439-1446.
(280) Oter, O.; Ertekin, K.; Dayan, O.; Cetinkaya, B. Photocharacterization of novel ruthenium dyes and their utilities as oxygen sensing materials in presence of perfluorochemicals. *J Fluoresc* **2008**, *18*, 269-276.

(281) Forcina, V.; García-Domínguez, A.; Lloyd-Jones, G. C. Kinetics of initiation of the third generation grubbs metathesis catalyst: Convergent associative and dissociative pathways. *Faraday Discuss* **2019**, *220*, 179-195.
(282) Gil-Sepulcre, M.; Böhler, M.; Schilling, M.; Bozoglian, F.; Bachmann, C.; Scherrer, D.; Fox, T.; Spingler, B.; Gimbert-Suriñach, C.; Alberto, R.; et al. Ruthenium water oxidation catalysts based on pentapyridyl ligands. *ChemSusChem* **2017**, *10*, 4517-4525.
(283) Fischer, C.; König, A.; Meißner, A.; Thede, R.; Selle, C.; Pribbenow, C.; Heller, D. Quantitative uv/vis spectroscopic investigations of the in situ synthesis of neutral μ-2-chloro-bridged dinuclear (diphosphine)rhodium complexes. *Eur J Inorg Chem* **2014**, *2014*, 5849-5855.
(284) Meissner, A.; Konig, A.; Drexler, H. J.; Thede, R.; Baumann, W.; Heller, D. New pentacoordinated rhodium species as unexpected products during the in situ generation of dimeric diphosphine-rhodium neutral catalysts. *Chemistry* **2014**, *20*, 14721-14728.
(285) Meißner, A.; Preetz, A.; Drexler, H. J.; Baumann, W.; Spannenberg, A.; König, A.; Heller, D. In situ synthesis of neutral dinuclear rhodium diphosphine complexes [{rh(diphosphine)(μ2-x)}2]: Systematic investigations. *ChemPlusChem* **2014**, *80*, 169-180.
(286) Stambuli, J. P.; Incarvito, C. D.; Buhl, M.; Hartwig, J. F. Synthesis, structure, theoretical studies, and ligand exchange reactions of monomeric, t-shaped arylpalladium(ii) halide complexes with an additional, weak agostic interaction. *J Am Chem Soc* **2004**, *126*, 1184-1194.
(287) Guilera, G.; Newton, M. A.; Polli, C.; Pascarelli, S.; Guino, M.; Hii, K. K. In situ investigation of the oxidative addition in homogeneous pd catalysts by synchronised time resolved uv-vis/exafs. *Chem Commun (Camb)* **2006**, 4306-4308.
(288) Solomon, E. I.; Neidig, M. L.; Schenk, G. 2.26 - magnetic circular dichroism of paramagnetic species. In *Comprehensive coordination chemistry ii*, McCleverty, J. A., Meyer, T. J. Eds.; Pergamon, 2003; pp 339-349.
(289) Dawber, J. G. The faraday effect, magnetic rotatory dispersion and magnetic circular dichroism. A review. *Analyst* **1964**, *89*, 755-762.
(290) Wolford, N. J.; Radovic, A.; Neidig, M. L. C-term magnetic circular dichroism (mcd) spectroscopy in paramagnetic transition metal and f-element organometallic chemistry. *Dalton Trans* **2021**, *50*, 416-428.
(291) Shin, J.; Gwon, S.; Kim, S.; Lee, J.; Park, K. Correlation between the c–c cross-coupling activity and c-to-ni charge transfer transition of high-valent ni complexes. *J Am Chem Soc* **2020**, *142*, 4173-4183.
(292) Neidig, M. L.; Carpenter, S. H.; Curran, D. J.; DeMuth, J. C.; Fleischauer, V. E.; Iannuzzi, T. E.; Neate, P. G. N.; Sears, J. D.; Wolford, N. J. Development and evolution of mechanistic understanding in iron-catalyzed cross-coupling. *Acc Chem Res* **2019**, *52*, 140-150.
(293) Daifuku, S. L.; Al-Afyouni, M. H.; Snyder, B. E. R.; Kneebone, J. L.; Neidig, M. L. A combined mössbauer, magnetic circular dichroism, and density functional theory approach for iron cross-coupling catalysis: Electronic structure, in situ formation, and reactivity of iron-mesityl-bisphosphines. *J Am Chem Soc* **2014**, *136*, 9132-9143.
(294) Daifuku, S. L.; Kneebone, J. L.; Snyder, B. E. R.; Neidig, M. L. Iron(ii) active species in iron–bisphosphine catalyzed kumada and suzuki–miyaura cross-couplings of phenyl nucleophiles and secondary alkyl halides. *J Am Chem Soc* **2015**, *137*, 11432-11444.
(295) Jo, H. H.; Lin, C.-Y.; Anslyn, E. V. Rapid optical methods for enantiomeric excess analysis: From enantioselective indicator displacement assays to exciton-coupled circular dichroism. *Acc Chem Res* **2014**, *47*, 2212-2221.
(296) Mortezaei, S.; Catarineu, N. R.; Duan, X.; Hu, C.; Canary, J. W. Redox-configurable ambidextrous catalysis: Structural and mechanistic insight. *Chem Sci* **2015**, *6*, 5904-5912.

(297) Fischer, C.; Beweries, T.; Preetz, A.; Drexler, H.-J.; Baumann, W.; Peitz, S.; Rosenthal, U.; Heller, D. Kinetic and mechanistic investigations in homogeneous catalysis using operando uv/vis spectroscopy. *Catal Today* **2010**, *155*, 282-288.
(298) Beweries, T.; Fischer, C.; Peitz, S.; Burlakov, V. V.; Arndt, P.; Baumann, W.; Spannenberg, A.; Heller, D.; Rosenthal, U. Combination of spectroscopic methods: In situ nmr and uv/vis measurements to understand the formation of group 4 metallacyclopentanes from the corresponding metallacyclopropenes. *J Am Chem Soc* **2009**, *131*, 4463-4469.
(299) Mansel, S.; Thomas, D.; Lefeber, C.; Heller, D.; Kempe, R.; Baumann, W.; Rosenthal, U. Stable rac-[1,2-ethylene-1,1‘-bis(η5-tetrahydroindenyl)]- zirconacyclopentanes. Syntheses, x-ray crystal structures, stability, and catalysis of ethylene polymerization. *Organometallics* **1997**, *16*, 2886-2890.
(300) Hopkins Leseberg, J. A.; Henke, W. C.; Douglas, J. T.; Oliver, A. G.; Sydora, O. L.; Blakemore, J. D. Spectroscopic interrogation of the reduction of model chromium precatalysts for olefin oligomerization. *Organometallics* **2022**, *41*, 2240-2251.
(301) Grauke, R.; Schepper, R.; Rabeah, J.; Schoch, R.; Bentrup, U.; Bauer, M.; Brückner, A. Impact of al activators on structure and catalytic performance of cr catalysts in homogeneous ethylene oligomerization – a multitechnique in situ/operando study. *ChemCatChem* **2019**, *12*, 1025-1035.
(302) Hoover, J. M.; Ryland, B. L.; Stahl, S. S. Mechanism of copper(i)/tempo-catalyzed aerobic alcohol oxidation. *J Am Chem Soc* **2013**, *135*, 2357-2367.
(303) Kumpulainen, E. T.; Koskinen, A. M. Catalytic activity dependency on catalyst components in aerobic copper-tempo oxidation. *Chemistry* **2009**, *15*, 10901-10911.
(304) Rabeah, J.; Bentrup, U.; Stosser, R.; Bruckner, A. Selective alcohol oxidation by a copper tempo catalyst: Mechanistic insights by simultaneously coupled operando epr/uv-vis/atr-ir spectroscopy. *Angew Chem Int Ed Engl* **2015**, *54*, 11791-11794.
(305) Walroth, R. C.; Miles, K. C.; Lukens, J. T.; MacMillan, S. N.; Stahl, S. S.; Lancaster, K. M. Electronic structural analysis of copper(ii)-tempo/abno complexes provides evidence for copper(i)-oxoammonium character. *J Am Chem Soc* **2017**, *139*, 13507-13517.
(306) Preetz, A.; Drexler, H. J.; Fischer, C.; Dai, Z.; Borner, A.; Baumann, W.; Spannenberg, A.; Thede, R.; Heller, D. Rhodium-complex-catalyzed asymmetric hydrogenation: Transformation of precatalysts into active species. *Chemistry* **2008**, *14*, 1445-1451.
(307) Connors, K. A. Binding constants — the measurement of molecular complex stability. *Bunsenges Phys Chem* **1987**, *91*, 1398-1398.
(308) Landis, C. R.; Halpern, J. Asymmetric hydrogenation of methyl (z)-.Alpha.-acetamidocinnamate catalyzed by [1,2-bis(phenyl-o-anisoyl)phosphino)ethane]rhodium(i): Kinetics, mechanism and origin of enantioselection. *J Am Chem Soc* **2002**, *109*, 1746-1754.
(309) Berry, D. B. G.; Codina, A.; Clegg, I.; Lyall, C. L.; Lowe, J. P.; Hintermair, U. Insight into catalyst speciation and hydrogen co-evolution during enantioselective formic acid-driven transfer hydrogenation with bifunctional ruthenium complexes from multi-technique operando reaction monitoring. *Faraday Discuss* **2019**, *220*, 45-57.
(310) Johnson, T. C.; Morris, D. J.; Wills, M. Hydrogen generation from formic acid and alcohols using homogeneous catalysts. *Chem Soc Rev* **2010**, *39*, 81-88.
(311) Boddien, A.; Mellmann, D.; Gartner, F.; Jackstell, R.; Junge, H.; Dyson, P. J.; Laurenczy, G.; Ludwig, R.; Beller, M. Efficient dehydrogenation of formic acid using an iron catalyst. *Science* **2011**, *333*, 1733-1736.
(312) Mellmann, D.; Barsch, E.; Bauer, M.; Grabow, K.; Boddien, A.; Kammer, A.; Sponholz, P.; Bentrup, U.; Jackstell, R.; Junge, H.; et al. Base-free non-noble-metal-catalyzed hydrogen generation from formic acid: Scope and mechanistic insights. *Chemistry* **2014**, *20*, 13589-13602.

(313) Grabow, K.; Bentrup, U. Homogeneous catalytic processes monitored by combined in situ atr-ir, uv–vis, and raman spectroscopy. *ACS Catal* **2014**, *4*, 2153-2164.
(314) Li, Y.; Molina de La Torre, J. A.; Grabow, K.; Bentrup, U.; Junge, K.; Zhou, S.; Bruckner, A.; Beller, M. Selective reduction of amides to amines by boronic acid catalyzed hydrosilylation. *Angew Chem Int Ed Engl* **2013**, *52*, 11577-11580.
(315) Das, S.; Addis, D.; Knopke, L. R.; Bentrup, U.; Junge, K.; Bruckner, A.; Beller, M. Selective catalytic monoreduction of phthalimides and imidazolidine-2,4-diones. *Angew Chem Int Ed Engl* **2011**, *50*, 9180-9184.
(316) Knöpke, L. R.; Reimann, S.; Spannenberg, A.; Langer, P.; Brückner, A.; Bentrup, U. Elucidating the directing effect of lewis acids on the reaction pathway in formal [3+3] cyclocondensation reactions: A comprehensive in situ spectroscopic study. *ChemCatChem* **2011**, *3*, 1459-1468.
(317) Reimann, S.; Knöpke, L. R.; Spannenberg, A.; Brückner, A.; Kühn, O.; Langer, P.; Bentrup, U. Identification of reaction intermediates in alcl3-mediated cyclocondensation reactions by simultaneous in situ atr-ftir and uv–vis spectroscopy. *Tetrahedron* **2013**, *69*, 3338-3347.
(318) Jones, C. W.; Tao, F.; Garland, M. V. Introduction to special issue on operando and in situ studies of catalysis. *ACS Catal* **2012**, *2*, 2444-2445.
(319) Bentrup, U. Combining in situ characterization methods in one set-up: Looking with more eyes into the intricate chemistry of the synthesis and working of heterogeneous catalysts. *Chem Soc Rev* **2010**, *39*, 4718-4730.
(320) Bruckner, A. Killing three birds with one stone--simultaneous operando epr/uv-vis/raman spectroscopy for monitoring catalytic reactions. *Chem Commun (Camb)* **2005**, 1761-1763.
(321) Davidi, D.; Noor, E.; Liebermeister, W.; Bar-Even, A.; Flamholz, A.; Tummler, K.; Barenholz, U.; Goldenfeld, M.; Shlomi, T.; Milo, R. Global characterization of in vivo enzyme catalytic rates and their correspondence to in vitro kcat measurements. *Proceedings of the National Academy of Sciences* **2016**, *113*, 3401-3406.
(322) Eunen, K. v.; Bakker, B. M. The importance and challenges of in vivo-like enzyme kinetics. *Perspectives in Science* **2014**, *1*,
(323) Ross, M. O.; Macmillan, F.; Wang, J.; Nisthal, A.; Lawton, T. J.; Olafson, B. D.; Mayo, S. L.; Rosenzweig, A. C.; Hoffman, B. M. Particulate methane monooxygenase contains only mononuclear copper centers. *Science* **2019**, *364*, 566-570.
(324) Banerjee, R.; Jones, J. C.; Lipscomb, J. D. Soluble methane monooxygenase. *Annu Rev Biochem* **2019**, *88*, 409-431.
(325) Lee, S. K.; Nesheim, J. C.; Lipscomb, J. D. Transient intermediates of the methane monooxygenase catalytic cycle. *J Biol Chem* **1993**, *268*, 21569-21577.
(326) Brazeau, B. J.; Lipscomb, J. D. Kinetics and activation thermodynamics of methane monooxygenase compound q formation and reaction with substrates. *Biochemistry* **2000**, *39*, 13503-13515.
(327) Nesheim, J. C.; Lipscomb, J. D. Large kinetic isotope effects in methane oxidation catalyzed by methane monooxygenase: Evidence for c-h bond cleavage in a reaction cycle intermediate. *Biochemistry* **1996**, *35*, 10240-10247.
(328) Jacobs, A. B.; Banerjee, R.; Deweese, D. E.; Braun, A.; Babicz, J. T., Jr.; Gee, L. B.; Sutherlin, K. D.; Bottger, L. H.; Yoda, Y.; Saito, M.; et al. Nuclear resonance vibrational spectroscopic definition of the fe(iv)(2) intermediate q in methane monooxygenase and its reactivity. *J Am Chem Soc* **2021**, *143*, 16007-16029.
(329) Ling, J.; Nestor, L. P.; Czernuszewicz, R. S.; Spiro, T. G.; Fraczkiewicz, R.; Sharma, K. D.; Loehr, T. M.; Sanders-Loehr, J. Common oxygen binding site in hemocyanins from

arthropods and mollusks. Evidence from raman spectroscopy and normal coordinate analysis. *J Am Chem Soc* **2002**, *116*, 7682-7691.
(330) Kipouros, I.; Stanczak, A.; Ginsbach, J. W.; Andrikopoulos, P. C.; Rulisek, L.; Solomon, E. I. Elucidation of the tyrosinase/o(2)/monophenol ternary intermediate that dictates the monooxygenation mechanism in melanin biosynthesis. *Proc Natl Acad Sci U S A* **2022**, *119*, e2205619119.
(331) Solomon, E. I.; Szilagyi, R. K.; DeBeer George, S.; Basumallick, L. Electronic structures of metal sites in proteins and models: Contributions to function in blue copper proteins. *Chem Rev* **2004**, *104*, 419-458.
(332) Solomon, E. I.; Light, K. M.; Liu, L. V.; Srnec, M.; Wong, S. D. Geometric and electronic structure contributions to function in non-heme iron enzymes. *Acc Chem Res* **2013**, *46*, 2725-2739.
(333) Neese, F.; Solomon, E. I. Mcd c-term signs, saturation behavior, and determination of band polarizations in randomly oriented systems with spin s >/= (1)/(2). Applications to s = (1)/(2) and s = (5)/(2). *Inorg Chem* **1999**, *38*, 1847-1865.
(334) Vaillancourt, F. H.; Yin, J.; Walsh, C. T. Syrb2 in syringomycin e biosynthesis is a nonheme feii alpha-ketoglutarate- and o2-dependent halogenase. *Proc Natl Acad Sci U S A* **2005**, *102*, 10111-10116.
(335) Matthews, M. L.; Krest, C. M.; Barr, E. W.; Vaillancourt, F. H.; Walsh, C. T.; Green, M. T.; Krebs, C.; Bollinger, J. M. Substrate-triggered formation and remarkable stability of the c-h bond-cleaving chloroferryl intermediate in the aliphatic halogenase, syrb2. *Biochemistry* **2009**, *48*, 4331-4343.
(336) Srnec, M.; Wong, S. D.; Matthews, M. L.; Krebs, C.; Bollinger, J. M., Jr.; Solomon, E. I. Electronic structure of the ferryl intermediate in the alpha-ketoglutarate dependent non-heme iron halogenase syrb2: Contributions to h atom abstraction reactivity. *J Am Chem Soc* **2016**, *138*, 5110-5122.
(337) Srnec, M.; Iyer, S. R.; Dassama, L. M. K.; Park, K.; Wong, S. D.; Sutherlin, K. D.; Yoda, Y.; Kobayashi, Y.; Kurokuzu, M.; Saito, M.; et al. Nuclear resonance vibrational spectroscopic definition of the facial triad fe(iv) horizontal lineo intermediate in taurine dioxygenase: Evaluation of structural contributions to hydrogen atom abstraction. *J Am Chem Soc* **2020**, *142*, 18886-18896.
(338) Srnec, M.; Solomon, E. I. Frontier molecular orbital contributions to chlorination versus hydroxylation selectivity in the non-heme iron halogenase syrb2. *J Am Chem Soc* **2017**, *139*, 2396-2407.
(339) Wong, S. D.; Srnec, M.; Matthews, M. L.; Liu, L. V.; Kwak, Y.; Park, K.; Bell, C. B., 3rd; Alp, E. E.; Zhao, J.; Yoda, Y.; et al. Elucidation of the fe(iv)=o intermediate in the catalytic cycle of the halogenase syrb2. *Nature* **2013**, *499*, 320-323.
(340) Long, C.; Han, J.; Guo, J.; Yang, C.; Liu, S.; Tang, Z. Operando toolbox for heterogeneous interface in electrocatalysis. *Chem Catalysis* **2021**, *1*, 509-522.
(341) Corby, S.; Tecedor, M.-G.; Tengeler, S.; Steinert, C.; Moss, B.; Mesa, C. A.; Heiba, H. F.; Wilson, A. A.; Kaiser, B.; Jaegermann, W.; et al. Separating bulk and surface processes in niox electrocatalysts for water oxidation. *Sustainable Energy & Fuels* **2020**, *4*, 5024-5030.
(342) Jiang, S. P. Solid-state electrochemistry and solid oxide fuel cells: Status and future prospects. *Electrochemical Energy Reviews* **2022**, *5*, 21.
(343) Ros, C.; Carretero, N. M.; David, J.; Arbiol, J.; Andreu, T.; Morante, J. R. Insight into the degradation mechanisms of atomic layer deposited tio2 as photoanode protective layer. *ACS Appl Mater Interfaces* **2019**, *11*, 29725-29735.
(344) Rossmeisl, J.; Qu, Z. W.; Zhu, H.; Kroes, G. J.; Nørskov, J. K. Electrolysis of water on oxide surfaces. *J Electroanal Chem* **2007**, *607*, 83-89.

(345) Roy, S.; Huang, Z.; Bhunia, A.; Castner, A.; Gupta, A. K.; Zou, X.; Ott, S. Electrocatalytic hydrogen evolution from a cobaloxime-based metal-organic framework thin film. *J Am Chem Soc* **2019**, *141*, 15942-15950.
(346) Lin, S.; Diercks, C. S.; Zhang, Y. B.; Kornienko, N.; Nichols, E. M.; Zhao, Y.; Paris, A. R.; Kim, D.; Yang, P.; Yaghi, O. M.; Chang, C. J. Covalent organic frameworks comprising cobalt porphyrins for catalytic co(2) reduction in water. *Science* **2015**, *349*, 1208-1213.
(347) Bozal-Ginesta, C.; Rao, R. R.; Mesa, C. A.; Liu, X.; Hillman, S. A. J.; Stephens, I. E. L.; Durrant, J. R. Redox-state kinetics in water-oxidation irox electrocatalysts measured by operando spectroelectrochemistry. *ACS Catal* **2021**, *11*, 15013-15025.
(348) Bozal-Ginesta, C.; Rao, R. R.; Mesa, C. A.; Wang, Y.; Zhao, Y.; Hu, G.; Anton-Garcia, D.; Stephens, I. E. L.; Reisner, E.; Brudvig, G. W.; et al. Spectroelectrochemistry of water oxidation kinetics in molecular versus heterogeneous oxide iridium electrocatalysts. *J Am Chem Soc* **2022**, *144*, 8454-8459.
(349) Sinha, S. B.; Shopov, D. Y.; Sharninghausen, L. S.; Stein, C. J.; Mercado, B. Q.; Balcells, D.; Pedersen, T. B.; Reiher, M.; Brudvig, G. W.; Crabtree, R. H. Redox activity of oxo-bridged iridium dimers in an n,o-donor environment: Characterization of remarkably stable ir(iv,v) complexes. *J Am Chem Soc* **2017**, *139*, 9672-9683.
(350) Goldsmith, Z. K.; Harshan, A. K.; Gerken, J. B.; Voros, M.; Galli, G.; Stahl, S. S.; Hammes-Schiffer, S. Characterization of nife oxyhydroxide electrocatalysts by integrated electronic structure calculations and spectroelectrochemistry. *Proc Natl Acad Sci U S A* **2017**, *114*, 3050-3055.
(351) Hisatomi, T.; Kubota, J.; Domen, K. Recent advances in semiconductors for photocatalytic and photoelectrochemical water splitting. *Chem Soc Rev* **2014**, *43*, 7520-7535.
(352) Kisch, H. Semiconductor photocatalysis--mechanistic and synthetic aspects. *Angew Chem Int Ed Engl* **2013**, *52*, 812-847.
(353) Wu, X.; Xie, S.; Zhang, H.; Zhang, Q.; Sels, B. F.; Wang, Y. Metal sulfide photocatalysts for lignocellulose valorization. *Adv Mater* **2021**, *33*, e2007129.
(354) Wu, X.; Luo, N.; Xie, S.; Zhang, H.; Zhang, Q.; Wang, F.; Wang, Y. Photocatalytic transformations of lignocellulosic biomass into chemicals. *Chem Soc Rev* **2020**, *49*, 6198-6223.
(355) Schmermund, L.; Jurkaš, V.; Özgen, F. F.; Barone, G. D.; Büchsenschütz, H. C.; Winkler, C. K.; Schmidt, S.; Kourist, R.; Kroutil, W. Photo-biocatalysis: Biotransformations in the presence of light. *ACS Catal* **2019**, *9*, 4115-4144.
(356) Cao, N.; Xi, M.; Li, X.; Zheng, J.; Qian, L.; Dai, Y.; Song, X.; Hu, S. Recent developments in heterogeneous photocatalysts with near-infrared response. In *Symmetry*, 2022; Vol. 14.
(357) Kreft, S.; Schoch, R.; Schneidewind, J.; Rabeah, J.; Kondratenko, E. V.; Kondratenko, V. A.; Junge, H.; Bauer, M.; Wohlrab, S.; Beller, M. Improving selectivity and activity of co2 reduction photocatalysts with oxygen. *Chem* **2019**, *5*, 1818-1833.
(358) Yang, S.; Hu, W.; Zhang, X.; He, P.; Pattengale, B.; Liu, C.; Cendejas, M.; Hermans, I.; Zhang, X.; Zhang, J.; Huang, J. 2d covalent organic frameworks as intrinsic photocatalysts for visible light-driven co(2) reduction. *J Am Chem Soc* **2018**, *140*, 14614-14618.
(359) Fischer, S.; Hollmann, D.; Tschierlei, S.; Karnahl, M.; Rockstroh, N.; Barsch, E.; Schwarzbach, P.; Luo, S.-P.; Junge, H.; Beller, M.; et al. Death and rebirth: Photocatalytic hydrogen production by a self-organizing copper–iron system. *ACS Catal* **2014**, *4*, 1845-1849.
(360) Tian, L.; Till, N. A.; Kudisch, B.; MacMillan, D. W. C.; Scholes, G. D. Transient absorption spectroscopy offers mechanistic insights for an iridium/nickel-catalyzed c–o coupling. *J Am Chem Soc* **2020**, *142*, 4555-4559.

(361) Fang, J.; Wang, Y.; Kurashvili, M.; Rieger, S.; Kasprzyk, W.; Wang, Q.; Stolarczyk, J. K.; Feldmann, J.; Debnath, T. Simultaneous hydrogen generation and exciplex stimulated emission in photobasic carbon dots. *Angew Chem Int Ed* **2023**, *n/a*, e202305817.
(362) El-Zohry, A. M.; Turedi, B.; Alsalloum, A.; Maity, P.; Bakr, O. M.; Ooi, B. S.; Mohammed, O. F. Ultrafast transient infrared spectroscopy for probing trapping states in hybrid perovskite films. *Commun Chem* **2022**, *5*, 67.
(363) Wang, B.; Yang, S.-Z.; Chen, H.; Gao, Q.; Weng, Y.-X.; Zhu, W.; Liu, G.; Zhang, Y.; Ye, Y.; Zhu, H.; et al. Revealing the role of oxygen vacancies in bimetallic pbbio2br atomic layers for boosting photocatalytic co2 conversion. *Appl Catal B Env* **2020**, *277*, 119170.
(364) Wu, X.; Xie, S.; Liu, C.; Zhou, C.; Lin, J.; Kang, J.; Zhang, Q.; Wang, Z.; Wang, Y. Ligand-controlled photocatalysis of cds quantum dots for lignin valorization under visible light. *ACS Catal* **2019**, *9*, 8443-8451.
(365) Chen, G.-Z.; Chen, K.-J.; Fu, J.-W.; Liu, M. Tracking dynamic evolution of catalytic active sites in photocatalytic co2 reduction by in situ time-resolved spectroscopy. *Rare Metals* **2020**, *39*, 607-609.
(366) Hu, Y.; Zhan, F.; Wang, Q.; Sun, Y.; Yu, C.; Zhao, X.; Wang, H.; Long, R.; Zhang, G.; Gao, C.; et al. Tracking mechanistic pathway of photocatalytic co2 reaction at ni sites using operando, time-resolved spectroscopy. *J Am Chem Soc* **2020**, *142*, 5618-5626.
(367) Coles, M. S.; Quach, G.; Beves, J. E.; Moore, E. G. A photophysical study of sensitization-initiated electron transfer: Insights into the mechanism of photoredox activity. *Angew Chem Int Ed Engl* **2020**, *59*, 9522-9526.
(368) Wang, X.; Kafizas, A.; Li, X.; Moniz, S. J. A.; Reardon, P. J. T.; Tang, J.; Parkin, I. P.; Durrant, J. R. Transient absorption spectroscopy of anatase and rutile: The impact of morphology and phase on photocatalytic activity. *J Phys Chem C* **2015**, *119*, 10439-10447.
(369) Xu, F.; Meng, K.; Cao, S.; Jiang, C.; Chen, T.; Xu, J.; Yu, J. Step-by-step mechanism insights into the tio2/ce2s3 s-scheme photocatalyst for enhanced aniline production with water as a proton source. *ACS Catalysis* **2022**, *12*, 164-172.
(370) Liu, F.; Shi, R.; Wang, Z.; Weng, Y.; Che, C.-M.; Chen, Y. Direct z-scheme hetero-phase junction of black/red phosphorus for photocatalytic water splitting. *Angew Chem Int Ed* **2019**, *131*, 11917-11921.
(371) Wu, K.; Chen, Z.; Lv, H.; Zhu, H.; Hill, C. L.; Lian, T. Hole removal rate limits photodriven h2 generation efficiency in cds-pt and cdse/cds-pt semiconductor nanorod-metal tip heterostructures. *J Am Chem Soc* **2014**, *136*, 7708-7716.
(372) Wu, K.; Rodriguez-Cordoba, W. E.; Liu, Z.; Zhu, H.; Lian, T. Beyond band alignment: Hole localization driven formation of three spatially separated long-lived exciton states in cdse/cds nanorods. *ACS Nano* **2013**, *7*, 7173-7185.
(373) Wu, K.; Zhu, H.; Liu, Z.; Rodriguez-Cordoba, W.; Lian, T. Ultrafast charge separation and long-lived charge separated state in photocatalytic cds-pt nanorod heterostructures. *J Am Chem Soc* **2012**, *134*, 10337-10340.
(374) Wu, K.; Du, Y.; Tang, H.; Chen, Z.; Lian, T. Efficient extraction of trapped holes from colloidal cds nanorods. *J Am Chem Soc* **2015**, *137*, 10224-10230.
(375) Zou, Q.; Lu, Y. C. Solvent-dictated lithium sulfur redox reactions: An operando uv-vis spectroscopic study. *J Phys Chem Lett* **2016**, *7*, 1518-1525.
(376) Patel, M. U.; Demir-Cakan, R.; Morcrette, M.; Tarascon, J. M.; Gaberscek, M.; Dominko, R. Li-s battery analyzed by uv/vis in operando mode. *ChemSusChem* **2013**, *6*, 1177-1181.
(377) Ríos-Reina, R.; Azcarate, S. M. How chemometrics revives the uv-vis spectroscopy applications as an analytical sensor for spectralprint (nontargeted) analysis. In *Chemosensors*, 2023; Vol. 11.

(378) Farahmand Nejad, M. A.; Ranjbar, S.; Parolo, C.; Nguyen, E. P.; Álvarez-Diduk, R.; Hormozi-Nezhad, M. R.; Merkoçi, A. Electrochromism: An emerging and promising approach in (bio)sensing technology. *Mater Today* **2021**, *50*, 476-498.
(379) Raj, S. I.; Jaiswal, A.; Uddin, I. Ultrasmall aqueous starch-capped cus quantum dots with tunable localized surface plasmon resonance and composition for the selective and sensitive detection of mercury(ii) ions. *RSC Advances* **2020**, *10*, 14050-14059.

6. Acknowledgements

The following funding sources are acknowledged for supporting this work; The Flemish Research Fund for project grant G0A0321N to B.F.S. and for the post-doctoral fellowship 12S1822N to X.W. The Anne T. and Robert M. Bass Stanford Graduate Fellowship to A.J.H. The National Institutes of Health grants R01DK031450 and R35GM145202 to E.I.S.

7. List of abbreviations

6MR	6-membered ring
8MR	8-membered ring
ATR	attenuated total reflection
BAS	Brønsted acid sites
BP/RP	black/red phosphorus
CB	conduction band
CBM	conduction band minimum
CCD	charge coupled device
CD	circular dichroism
CHHP	cyclohexyl hydroperoxide
COD	cyclooctadiene
cod	cylooctadiene group
coe	cyclooctene complex
CASPT2	complete active space perturbation theory 2
CT	charge transfer
CV	cyclic voltammetry
CVB	covalent bonds
CVE	cumulative variance explained
DQ	double-quantum
DRIFTS	diffuse reflectance infrared fourier transform spectroscopy
DRS	diffuse reflectance spectroscopy
ECCD	Exciton-Coupled Circular Dichroism
ee	enantiomeric excess
EPR	electron paramagnetic resonance
ESA	excited state absorption
EVE	ethyl vinyl ether
EXAFS	extended X-ray absorption fine structure
FMO	frontier molecular orbitals
FTIR	fourier-transform infrared spectroscopy
GC	gas chromatography
GSB	ground state bleach

HAA	hydrogen atom abstraction
HCP	hydrocarbon pool
HMB^+	hexamethylbenzenium
HOMO	highest occupied molecular orbitals
HPLC	high performance liquid chromatography
HTS	high-throughput screening
IR	infrared
KIE	kinetic isotope effect
K-M	Kubelka-Munk
LAS	Lewis acid sites
LC	liquid chromatography
LMCT	ligand-to-metal charge transfer
LSPR	localized surface plasmon resonance
LUMO	lowest unoccupied orbitals
MAS	magic angle spinning
MCD	magnetic circular dichroism
MCR	multivariate curve resolution
MCR-ALS	multivariate curve resolution-alternating least squares
MES	modulation excitation spectroscopy
MLCT	metal-to-ligand charge transfer
MMAO	modified methylaluminoxane
MOF	metal-organic framework
MS	mass spectrometry
MTA	methanol-to-aromatics
MTG	methanol-to-gasoline
MTH	methanol conversions to hydrocarbons
MTM	methane to methanol
MTO	methanol-to-olefins
NMI	*N-methylimidazole*
NMR	Nuclear magnetic resonance
NNMF	non-negative matrix factorization
NPs	nanometer particles
NRs	nanorods
NRVS	nuclear resonance vibrational spectroscopy
OAT	oxygen atom transfer
OCP	open-circuit potential
ODH	oxidative dehydrogenation
OER	oxygen evolution reaction
PCA	principal components analysis
PDI	*N*,*N*-bis(2,6-diisopropylphenyl)-perylene-3,4,9,10-bisdicarboximide
PP	μ-chloro dinuclear diphosphine
PP_3	$P(CH_2CH_2PPh_2)_3$
PTZ	Phenothiazine
QDs	quantum dots
QM/MM	quantum mechanics/molecular mechanics
RFDR	radio frequency driven recoupling
RFQ	rapid freeze quench

rR	resonance Raman
RWGS	reverse water-gas shift
SAC	single atom catalysts
SCR	Selective catalytic reduction
SE	stimulated emission
sMMO	soluble methane monooxygenase
SOC	spin orbit coupling
SSITKA	steady state isotope transient kinetic analysis
T&R	transmission and reflectance
TA	transient absorption
TAP	transient analysis of products
TAS	transient absorption spectroscopy
TBAF	tetra-n-butylammonium fluoride
TD-DFT	time-dependent density-functional theory
TEMPO	(2,2,6,6-tetramethylpiperidin-1-yl)oxyl
TMI	transition metal ions
TMO	transition metal oxides
TOF	turnover frequency
TON	turnover number
TS	Transition state
Ty	tyrosinase
UV-VIS-NIR	ultraviolet-visible-near infrared
VB	valence band
VT	variable-temperature
VTVH	variable-temperature-variable-field
WGS	water-gas shift
XANES	X-ray absorption near edge structure
XAS	X-ray absorption spectroscopy
XRD	X-ray diffraction

8. Biographies

Edward I. Solomon

Edward I. Solomon grew up in North Miami Beach, FL, received his Ph.D. at Princeton (with D. S. McClure), and was a postdoctoral fellow at The Ørsted Institute (with C. J. Ballhausen) and then at Caltech (with H. B. Gray). He was a professor at the Massachusetts Institute of Technology until 1982, when he joined the faculty at Stanford University, where he is now the Monroe E. Spaght Professor of Humanities and Sciences and Professor of Photon Science at the SLAC National Accelerator Lab. He has been an invited professor in Argentina, Australia, Brazil, China, France, India, and Japan. Prof. Solomon's research is in the fields of physical inorganic chemistry and bioinorganic chemistry with emphasis on the application of a wide range of spectroscopic methods combined with QM calculations to elucidate the electronic structure of transition metal sites and its contribution to physical properties and reactivity. He has received a wide range of medals and awards and is a member of the National Academy of

Sciences and the American Academy of Arts and Sciences and a fellow in the American Association for the Advancement of Science and the American Chemical Society.

Alexander Heyer

Alexander J. Heyer received his B.S. in chemistry at the University of Virginia where he researched proton-coupled electron transfer in Mo and W scorpionate complexes with Professor Dean Harman. He is now a Ph.D. student in inorganic chemistry at Stanford University in Professor Edward Solomon's research group. Using both spectroscopic and computational methods, he studies methane oxidation in Cu and Fe zeolites, and his research is supported by the Anne T. and Robert M. Bass Stanford Graduate Fellowship.

Bert F. Sels

Bert F. Sels (1972), currently full professor at KU Leuven (Belgium), obtained his Ph.D. in 2000 in the field of heterogeneous oxidation catalysis under the guidance of Prof. Pierre Jacobs. He was awarded the DSM Chemistry Award in 2000, the Incentive Award by the Belgian Chemical Society in 2005, and the international Green Chemistry Award in 2015. He currently leads the Centre for Sustainable Catalysis and Engineering (CSCE), and is active in designing heterogeneous catalysts for future challenges in industrial organic and environmental catalysis. His expertise includes heterogeneous catalysis in biorefineries, design of hierarchical zeolites and carbons, and the spectroscopic and kinetic study of active sites for small-molecule activation. He is cochair of the Catalysis Commission of the International Zeolite Association (IZA) and cofounder of the European Research Institute of Catalysis (ERIC). He is also a member of the European Academy of Sciences and Arts, member of the international advisory board of ChemSusChem (Wiley), and associate editor of ACS Sustainable Chemistry & Engineering.

Dieter Plessers

Dieter Plessers obtained his M.Sc. in Bioscience Engineering focused on catalytic technology from KU Leuven in 2017, with a Master's thesis on the identification of the active sites in copper- and iron-exchanged zeolites for the selective oxidation of methane to methanol. Supported by a grant from the Research Foundation - Flanders (FWO), he obtained a Ph.D. at the Center for Sustainable Catalysis and Engineering (CSCE) under the guidance of Prof. Bert Sels, where he used spectroscopy and kinetic analyses to identify the copper speciation on copper-exchanged zeolites and quantify their reactivity in methane activation. This topic continues to be his primary research interest as a postdoctoral researcher in the framework of an FWO research grant.

Fatima Rammal

Fatima Rammal received in 2015 her B.Sc. in chemistry from the Lebanese university, Beirut, and her Master's degree in organic and pharmaceutical chemistry in 2017 from the University of Paris Saclay, France. In December 2020, she obtained her Ph.D. degree in organic and photochemistry from the University of Caen, France, under the supervision of Dr Sami Lakhdar. During her research, she developed novel visible light mediated processes for the aromatization of polycyclic compounds, as well as for the functionalization of *N*-heteroarenes using several

non-activated radical precursors such as alkane, methanol, silane, and [1.1.1]propellane. Since February 2021, she is a postdoctoral researcher in the group of Prof. Bert Sels at the center for sustainable catalysis and engineering, KU Leuven, Belgium, working on the heterogeneous catalysis for biomass valorization and CO_2 conversion.

Jing Ma

Jing Ma received her B.Sc. in chemical engineering from the Sichuan University in 2019. In 2021, she obtained her M.Sc. in chemical system engineering at the University of Tokyo. In Tokyo she researched the influence of Al distribution in ZSM-5 zeolites on MTO reactions by transient kinetic methods, working with Professor Ogura Masaru and Dr. Takahiko Moteki. Supported by a grant from the FWO, she is currently pursuing a Ph.D. at KU Leuven under the guidance of Professor Bert Sels. Her research focuses on the investigation of methane oxidation in copper-exchanged zeolites by spectroscopic methods.

Max L. Bols

Max L. Bols received his B.Sc. and M.Sc. in bioscience engineering at the KU Leuven in 2015, doing his master's thesis on the identification of the active site in iron zeolites for methane activation. Upon graduation, he started a Ph.D. with Dr. Benjamin Snyder, Prof. Bert Sels and Prof. Robert Schoonheydt on the synthesis, kinetics, and spectroscopic characterization of transition metal active sites in zeolites, supported by a FWO research grant. He continued this research as an FWO postdoctoral fellow, in collaboration with Prof. Edward Solomon at Stanford University. He is now a postdoctoral researcher at the Laboratory of Chemical Technology of Ghent University working on molecular modelling, spectroscopy, and kinetic studies for the characterization of heterogeneous catalysts.

Robert A. Schoonheydt

Robert A. Schoonheydt is emeritus professor of the KU Leuven, where he obtained his bioengineering degree in 1966 and his Ph.D. in 1970 under the guidance of Prof. Jan B. Uytterhoeven. He did a postdoc in the chemistry department of the Texas A&M University under the guidance of Jack H. Lunsford on adsorption of SO_2 on MgO. His research interests at the KU Leuven are the surface chemistry of clay minerals and zeolites with special emphasis on transition metal ions and spectroscopy. Presently he is a member of an international research collaboration of zeolite chemists, spectroscopists, and quantum chemists on active sites in Cu- and Fe-zeolites for selective oxidation, NO_x abatement, and electrophilic aromatic substitution reactions. He was dean of the Faculty of Bioscience Engineering from 1998 until 2004 and president of the International Association for the Study of Clays from 2001 until 2005.

Sara Navarro-Jaén

Sara Navarro-Jaén received her Ph.D. degree in Science and Technology of New Materials from the University of Seville (Spain) in 2019, under the supervision of Prof. José A. Odriozola. She then joined the UCCS CNRS laboratory (France) as a postdoctoral fellow in the groups of Dr. Andrei Khodakov and Prof. Franck Dumeignil. Since 2022 she works as a researcher at KU Leuven (Belgium), in the group of Prof. Bert Sels. Her research interests focus on the design of catalytic materials with environmental applications and the understanding of the

underlying reaction mechanisms, ranging from conversion of GHGs into fuels and chemicals to biomass valorization.

Xuejiao Wu

Xuejiao Wu received her B.Sc. degree (2015) from Xiamen University and obtained her Ph.D. degree (2020) from Xiamen University under the supervision of Prof. Ye Wang. She then carried out postdoctoral research at Prof. Bert F. Sels group at KU Leuven. Her research focuses on the valorization of lignocellulose, in particular by photocatalytic approaches.

9. Abstract figure

